CONSEJO SUPERIOR DE
INVESTIGACIONES CIENTÍFICAS

UNIVERSIDAD AUTÓNOMA DE MADRID

DISEÑO Y PROCESAMIENTO DE NUEVOS MATERIALES COMPUESTOS CERÁMICA-METAL (BIOCERMETS) PARA SU USO EN IMPLANTES MÉDICOS

Memoria presentada para optar al grado de
DOCTOR EN CIENCIAS FISICAS

ANTON SMIRNOV

Director:
Dr. JOSÉ FLORINDO BARTOLOMÉ GÓMEZ

Instituto de Ciencia de Materiales de Madrid
Madrid 2016

CONSEJO SUPERIOR DE
INVESTIGACIONES CIENTÍFICAS

UNIVERSIDAD AUTÓNOMA DE MADRID

DESIGN AND FABRICATION OF NEW CERAMIC-METAL COMPOSITES (BIOCERMETS) FOR HARD TISSUE REPLACEMENT APPLICATIONS

Thesis submitted for the degree of
DOCTOR OF PHILOSOPHY IN PHYSICS

ANTON SMIRNOV

Supervisor:
Dr. JOSÉ FLORINDO BARTOLOMÉ GÓMEZ

Instituto de Ciencia de Materiales de Madrid
Madrid 2016

To my parents

ACKNOWLEDGEMENTS

First of all, I thank Prof. José Serafín Moya for the opportinity to start the work at the Instituto de Ciencia de Materiales de Madrid (ICMM - CSIC). His knowledge and assistance will always be remembered. Thank you for intellectual contribution to my research and support during my studies.

Also, I would like to thank my tutor Prof. Miguel Manso Silván for his academic guidance and support.

The success of this thesis is attributed to the extensive support and assistance from my supervisor, Dr. José Florindo Bartolomé. I deeply thank him for his invaluable advice and guidance throughout the research work, which was done at the Department of Biomaterials and Bioinspired Materials of Instituto de Ciencia de Materiales de Madrid (ICMM - CSIC). I would like to express my gratitude for his help whenever I had a problem with my work or any problem during my staying in Spain. Thank you for unlimited patience and for pushing me to learn and grow while reminding me to laugh and have fun throughout the work as well as being my professional guru and friend.

Prof. Frank A. Müller and his team are gratefully acknowledged for the guidance and teaching during the experimental work, which was done at the laboratories of Otto Schott Institute of Materials Research (Jena, Germany). Danke (‘Thank you’) for your support and friendship. I would especially like to thank André, Clemens and Anne for their patience and help.

I would like to thank Prof. Ramón Torrecillas San Millán, director of the Nanomaterials and Nanotechnology Research Center (Oviedo, Spain), and his group for

sintering zirconia based composites for this project. In particular I would like to thank Toño, Teresa, Belen and Carlos for their kindness, help and friendship.

I'd like to thank to Mª Carmen Muñoz and Juan Ignacio Beltrán for theoretical calculations.

I would like to express my thank to Dr. Ramiro Couceiro Otero (Health Research Institute of Santiago, Santiago de Compostela, Spain), Dr. Arturo Martínez–Insúa (Instituto de Cerámica de Galicia, Universidad de Santiago de Compostela, Spain) and Dr. Roberto López-Píriz (Minimally Invasive Surgery Center, Cáceres, Spain) for their support in preparing meticulous clinical and statistical expertise as well as for clarifying results obtained *in vitro* and *in vivo* studies of the specimens used in this work.

I also would like to thank my friends and colleagues; Ivan, Pedro, Teresa, Maviael, Lola, Rocio, Nines, Leticia, Raul and Gustavo for their encouragement and friendship. I am grateful to all staff of the Instituto de Ciencia de Materiales de Madrid for their kindness and support.

Most importantly, I would like to thank my parents and family. This PhD degree could not have been possible without their endless love, encouragement and support. My special thanks are due to MDSGV for her love, encouragement and immeasurable support.

Last, but not least, I would like to thank all the organizations that financially supported this work, including Spanish National Research Council (JAE PreDoc 2010 fellowship), Spanish Ministry of Science and Innovation (project MAT2012-38645) and German Academic Exchange Service (project Re. 57050270).

Madrid, February 2016

Anton Smirnov

RESUMEN

Hasta la fecha los biomateriales utilizados en implantes estructurales han sido seleccionados por sus propiedades mecánicas y por tener una influencia nula o muy pequeña en los tejidos vivos que los rodean. Estos materiales satisfacen exclusivamente las condiciones de carga impuestas en entornos fisiológicos pero no reproducen fielmente las propiedades mecánicas, químicas y la compleja arquitectura del hueso. La diferencia entre las propiedades elásticas correspondientes al implante y el hueso adyacente genera una desigual aplicación de carga que provoca la pérdida de fijación del implante y su posible rotura. La naturaleza magnética de los implantes de acero y los formados por aleaciones de Co-Cr provoca una interacción con los campos magnéticos durante las pruebas de diagnósticos realizadas por resonancia magnética nuclear (RMN), lo que da lugar a calentamiento y/o movimiento del implante o artefactos en las imágenes producidas. Las sensibilidad y/o alergias a los implantes metálicos y la posible relación con efectos cancerígenos desarrollados en un periodo corto de tiempo hacen imperativa la eliminación del uso de metales tóxicos en los implantes. Por otro lado, los materiales cerámicos que se utilizan hoy en día (alumina y circona) presentan problemas de fragilidad y envejecimiento. Además, los diferentes materiales usados en prótesis articulares (polímero principalmente) presentan importantes problemas clínicos debidos a su gran desgaste y la generación de partículas.

Por lo tanto, tras décadas de investigación todavía existe la necesidad de desarrollar implantes con adecuadas propiedades mecánicas, biocompatibilidad, alta resistencia a la corrosion y bajo desgaste, así como una buena osteointegración. (Fig. 1).

Fig.1. Propiedades que un biomaterial ideal debe tener

En la presente tesis se han desarrollado nuevos materiales multifuncionales con matrices cerámicas (3Y-TZP, Al_2O_3) con alta dureza, resistencia al desgaste e inercia química reforzados con un metal (Tántalo) no tóxico ni magnéticos mediante diferentes rutas de procesamiento de polvos (homogeneización en vía líquida o vaporización por láser) y sinterización (sin presión, prensado en caliente o por descarga de plasma) y con diferentes microarquitecturas (nano-micro-macro).

Se han evaluado las propiedades mecánica tanto en condiciones críticas como subcríticas (fatiga) y las propiedades tribológicas, obteniéndose materiales con altas prestaciones mecánicas. Además también se han determinado las propiedades frente al envejecimiento acelerado, indicando que los materiales desarrollados tienen un comportamiento estable frente al envejecimiento. Por otro lado se ha evaluado su biocompatibilidad mediante estudios de proliferación celular *in vitro* (células madre mesenquimales humanas) e *in vivo*

(conejos y perros), que han puesto de manifiesto que estos materiales presentan una alto grado de biocompatibilidad. También, se han realizado estudios de RMN de los materiales implantados, demostrando su completa compatibilidad con esta técnica de diagnóstico.

Esta nueva familia de biomateriales muestra una combinación óptima de propiedades (mecánicas, tribológicas y biológicas) que son obtenidas mediante una sinergia de mecanismos a multiples escalas. Esto abre la posibilidad de producir nuevos biomateriales con propiedades específicas para su uso en una gran variedad de aplicaciones como materiales implantables. Algunos ejemplos del rango de estas aplicaciones incluyen implantes articulares (rodilla, cadera, hombro, tobillo), implantes dentales (pernos y pilares), implantes espinales (fijación lumbar y cervical, mecanismos de estabilización, espaciadores, injertos de fusión), fijaciones óseas (tornillos, placas, etc.), y cirugía maxilofacial (Fig. 2).

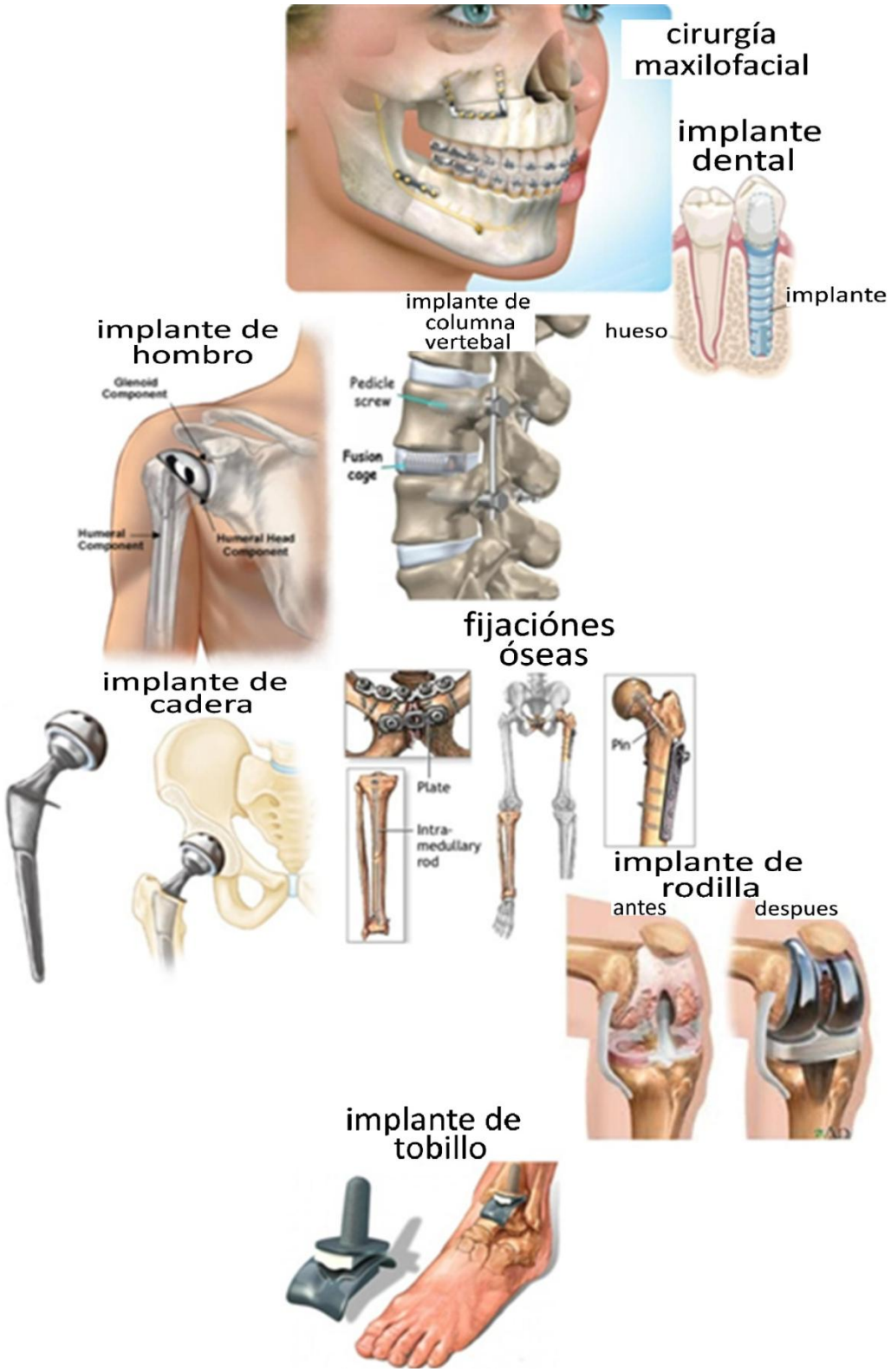

Fig.2. Implantes médicos estructurales

ABSTRACT

Traditional biomaterials for hard tissue replacement up to now have been selected based on their mechanical properties and their ability to remain inert *in vivo*; this selection has provided materials that satisfy only physiological loading conditions but do not duplicate the mechanical, chemical, and architectural properties of bone. Mismatch of mechanical properties between an implant and surrounding bone may lead to stress and strain imbalances that cause implant loosening and eventual failure. Magnetic nature of stainless steel and cobalt-chromium implants provokes an interaction with the magnetic fields present during MR imaging that result in device movement, device heating or development of an artefact on the collected image. Sensitization and/or elicitation of contact allergy to orthopaedic metallic implants and possible carcinogenic (cancer causing) effects in the medium-short time, then in the near future any toxic metal containing implant has to be avoided. Ceramic implants (alumina and zirconia) present low toughness and susceptibility to flaws, when introduced either during processing or in service. Additionally, zirconia (Y-TZP) ceramics show aging problems. In spite of the various forms of materials combination used for prosthetic implants, the wear of the articulating surface has been the major problem encountered in clinics, especially in the case of total bone replacement.

Therefore, after decades of research there is still a need for developing implants with suitable mechanical properties, biocompatibility, high corrosion resistance and low wear, as well as a good osseointegration (Fig. 1).

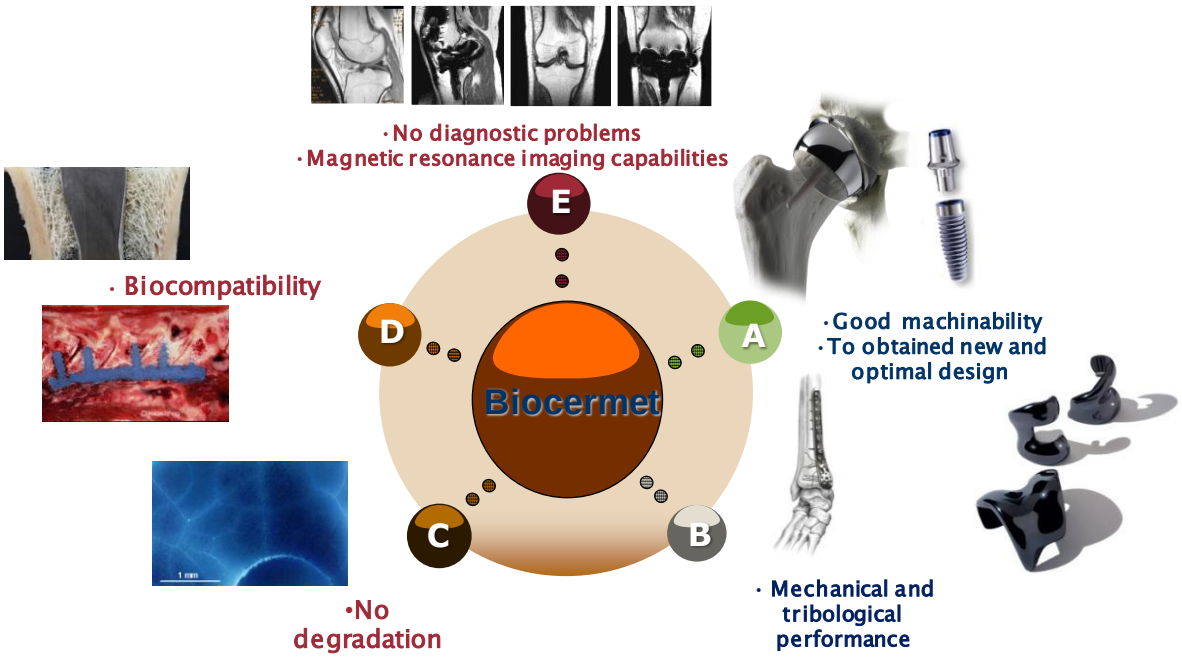

Fig.1. Unique properties that any biomaterial should posses

In the present PhD Thesis new multifunctional materials containing chemically inert nature, wear resistance and hardness ceramics (3Y-TZP, Al_2O_3) reinforced by non-toxic and non-magnetic metal (Tantalum) were fabricated by different routes of ceramic powders mixture preparation (wet mixing and laser vaporization) and sintering (without and with applied pressure). The variety of formed structural architectures from nano to micro-macro levels ensure excellent composites' mechanical properties under static and cyclic loading accompanied by a tribological performance. In comparison with commercially available tetragonal zirconia stabilized with 3 mol% of yttria, the obtained compositions showed significant enhancement of resistance towards low-temperature degradation.

In vitro studies (mesenquimal cells) and *in vivo* studies in New Zealand white rabbits and Beagle dogs revealed that 3Y-TZP/Ta biocermets appeared to be biocompatible. Moreover, Magnetic Resonance Imaging (MRI) results confirmed compatibility of this diagnostic technique with the new developed biocermet.

These new family of biomaterials has an optimal combination of properties (mechanical, tribological and biological) that have been developed using synergistic mechanisms at multiple lengths scales. This opens the possibility to produce novel biomaterials with such properties to make implants for a variety of different hard tissue replacement applications. Some examples of the range of applications include load bearing applications (hip, knee, shoulder, ankle), plates for fractures, dental implants (posts), screws and staples, spinal implants, maxillofacial surgery to name just a few (Fig. 2).

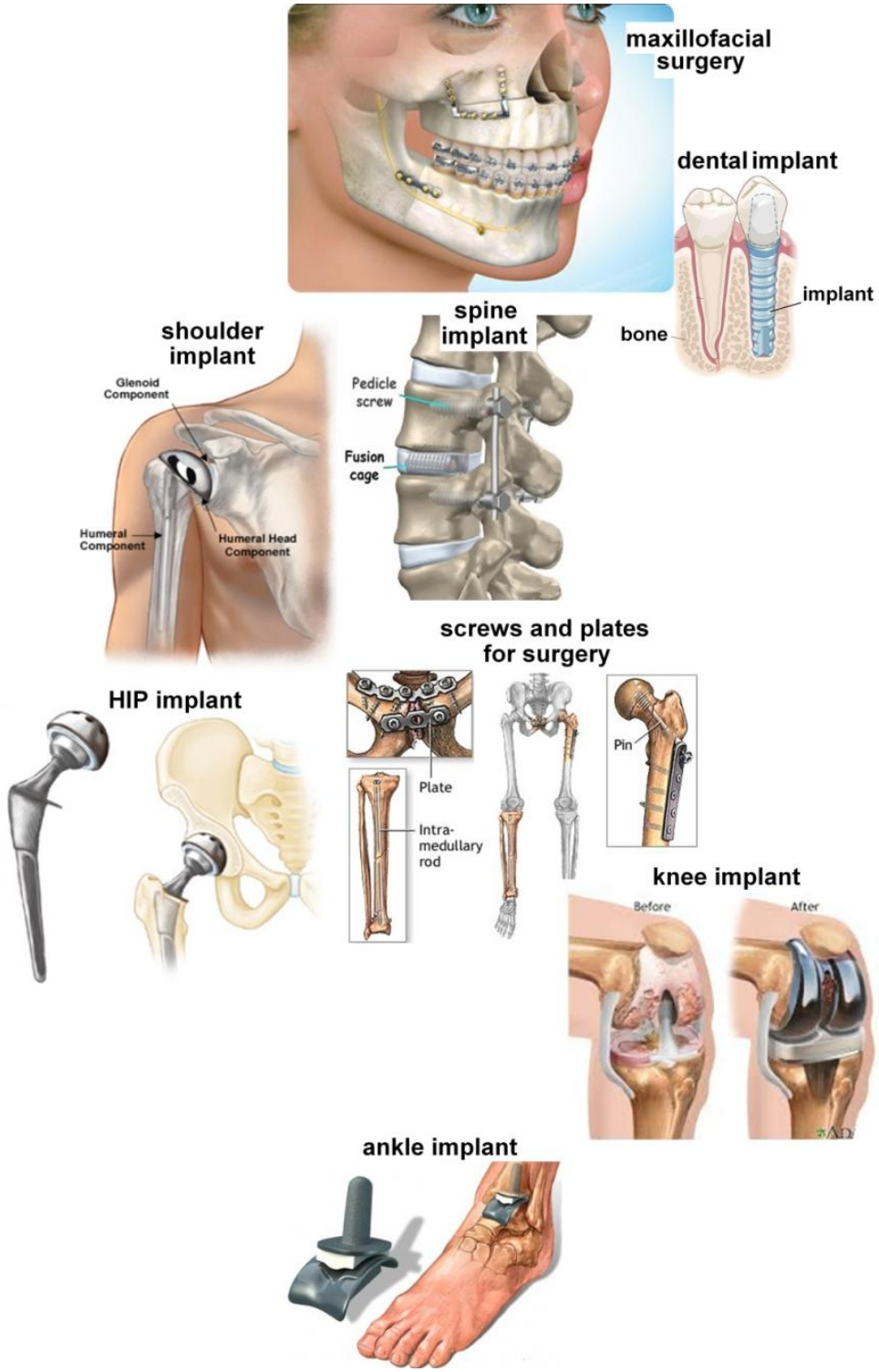

Fig.2. Hard tissue replacement implants

INDEX/ÍNDICE

1

Introduction

1.1 STATE OF THE ART

Worldwide, the number of people affected from bone and joint disorders was estimated to be 1.78 billion in 2012, with spinal and lower extremity disabilities being the most prevalent [1]. In 2010-2011, the number of musculoskeletal surgeries in the US alone was 3.79 million [2], with joint arthroplasty accounting for more than half of this total [3-7]. Further, from a global perspective, approximately 2.9 million joint replacement surgeries take place annually, including more than 1.4 million hip, 1.1 million knee and over 100000 shoulder replacements [8]. Fig.1.1-1 represents the biomaterials market by area of clinical focus, 2011 ($ millions).

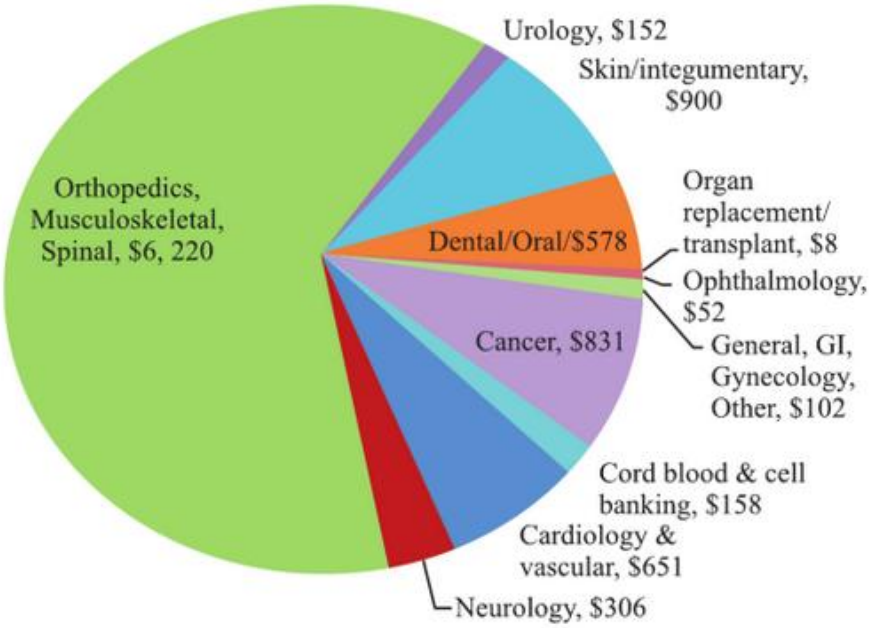

Fig.1.1-1. Status of biomaterial application for various tissue/organ regeneration and its market value. Source: MedMarket Diligence, LLC; Report #S520, "Tissue Engineering, Cell Therapy and Transplantation: Products, Technologies & Market Opportunities, Worldwide, 2009-2018."

During the last decades of the 20th century more than 40 different materials (ceramics, metals, polymers, composites) used for the treatment, repair and replacement of over 40 different parts of the human body including skin, muscle, blood vessels, nerves, and

bone tissue (Fig.1.1-2). The field of biomaterials is multidisciplinary and the design of biomaterials requires the synergistic interaction of materials science, biological science, chemical science, medical science and engineering.

In order to properly assess the performance of a biomaterial or of an implant, studies must be focused on different aspects, concerning both the intrinsic properties of the materials and the responses of the human body to the introduced devices. First, the mechanical, physical, and chemical behavior of the material in the biological environment must be studied, i.e. its resistance to fracture, fatigue, wear, corrosion. Then, its biocompatibility must be investigated and verified, by the analysis and identification of the reactions which occur at the interface between the material and live tissue, for example at the interface between the bone and the prosthesis or the graft. Thus, the success of an implant in the body depends on several factors, such as the materials properties, the design, and the biocompatibility as well as other factors out of engineer control, including the technique of surgery, the health of the patient, and the degree of his activities.

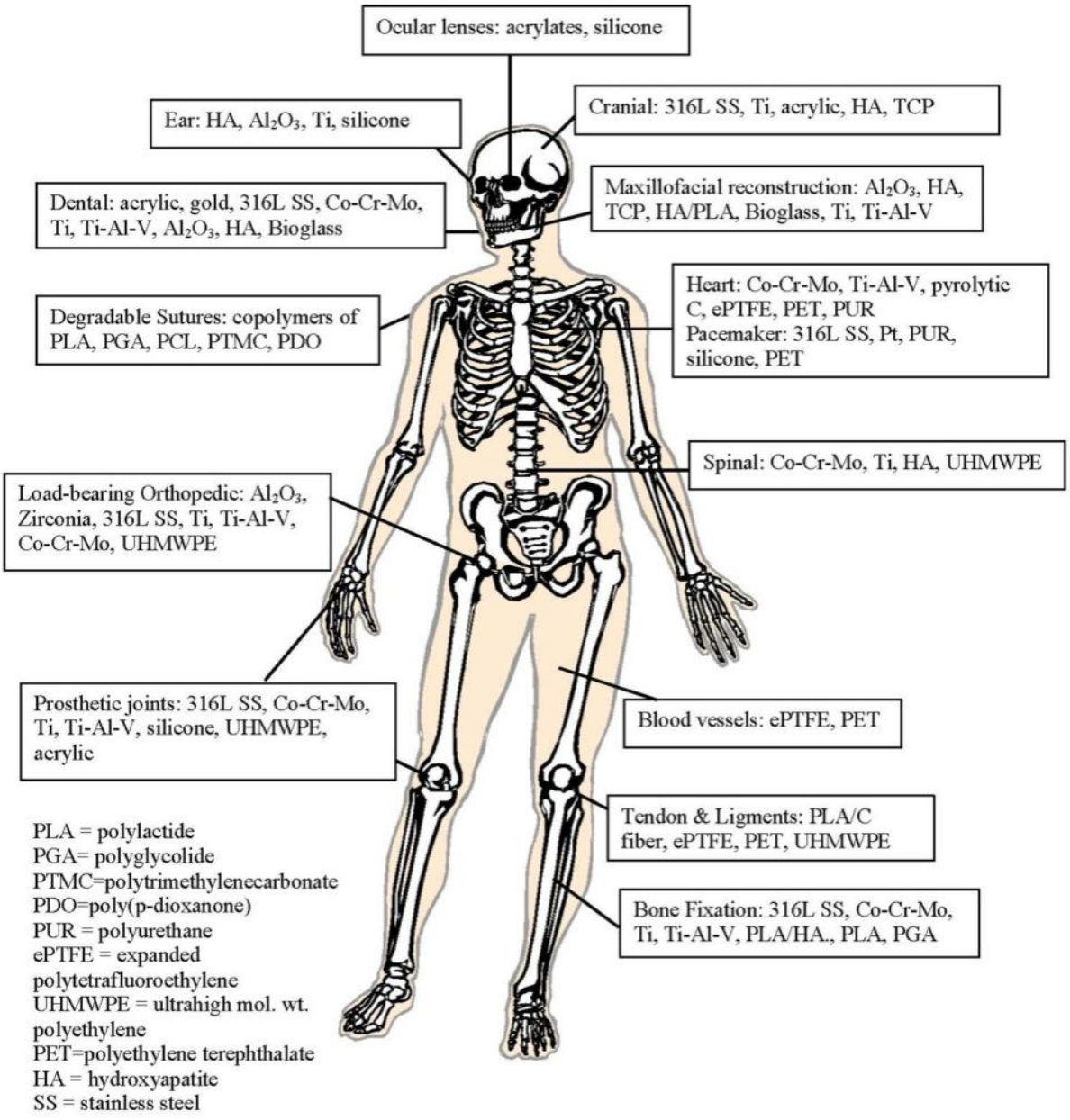

Fig.1.1-2. Materials for biomedical applications [9]

1.2 ARTIFICIAL BIOMATERIALS FOR IMPLANTS

All biomaterials are being developed to maintain a balance between the mechanical properties of the replaced tissues and the biochemical effects of the material on the tissue. Both areas are of great importance as far as the clinical success of materials is concerned. However, in most (if not all) implants integrated in biological systems, a range of properties is required e.g. elastic properties similarity, no diagnostic problems, osseointegration, no post-operative infection problems etc.

The ideal material or material combination should exhibit the following properties:

- A biocompatible chemical composition to avoid adverse tissue reactions
- Excellent resistance to degradation (e.g., corrosion resistance for metals or resistance to biological degradation in polymers)
- Acceptable strength to sustain cyclic loading endured by the joint
- A low modulus to minimize bone resorption
- High wear resistance to minimize wear debris generation

Therefore, often a clinical need can only be fulfilled by a designed material, which exhibits a complex combination of some of the above mentioned properties. In general, most artificial biomaterials for implants can be divided into the following categories: metals, polymers, ceramics, and composites.

1.2.1 Polymeric biomaterials

Polymeric biomaterials are usually used for their flexibility and stability, but have also been used for low friction articulating surfaces. Their applications range from facial prostheses to tracheal tubes, from kidney and liver parts to heart components, and from dentures to hip and knee joints. The main advantages compared to metal or ceramic materials are its easy manufacturability that allows to produce different shapes (latex, film, sheet, fibers, etc.), low coefficients of friction, reasonable cost, and wide range of

mechanical and physical properties. However, polymeric materials easily absorb water and biomolecules from the biological medium. They also may release degradation substances such as toxic monomers, catalysts or additives in the body.

One of the most common biomaterials combinations used for heavy load bearing applications is the ultrahigh molecular weight polyethylene (UHMWPE) against ceramics or metals. This material is virtually inert in the body environment and has excellent wear-resistance characteristics; furthermore, it has a very low coefficient of friction when in contact with the materials used for the ball component of the socket. It is used as the bearing surface in total joint arthroplasty, and it has found 90% success rates in 15 years with metal on polyethylene [10]. Nevertheless, it has been reported that fine UHMWPE wear debris, generated primarily at the interface between the femoral head and the acetabular cup, promotes osteolysis [11, 12]. This wear particle induced bone loss is one of the main problems affecting the long-term stability of UHMWPE in load bearing implants [13, 14]. Fig.1.2-1 shows morphologies of worn UHMWPE of a polyethylene liner and knee articulating surface. In addition, these materials cannot replace other materials if the higher strengths and fracture toughness are needed in bio-application.

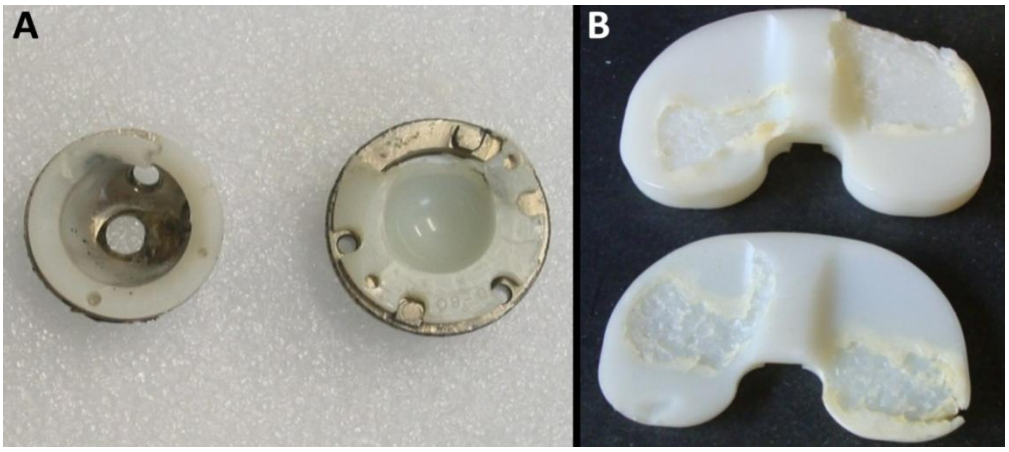

Fig.1.2-1. Representative images of retrieved polyethylene liner (A) and articulating suface (B) from patients with extensive wear, delamination and cracks

1.2.2 Metals and metallic alloys for bioapplication

Metals and metallic alloys are the most common materials used for total bone replacement or implant fixations, as the mechanical properties of metals meet the requirements for load bearing bone applications. There are three main metal alloys used in the production of joint prostheses: stainless steel based alloys; cobalt alloys; and titanium alloys. However, orthopaedic metallic implants are associated with local and remote adverse tissue responses. Generally, these adverse effects are mediated by the degradation products of implanted materials, which are primarily generated by wear and corrosion of metals in body fluids (Fig.1.2-2). Corrosion products can accumulate tissues encapsulating the implant [15].

Fig.1.2-2. Corrosion that led to chromium and cobalt poisoning

Corrosion releases metal ions which enter the bloodstream and become concentrated in the erythrocytes. Thus, metal ions may enter cells and remain in local tissues or they can be transported throughout the body, which can lead to cytotoxic, genotoxic and immunological effects, either locally or at the distance from the implant [16].

It has been found, that in the particular cases the ions of nickel, chromium and cobalt, which are released from SUS 316L or Co–Cr alloys respectively, lead to the hypersensitivity reactions and even to carcinogenesis (Fig. 1.2-3) [17-21].

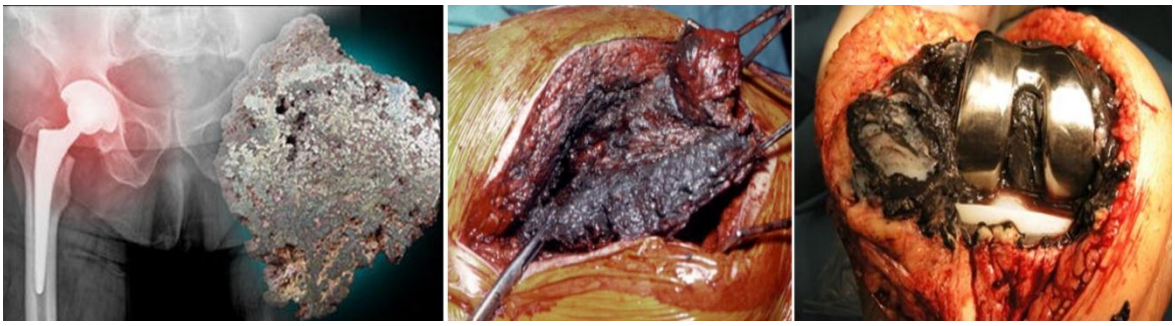

Fig.1.2-3. Metal poisoning (left), pseudotumor formation (middle) and metallosis (right) of metal implants

Moreover, magnetic and non-magnetic metallic devices of certain geometries interact with the magnetic field when the patients are observed by magnetic resonance imaging (MRI) causing heating and even movement of the implant. Of secondary concern is the possibility of imaging the artefacts that can compromise the procedure and image quality, black area on the Fig.1.2-4 (right), meanwhile X-Ray technique not produce image artifact (Fig.1.2-4, left).

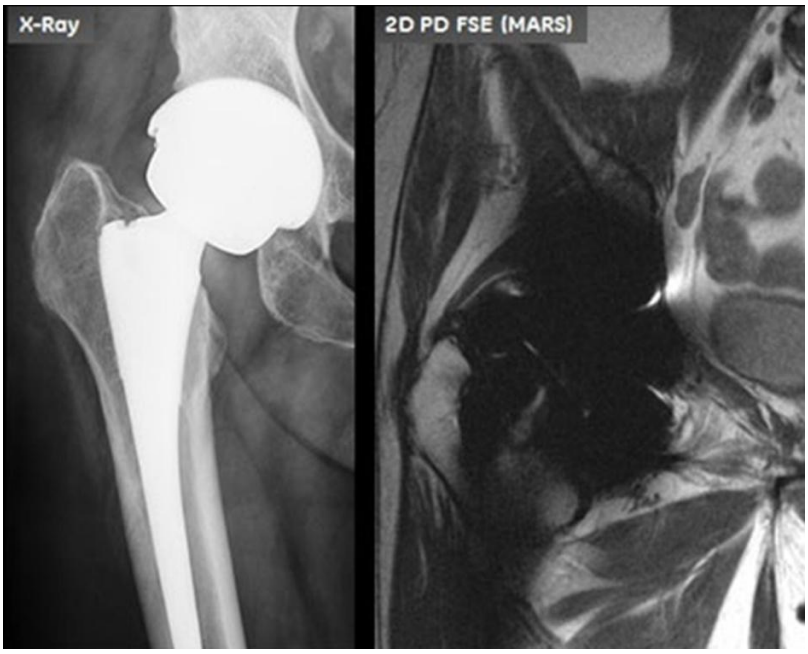

Fig.1.2-4. Image artifacts of metallic implants in MRI (right) [22]

1.2.3 Ceramics biomaterials

Ceramics have a great potential in the biomedical field, thanks to their compatibility with the physiological environment, their strength and wear resistance. Ceramics are also very attractive for dental applications, because of their chemical inertness and their aesthetics. Thus, bioceramics are mainly used in the musculo-skeleton system, for orthopaedic and dental devices: the main applications include replacement for hip, knee, teeth, as bone gaps filler.

Nevertheless, ceramics have some disadvantages. One of the most important drawbacks of ceramic materials is their brittle nature characterized by low fracture toughness. The load applied to the brittle ceramic can result in very fast catastrophic growth of micro-cracks, existing in virtually any material, and as a consequence – to the final unpredictable fracture (Fig.1.2-5). This phenomenon is particularly noticeable if the dynamic load applied such as: impacts, strokes etc. Thus, not only the ceramic-bone contact area, but also the ceramic implant itself, under certain conditions might become the expected point of fracture.

Fig.1.2-5. Catastrophic failure of ceramic's implant components [23]

1.2.4 Composite biomaterials

Composite material is made by combining two or more materials – often ones that have very different properties and which are separated by interfaces. The two materials work together to give the composite unique properties.

Nowadays, more often all typically used biomaterials are replaced with composites in which the combination of dissimilar materials can show superior properties compared with their pure counterparts. Composite biomaterials are used in the cardiovascular, oral and maxillofacial surgery applications, in the field of dentistry as restorative materials or dental cements. The study in this PhD thesis is focused on the development and characterization ceramic/metal composites. By working with this type of composites opens the possibility of integrating the dissimilar properties of ceramics and metals in the composites, thus achieving properties that would never be achieved by using separately the components.

1.3 CERAMIC/METAL COMPOSITES (CERMETS)

The idea of mixing brittle ceramic and ductile metal is used to improve fracture toughness of the first [24-30]. Metal particles in a ceramic matrix disperse the energy of propagating cracks and as a result increase the fracture toughness of the material. Usually the systems incorporated are in the form of particles, whiskers, fibres, flake, etc. The bridging ligaments exert closure stresses that reduce the stress intensity at the crack tip and offer resistance to further crack propagation. As plotted in Fig.1.3-1, the bridging effect occurs when the metal particles either dissipate the elastic energy when they break (1, 9), debond from the ceramic matrix and pull out (2, 8) or shed load from the crack tip while remaining intact (3, 7). Additionally, the crack deflection effect occurs when a crack tip meets with a particle that forces the crack to change direction of its growth (4). On the other hand, ductile inclusions provide blunting of crack tips (5) or stress-releasing plastic deformation in the process zones of growing cracks (6). The magnitude of the crack closure is based on the stress–strain relation of the ligaments, which is influenced by the ligament yield stress, diameter, orientation, volume fraction and the nature of the ceramic/metal interface.

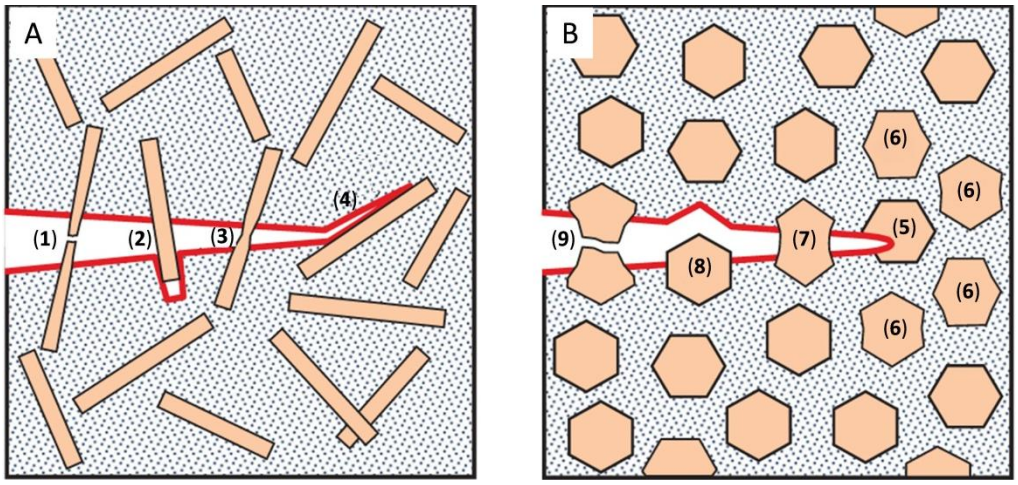

Fig.1.3-1.Toughening mechanism in monolithic ceramic reinforced by ductile particles of various shapes [31]

1.3.1 Cermets for hard tissue replacements

However, in spite of the use of ceramic matrix composites reinforced with bio-compatible, metals for heavy load-bearing hard tissue replacement application are highly attractive, research data in this field are still scarce. Only a few papers can be found in the literature investigating the mechanical and biological properties of bioinert (zirconia, alumina) and bioactive (hydroxyapatite, bioactive glass or apatite-wollastonite) materials reinforced with metal particles (titanium, stainless steel or silver) [32-44].

The most obvious advantage of cermets is that they can favorably combine the often dissimilar properties of ceramic and metal components in one material. Because of the many possible combinations of components this field is very creative, since it provides the opportunity to invent an almost unlimited set of new materials with a large spectrum of known and as yet unknown properties. Therefore, another driving force in the area of cermet materials is the possibility to create multifunctional materials. Biomaterials require to suit in a specific application, apart from biomechanical stability other necessary functionalities. These functionalities can consist of engineered surfaces for

fast integration (osteointegration, osteoconduction, osteoinduction - bone morphogenetic proteins (BMP), bone growth, collagen) and valuable prevention of implant-associated infections (antibacterial capability), high structural properties (fatigue resistance, hardness, low wear, etc.) and mechanical similarity of the biomaterial to the host, replaced tissue enabling new and optimal designs (entire total hip arthroplasty construct rather than on the abrasive wear resistance of the bearing couple per se), absent of diagnostic problems related with MRI procedure and electrical conductivity of the composites to could be machined by electric discharge machining (EDM) technique (metal content near the percolation threshold ~ 16 vol.%), etc. On the other hand, multi-functionality within a material can be integrated on several dimensional scales with increasing interconnectivity between phases and engineering difficulty as the scale decreases [45].

Bartolomé et al. (Instituto de Ciencia de Materiales de Madrid - CSIC) developed for the first time a new-macro-micro-nano 3Y-TZP/Nb biocermet with high flaw tolerance behavior, similar to the one of natural bone by conventional powder processing. In these ceramic-metal composites, structural synergism with toughening mechanisms operating at different scales is achieved through the incorporation to alumina matrix of both niobium lamellar shape macroparticles and zirconia nanoceramic [24, 27]. This possibility clearly reveals the power of ceramic-metal composite (BIOCERMETS) materials to generate complex multifunctional structures that are hierarchically organized at the nano-, micro-, and meso-levels to meet the overall system goals. However a limited number of biocompatible materials can be selected for developing of cermets for biomedical application. Zirconia, alumina, and tantalum induce a good biological response in the host tissues, which has led to use them extensively as

structural biomaterials. This is the reason why such materials have been chosen as starting materials for manufacturing the biocermets for this new PhD Thesis.

1.3.2 Starting materials

1.3.2.1 Tantalum as biomaterial

In present study tantalum was chosen as a reinforcement phase for manufacturing the ceramic-based biocomposites. Physical and mechanical properties of tantalum are given in Table 1.3-1.

Table 1.3-1. Physical and mechanical properties of tantalum

Property/Characteristic	**Tantalum**
Composition	Ta
Group	V
Period	6
Atomic number	73
Tensile strength	172 – 1400 MPa
Vickers hardness	870 – 1200 MPa
Fracture toughness	90 – 150 MPa·$m^{1/2}$
Elastic modulus	185 GPa
Melting point	3000°C
Thermal expansion coefficient	6.73 x 10^{-6}/°C
Density	16.6 – 16.9 g/cm^3
Magnetic susceptibility	178 x 10^{-6}

Chemical qualities of implant surfaces have been identified as one of significant factors related to the selection of the implant material. These factors are important as they are responsible for the tendency of the surface to adsorb foreign atoms or molecules and are

therefore connected to the chemical aspects of biocompatibility. responsible for the tendency of the surface to adsorb foreign atoms or molecules and are therefore connected to the chemical aspects of biocompatibility.

As freshly exposed metallic surfaces are normally not in equilibrium with their surrounding environments, surface oxides, in our case is Ta_2O_5 oxide, will quickly form on all non-noble metals. It means that under normal clinical conditions all metallic implants will be covered with a surface oxide or oxides that are highly protective [46]. It also means that true contact between the implant metal and the host tissue will never be established. Instead, contact will occur between the tissue and the surface oxides of the implant. The chemical properties of oxides are much different than those of the unoxidized metals. The biocompatibility of the oxides is the relevant biomaterial parameter in implantology. The presence of these oxides which do not denature proteins and thus permits osteointegration [47]. Additionally, stable oxide layer prevents an exchange of electrons and thus any redox reaction.

Tantalum metal is very interesting for biomedical application because it is a relative inert material showing high *in vivo* safety with good mechanical properties in term of fracture toughness and workability [48-51]. The oxidation layer on its surface is very stable leading to excellent corrosion–erosion resistance also in a highly acidic environment, with no significant weight or roughness changes in comparison to titanium and stainless steel implants [50]. Many studies demonstrate excellent biocompatibility of tantalum in a variety of situations including, those applications involving general, neuro- and bone surgery [52-55]. Multiple medical devices have been fabricated with this material, including: pacemaker electrodes foil and mesh for nerve repair, and cranioplasty plates (Fig.1.3-2). Tantalum which has excellent X-ray visibility and low magnetic susceptibility is often used for X-ray markers for stents [56].

In orthopedic tantalum metal is used for manufacturing of structural component for primary and revision total hip and knee replacements and, more recently, in spine surgery [57].

Fig.1.3-2. Medical devices produced from tantalum metal

Additionally, porous tantalum-based trabecular metal material has been used to create a new dental implant that includes a metal design that emulates human cancellous bone (Fig. 1.3-3A). The porous tantalum three-dimensional enhancement of titanium dental implant surface allows for combining bone ongrowth together with bone ingrowth, or osseoincorporation. Trabecular metal implant technology has enjoyed excellent results for orthopedic implants and implant dentistry [58-62] (Fig. 1.3-3 B).

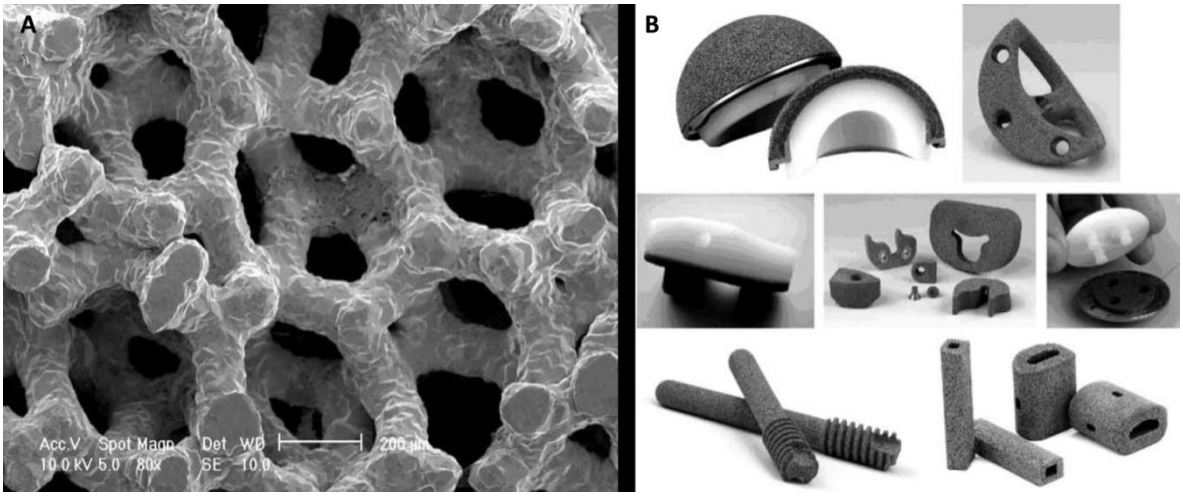

Fig.1.3-3. Scanning electron microscopy of porous tantalum (A) and multiple orthopaedic applications for porous tantalum (B) [57]

References indicate that there is no known human disease which is attributable to tantalum, that systemic poisonings in industrial situations are unknown, and this metal

and their compounds are not listed as presumptive or possible carcinogens. Therefore, the combination of excellent mechanical properties, resistance to chemical attack and arouse very little adverse biological response in either reduced or oxidized forms lead to use tantalum as a human implant material.

1.3.2.2 Zirconia and Alumina as biomaterials

Dozens of dense ceramics have been tested as promising candidates for bio-applications, but only few of them have achieved human clinical application. These are alumina, zirconia, and bioactive glasses. The two first of above mentioned ceramics form the basis of experimental manufacturing of new bio-composites. It would be useful to bring some information on the ceramics' properties and applications (Table 1.3-2).

Table 1.3-2. Physical and mechanical properties of alumina and zirconia ceramics

Property/Characteristic	**Alumina**	**Zirconia**	
Composition	Al_2O_3	Mg–PSZ	Y–TZP
Flexural strength	400 – 580 MPa	400 – 580 MPa	700 – 1500 MPa
Vickers hardness	18.0 – 23.0 GPa	10.0 – 12.0 GPa	11.0 – 12.5 GPa
Fracture toughness	3.3 – 4.2 MPa·$m^{1/2}$	2.9 – 16.0 MPa·$m^{1/2}$	4.5 – 20 MPa·$m^{1/2}$
Elastic modulus	380 GPa	200 – 250 GPa	210 – 233 GPa
Mean grain size	<1.8 µm	50 µm	0.1 – 0.6µm
Thermal expansion coefficient	8 x 10^{-6}/°C	7 – 10 x 10^{-6}/°C	11 x 10^{-6}/°C
Density	3.98 g/cm^3	5.66 – 5.77 g/cm^3	6.00 – 6.05 g/cm^3

1.3.2.2.1 Alumina

Interest in polycrystalline bioceramics started in 1970 when Dr. Pierre Boutin implanted the first hip prostheses with Al_2O_3 ceramic bearings [63, 64]. His success led to a string of ceramic biomaterial innovations, with patents appearing shortly thereafter claiming various ceramics, including Al_2O_3, as viable orthopedic materials [65-68]. Recognizing

a potential for limb reconstruction and correction of skeletal defects in veterans, the US Defense Department investigated and demonstrated the usefulness of porous Al_2O_3 as a bone scaffold in 1972 [69], and a similar Scandinavia study in 1973 established its osseointegration effectiveness [70]. Al_2O_3 has been the most widely used structural ceramic in total hip arthroplasty (THA) for the past approximately 50 years, typically in articulation against polyethylene [71] or itself [72, 73]. Its success in THA led to its adoption in other joints including knee [74, 75], elbow [76], ankle [77], wrist [78], phalanges [79], spine [80, 81], and also in bone reconstruction [82]. Industrial specifications for its composition, processing and properties have been issued [83, 84]. It has been repeatedly shown to be biocompatible [64, 85], possessing high hardness and a low coefficient of friction, all of which significantly reduces the occurrence of wear debris [86].

Despite the mentioned good properties of alumina, such as high mechanical strength, elastic modulus, high compression resistance, optimal chemical properties, its brittleness must not be forgotten [87, 88]: its fracture toughness is only ~ 4 $MPa \cdot m^{1/2}$ and it is also sensitive to slow crack propagation under a stress intensity factor K_I lower than the critical value K_{IC}. Although enhanced reliability has been realized with process improvement, including increased raw material purity, refinement of its microstructure, use of hot-isostatic pressing (HIP), and inclusion of post-manufacturing proof testing [89]. Fig.1.3-4 shows first, second, and third generation alumina on alumina bearings in hip prostheses which completely fulfill the ISO requirements for medical-grade alumina implants [90]. The latter generation of alumina ceramics was manufactured using HIP.

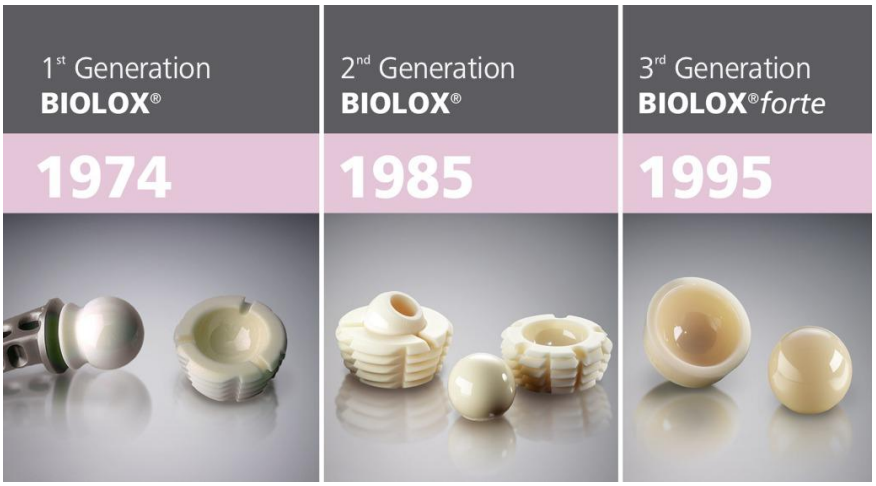

Fig.1.3-4. Biomedical grades of Biolox alumina belonging to the first, second, and third generation of biomedical implants [91]

1.3.2.2.2 Zirconia

Continuing concerns over *in vivo* fractures of Al_2O_3 femoral heads and liners in total hip arthroplasty in the 1980s led to the introduction of zirconia ceramics in 1985 [92] including partially stabilized zirconia using magnesia (Mg-PSZ) and a yttria-doped composition known as Tetragonal Zirconia Polycrystals (Y-TZP) [92-94]. These ceramics represented a new generation of implants. They were biocompatible [85] and had approximately twice the strength and toughness of Al_2O_3 [94]. They also had exceptionally low coefficients of friction and lower wear on polyethylene. They promised to provide a new level of care and safety over metallic and Al_2O_3 implants [92, 95-97]. Their improved mechanical properties were achieved by taking advantage of a polymorphic phase transformation that occurs in doped zirconia known as phase transformation toughening [98]. This mechanism involves the metastabilization of a high-temperature tetragonal phase through the incorporation of magnesia, yttria, or other dopants. In the presence of an advancing crack, the metastable phase transforms to its stable monoclinic polymorph with an accompanying volume increase of ~ 4-5%. The sudden volume change exerts compressive forces on the crack tip, thereby slowing or arresting its propagation (Fig.1.3-5).

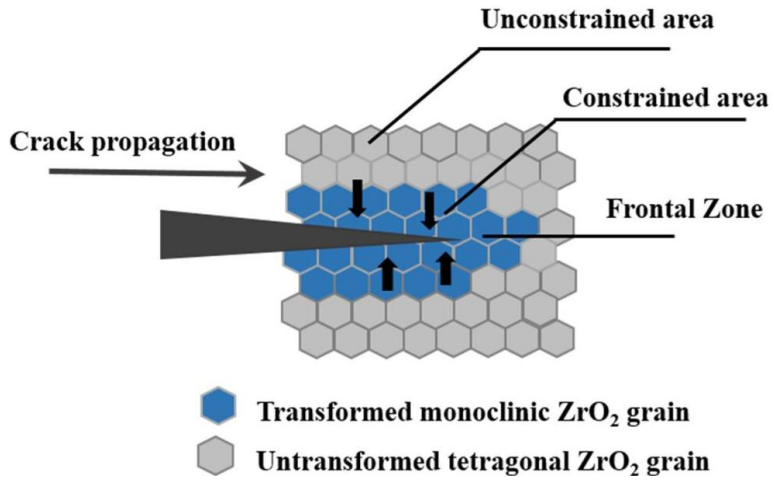

Fig.1.3-5. Schematic illustration of stress-induced phase transformation toughening [99]

Mg-PSZ implants entered the marketplace and an industrial standard for their composition, processing and properties was created [100]. However, the strength of Mg-PSZ was inferior to Y-TZP, so, considerable physician interest and rapid uptake of Y-TZP ceramics occurred after its clearance by US and EU regulatory bodies. Over 600,000 Y-TZP femoral heads were implanted between 1985 and the turn of the century largely based on bench test data, with little clinical evidence as to the material‘s longer-term effectiveness [101, 102]. There were initially few reported *in vivo* failures [97], but a change in manufacturing methods (from batch to tunnel furnace) by the leading vendor of Y-TZP in 1998 resulted in a significant increase in fractures beginning in 2000, many occurring only months after implantation [102]. Independent investigations by a number of scientific groups in cooperation with regulatory agencies highlighted the material‘s inherent instability [101-103]. After more than a decade of use, Y-TZP was withdrawn from the US and EU markets in 2001 and its industrial standard was subsequently abandoned [104]. Despite its improved initial strength, Y-TZP possesses one critical weakness. It may spontaneously transform to its stable monoclinic form under *in vivo* conditions. This effect has become known as low-temperature hydrothermal degradation (LTD) or aging [105].

Aging occurs through a slow surface transformation to the monoclinic stable phase. This transformation begins in individual particles on the surface through a mechanism of stress corrosion. The initial transformation of specific particles can be related to a state of imbalance: greater particle size, lower yttria content, specific guidance from the surface, the presence of residual stress, or even the presence of a cubic phase. The transformation occurs by nucleation and growth processes. This phenomenon leads to a cascade of events occurring in neighboring particles, leading to an increase in volume that stresses the particles and results in subcritical crack growth (SCG), offering a way for water to penetrate inside the material. Nucleation on a particular grain at the surface leading to microcracking and stresses to the neighbors (Fig. 1.3-6A). Growth of the transformed zone leading to extensive microcracking and surface roughening. Transformed grains are gray. Red path represents the penetration of water due to microcracking around the transformed grains (Fig. 1.3-6B and Fig. 1.3-6C).

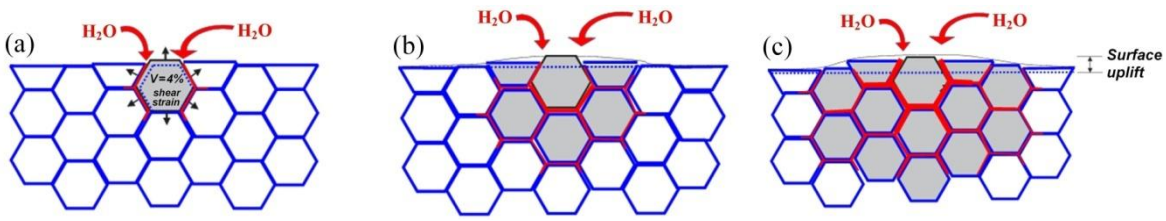

Fig.1.3-6. Scheme of ageing in cross section [106]

The transformation results in increased implant surface roughness, enhanced wear, weakening of the material and eventual fracture [101-103, 107, 108]. Despite its withdrawal from EU and US markets, Y-TZP femoral heads are still available for implantation in Asia, and recent physical chemistry analyses suggest that the unconstrained transformation experienced by the original EU manufacturer may be limited and controlled through improved processing and careful assessment before clinical use [109]. Y-TZP is also extensively used and preferred as esthetic and

functional dental prostheses [110], although concerns have also been raised about its longevity in this application due to low-temperature hydrothermal degradation [111]. LTD is therefore considered the Achilles‘ heel of zirconia with its occurrence being highly dependent on its microstructure; therefore the overall process must be strictly controlled and any change in one of the process steps must be carefully assessed. In other, simple terms, Y-TZP may perform better than Al_2O_3 but is less robust as far as industrial variations are concerned.

1.3.2.2.3 Ceramics containing mixtures of Al_2O_3 and ZrO_2

To overcome the low toughness of alumina and the ageing sensitivity of zirconia, a group of new ceramics containing mixtures of Al_2O_3 and ZrO_2 have been proposed for biomedical applications. The idea supporting the development of these materials is the belief that they represent a way to benefit from the good mechanical properties of alumina, especially hardness, at the same time improving the toughness of the composite by means the zirconia transformation toughening, without the major drawback of the ageing under steam or body fluid.

At one end of the composition spectrum is zirconia-toughened alumina (ZTA) [112, 113]. ZTA is a fully dense ceramic consisting typically of about 7 wt.% to 25 wt.% unstabilized ZrO_2 or Y-TZP incorporated into an Al_2O_3 matrix [114, 115]. At the opposite end of the spectrum, but still consisting of Al_2O_3 and ZrO_2, is alumina-toughened zirconia (ATZ). ATZ is also a completely dense ceramic composed of 80 wt.% Y-TZP and 20 wt.% Al_2O_3 [116].

It is known that the mechanical properties and ageing resistance of ZrO_2/Al_2O_3 composites can be considerably increased by reducing the corresponding grain sizes and by improving the homogeneity of the phase dispersion [117]. In ZTA ceramics narrow

grain size distribution as well as their concentration and isolation, i.e. the absence of aggregates, are important for the inhibition of intergranular water diffusion which would lead to a premature transformation [118]. For ATZ the dispersion and size distribution of the Al_2O_3 grains are even more critical for the LTD behaviour because of the large proportion of t-ZrO_2 [119], although its influence is retarded due to the presence of the non-transforming Al_2O_3 phase.

As might be expected, this broad range of Al_2O_3-ZrO_2 mixtures resulted in noticeable differences in properties, but all were superior to both pure Al_2O_3 and Y-TZP. All have been tested and determined to be biocompatible [120, 121]. They have excellent strength, toughness and hardness [113, 122, 123] and are highly abrasion [124] and wear resistant [125-131]. Clinical studies using these devices have been ongoing since their introduction with acceptable overall outcomes [129, 132-135]. Although research has been done on many different types of ZTA/ATZ ceramic, only a few compositions have been developed into commercially competitive large-scale products. Companies that produce commercially available ceramics containing mixtures of Al_2O_3 and ZrO_2 for hip arthroplasty are presented in Table 1.3-3.

Table 1.3-3. Product descriptions and manufacturers for ZTA/ATZ hip implants

Manufacturer	Product Name	Availability	Zirconia	Alumina	Stabilizers	Additives
Zirconia Toughened Alumina or ZTA						
CeramTec AG [91]	Biolox Delta	Currently on the market	22.5wt%	76.1wt%	Yttria	1.4wt% (chromium, strontium and others)
Kyocera Medical [136]	Bioceram, AZ209	Currently on the market in Japan	19wt%	79wt%	No	2wt% other
Alumina Toughened Zirconia or ATZ						
Mathys Ltd [137]	Ceramys	Currently on the market	80wt%	20wt%	Yttria	No

Fig. 1.3-7 exhibits fourth generation Biolox Delta alumina matrix components produced by HIP which demonstrate reduction in wear and increase in strength compared to third generation of Biolox Forte Bearings [138]. Other medical ceramic suppliers are working on developing ZTA/ATZ biomaterials, but these new materials have not yet been commercialized.

Fig.1.3-7. Biolox Delta: The newest generation of ceramics [91]

1.4 REFERENCES

[1] The Bone and Joint Decade - Global Alliance for Musculoskeletal Health, http://bjdonline.org/key-facts-and-figures/, (2015).

[2] Weiss AJ and Elixhauser A. Trends in Operating Room Procedures in U.S. Hospitals, 2001-2011. *Healthc. Cost Util.Proj.*, 2014;1–14.

[3] Kurtz SM, Ong KL., Lau E., Bozic K.J. Impact of the Economic Downturn on Total Joint Replacement Demand in the United States. *J. Bone Jt. Surg.*, 2014; 96:624-630.

[4] Bernstein J. The Folly of Forecasting. *Clin. Orthop. Relat. Res.*, 2013; 471:1415-1418.

[5] Kim SH, Wise BL, Zhang Y, Szabo RM. Increasing Incidence of Shoulder Arthroplasty in the United States. *J.Bone Jt. Surg.*, 2011; 93:2249-2254.

[6] Day JS, Lau E, Ong KL, Williams GR, Ramsey ML, Kurtz SM. Prevalence and Projections of Total Shoulder and Elbow Arthroplasty in the United States to 2015. *J. Shoulder Elb. Surg.*, 2010; 19:1115-1120

[7] Mendenhall S. 2014 Hip and Knee Implant Review. *Orthop. Netw. News*, 2011; 22.

[8] Vetalice JA. Orthopaedic Industry Annual Report - Focus on Joint Replacement. *OrthoKnow*, 2012; 1-8.

[9] Anne MM. http://www.myoops.org/cocw/mit/NR/rdonlyres/Materials-Science-and-Engineering/3-051JSpring2004/255E8CCE-5D54-4ED7-A582C85F886FE865/0/lecture_1.pdf

[10] Aherwar A, Singh AK, Patna A. Current and future biocompatibility aspects of biomaterials for hip prosthesis. *AIMS Bioengineering*, 2016; 3:23-43.

[11] Cooper RA, McAllister CM, Borden LS, BauerTW. Polyethylene debrisinduced osteolysis and loosening in uncemented total hip arthroplasty: a cause of late failure, *Journal of Arthroplasty*, 1992; 7:285-290.

[12] Hongtao L, Shirong G, Shoufan C, Shibo W. Comparison of wear debris generated from ultra high molecular weight polyethylene *in vivo* and in artificial joint simulator. *Wear*, 2011; 271:647–652.

[13] Edidin AA, Rimnac CM, Goldberg VM, Kurtz SM. Mechanical behavior, wear surface morphology, and clinical performance of UHMWPE acetabular components after 10 years of implantation. *Wear*, 2001; 250:152–158.

[14] Sobieraj MC, Rimnac CM. Ultra high molecular weight polyethylene: mechanics, morphology, and clinical behavior, *J Mech Behav Biomed Mater*., 2009; 2:433-443.

[15] Enderle J, Bronzino J. Introduction to Biomedical Engineering. Published: March 2011, Academic Press ISBN: 978-0-12-374979-6

[16] Doorn PF, Campbell PA, Worrall J, Benya PD, McKellop HA, Amstutz HC. Metal wear particle characterization from metal on metal total hip replacements: transmission electron microscopy study of periprosthetic tissues and isolated particles. *J Biomed Mater Res*., 1998;42:103–11.

[17] Dunstan E. Chromosomal Aberrations in the Peripheral Blood of Patients with Metal-on-Metal Hip Bearings. *JBJS*, 2008; 90:517-522.

[18] Pandit H, Jones GS, McLardy SP, Gundle R, Whitwell D, Gibbons CL, Ostlere S, Athanasou N, Gill HS, Murray DW. Pseudotumours associated with metal-on-metal hip resurfacings. *JBJS*, 2008; 90:847-851.

[19] Hallab NJ, Jacobs JJ. Biologic effects of implant debris. *Bull NYU Hosp Jt Dis*., 2009; 67:182-8.

[20] Bahraminasab M, Sahari BB, Edwards KL, Farahmand F, Arumugam M, Hong TS. Aseptic loosening of femoral components – A review of current and future trends in materials used. *Materials & Design*, 2012; 42:459-70.

[21] IARC monographs on the evaluation of carcinogenic risks to humans: International Agency for Research on Cancer; 2001.

[22] Choi SJ, Koch KM, Hargreaves BA, Stevens KJ, Gold GE. Metal artifact reduction with MAVRIC SL at 3-T MRI in patients with hip arthroplasty. *AJR Am J Roentgenol*., 2015; 204:140-7

[23] Yoo JJ, Kim YM, Yoon KS, Koo KH. Song WS. Kim HJ. Alumina-on-alumina total hip arthroplasty. A five-year minimum follow-up study. *J Bone Joint Surg Am*., 2005; 87:530-5.

[24] Bartolomé JF, Gutiérrez-González CF, Torrecillas R. Mechanical properties of alumina–zirconia–Nb micro–nano-hybrid composites. *Compos. Sci. Technol.*, 2008; 68:1392-1398.

[25] Kameo K, Friedrich K, Bartolomé JF, Díaz M, López-Esteban S, Moya JS. Sliding wear of ceramics and cermets against steel. *J. Eur. Ceram. Soc.*, 2003; 23:2867-2877.

[26] Díaz M, Bartolomé JF, Requena J, Moya JS. Wet processing of mullite/molybdenum composites. *J. Eur. Ceram. Soc*., 2000; 20:1907-1914.

[27] Gutierrez-Gonzalez CF, Bartolomé JF. Damage tolerance and R-curve behavior of Al_2O_3–ZrO_2–Nb multiphase composites with synergistic toughening mechanism. *J. Mater. Res*., 2008; 23:570-578.

[28] Moya JS, Díaz M, Gutierrez-Gonzalez CF, Diaz LA, Torrecillas R, Bartolomé JF. Mullite-refractory metal (Mo, Nb) composites. *J. Eur. Ceram. Soc*., 2008; 28:479-491.

[29] Rodriguez-Suarez T, Bartolomé JF, Moya JS. Mechanical and tribological properties of ceramic/metal composites: A review of phenomena spanning from the nanometer to the micrometer length scale. *J. Eur. Ceram. Soc*., 2011; 32:3887-3898.

[30] Torrecillas R, Espino AM, Bartolomé JF, Moya JS. Functionally graded zircon-molybdenum materials without residual stresses. *J. Am. Ceram. Soc*., 2000; 83:454-456.

[31] Ovidko IA. 2015. Micromechanics of fracturing in nanoceramics. *Phil. Trans. R. Soc.,* 2015*;* 373:20140129.

[32] Ning, CQ, Zhou Y. *In vitro* bioactivity of a biocomposite fabricated from HA and Ti powders by powder metallurgy method. *Biomaterials*, 2002; 23:2909-15.

[33] Arifin A, Sulong AB, Muhamad N, Syarif J, Ramli MI. Material processing of hydroxyapatite and titanium alloy (HA/Ti) composite as implant materials using powder metallurgy: A review. *Materials and Design*, 2014; 55:165–175

[34] Verne E, Bona E, Bellosi A, Brovarone CV, Appendino P. Na_2O-CaO-SiO_2 glass-ceramic matrix biocomposites. *J Mater Sci*., 2001; 36:2801-7.

[35] Pattanayak DK, Prasad RC, Rao BT, Rama Mohan TR. Apatite wollastonite titanium biocomposites: Synthesis and *in vitro* evaluation. *J Am Ceram Soc.*, 2006; 89: 2172-6.

[36] Chu CL, Xue XY, Zhu JC. *In vivo* study on biocompatibility and bonding strength of hydroxyapatite-20vol.%Ti composite with bone tissues in the rabbit. *Biomed Mater Eng.*, 2006; 16:203-13.

[37] Claxton E, Taylor BA, Rawlings RD. Processing and properties of a bioactive glass-ceramic reinforced with ductile silver particles. *J Mater Sci.*, 2002; 37:3725-32.

[38] Fan X, Chen J, Zou J-P, Wan Q, Zhou Z-C, Ruan J-M. Bone-like apatite formation on HA/316L stainless steel composite surface in simulated body fluid. *Trans Nonferrous Met Soc China*, 2009; 19:347-52.

[39] Nath S, Kalmodia S, Basu B. Densification, phase stability and *in vitro* biocompatibility property of hydroxyapatite-10wt.% silver composites. *J Mater Sci Mater Med.*, 2010; 21:1273–1287.

[40] Chang Q, Chen DL, Ru HQ, Yue XY, Yu L, Zhang CP. Toughening mechanisms in iron-containing hydroxyapatite/titanium composites. *Biomaterials*, 2010; 31:1493-1501.

[41] Fernandez-Garcia E, Gutierrez-Gonzalez CF, Fernandez A, Torrecillas R, Lopez-Esteban S. Processing and Spark Plasma Sintering of zirconia/titanium cermets *Ceramics International*, 2013; 39:6931–6936.

[42] Fernandez-Garcia E, Chen X, Gutierrez-Gonzalez CF, Fernandez A, Lopez-Esteban S, Aparicio C. Peptide-functionalized Zirconia and New Zirconia/Titanium Biocermets for Dental Applications. *J Dent.*, 2015; 43:1162-74.

[43] Fernandez-Garcia E, Guillem-Marti J, Gutierrez-Gonzalez CF, Fernandez A, Ginebra MP, Lopez-Esteban S. Osteoblastic cell response to spark plasma-sintered zirconia/titanium cermets. *J Biomater Appl*., 2015; 29:813-23

[44] Guzman R, Fernandez-García E, Gutierrez-Gonzalez CF, Fernandez A, Lopez-Lacomba JL, Lopez-Esteban S. Biocompatibility assessment of spark plasma-sintered alumina-titanium cermets. *J Biomater Appl*., 2016; 30:759-69.

[45] Momoda LA. The Future of Engineering Materials: Multifunction for Performance-Tailored Structures. The Bridge (USPS 551-240), 2004; 34:No. 4.

[46] Muster D, Demri TJ, Hage Ali M. Physicochemical characterization of surface and interface on biomaterials and coatings. In: Encyclopedic handbook of biomaterials and bioengineering. Wise DL, Trantolo DJ, Altobelli DE, Yaszemski MJ, Gresser JD, Schwartz ED, editors.Part A. Vol. 1. New York: Marcel Dekker; 1995.

[47] Zitter H, Plenk Jr.H. The electrochemical behaviour of metallic implant materials as an indicator of their biocompatibility. *J. Biomed. Mater. Res.*, 1987; 21:881 – 896.

[48] Park JB. Biomaterials science and engineering. New York: Plenum Press 1984; 217.

[49] Plenk Jr.H, Danhel-Mayrhauser M, Reichsthaler J, Schuh E. The bone-tantalum interface in the double blade implant ‘‘Implandent Austria’’, A clinical and histomorphometrical evaluation. In:Biomaterial-tissue interfaces. Doherty PJ, Ed Oxford: Elsevier Science 1992; 73

[50] Black J. Biological performance of tantalum. *Clin Mater.*, 1994; 16:167-173.

[51] Stackpool GJ, Kay AB, Morton P, Harvey EJ, Tanzer M, Bobyn JD. Bone ingrowth characteristics of porous tantalum: A new material orthopaedic implant. Orthopaedic research society, editor. *Proceedings of Combined Orthopaedic Research Societies Meeting*. Chicago: Rider Dickerson Inc 1995; 45.

[52] Matsuno H, Yokoyama A, Watari F, Uo M, Kawasaki T. Biocompatibility and osteogenesis of refractory metal implants, titanium, hafnium, niobium, tantalum and rhenium. *Biomaterials*, 2001; 22:1253-1262.

[53] Bartolomé JF, Moya JS, Couceiro R, Gutiérrez-González CF, Guitián F, A. Martinez-Insua A. *In vitro* and *in vivo* evaluation of a new zirconia/niobium biocermet for hard tissue replacement. *Biomaterials*, 2016; 76:313-320.

[54] Findlay DM, Welldon K, Atkins GJ, Howie DW, Zannettino ACW, Bobyn D. The proliferation and phenotypic expression of human osteoblasts on tantalum metal. *Biomaterials*, 2004; 25:2215-2227.

[55] C.B. Johansson, T. Albrektsson, A removal torque and histomorphometric study of commercially pure niobium and titanium implants in rabbit bone, *Clin Oral Implants Res.*, 1991; 21:24-29.

[56] Hermawan H, Ramdan D, Djuansjah JRR. Metals for Biomedical Applications, Biomedical Engineering - From Theory to Applications, Prof. Reza Fazel (Ed.), ISBN: 978-953-307-637-9, InTech, DOI: 10.5772/19033.

[57] Maccauro G, Iommetti PR, Muratori F, Raffaelli L, Manicone PF, Fabbrician C. An Overview about Biomedical Applications of Micron and Nano Size Tantalum. *Recent Patents on Biotechnology*, 2009; 3:157-165.

[58] Macheras GA, Papagelopoulos PJ, Kateros K, Kostakos AT, Baltas D, Karachalios TS. Radiological evaluation of the metal-bone interface of a porous tantalum monoblock acetabular component. *J Bone Joint Surg Br*., 2006; 88:304-309.

[59] Wigfield C, Robertson J, Gill S, Nelson R. Clinical experience with porous tantalum cer vical interbody implants in a prospective randomized controlled trial. *Br J Neurosurg*., 2003; 17:418-425.

[60] Nasser S, Poggie RA. Revision and salvage patellar arthroplasty using a porous tantalum implant. *J Arthroplasty*, 2004; 19:562-572.

[61] Unger AS, Lewis RJ, Gruen T. Evaluation of a porous tantalum uncemented acetabular cup in revision total hip arthroplasty. Clinical and radiological results of 60 hips. *J Arthroplasty*, 2005; 20:1002-1009.

[62] Cohen R. A porous tantalum trabecular metal: basic science. *Am J Orthop*., 2002; 31:216-7.

[63] Boutin P. Total arthroplasty of the hip by fritted aluminum prosthesis. Experimental study and 1st clinical applications. *Orthop Traumatol Surg Res*., 2014; 100:15-21.

[64] Boutin P, Christel P, Dorlot J-M, Meunier A, DeRoquancourt A, Blanquaert D, S. Herman S, Sedel L, et al. The use of dense alumina–alumina ceramic combination in total hip replacement. *J. Biomed. Mater. Res*., 1988; 22:1203–1232.

[65] Scales JT, Goddard D. Prosthetic Acetabular Devices US Patent 3698017 (1972).

[66] Mittelmeier H, Karpf K, Moser H. Hip Joint Prosthesis US Patent 3894297 (1975).

[67] Zeibig A, Locke H. Ceramic Implant US Patent 3979779 (1976).

[68] Klawitter JJ, Bhatti NA. Ceramic Prosthetic Implant Suitable for a Knee Joint Plateau US Patent 4000525 (1977).

[69] Hulbert SF, Klawitter JJ, Sauer BW, Matthews JR. Characterization of tissue ingrowth into porous bioceramics. *Tech. Rep. Off. Nav. Res*., 1972; 2:1–137.

[70] Lyng S, Sudmann E, Hulbert SF, Sauer BW. Fixation of permanent orthopaedic prosthesis use of ceramics in the tibial plateau. *Acta Orthop.Scand*., 1973; 44:694–701.

[71] Sugano N, Nishii T, Nakata K, Masuhara K, Takaoka K. Polyethylene sockets and alumina ceramic heads in cemented total hip arthroplasty—a ten-year study. *J. Bone Jt. Surg.*, 1995; 77:548–556.

[72] Murphy S. Alumina ceramic–ceramic bearings in THA: the new gold standard. *Orthopedics*, 2002; 25:2–3.

[73] Murphy SB, Ecker TM, Tannast M. Two- to nine-year clinical results of alumina ceramic-on-ceramic THA. *Clin. Orthop. Relat. Res*.,2006; 453:97–102.

[74] Bal BS, Garino J, Ries M, Oonishi H. Ceramic bearings in total knee arthroplasty. *J. Knee Surg*., 2007; 20:261–270.

[75] Nakamura S, Kobayashi M, Ito H, Nakamura K, Ueo T, Nakamura T. The Bi-Surface Total Knee Arthroplasty: Minimum 10-Year Follow-Up Study, *Knee*, 2010; 17:274–278.

[76] Nishida K, Hashizume K, Nasu Y, Kishimoto M, Ozaki T, Inoue H. 5-22-Year Follow-Up Study of Stemmed Alumina Ceramic Total Elbow Arthroplasties with Cement Fixation for Patients with Rheumatoid Arthritis. *J. Orthop. Sci.*, 2014; 19:55–63.

[77] Kosugi S, Taniguchi A, Tomiwa K, Kurokawa H, Tanaka Y. TNK ankle – the ceramic 2 – component total ankle prosthesis. *Clin. Res. Foot Ankle*, 2014; 2:141.

[78] Hatano H, Morita T, Kobayashi H, Otsuka H. A ceramic prosthesis for thetreatment of tumours of the distal radius. *J. Bone Jt. Surg*., 2006; 88:1656–1658.

[79] Doe K, Kuwata KN, Shinya K. Alumina ceramic finger implants: a preliminary biomaterial and clinical evaluation. *J. Hand Surg. Am*., 1984; A9:740–749.

[80] Nguyen NQ, Kafle D, Buchowski J, Park K-W, Chang B-S, Lee C-K, Yeom JS. Ceramic fracture following cervical disc arthroplasty. *J. Bone Jt. Surg*., 2011; 93:1–4.

[81] Oda Y, Miyatake S, Tokuriki Y, Handa H. Alumina ceramics (bioceram) as the implant material in anterior cervical fusion. *Nihon Geka Hokan*., 1981; 50:352-7.

[82] Huckstep RL, Sherry E. Replacement of the proximal humerus in primary bone tumours. *Aust. N. Z. J. Surg*., 1996; 66:97–100.

[83] Standard Specification for High- Purity Dense Aluminum Oxide for Medical Applications, ASTMF603-00 (2000).

[84] Implants for Surgery – Ceramic Materials – Part 1: Ceramic Materials Based on High Purity Alumina, ISO 6474 - 1 (2010).

[85] Piconi C, Maccauro G, Muratori F, DelPrever EB. Alumina and zirconia ceramics in joint replacements. *J. Appl. Biomater. Biomech*., 2003; 1:19–32.

[86] Roy RS, Mondal A, Chanda A, Basu D, Mitra MK. Sliding wear behavior of submicron-grained alumina in biological environment. *J. Biomed. Mater. Res*., 2007;83:257-262.

[87] Koo KH, Ha Y-C, Jung WH, Kim S-R, Yoo JJ, Kim HJ. Isolated fracture of the ceramic head after third- generation alumina-on-alumina total hip arthroplasty, *J. Bone Jt. Surg*., 2008; 90:329–3362.

[88] Garino JP. The reliability of modern alumina bearings in total hip arthroplasty—update to a 2006 report. *Semin. Arthroplasty*, 2013; 24:193–201.

[89] Jung YL, Kim S-Y. Alumina-on-polyethylene bearing surfaces in total hip arthroplasty. *Open Orthop. J*., 2010; 4:56–60.

[90] Implants for Surgery – Ceramic materials based on high purity alumina ISO 6474:1994.

[91] https://www.ceramtec.com/ceramic-materials/biolox/

[92] Cales B. Zirconia ceramic for improved hip prosthesis—a review, in: 6th Biomater. Symp. Ceram. Implant Mater. Orthop. Surg., Gottingen, Germany, 1994:2–8.

[93] Piconi C, Maccauro G. Zirconia as a ceramic biomaterial. *Biomaterials,* 1999; 20:1–25.

[94] Masaki T. Mechanical properties of toughened ZrO_2–Y_2O_3 ceramics. *J. Am. Ceram. Soc*., 1986; 69:638–640.

[95] Drouin JM, Cales B. Yttria-stabilized zirconia ceramic for improved hip joint head, in: 7th Int. Symp. Ceram. Med. Butterworth–Heinemann, Turku,Finland, 1994:30–33.

[96] Cales B, Stefani Y, Lilley E. Long term *in vivo* and *in vitro* aging of a zirconia ceramic used in orthopaedy. *J. Biomed. Mater. Res*., 1994; 28:619–624.

[97] Cales B, Stefani Y. Mechanical properties and surface analysis of retrieved zirconia hip joint heads after an implantation time of two to three years. *J.Mater. Sci*., 1994; 5:376–380.

[98] Hannink RHJ, Kelly PM, Muddle BC. Transformation toughening in zirconia-containing ceramics. *J. Am. Ceram. Soc*., 2000; 83:461–487.

[99] Palmero P. Structural Ceramic Nanocomposites: A Review of Properties and Powders' Synthesis Methods. *Nanomaterials*, 2015; 5:656-696.

[100] Standard Specification for High- Purity Dense Magnesia Partially Stabilized Zirconia (Mg-PSZ) for Surgical Implant Applications, ASTMF2393-10 (2010).

[101] Clarke IC, Manaka M, Green DD, Williams P, Pezzotti G, Kim Y-H, Ries M, Sugano N, et al. Current status of zirconia used in total hip implants. *J.Bone Jt. Surg*., 2003; 85:73–84.

[102] Chevalier J, Gremillard L, Deville S. Low-temperature degradation of zirconia and implications for biomedical implants. *Ann. Rev. Mater. Res*., 2007; 37:1–32.

[103] Masonis JL, Bourne RB, Ries MD, McCalden RW, Salehi A, Kelman DC. Zirconia femoral head fractures. *J. Arthroplasty,*2004; 19:898–905.

[104] Standard Specification for High- Purity Dense Yttria Tetragonal Zirconium Oxide Polycrystal (Y-TZP) for Surgical Implant Appications, ASTMF1873-98(2007).

[105] Chevalier J, Gremillard L, Virkar AV, Clarke DR. The tetragonal-monoclinic transformation in zirconia: lessons learned and future trends. *J. Am. Ceram. Soc*., 2009; 92:1901–1920.

[106] Chevalier J. What future for zirconia as a biomaterial? *Biomaterials*, 2006; 27:535-43.

[107] Santos EM, Vohra S, Catledge SA, McClenny MD, Lemons J, Moore KD. Examination of surface and material properties of explanted zirconia femoral heads. *J. Arthroplasty*, 2007; 9:30-34.

[108] Maccauro G, Piconi C, Burger W, Pilloni L, De Santis E, Muratori F, Learmonth ID. Fracture of a Y-TZP ceramic femoral head. *Bone Jt. Surg*., 2004; 86:1192–1196.

[109] Pezzotti G. Bioceramics for hip joints: the physical chemistry viewpoint. *Materials*, 2014; 7:4367–4410.

[110] Hisbergues M, Vendeville S, Vendeville P. Zirconia: established facts and perspectives for a biomaterial in dental implantology. *J. Biomed. Mater. Res. Part B Appl. Biomater*., 2009; 88:519–529.

[111] Kohorst P, Borchers L, Strempel J, Stiesch M, Hassel T, Bach F-W., Hübsch C. Low-temperature degradation of different zirconia ceramics for dental applications. *Acta Biomater*., 2012; 8:1213–1220.

[112] Insley GM, Streicher RM. Next generation ceramics based on zirconia toughened alumina for hip joint prostheses. *Key Eng. Mater*., 2004; 254:675–678.

[113] Nakanishi T, Sasaki M, Ikeda J, Miyaji F, Kondo M. Mechanical and phase stability of zirconia toughened alumina. *Key Eng. Mater*., 2007; 330–332:1267–1270.

[114] Hori S, Yoshimura M, Somiya S. Strength-toughness relations in sintered and isostatically hot-process ZrO_2-toughened Al_2O_3. *J. Am. Ceram. Soc*., 1986; 69:169–172.

[115] Magnani G, Brillante A.Effect of the composition and sintering process on mechanical properties and residual stresses in zirconia–alumina composites. *J. Eur. Ceram. Soc*., 2005; 25:3383–3392.

[116] Begand S, Oberbach T, Glien W. ATZ—a new material with a high potential in joint replacement. *Key Eng. Mater*., 2005; 284:983–986.

[117] Zhan GD, Kuntz J, Wan J, Garay J, Mukherjee AK. A Novel Processing Route to Develop a Dense Nanocrystalline Alumina Matrix (<100 nm) Nanocomposite Material. *J. Am. Ceram. Soc*., 2003; 86:200-202.

[118] Deville S, Chevalier J, Dauvergne C, Fantozzi G, Bartolomé JF, Moya JS, Torrecillas R. Microstructural Investigation of the Aging Behavior of (3Y-TZP)-Al_2O_3 Composites. *J. Am. Ceram. Soc,* 2005; 88:1273-1280.

[119] Kohorst P, Borchers L, Strempel J, Stiesch M, Hassel T, Bach F-W, Hübsch C. Low-Temperature Degradation of Different Zirconia Ceramics for Dental Applications. *Acta Biomater*., 2012: 8:1213-1220.

[120] Willmann G, Von-Chamier W, Pfaff H, Rack R. Biocompatibility of a new alumina matrix biocomposite AMC. *Key Eng. Mater.*, 2002; 192–195:569–574.

[121] Kohal RJ, Baechle M, Han JS, Hueren D, Huebner U, Butz F. *In vitro* reaction of human osteoblasts on alumina- toughened zirconia. *Clin. Oral Implants Res.*, 2009*;* 20:1265–1271.

[122] Kuntz M, Pandorf T, Chen W. Material properties and life time of a high performance alumina matrix composite for use in total joint replacement. *J. Med. Biomech,*2009; 24:363–368.

[123] Begand S, Oberbach T, Glien W. Investigatons of the mechanical properties of an alumina toughned zirconia ceramic for an application in joint prostheses. *Key Eng. Mater*., 2005; 284–286:1019–1022.

[124] Kamiya H, Sakakibara M, Sakurai Y, Jimbo G, Wada S. Erosion wear properties of tetragonal $ZrO_2(Y_2O_3)$−toughened Al_2O_3composites. *J. Am. Ceram. Soc*., 1994; 77:666–672.

[125] Kerkwijk B, Winnubst L, Mulder EJ, Verweij H. Processing of homogeneous zirconia-toughened alumina ceramics with high sliding wear resistance. *J. Am. Ceram. Soc*., 1999; 82:2087–2093.

[126] Insley GM, Turner I, Fisher J, Streicher RM. In-vitro testing and validation of zirconia toughened alumina (ZTA), in: J.P. Garino, G. Willmann (Eds.), Bioceram. Jt. Arthroplast. Proc. 7th Int. Biol. Symp., Thieme Publishing Group, 2015: 26–31.

[127] Clarke IC, Pezzotti G, Green DD, Shirasu H, Donaldson T. Severe simulation test for run-in wear of all- alumina compared to alumina composite THR, in: J.A. D'Antonio, M. Dietrich (Eds.), Bioceram. Altern. Bear.Jt. Arthroplast, Steinkopff Verlag, Darmstadt, 2006:11–20.

[128] Clarke IC, Green D, Williams P, Donaldson T, Pezzotti G. US perspective on hip simulator wear testing of BIOLOX®delta in 'Severe' test modes, in: F.Benazzo, F. Falez, M. Dietrich (Eds.), Bioceram. Altern. Bear. Jt. Arthroplast,Steinkopff Verlag, Darmstadt, 2006:189–205.

[129] Clarke IC, Green DD, Williams PS, Kubo K, Pezzotti G, Lombardi A, Turnbull A, Donaldson TK. Hip-simulator wear studies of an alumina−matrix composite (AMC) ceramic compared to retrieval studies of AMC balls with 1–7 years follow-up. *Wear*, 2009*;* 267:702–709.

[130] Oberbach T, Begand S, Glien W. In-vitro wear of different ceramic couplings. *Key Eng. Mater.*, 2007;330-332*:*1231–1234.

[131] Begand S, Oberbach T, Glien W. Tribological behaviour of an alumina toughened zirconia ceramic for an application in joint prostheses. *Key Eng.Mater*., 2006; 309–311 :261–1264.

[132] Hamilton WG, McAuley JP, Dennis DA, Murphy JA, Blumenfeld TJ, Politi J. THA with delta ceramic on ceramic: results of a multicenter investigational device exemption trial. *Clin. Ortho. Relat. Res*., 2010; 468:358-366.

[123] Callaghan JJ, Liu SS. Ceramic on crosslinked polyethylene in total hip replacement: any better than metal on crosslinked polyethylene? *Iowa Orthop. J*.,2009; 29:1-1.

[134] Bergschmidt P, Lohmann C, Bader R, Finze S, Lukas C, Ruther W, W, Preliminary clinical results of the multigen plus total knee system with a ceramic femoral component – a national duo – centre study. *Eur. Musculoskelet. Rev*., 2009; 1:82–85.

[135] Thomas I, Milan J, Thomas-Peter R, Martin R, van den Daeelen L, Stockl B. Preliminary Results of a New Nanocrystalline Dispersion Ceramic 'Ceramys,' , 2009:1–4. <http://www.mathysmedical.com/>

[136] http://kyocera-md.com/fields/medical.html

[137] http://www.mathysmedical.com/index.php?id=1&L=1

[138] Stewart TD, Tipper JL, Insley G, Streicher RM, Ingham E, Fisher J. Long-term wear of ceramic matrix composite materials for hip prostheses under severe swing phase microseparation. *J Biomed Mater Res B Appl Biomater*., 2003; 15:567-73.

2

Motivation

2.1 MOTIVATION

The main objective of this thesis is to design and develop new multifunctional ceramic-metal (biocermets) biomaterials for hard tissue replacement with improved, biomechanical performance, reability and functionality.

For this reason different ceramic matrix (3Y-TZP, 3Y-TZP/Al_2O_3) reinforced with biocompatible tantalum metal will be chosen. These materials, with an optimal combination of properties (mechanical, tribological and biological) will be developed controlling the processing parameters related to the microstructure at multiple lengths scales to optimize their microarquitecture.

More recent investigations have accentuated several challenging tasks of composites' microstructural design that still remain unresolved. For example, the yttrium content and distribution in the zirconia matrix composition is of great consideration due to its influence on the toughening mechanism of zirconia [1-9]. Traditionally known methods of doped zirconia powders' production do not allow obtaining a homogeneous yttria distribution in Y-TZP powders that consequently provoke the degradation of mechanical properties during low temperature degradation because of spontaneous tetragonal to monoclinic phase transformation [10-13].

The attempt to minimize the degradation at low temperature of Y-TZP includes reducing the particle size, increasing the content of a stabilizing oxide, or even the formation of composites with aluminum oxide (Al_2O_3). It is known that alumina addition to TZP even in small amounts can improve ageing resistance of the zirconia [14-17].

However, the mechanical properties of ceramics containing mixtures of Al_2O_3 and ZrO_2 described in literature differ by a huge amount because they depend to a large extend on the ratio and homogeneity of the phase distribution, on the grain size and porosity, and

on processing as well as sintering conditions [4, 18-22]. Therefore, one of the aims of present research is to find or develop a new reliable powder processing route to avoid inhomogeneity in the yttria distribution and obtain homogeneous dispersion of zirconia and alumina and, consequently, optimize the microstructure, mechanical properties and improve ageing resistance of ceramics.

In addition, the problem of fatigue behavior assessment of these biocomposites containing discrete metallic particles till present time has not attained enough attention and is of great importance from both scientific and practical point of view. Although, the previous studies [23-27] revealed that the monolithic zirconia is less sensitive to cyclic stresses than the ceramic-metal composition, the idea of the replacement of niobium with alternative metallic tantalum, a refractory metal with higher tensile strength (TS), elastic modulus (E) and yield strength (σ) (TS_{Ta}~485 MPa, E_{Ta}~186 GPa and σ_{YTa}~380 MPa vs TS_{Nb} ~330 MPa, E_{Ta}~ 105 GPa and σ_{YNb} ~240 MPa) [28] as reinforcing phase appears to be particularly interesting. Study on the fatigue strength as an integrity characteristic for zirconia-tantalum compositions will aim to estimate the features and mechanisms of subcritical crack growth and its influence on the toughening mechanisms existing in these biocomposites.

Moreover, the phenomena of friction and wear in knee and hip prostheses as the main (direct and indirect) cause of failure of implants have been addressed by many authors [29-33]. Those studies highlighted the crucial importance of wear assessment in the functional performance of these devices. The choice of the materials for the head and the cup took into consideration not only properties such as mechanical resistance, biocompatibility and corrosion resistance, but also friction and wear. Consequently, the tribological assessment should be carried out by sliding wear testing.

MRI is safe and appropriate noninvasive technique for diagnosing and treating medical conditions. However presence of metal in implants can distort the MRI image. In order to ensure MRI compatibility with the new developed biocermet, the MRI studies should be realized as well.

Besides mechanical and tribological properties, materials used for biomedical applications must always be biocompatible. Thereby, *in vivo* and *in vitro* studies of a novel zirconia/Ta biocermets for hard tissue replacement will be carried out as well.

In order to obtain systematic data, the entire research on the development of new biocermets will be divided into three major blocks referring to the methods of manufacturing. The diagram in Fig.2.1-1 presents the outline of the strategies.

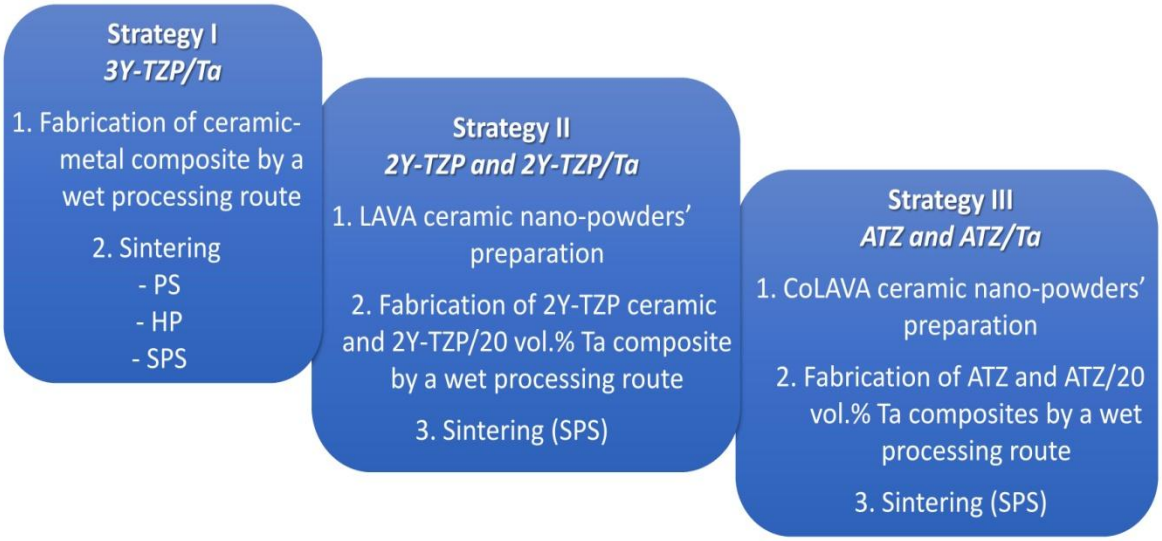

Fig.2.1-1. Schematic outline of the experimental manufacturing

2.2 REFERENCES

[1] Matsui M, Soma T, Oda I. Stress-induced transformation and plastic deformation for Y_2O_3-containing zirconia polycrystals. *J Am Ceram Soc.*,1986; 69:198–203.

[2] Sakuma T, Eda H, Sato H. Composition optimization of ZrO_2–Y_2O_3 alloys to improve the fracture toughness. Science and technology of Zirconia III. *Adv Ceram.,* 1988; 24:357–63.

[3] Masaki T, Sinjo K. Mechanical properties of highly toughened ZrO_2–Y_2O_3.*Ceram Int.,* 1987; 13:109–12.

[4] Vasylkiv O, Sakka Y, Skorokhod VV. Low-temperature processing and mechanical properties of zirconia and zirconia–alumina nanoceramics. *J Am Ceram Soc.,* 2003; 86:299–304.

[5] Yamashita I, Tsukuma K. Phase separation and hydrothermal degradation of 3 mol% Y_2O_3–ZrO_2 ceramics. *J Jap Ceram Soc.,* 2005; 113:530–3.

[6] Lange FF. Transformation toughening: Part 1—Size effects associated with the thermodynamics of constrained transformations. *J Mater Sci*.,1982; 17:225–34.

[7] Basu B, Vleugels J, Van Der Biest O. Toughness tailoring of yttria-doped zirconia ceramics. *Mater Sci Eng.,* 2004; 380:215–21.

[8] Basu B, Vleugels J, Van Der Biest O. Microstructure–toughness–wear relationship of tetragonal zirconia ceramics. *J Eur Ceram Soc*., 2004; 24:2031–40.

[9] Basu B, Vleugels J, Van Der Biest O. Transformation behaviour of tetragonal zirconia: role of dopant content and distribution. *Mater Sci Eng*., 2004; 366:338–47.

[10] Lee JK, Kim H. Surface crack initiation in 2Y-TZP ceramics by low temperature aging. *Ceram Int.,* 1994; 20:413–8.

[11] Kubo T, Machida N, Sakai H, Shigematsu T. Isothermal tetragonal to monoclinic phase transition around room temperature in 2.0 mol% yittria-doped zirconia ceramics. *J Jap Soc Powder and Powder Metall.,* 1999; 46: 496–501.

[12] Yasuda K, Arai S, Itoh M, Wada K. Influence of Y_2O_3 distribution on the rate of tetragonal to monoclinic phase transformation of yttria-stabilized zirconia during hydrothermal aging. *J Mater Sci*., 1999; 34:3597–604.

[13] Li JF, Watanabe R, Zhang BP, Asami K, Hashimoto K. X-ray photo-electron spectroscopy investigation on the low-temperature degradation of 2 mol% ZrO_2–Y_2O_3ceramics. *J Am Ceram Soc*., 1996; 79:3109–12.

[14]. Ross IM, Rainforth WM, McComb DW, Scott AJ, Brydson R. The role of trace additions to yttria-tetragonal zirconia polycrystals (Y-TZP). *Scripta Materialia*, 2001; 45:653-60.

[15] Lee SK, Tandon R, Readey MJ, Lawn BR. Scratch damage on zirconia ceramics. *J Am Ceram Soc.*, 2000; 83:1428-32.

[16] Zhang F, Vanmeensel K, Inokoshi M, Batuk M, Hadermann J, Van Meerbeek B, Naert I, Vleugels J. Critical influence of alumina content on the low temperature degradation of 2–3 mol.% yttria-stabilized TZP for dental restorations. *J. Eur. Ceram. Soc*., 2015; 35:741–750.

[17] Suffner J, Lattemann M, Hahn H, Giebeler L, Hess C, Garcia Cano I, Dosta S, Guilemany M, Musa J, Locci C, Licheri AM, Orru R, Cao G. Microstructure evolution during spark plasma sintering of metastable (ZrO_2–3 mol% Y_2O_3)–20 wt% Al_2O_3 Composite Powders. *J. Am. Ceram. Soc.,* 2010; 93:2864-2870.

[18] Chevalier J, Gremillard L. Ceramics for medical applications: A picture for the next 20 years. *J. Eur. Ceram. Soc*., 2009; 29:1245-1255.

[19] Nevarez-Rascon A, Aguilar-Elguezabal A, Orrantia E, Bocanegra-Bernal M. On the wide range of mechanical properties of ZTA and ATZ based dental ceramic composites by varying the Al_2O_3 and ZrO_2 content. *Int. J Refract Met H.*,2009; 27:962-970.

[20] Kirsten A, Begand S, Oberbach T, Telle R, Fischer H. Subcritical crack growth behavior of dispersion oxide ceramics. *J Biomed Mater Res.,* 2010; 95**:** 202-210.

[21] Sommer F, Landfried R, Kern F, Gadow R. Mechanical properties of zirconia toughened alumina with 10–24 vol.% 1.5 mol% Y-TZP reinforcement. *J Eur Ceram Soc.*, 2012; 32:3905-3910.

[22] Tang D, Lim HB, Lee KJ, Lee CH, Cho WS. Evaluation of mechanical reliability of zirconia-toughened alumina composites for dental implants. *Ceram Int.*, 2012; 38:2429-2436.

[23] Venkateswara Rao KT, Odette GR, Ritchie RO. On the contrasting role of ductile-phase reinforcements in the fracture toughness and fatigue-crack propagation resistance of TiNb/γ-TiAl intermetallic-matrix composites. *Acta Metall et Mater.*, 1192; 40:353–361.

[24] Venkateswara Rao KT, Odette GR, Ritchie RO. Ductile-reinforcement toughening in γ-TiAl intermetallic-matrix composites under monotonic and cyclic loading: Effect on fracture toughness and fatigue-crack propagation resistance. *Acta Metall et Mater.*, 1994; 42:893–911.

[25] Venkateswara Rao KT, Soboyejo WO, Ritchie RO. Ductile-phase toughening and fatigue-crack-growth in Nb-reinforced molybdenum disilicide intermetallic composites. *Metall Trans*., 1992; 23:2249–2257.

[26] Ritchie RO. Mechanisms of fatigue-crack propagation in ductile and brittle solids *Inter J Fracture*, 1999; 100: 55–83.

[27] Smirnov A, Gutiérrez-González CF, Bartolomé JF. Cyclic fatigue life- and crack-growth behavior of zirconia-niobium composites. *J. Am. Ceram. Soc.*, 2013; 96:1709-1712.

[28] ASM Handbook. 10th ed. Materials Park, OH: ASM International; 2000

[29] Hall RM, Unsworth A. Friction in hip prosthesis. *Biomat*., 1997; 18:1017–1026.

[30] Ahlroos T, Saikko V. Wear of prosthetic joint materials in various lubricants. *Wear*, 1997; 211:113-119.

[31] McKellop H, Lu B, Benya P. Friction lubrication and wear of cobalt-chromium, alumina and zirconia hip prostheses compared on a joint simulator Proceedings of the ORS 38th Annual Meeting, Washington, DC, 1992.

[32] Unsworth A, Hall RM, Burgess IC, Wroblewski BM, Streicher RM, Semlitsch M. Frictional resistance of new and explanted artificial hip joints. *Wear*, 1995; 190:226–231.

[33] Oonishi H, Kawai H, Igaki H, Takayama Y. Comparisons of wear of UHMWPE sliding against metal and alumina in total hip prosthesis-wear test and clinical results. *J Biomech*., 1990; 23:382.

3

Zirconia/Tantalum system: Processing and Characterization

3.1 EXPERIMENTAL PART

3.1.1 Introduction

Fig.3.1-1 represents the first block that establishes the primary production-based experimental manufacturing with zirconia matrix composition reinforced by tantalum (Ta) metal particles. There were three sintering routes Spark Plasma Sintering (SPS), Pressureless Sintering (PS) and Hot Press Sintering (HP) applied to the starting mixtures purposing to produce samples for further closer consideration on possible variations of the sintering parameters with further evaluation of obtained samples' microstructures and properties. This evaluation includes X-ray diffraction (XRD), scanning electron microscopy (SEM) and transmission electron microscopy (TEM) as well as tests for assessing the wear, LTD evaluation and mechanical properties such as bending strength, fracture toughness, microhardness, damage tolerance and fatigue behavior.

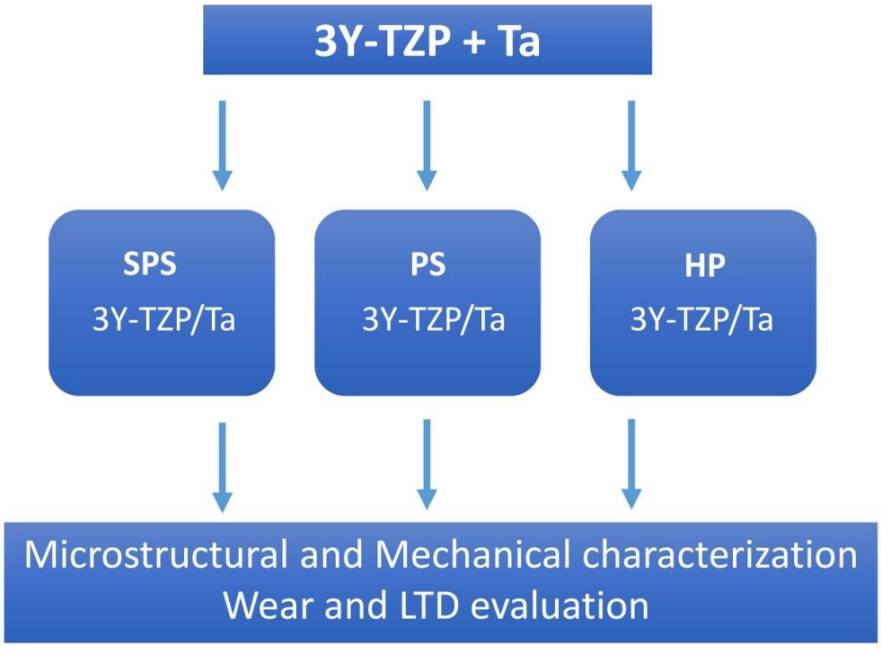

Fig.3.1-1. Strategy I on experimental manufacturing 3Y-TZP/Ta composite

3.1.2 Raw Materials

The following commercially available powders have been used as raw materials:

- Tetragonal zirconia polycrystals (3Y-TZP, 3 mol. % Y_2O_3; TZ-3YS-E, Tosoh Corp., Tokyo, Japan), with an average particle size of d_{50} = 0.26 ± 0.05 µm, with specific surface area of 16 ± 3 m^2/g
- Tantalum (99.97% purity, Alfa Aesar, Ward Hill, MA, USA) with an average particle size d_{50} = 44µm. (Fig. 3.1-2A)

3.1.3 Processing of ceramic-metal powder

3.1.3.1 Tantalum milling

It was shown in the previous works [1, 2] that milled Niobium particles with high aspect ratio distributed in zirconia matrix with optimal interfacial strength is a critical factor for the successful development of tougher ceramic-metal composite. Lamellar flake shape Nb particles showed tortuous crack paths and demonstrated significant crack bridging and deflection by elongated Nb grains. Based on previous, Tantalum raw powder was also attrition milled with zirconia balls in a Teflon container for 4 hours using isopropyl alcohol as liquid media.

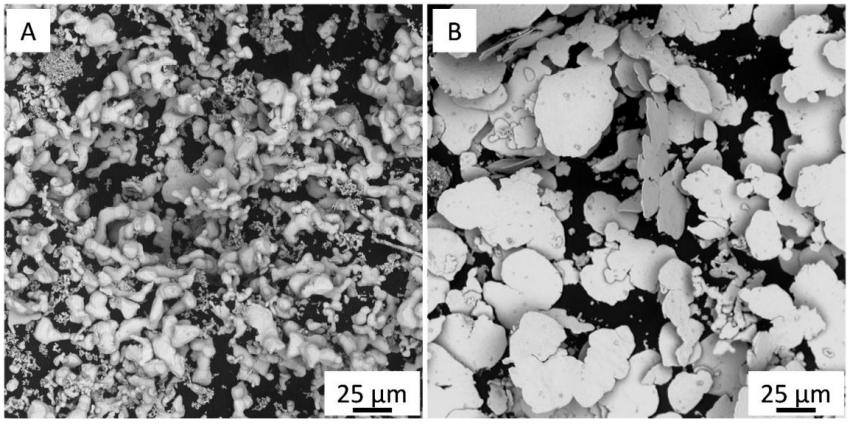

Fig.3.1-2. Scanning Electron Micrographs of tantalum metallic powder as received (A) and after 4 h wet ball-milling (B)

The ball-milled powder consists of flake-like deformed Ta particles (each flake is probably a single deformed original particle) with a high aspect ratio around 50:1 and a mean size of 42 μm. (Fig. 3.1-2B).

The tantalum powder before and after milling was analyzed by X-ray diffraction (XRD). The specimens for the XRD measurements were prepared by suspending a small volume of Ta powder in acetone directly on a Si (510) single-crystal wafer within a specially made supporting assembly and drying the suspension by evaporating the acetone. An evenly spread distribution on Ta powder was observed. The X-ray diffraction powder patterns were collected at diffraction angles 2θ ranging from 35° to 100°. Position and intensity of the peaks were found in the Powder Diffraction File (PDF) 004-0788 from the International Centre for Diffraction Data (ICDD).

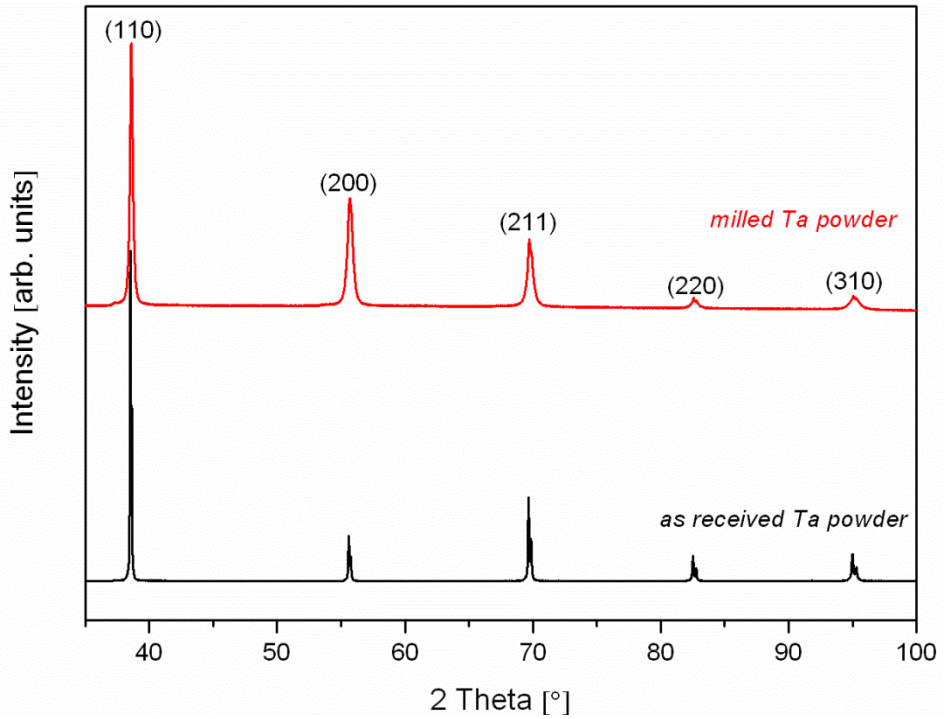

Fig.3.1-3. XRD analysis of Ta powder before (–) and after milling (–). The 200 and 110 reflections of Ta for an as-received and milled powder. Upon ball-milling, pronounced texturing and broadening occurs as a result of deformation and the increase of lattice strain

The ball-milled Ta powder can be textured by the milling process. This texture of the deformed metal particles is revealed by XRD (Fig.3.1-3). A strong preference for the deformed crystallites to have their (200) reflection parallel to the specimen surface occurred. A strong preference for the {100} type of lattice planes to be parallel to the surface was reported for cold-rolled polycrystalline bcc metals [3].

Ball-milling and cold-rolling imply that the material is flattened in between compressing surfaces; that is, the balls in the ball-milling equipment used here and both rolls in rolling apparatus. The texture can be explained as follows. The most particles that deformed were flattened into flakes, which, after being suspended in acetone (in the procedure for specimen preparation for XRD analysis), position on to the Si substrate with strong tendency for their flat sides to be parallel to the surface of the Si substrate. On the other hand, the measurements of the Ta powders showed that the XRD lines become substantially broadened upon ball-milling (Fig.3.1-3). This broadening can be ascribed to the introduction of lattice microstrain.

3.1.3.2 Zirconia/Tantalum slurry preparation

3Y-TZP/Ta slurry with a solid load of 80 wt.% was prepared using distilled water as liquid media and a 3 wt.% addition of an alkali-free organic polyelectrolyte as surfactant [4] with the following proportions (in vol. %) of zirconia (3Y-TZP), and tantalum: 80 zirconia/20 Ta. Then, the wet mixture was homogenized by 24 h milling with zirconia balls in a polyethylene container and then dried. Powder slurry preparation is described in detail below in Chapter 8, Section 8.8.2.1. The obtained powders were compacted by pressureless sintering, hot press, and spark plasma sintering.

3.1.4. Sintering

3.1.4.1 Pressureless sintering (PS)

Four powder mixtures compositions with the following ZrO_2 to Ta ratio (in vol.%): 95/5Ta, 90ZrO_2/10Ta, 85ZrO_2/15Ta and 80ZrO_2/20Ta were prepared. The mixed powders were cold isostatically pressed to cylindrical green samples (≈9 mm in diameter and 50 mm in length) at 200 MPa and sintered in argon atmosphere at 1500 °C for 2 hours before being cooled down to room temperature. Heating and cooling rate 5 °C/min was used.

3.1.4.2 Hot press sintering (HP)

The powders were hot pressed at 1400 °C during 1 h with heating and cooling rates of 600 °C/h in an inert 100% Ar atmosphere. On reaching the hot-pressing temperature, a uniaxial pressure of 45 MPa was applied. Both pressure and temperature were held for 1 hour. As a result discs of 50 mm diameter and 5 mm thickness and 16 mm diameter and 12 mm thickness were obtained.

3.1.4.3 Spark plasma sintering (SPS)

The powders were placed into a graphite die with an outside diameter of 20 mm and 50 mm and subsequently vacuum-sintered according to the next scheme: *(i)* the samples were heated from room temperature to 600 °C at a rate of 600 °C/min, using a pressure of ~ 10 MPa; *(ii)* From 600 °C to 1100 °C a heating rate of 200 °C/min and a pressure of ~ 10 MPa was applied; *(iii)* From 1100 °C to 1400 °C a heating rate of 50 °C/min and pressure of 80 MPa were applied and maintained further for 3 minutes.

3.1.5 Characterization of dense material

3.1.5.1 Density measurement

Bulk densities were measured as explained in Chapter 8, Section 8.5.6 of Experimental setup and data analysis. The relative density of the sintered 3Y-TZP/Ta composites was compared with theoretical value, which was calculated according to the rule of mixtures.

3.1.5.2 X-Ray Diffraction (XRD)

In order to measurement t-m transformation in zirconia matrix XRD analyses of the sintered samples were conducted in a step scanning mode at diffraction angles 2θ ranging from 27° to 33° (step size 0.01°, scan speed 0.06°/min). Position and intensity of the peaks were found in the Powder Diffraction File (PDF) 01-083-0113 and 00-024-1165 from the International Centre for Diffraction Data (ICDD) for tetragonal and monoclinic zirconia, respectively. The monoclinic phase content of different surfaces was calculated using Equations 8.5-2 and 8.5-3 (Chapter 8).

3.1.5.3 Microstructural characterization

For the metallographic examination specimens were hot mounted into the resin powder and then processed under heat and high pressure. Specimen surfaces were polished down to 1 µm diamond slurry finish to enable characterization of microstructure by tabletop scanning electron microscopy (SEM) and focused ion beam scanning electron microscope (FIB-SEM). SPS sintered specimens were studied by transmission electron microscopy (TEM) as well.

3.1.5.4 Fracture surface roughness reconstruction (for HP and SPS samples)

Roughness reconstruction and colored height map of the composites fracture surface after biaxial and fatigue tests were carried out by using tabletop SEM with the 3D Roughness

reconstruction application. The field of view area for the height map calculation was 490 μm^2 (×550).

3.1.5.5 Ab initio density-functional calculations (for SPS samples)

Density functional ab-initio calculations [5] were performed for the ZrO_2-Ta interfaces using SIESTA code [6] within the generalized gradient approximation (GGA) [7]. The employed basis set for the Ta, Zr and oxygen have been described previously [8]. This work was performed by the group of Mª Carmen Muñoz (ICMM-CSIC).

3.1.5.6 Mechanical properties

3.1.5.6.1 Hardness measurement

The Vickers hardness, *Hv*, was measured using a Vickers diamond indenter on polished surfaces, with applied load of 490 N with an indentation time of 10 s. The corresponding indentations sizes were determined using tabletop SEM. The magnitude of the Vickers hardness was determined according to the Equation 8.5-5 (Chapter 8). The hardness results were averaged over 10 indentations per specimens.

3.2.5.6.2 Three point flexural test (for PS samples)

The tests were performed at room temperature using a universal testing machine Shimadzu [9]. The specimens in the form of prismatic bars with dimensions of 3.0 × 4.0 × 45 mm^3 were loaded to failure with a crosshead speed of 0.5 mm/min and a span of 40 mm. The strength, σ_f, was calculated using Equation 8.5-6 in Chapter 8. The Young's modulus was obtained from the slopes of load–deflection curves of three point bending tests. A static extensometer was used to measure the deflection with an error in the measurement of 0.1%.

3.1.5.6.3 Fracture toughness test

The three point bending loading scheme was applied for the fracture toughness determination. The single edge notched beam (SENB) specimen configuration of prismatic bars cut from the pieces (50 mm of diameter or length) and previously sintered (length of 45 mm, a thickness of 4 mm, and a width of 3 mm), was used for fracture toughness testing of ceramic-metal composite. A prenotch was made with diamond saw and then precrack was produced using a razor blade. The dimensions of *a* notch length-to specimen width ratio, *a*/*W*, was 0.4. The tensile surface was polished down to 1 µm. Cross-head displacement speeds of 0.5 mm/min and 40 mm span were used. Fracture toughness, K_{IC} values were calculated in accordance with standard test method [10] using Equations 8.5-15 (Chapter 8).

3.1.5.6.4 Biaxial flexural test (for HP and SPS samples)

Twelve specimens of each HP- and SPS – sintered composition were subjected to a biaxial flexural strength test in a universal testing machine at a crosshead speed of 0.5 mm/min. The definitive fracture load was recorded for each specimen and the biaxial flexural strength was calculated from an Equation 8.5-7 (Chapter 8) in accordance with ISO 6872 [11].

3.1.5.6.5 Damage tolerance

The damage tolerance of the SPS specimens was measured by analyzing the strength data for specimens as a function of indentation load. Indentation cracks are simple to generate and because they are sharp and rather short, they are believed to behave like natural cracks. Indentation strength tests were performed using the discs prepared with the same preparation technique such as in flexural testing. The controlled Vickers indentation flaws at a load between 9.8 N and 490 N were placed at the centers of the tensile faces of each

specimen. The mechanical tests were performed immediately after indentation to avoid any subcritical crack growth due to stress corrosion effects. Special effort was made to examine all specimens after testing using scanning electron microscopy reflected light optical microscopy, to verify that the indentation contact site acted as the origin of failure.

3.1.5.6.6 Biaxial flexure fatigue test (for HP and SPS samples)

In order to study the fatigue behavior, specimens with the same dimensions as for the biaxial flexural strength tests were subjected to a sinusoidal cyclic loading in electromagnetic testing machine operating under load control at 20 Hz (Chapter 8, section 8.5.7.5). The stress ratio was equal to 0.1 and the fatigue cycle was limited at 10000000 cycles for samples without failure.

3.1.5.6.7 Biaxial flexure fatigue test of indented SPS specimens

Indentation fatigue life was analyzed following the same protocol that in the case of the flaw tolerance measurements but the samples were subjected to a sinusoidal cyclic loading. Indentation prints have been introduced in the tensile surfaces of all of the test discs. In order to obtain equivalent initial flaw size load of 196 N and 294 N was selected for ceramic and in ceramic-metal composites, respectively. The crack length was measured discontinuously by means of a tabletop SEM microscope.

3.1.5.7. Wear experiments

The wear tests were carried out using a pin-on-flat tribometer as a material screening test in accordance with ASTM F732-00 standard [12]. The following materials were used: flat-ended ultra-high molecular weight polyethylene (UHMWPE) circular cylinder as the pin material and SPS sintered zirconia and zirconia-tantalum disks as the plate material. The tangential friction force between the pin and the plate was measured by the strain gauges

fixed on leaf springs attached to the transverse bar holding the wear pin. The strain-gauge output voltage was passed through an amplifier and plotted on a chart recorder. Subsequently, by converting this voltage to friction force, friction coefficient data were collected. A constant force of 25 N was applied, resulting in an apparent contact pressure of about 3.54 MPa, a value similar to those borne by the femoral heads [13]. A sliding velocity of 0.06 m/s was applied. Detailed description of experimental set-up and procedures are explained in Chapter 8, Section 8.5.8.

The wear rate '*W*' in mm^3/m was calculated using Equation 8.5-17 (Chapter 8). Volume loss of the polymer specimen was determined by dividing the experimental weight loss by the density (ρ=0.945 g/cm^3) of the polymer. The worn surfaces were analyzed using a tabletop scanning electron microscope (Chapter 8, Section 8.5.5.1).

3.1.5.8. Low temperature degradation (LTD)

Aging experiments were carried out in an autoclave at 134°C under a pressure of 200 kPa for up to 30 h. The SPS sintered samples were placed into the autoclave and left in a steam atmosphere. The tetragonal-to-monoclinic transformation was evaluated up to 30 hours. At predefined time, the test was interrupted in order to measure the surface t–m transformation by means of XRD using Equation 8.5-2 and 8.5-3 (Chapter 8). The tetragonal-to-monoclinic transformation was evaluated up to 30 hours and the diverse XRD patterns were collected.

3.1.5.9 Magnetic Resonance Imaging (MRI)

The SPS sintered disks were half vertically immersed into the Agarose gel with saline solution (1.6%). Magnetic resonance imaging studies were conducted on a 9.4 T MR system (Bruker Biospin, Ettlingen, Germany) with 440 mT/m gradients, and using a combination of a linear birdcage resonator of 7 cm of diameter, for signal transmission, and

a 2x2 arrayed surface coil for signal detection (both from Bruker Biospin, Ettlinglen, Germany). Typical clinical MRI sequence parameters were chosen: spin echo (T1, T2), gradient echo (GRE), and echo planar (EPl) and were similar to routine clinical protocol. All MRI experiments were conducted at Clinical Neurosciences Research Laboratory of University Clinical Hospital of Santiago de Compostela (Santiago de Compostela, Spain).

3.2 RESULTS AND DISCUSSION

The biocermet 3Y-TZP with 20 volumetric % of Niobium designed previously by Bartolomé et al. [1, 2] turned out to be a good prototype in a sense of the quantitative amount of metallic reinforcement for zirconia ceramic matrix. The content of metal phase, (20 vol.%, over the percolation threshold) was defined as the optimum for certain reasons. First, the composite possess the electrical conductivity as a technological characteristic of machinability in case if advanced machining methods should be used to obtain more sophisticated shapes of the bio implants. Second, the excellent mechanical performance under critical and subcritical loading conditions [14] of these synergistically toughened ceramic–metal composites, due to the anticipated interactions between crack bridging and stress-induced phase transformation, combined with high degree of biocompatibility [15] makes it as attractive and tolerant for the hostile environment within the body in addition to the cyclic loads imposed upon it during gait. Additionally, this 3Y-TZP/Nb composite exhibits an optimal combination of ‘‘aging free’’ and tribological characteristics [16, 17]. Consequently, guided by these observations one proposed to start designing the new zirconia-based biocermet and embedding of the same amount of metallic Tantalum as a reinforcement phase.

3.2.1 Pressureless sintering

Pressureless sintering is attractive sintering method to produce ceramic products, mainly due to its simplicity and cost compared to other methods. Therefore, it was important in this study to compare the microstructure and properties of biocermets produced by this simple technique with more advanced and expensive ones.

3.2.1.1 Microstructure and mechanical properties

An electron micrograph of 3Y-TZP/Ta composite is shown in Fig.3.2-1. In this micrograph the darker phase is zirconia; bright is Ta and black is porosity. The tantalum particles are uniformly dispersed in the matrix.

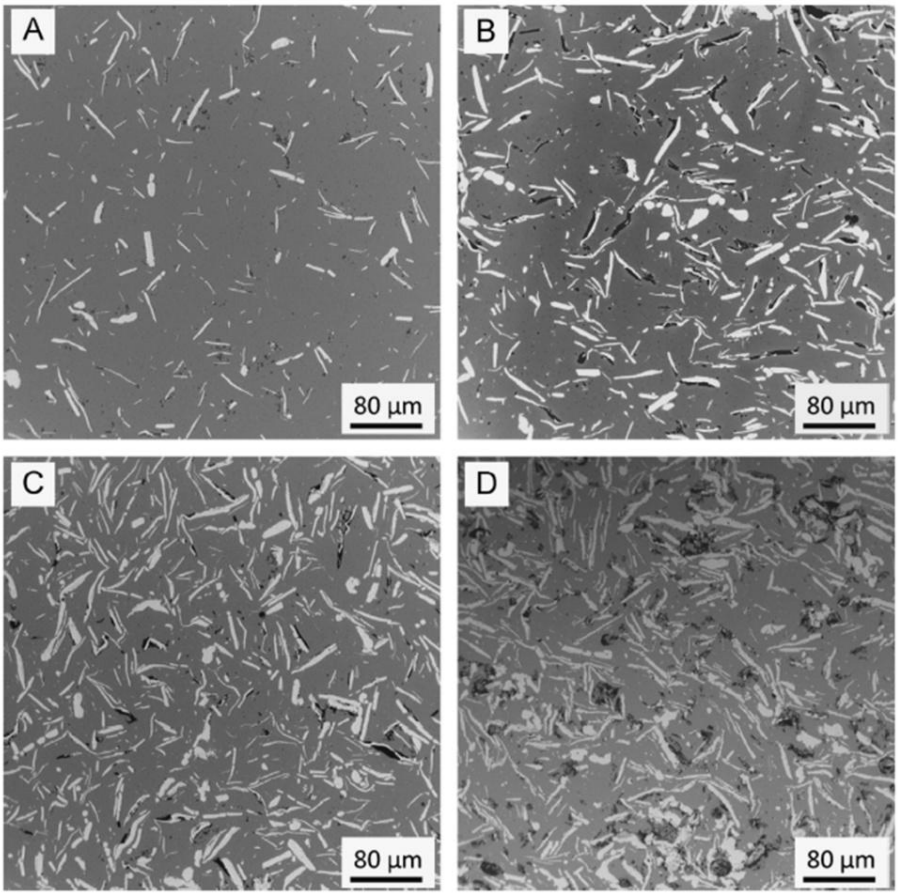

Fig.3.2-1. SEM micrograph of microstructure in zirconia – (A) 5 vol%, (B) 10 vol% (C) 15 vol% and (D) 20 vol% Ta composite

Mechanical properties of PS sintered composites are presented in Table 3.2-1. It was found that the addition of only 5, 10 and 15 vol. % of Ta particles to the 3Y-TZP matrix produces reinforcement effect which appears as increase of fracture toughness up to 12.1 MPa $m^{1/2}$, 12.8 $MPam^{1/2}$ and 14 MPa $m^{1/2}$ respectively. These results were compared with the characteristics of monolithic zirconia (last column in the Table 3.2-1) sintered under the same conditions.

Table 3.2-1. Mechanical properties and transformability of PS composites with various volume % content of Tantalum

	3Y-TZP / 5 Ta	3Y-TZP / 10 Ta	3Y-TZP / 15 Ta	3Y-TZP / 20 Ta	3Y-TZP
Elastic modulus *E* (GPa)	198 ± 5	191 ± 7	182 ± 8	136 ± 4	190 ± 8
Flexural strength *σf* (MPa)	438 ± 14	531 ± 17	697 ± 21	406 ± 12	787 ± 10
Vickers hardness *HV* (GPa)	7.9 ± 0.2	5.7 ± 0.3	5.4 ± 0.3	4 ± 0.3	9.8 ± 0.1
Toughness K_{Ic} ($MPa \cdot m^{1/2}$)	12.1 ± 0.33	12.8 ± 0.42	14 ± 0.47	8.9 ± 0.44	9.1 ± 0.12
Transformability V_t (%)	13.5	15.2	24.3	11.4	9.1
Density	96% th.	95% th.	95% th.	90% th.	98% th.

The increase in toughness may be due to the ductile metallic phase, which can absorb the energy of crack propagation during fracture, and could enhance crack deflection and bridging as well as stress relaxation near the crack tip. In addition to this, the higher transformability of zirconia occurred because of the presence of solid solution of Ta_2O_5. On the starting Ta powder surface the tantalum oxide (Ta_2O_5) is always present as passivated oxide layer. The phase diagram for the zirconia-rich portions of the Ta_2O_5–ZrO_2 system [18] at temperatures in excess of 1400 °C indicates limited solubility of the pentavalent oxide in zirconia (~2 mol% $TaO_{2.5}$). However, co-doping with yttria has been observed to enhance their solubility in the tetragonal phase [19–21]. The occurrence of this oxide in bulk Y_2O_3 stabilized ZrO_2 increases the transformability of zirconia matrix. The enhanced transformability is related to the alloying effect on the tetragonality (c/a – cell parameters ratio) of stabilized tetragonal ZrO_2, so the addition of this oxide increases the tetragonal distortion of the cubic lattice. When a trivalent oxide, like Y_2O_3, is added to ZrO_2 as

stabilizer, certain amount of lattice defects i.e. oxygen vacancies, are produced in the ZrO_2 lattice. The effect of doping with pentavalent oxides such as Ta_2O_5 (cationic radii in the +5 oxidation state ~0.68 Å) indicates that ions reside as substitutional defects in the zirconium lattice (ionic radius of the Zr4+ ion is 0.79 Å), annihilating the oxygen vacancies generated by yttria doping. Since oxygen vacancies are effective in stabilizing the tetragonal structures, the destabilizing effect of Ta doping can be attributed to the decreased concentration of oxygen vacancies [20, 21]. In order to determine the content of solid solution (SS) in sintered samples EDX measurements were carried out. Analyses of 100 random points were conducted to obtain a semi-quantitative basis for the tantala distribution in the sintered microstructures. The fraction of Ta_2O_5 was found lower than 2 mol% and no additional phases were detected.

Fractographic studies of the materials showed evidence of bridging and plastically deformed tantalum lamellar particles (Fig.3.2-2), except for the composition with 20 vol.% Ta. In this particular case the dominant failure mechanism is metal particle pull-out. No evidence of plastic deformation was observed. Residual porosity remains at the ceramic–metal interface (Fig. 3.2-2D).

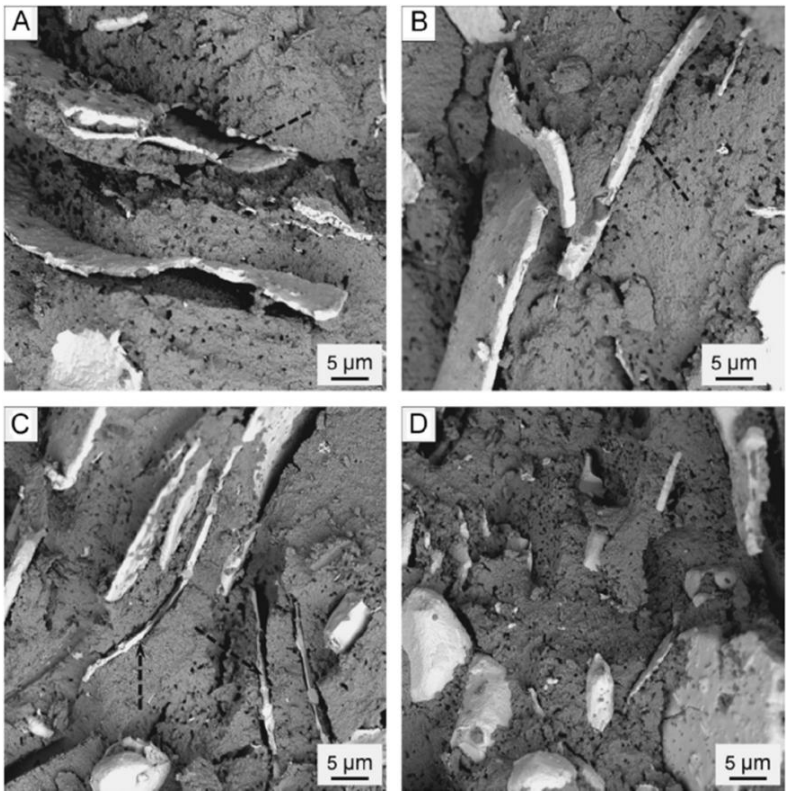

Fig.3.2-2. SEM micrographs of the fracture surface of zirconia – Ta (A – 5 vol.%, B – 10 vol.%, C – 15 vol.% and D – 20 vol.%) composite. Dashed black arrows show the plastic deformation of tantalum particles

Hereby, crack bridging of the elastic–plastic deformations of ductile metal particles associated with the transformation mechanism in zirconia matrix lead to enhancement the fracture toughness of ceramic– metal composites fabricated by pressureless sintering.

The lower value in strength and fracture toughness of 3Y-TZP/20 vol.% Ta composite is related to ceramic–metal interface porosity. In spite of enhanced properties of compositions with content of Ta less than 20 vol.% these materials are electrically non-conductive and consequently it is difficult to produce complex shapes or geometries from them, for example in case of implants. In order to obtain dense materials with 20 vol.% of Ta, composites were sintered by Hot Press and Spark Plasma Sintering techniques.

3.2.2 Hot Press sintering

3.2.2.1 Microstructure and mechanical properties

Dense (>98 th.%) and homogeneous ceramic–metal composites were initially fabricated from 3Y-TZP and tantalum (20 vol.%) powders. An electron micrograph of 3Y-TZP/Ta composite is shown in Fig.3.2-3.

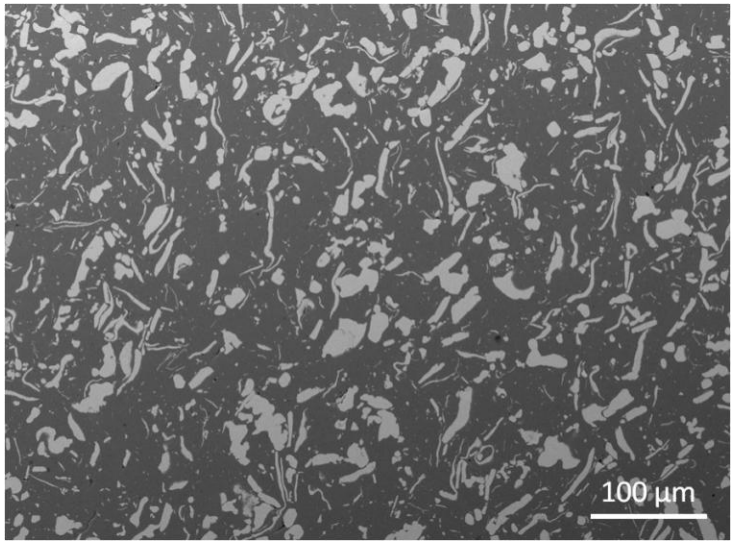

Fig.3.2-3. SEM micrograph of microstructure in 3Y-TZP/20 vol.% Ta composite

In this micrograph the darker and bright phases are zirconia and tantalum grains, respectively. The tantalum particles are uniformly dispersed in the matrix and no porosity is observed. As can be seen, the 3Y-TZP/Ta interface is well bonded and no microcracks are observed.

According to the biaxial test, the 3Y-TZP/Ta material exhibited higher strength value (992 ± 13 MPa) in comparison with pure zirconia one (960 ± 10 MPa) [14] tested under nearly equal values of elastic modulus. The SEM observations of the fracture surfaces showed that the major toughening mechanism is the plastic deformation with further partial debonding of tantalum particles (Fig.3.2-4).

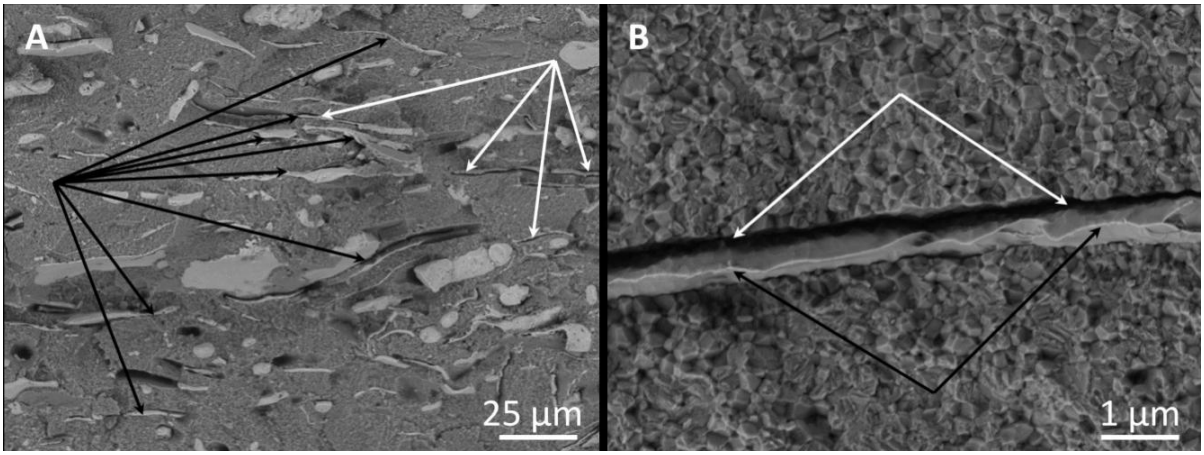

Fig.3.2-4. Fracture surface for cracks extending at the 3Y-TZP/Ta interface. Black arrows show the plastic deformation of a tantalum grains. White arrows show the decohesion between the matrix and the tantalum particle

In addition to this, as has been mentioned above, the increase in toughness occurred because of the presence of solid solution of Ta_2O_5 enhances the transformability of zirconia. It was found that the transformability in 3Y/TZP-Ta composite is around 21%, while in 3Y-TZP ceramic is only about 4%. Therefore the presence of plastic deformation of tantalum particles with the high transformability in ceramic-metal composite causes the increase of the average fracture toughness to 16 ± 0.6 MPa $m^{1/2}$ which significantly exceeds the values for monolithic ceramic (8 ± 0.5 MPa $m^{1/2}$).

The embedding of a ductile metallic phase into a brittle matrix increases not only their fracture toughness, but also influences the fatigue performance [14, 22]. For these reasons, dealing with the complexities of subcritical crack propagation under cyclic loads must be considered as an important task for the structural design of ductile-phase toughened brittle-matrix composites. To date, studies on the mechanical properties of such ductile-particle reinforced brittle materials have focused on strength and fracture-toughness behaviour, in particular on the contributions to toughening under monotonic loading conditions [23-27]. Conversely, very few investigations have been focused on the composite behaviour under

cyclic load. These studies have shown that toughening is far less effective in fatigue simply because of the premature failure of ductile phase. Indeed, the fatigue sensitivities, characterized by the slopes of *S-N* curves, are often lower for unreinforced than for reinforced matrixes [14, 28-31]. Therefore, fatigue analysis and fatigue strength prediction are highly required especially for the case of fail-safe or damage tolerance design for structural components like biomedical implants. Accurate prediction of fatigue life is a challenge in ceramic-metal composites due to the complicated nature of fatigue crack initiation and propagation, the interfaces' properties and complex material behavior under loading and unloading regimes. In this end, high cycle fatigue analysis was carried out, coupled with microstructural characterization, in order to assess the fatigue performance and the mechanisms of bulk material fracture. The results for cyclic fatigue lives for the disk specimens are presented in semi logarithmic form as peak stress versus cycles to failure (*N*) in Fig.3.2-5. The tests were interrupted at $N = 10^7$ cycles, for samples without failure. These samples are marked by an arrow symbol. It was found that fatigue limit for 3Y-TZP/Ta, 3Y-TZP/Nb [14] and 3Y-TZP is around 850 MPa, 400 MPa and 930 MPa, respectively. The data obtained from the fatigue tests allowed the construction of *S–N* curves presented in Fig.3.2-5, which shows that the fatigue behavior of monolithic zirconia and 3Y-TZP/Ta composite is different from the behavior of the 3Y-TZP/Nb composite.

The first conclusion that can be drawn from the obtained dependencies of stress amplitude σ_{max} vs cycles to failure *N* is that 3Y-TZP/Nb composite exhibit fatigue behavior in contrast to 3Y-TZP /Ta composite and monolithic zirconia. This can be seen from the fact that in the *S–N* plots the stress $\sigma_{\max}$ for 3Y-TZP/Nb composite decreases with the cycles to failure *N*. Moreover, the slope of the discussed dependency $\sigma_{\max}$ vs log *N* is smaller for the zirconia and 3Y-TZP/Ta composite when compared to the 3Y-TZP/Nb composite.

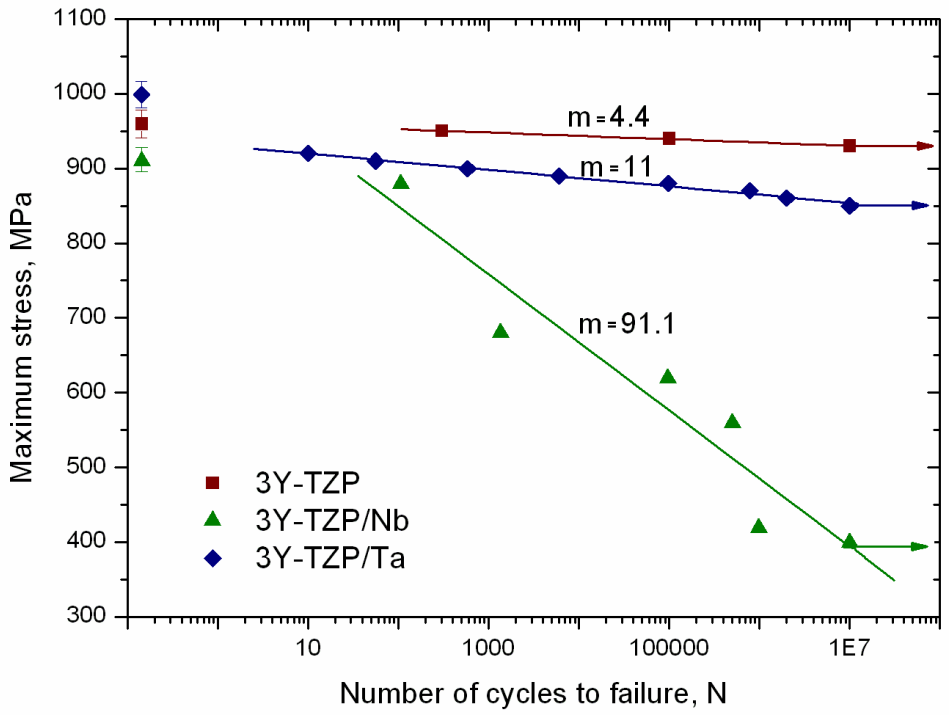

Fig.3.2-5. Fatigue resistance *S–N* curves with values of slopes (m) for HP sintered specimens. Ultimate flexural strength of materials is given as well

Therefore, the sensitivity to cyclic stresses is higher in the 3Y-TZP/Nb cermet than for the monolithic zirconia and 3Y-TZP/Ta composite. Higher slope in Fig.3.2-5 indicates increased accumulation of damage during the cyclic loading. Unreinforced zirconia essentially shows no cyclic stress sensitivity upon fracture and is thus represented as a near horizontal line in the *S–N* plot due to absence of any toughening mechanism and consequently displays low fracture toughness that lead to brittle fracture. Meanwhile in spite of 3Y-TZP/Ta composite exhibits the similar slope as zirconia ceramic the value of its fracture toughness is higher therefore it allows avoid brittle fracture and prevent catastrophic failure.

Analyses of the fracture surfaces after static and cyclic bending tests indicate distinct failure modes of the metal particles for the 3Y-TZP/Ta ceramic-metal composites. In the fatigue region the microstructure of 3Y-TZP/Ta is somewhat similar to the fast fracture

one, but it is evident that smoothing plastic deformation of the metal particles occurred. This is verified by measuring composite's fracture surface roughness. Fig.3.2-6 represents of 3D Roughness fracture surface region of the 3Y-TZP/Ta composite with *Ra* (μm) roughness after biaxial strength and fatigue test. The field of view area for heightmap calculation was 490 μm^2 (×550).

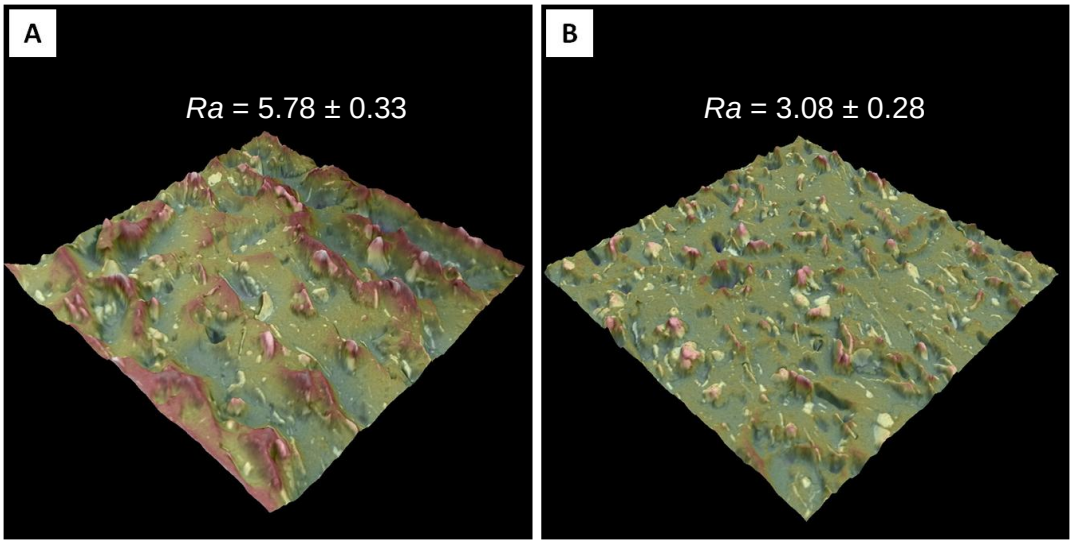

Fig. 3.2-6. 3Y-TZP/Ta composite's fracture surface 3D roughness image after biaxial flexure (A) and fatigue (B) test

Thus, it is possible to hypothesize a fatigue fracture mechanism for ceramic–metal composite. In a first step damaging occurs by cracking of the ceramic network and local debonding at the interface. Coalescence of cracks and debonded zones then takes place, leading to larger cracks; these cracks propagate until a critical dimension is reached, and the fast fracture occurs. The dimension of the fatigue zone can be quite small.

This suggests that the overall fatigue resistance of the composite is not produced by the bridging metallic particles of large cracks, but by the microcracking, blunting and debonding process for small cracks length. The fatigue cracks reaches the interface between the ceramic and metal particles and it is stopped by abrupt change in the local stress–strain

field. The difference in the crack-tip opening displacement between the ductile particle and the brittle matrix will cause the crack to be locally blunted that reduces the stress at the crack tip through elastic loading. In addition, the effects of the residual stress due to thermal expansion coefficients (CTE) mismatch between 3Y-TZP (8.44×10^{-6} °C^{-1}) and Ta (6.73×10^{-6} °C^{-1}) have to be taken into consideration. The metal particles with lamellar-flacky shape set under compressive residual stresses, act as a barrier which delays the crack propagation and increases the fatigue life under cycle conditions.

The difference between the fatigue behaviour in 3Y-TZP/Ta and 3Y-TZP/Nb composite will be explained in the next section on spark plasma sintering.

3.2.3 Spark plasma sintering

Spark plasma sintering has become a popular and powerful technique for ceramic consolidation, however, this technique was in the first time applied to produce the biocermet reinforced by Tantalum for this research project.

3.2.3.1 Microstructure and mechanical properties

Scanning electron micrographs corresponding to 3Y-TZP/20 vol.% Ta composites are shown in Fig.3.2-7. The microstructures of composites sintered by SPS and HP (Fig.3.2-3) are similar. In these micrographs, the darker and bright phases correspond to zirconia and metal grains, respectively. The metallic particles are uniformly dispersed in the matrix and no porosity is observed. As can be seen, the 3Y-TZP/Ta interface is well bonded and no microcracks are observed.

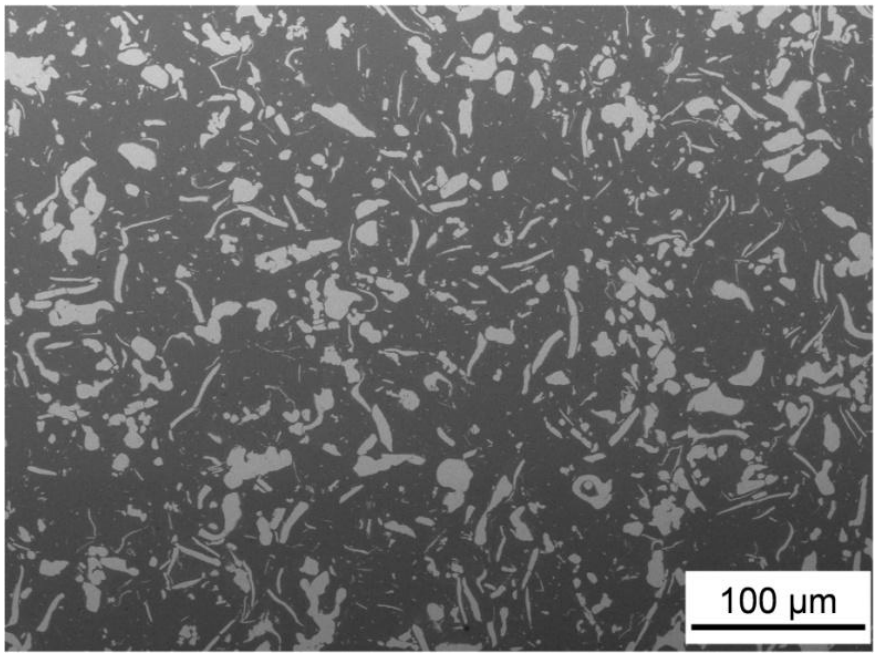

Fig.3.2-7. Scanning electron images corresponding to the microstructure of 3Y-TZP/20 vol.% Ta composite

The high resolution transmission electron micrograph shows a direct contact between both grains at the interfaces without any additional phases (Fig.3.2-8). Only a solid solution of Ta_2O_5 in ZrO_2 can take place [32, 33] but not formation of an interface phase as it has been observed.

A detailed analysis of the micrograph of Fig. 3.2-8 allowed us to determine the presence of (111) crystallographic planes corresponding to the equivalent cubic zirconia crystals parallel to the Ta (110). Additionally, Ta (10-1) planes are also detected (see the FT image inset of Fig.3.3-8), so it can be concluded that <111> direction of Ta crystal is perpendicular to the picture plane. In this regard, a perpendicular plane to the {110} and {111} families is the plane Ta(0-1-2). Considering the geometry of Fig.3.2-8, the only plausible ZrO_2 planes parallel to this one are the ZrO_2{110}. So that, we can assign the picture interface to be Ta(1-1-2)/ZrO_2(3-30). This interface has a mismatch of 16% and has not been previously observed in the similar system 3Y-TZP/Nb [2].

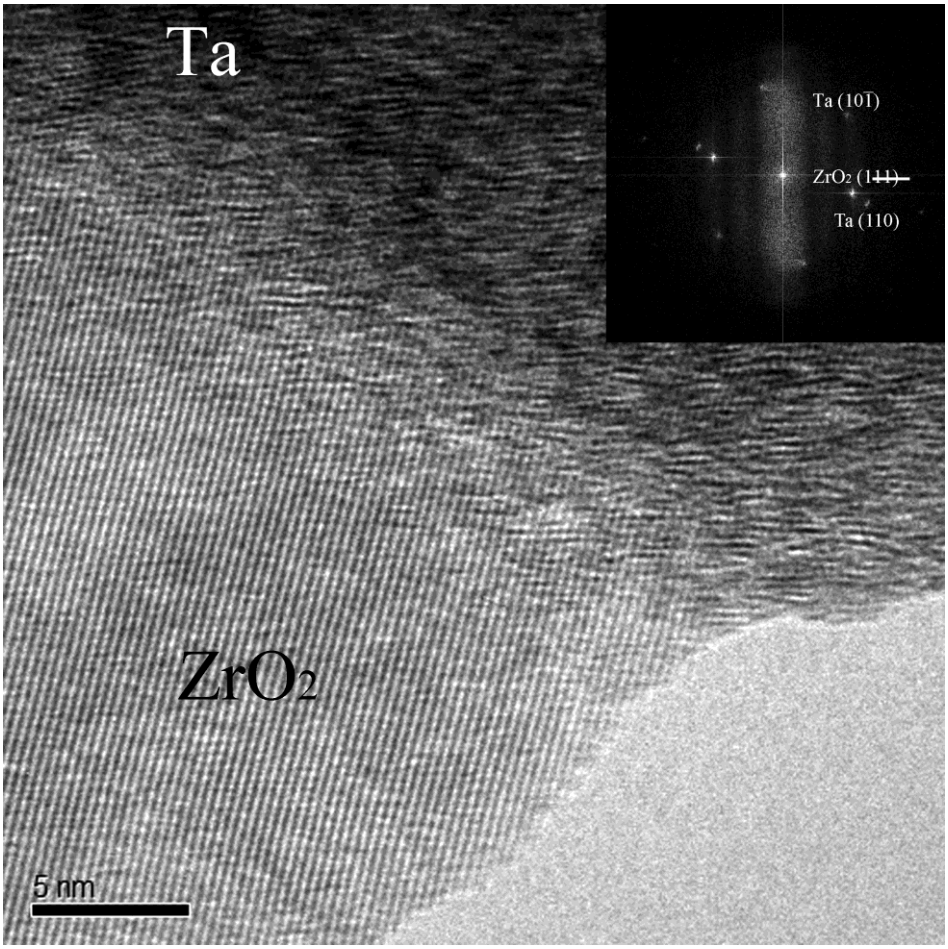

Fig.3.2-8. HRTEM image of the Ta/3Y-TZP interface

In this sense, the presence of (012) cleaving planes in milled Ta grains, could be the origin of such planes at the interface [34].

The physical and chemical properties of the bonds are dictated by the phase boundary between the metal and the ceramic. The interfacial properties can be described as a function of their structure and bonding strength. Table 3.2-2 shows the work of separation (*Wsep*) of the calculated interfaces. Both interfaces present similar works of separation for analogous crystallographic directions, although the values are slightly larger for the Ta-based interfaces. The *Wsep* is very different depending on the polarity of the ZrO_2. The polar ZrO_2 (100) surface has a larger number of dangling bonds per unit area and consequently a larger surface energy, see Table 3.2-2.

Table 3.2-2. Work of separation (W_{SEP}) and interface Metal-O shortest distances for the different interfaces

ZrO_2-M interface	d_{M-O} (Å)	W_{SEP} (J/m^2)	$2\sigma_{ZrO2}$ (J/m^2)	$2\sigma_M$ (J/m^2)
(111)-Ta(100)	2.15	2.23	2.11	5.72
(100)-Ta(100)	2.05	10.18	13.42	6.48
(3-30)-Ta(1-1-2)	2.16	2.22	3.08	6.06
(111)-Nb(100) [2]	2.22	1.84	2.03	4.50
(100)-Nb(100) [2]	2.10	9.02	13.31	5.29

These interfaces formed along the (100) direction present a very high *Wsep* due to the avidity of ZrO_2 surface oxygens to saturate and thus to form a strong metal-oxygen bonds at the interface.

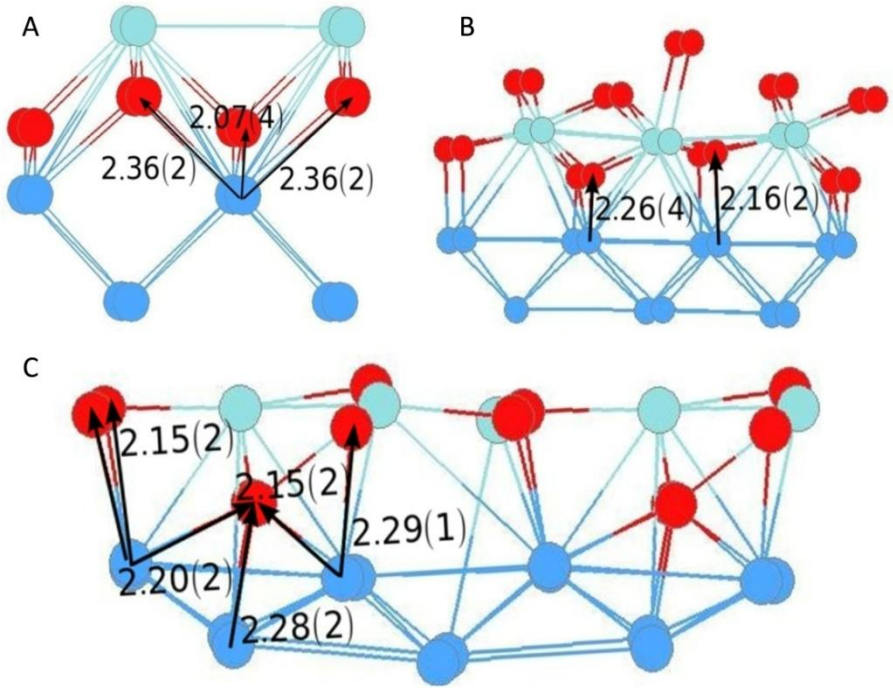

Fig.3.2-9. Atomic sketch of the atomic structure for the 3 ZrO_2/Ta interfaces: a) (100)/(100), b) (111)/(100) and c) (3-30)/(1-1-2) , respectively. In the color code green corresponds to Zr, red to O and blue to metal atoms. The arrows show the smallest metal-O distances and between parenthesis the number of occurrences along the perpendicular direction in the depicted cell, which have an area of a) 51.00, b) 43.71 and c) 55.79 Å^2

Wsep correlates also with the number of short interface bonds and bond density per interface area, as indicated in Fig.3.2-9, where a schematic representation of the equilibrium structures is shown for the Ta-ZrO_2 interfaces.

In Fig.3.2-9 the shortest bonds and a large density of bonds at the interface (8/51 bonds/$Å^2$) occurs for the (100)/(100) orientation, which corresponds to the highest *Wsep*, see Table 3.3-2, while the (111)/(100) and (3-30)/(1-1-2) orientation show larger bonds and smaller densities of 6 bonds/43.71$Å^2$ and 9 bonds/55.79$Å^2$ respectively, corresponding to smaller *Wsep*.

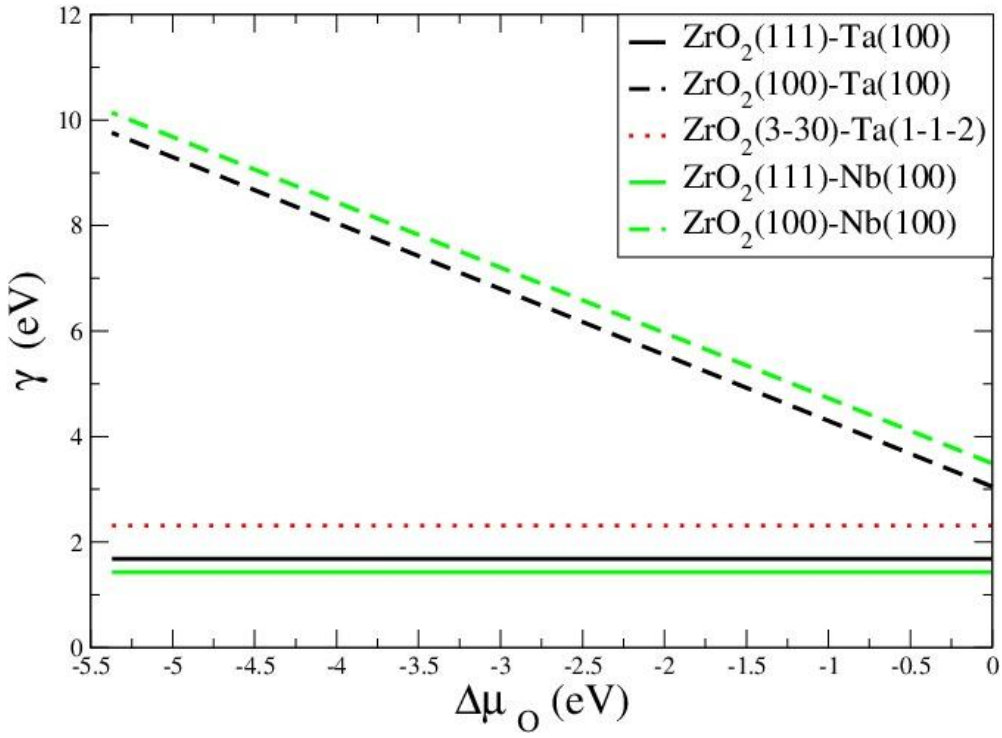

Fig.3.2-10. Interfacial energy (difference of the interface energy minus the bulk energy of all the interface atoms) vs the delta of the oxygen chemical potential $\Delta\mu_0$ (difference of the μ_0 at the interface minus the μ_0 at the O_2 molecule, which we obtain 5.37 eV). Notice that the experiments are synthesized at low μ_0, so the interface regime is close to the left side of the graph

On the other hand the thermodynamic stability of all composite interfaces are plotted in Fig.3.2-10 which shows that interfaces with non-polar ZrO_2 orientations are more stable

than the polar ones, particularly close to the negative chemical potential limit which corresponds to the experimental conditions of low oxygen partial pressure.

Therefore, ZrO_2–metal composites may present diverse interfaces with different strength, being the strongest the less stable, and consequently composite may show moderated interface strength. As can be inferred from Fig.3.2-10, the (3-30)/(1-1-2) interface orientation, repeatedly observed in HRTEM study, is thermodynamically stable. In addition, due to the lamellar shape of Ta particles, it is expected that different ZrO_2 orientations form interfaces with the Ta (100) surface. For those interface orientations the *Wsep* ranges going from high (~10 J/m^2) to medium values (~2 J/m^2), which will favor energy dissipation through mechanisms like crack deflection and crack bridging.

The results concerning the mechanical evaluation of the composites are enclosed in the Table 3.2-3 below.

Table 3.2-3. Densities and mechanical properties of the all studied specimens as well as volume fractions of tetragonal "t" and monoclinic "m" zirconia in polished and fractured surfaces of the ceramic specimens and the resulting transformabilities of tetragonal zirconia

Specimen	Density [% φ_{th}]	Elastic modulus E [GPa]	Flexural strength σ_f [MPa]	Hardness HV [GPa]	Fracture toughnes K_{Ic} [MPa $m^{1/2}$]	Volume fractions of t- and m-ZrO_2 [vol%]				Transformability of t-ZrO_2 V_{trans}
						Polished		Fractured		
						t	m	t	m	
3Y-TZP	99	198±5	1217±10	13±0.3	6±0.3	98.9	1.1	97.1	2.7	1.8
3Y-TZP/Ta	98	194±7	970±18	9±0.7	16±0.9	94.1	5.9	76.9	23.1	17.2
3Y-TZP/Nb	98	179±6	850±20	10±0.8	15±1	97.8	2.2	78.7	21.3	19.2

The mean biaxial flexural strength corresponding to 3Y-TZP, 3Y-TZP/Ta and 3Y-TZP/Nb are 1217 MPa, 970 MPa and 850 MPa, respectively. As a direct consequence of the smaller critical grain size in ZrO_2, the bending strength of the monolithic ceramic is higher than the

strength corresponding to both zirconia-metal composites. The Young's moduli of the composites (≈ 200 GPa) were found to be very close to the values predicted by the rule of mixtures by Voigt and Reuss models. The composites exhibited a higher toughness value (16 ± 0.9 $MPa \cdot m^{1/2}$ and 15 ± 1 $MPa \cdot m^{1/2}$, for 3Y-TZP/Ta and 3Y-TZP/Nb composites, respectively) than the 3Y-TZP (6 ± 0.3 $MPa \cdot m^{1/2}$). The increase in toughness must be due to the ductile metallic phase, which can absorb the energy of crack propagation during fracture, and could enhance crack deflection and bridging as well as stress relaxation near the crack tip. In addition, this increase has occurred because of the presence of solid solution of pentavalent oxides such as Nb_2O_5 and Ta_2O_5, enhancing the transformability of zirconia. Table 3.2-3 shows the monoclinic volume fraction estimated on polished and fractured surfaces of monolithic zirconia and zirconia-metal composites. The results show that in the monolithic ZrO_2 only about 3 vol.% of the tetragonal zirconia transformed to the monoclinic phase during the failure. Moreover, the analysis of XRD data proved that the fraction of zirconia transformation considerably increases for zirconia-metal composites. The modest monolithic zirconia toughness value can be explained by the low transformation of zirconia after fracture unlike ceramic-metal composites (Table 3.2-3).

Analyses of the fracture surfaces after bending tests indicate two distinct failure modes of the metal particles; the tantalum particles fracture surface bears little resemblance to typical ductile necking associated with void coalescence, such as those shown for niobium particles (Fig. 3.2-11A and 3.2-11B).

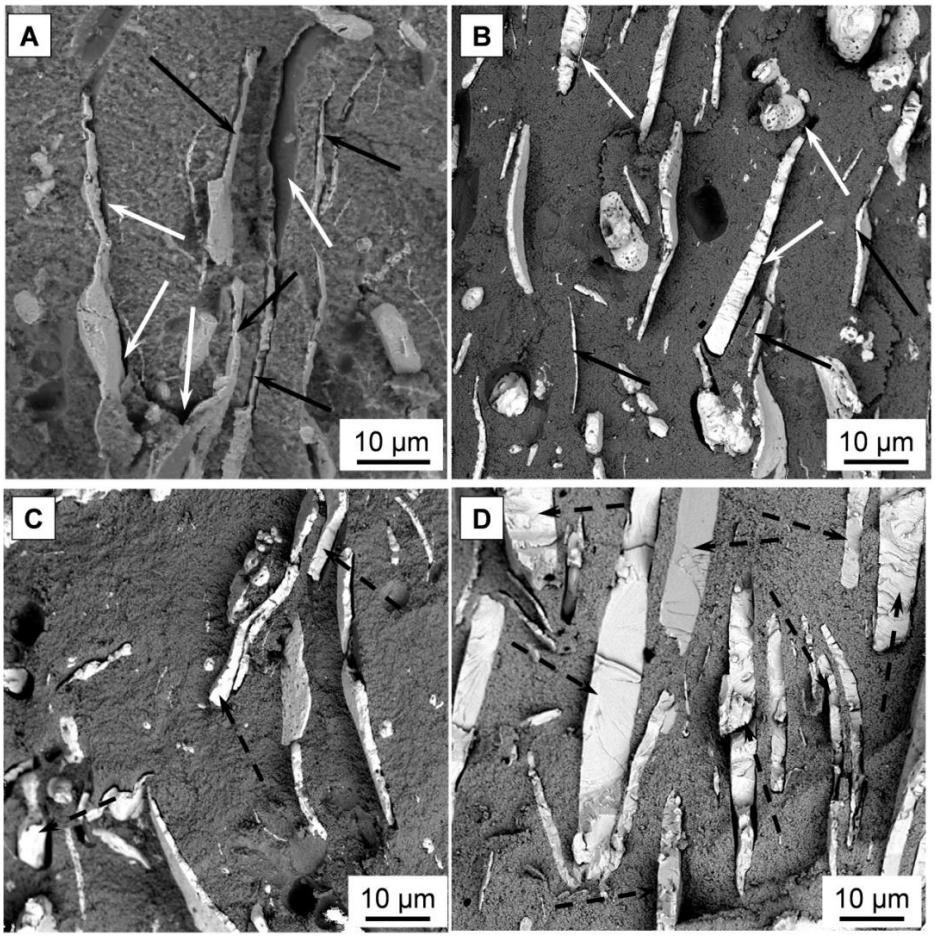

Fig.3.2-11. Fracture surfaces of SPSed 3Y-TZP/Nb (A, C) and 3Y-TZP/Ta (B, D) composites after bending and fatigue test, respectively

Black arrows in Fig.3.2-11 show plastic deformation of metallic particles White arrows show decohesion between the matrix and the metallic particles. Dashed black arrows show the cleavage of metallic particles. Also, nearly planar facets form between ridges and valleys, reminiscent of brittle cleavage or intergranular decohesion have been observed in tantalum particles, in accordance with previous studies [35].

In order to investigate microstructural evolution of 3Y-TZP/Ta composites with indentation crack propagation FIB technique was used. Fig.3.2-12 shows the FIB-SEM image of crack-microstructure details along the path of crack.

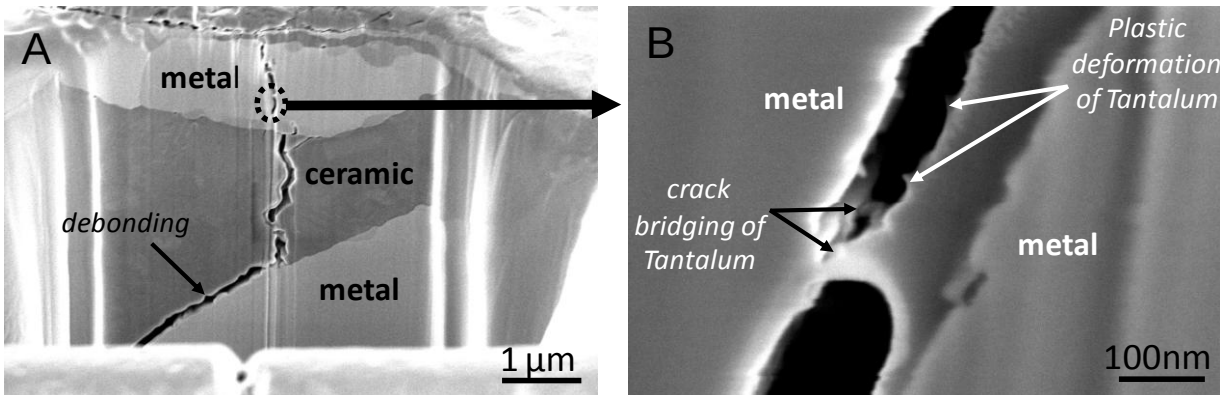

Fig.3.2-12. FIB-SEM image of crack propagation in the zirconia-tantalum composite. Arrows indicate interface debonding between the metal particles and the ceramic (A), plastic deformation (B) and crack bridging of ligament (B)

The presence of micron-sized metal particles in ceramic matrix lead to void nucleation, growth, and coalescence, either by particle fracture or by particle/matrix interface debonding. These observations also confirm the presence of plastic deformation and crack bridging of tantalum particles.

The theoretical analysis, besides the interface strength (*Wsep*) also provides information of the surface energies (σ), with which we can estimate the region responsible of a failing material when a crack propagates, being the interface, metal or ceramic if the lowest value is the Wsep, the σ_{Metal} or the σ_{ZrO2} respectively, see Table 3.2-2. Since with our calculations we only obtain the elastic contribution to the mechanical properties, we expect that the plastic reinforcement mechanisms, such as bridge mechanism, will take place only if the σ_{Metal} is the lowest value, otherwise a failure of the system is expected via debonding. We observe that only those interfaces formed by the strongly polar ZrO_2 (001) orientation show such high *Wsep* for the σ_{Metal} to be the lowest value and therefore reinforce the ceramic phase, regardless of the metal employed. Together with the experimental fracture surface analysis we believe the crack propagates to an interface and then either continues thought the interface, if the particle is large, causing decohesion or suffer some energy dissipation

mechanisms, if the particle is not so large and with a high aspect ratio. The latter would be due to the crack eventually entering into an interface with polar ZrO_2 termination, which shows a high *Wsep*, and then forcing the crack to pass through the metal with the correspondent plastic dissipation. Furthermore, not only must the metal particle-matrix bond be strong enough for load transfer and energy dissipation by metal particle plastic deformation but it must remain sufficiently weak to support cleavage and therefore act as a crack entrapment if the metal particle is large or with low plasticity.

Fig.3.2-13 shows a plot of the indentation load versus the strength of indented samples. Each data point represents the mean of about twelve specimens at a given load. In order to calculate the best fitting to the data from studied materials linear regression equation was used. It was found that the slopes of monolithic zirconia and ceramic-metal composites were 0.30 and 0.06, respectively. The smaller slope of the ceramic-metal composites indicate that this behaviour allowing to exhibit greater indentation strength and flaw tolerance than the monolithic ceramic. The explanation for this difference in slopes is that cermets exhibits better crack growth resistance behaviour in which the toughness increases with increasing crack length. Brittle materials which show no rising R-curve behavior, present a slope of 1/3 (dashed line in Fig.3.2-13) and materials with slopes lower than 1/3 are expected to have R-curve behavior. For a given indentation flaws 3Y–TZP/Ta and 3Y-TZP/Nb composites always have higher values for the fracture strength, which means that the damage tolerance of these composites are higher than for monolithic zirconia ceramic. Although 3Y-TZP un-indented ceramic exhibits the highest value of the fracture strength, the fail of strength of the indented ceramic-metal composites is lower than in the zirconia samples.

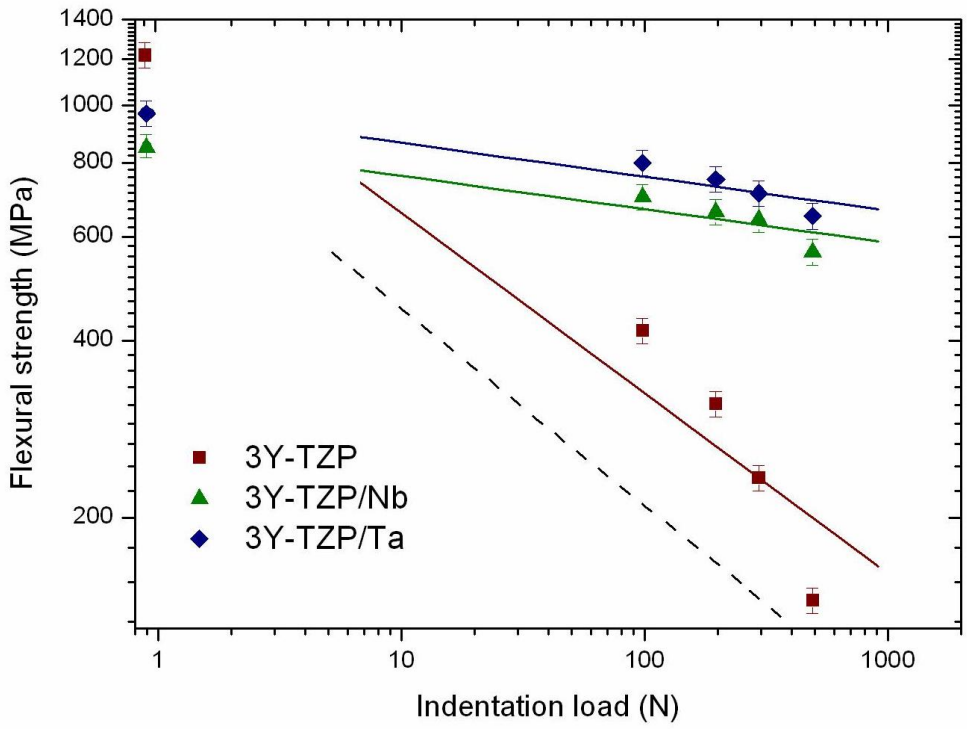

Fig.3.2-13. Indentation load versus strength plots of 3Y-TZP/Ta, 3Y-TZP/Nb composites and zirconia ceramic. The indentation-strength data to the $P^{-1/3}$ strength response is shown by the diagonal dashed line

Despite efforts to improve the toughness of brittle-matrix composites, little attention has been paid to their performance under cyclic loading. In this end, biaxial fatigue testing method was used to characterize the cyclic fatigue crack-growth behavior of ceramic and ceramic-metal composites.

The results for cyclic fatigue lives for the disk specimens are presented in semi logarithmic form as peak stress versus cycles to failure (*N*). The flexural strengths, σ_f, of the materials are given as well (Fig.3.2-14). For interpretation of materials fatigue data the exponential model was used. The estimation of the model parameters was based on linear regression analysis.

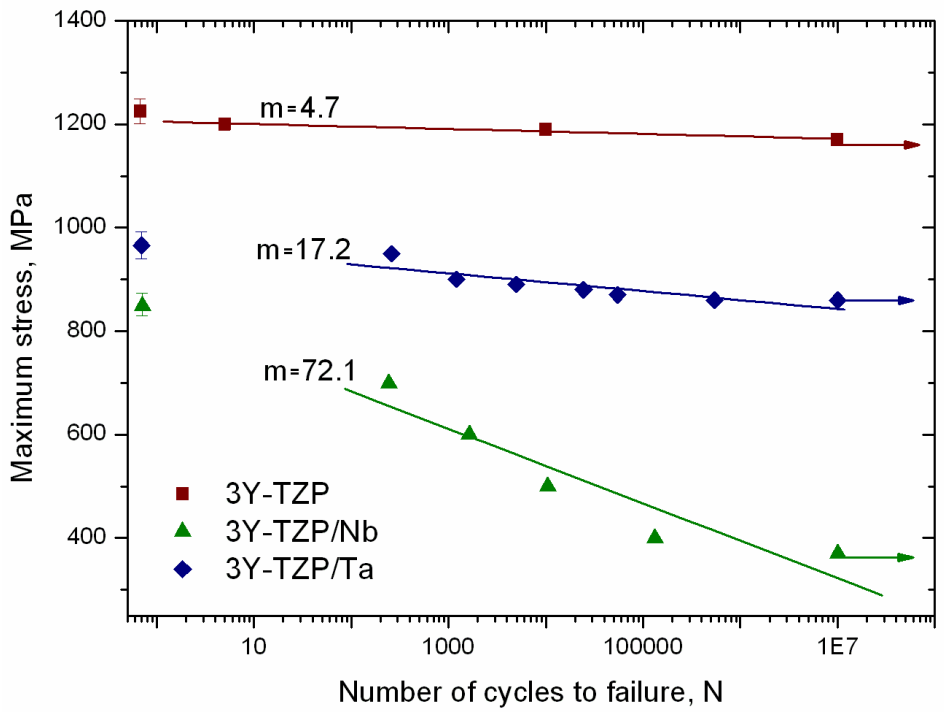

Fig.3.2-14. Fatigue resistance *S–N* curves with values of slopes for un-indented polished specimens

It was preliminary found (Fig.3.2-5) that the fatigue limits for hot pressed (HP) samples of 3Y-TZP, 3Y-TZP/Ta, and 3Y-TZP/Nb [14] were around 930 MPa, 850 MPa, and 400 MPa respectively. For the SPS manufactured samples, the fatigue limits were 1200 MPa, 860 MPa and 370 MPa respectively (Fig.3.2-14). Outstanding higher flexural strength value of SPS produced monolithic zirconia could be explained by the decreased grain size. However, similar to the Hot Pressed 3Y-TZP, almost horizontal S-N curve of SPS 3Y-TZP represents ceramic's fatigue non-sensitivity. It can be concluded that HP and SPS zirconia is too brittle, with no presence of any transformation toughening mechanism. This may be attributed to the nanoscale nature of the zirconia grains, below the critical transformation size. Thus, for all practical purposes, HP and SPS zirconia does not show evidence of cyclic fatigue behavior.

Cyclic fatigue effects in ceramic-metal composites are attributed to cyclic degradation of the bridging zone leading to a reduction of its shielding capacity. A “cyclic cleavage” mechanism has been proposed to explain this degradation in the case of bcc metals [36-39]. The increased strain rate associated with high frequency (20 Hz) cyclic loading promotes rapid fatigue-crack growth in the metal phase by "cyclic cleavage", rather than by ductile mechanisms seen in flexural strength tests (Fig.3.2-11). Therefore, the early fatigue failure of metal particles limits the effectiveness of ductile-phase toughening under cyclic loading [40]. Crack trapping and re-nucleation of the fatigue crack in the ductile phase associated with blunting (via interfacial decohesion for metal particles) [41], and coplanar bridging from multiple and discontinuous crack fronts are expected to provide the main contributions to the fatigue crack growth resistance [29, 42].

Niobium has similar physical and chemical properties to those of the element tantalum but it shows a smaller elastic modulus (105 GPa vs186 GPa) and yield strength (240 MPa vs 380 MPa) than tantalum [43]. Since theoretical simulation points to similar interfaces constituted by both Ta and Nb metals, the most relevant role to explain the differences in the fatigue curves of both composites must come from the relative weight of the elastic and plastic regime of the bulk metals. Therefore niobium metallic particles show higher level of plastic deformation under bending stress than tantalum metallic particles and, consequently, higher fracture surface roughness. Under dynamic loading, tantalum failed by an elastic process which progresses by the nucleation of distributed nanoscale voids, followed by void growth and link-up of clusters of voids with rather sharp cracks between voids with little intervoid deformation, in contrast to the niobium behavior where extensive necking was observed. Fig.3.2-15 represents 3D roughness images with roughness values (*Ra*, μm) corresponding to composites fracture surfaces after biaxial bending and fatigue tests.

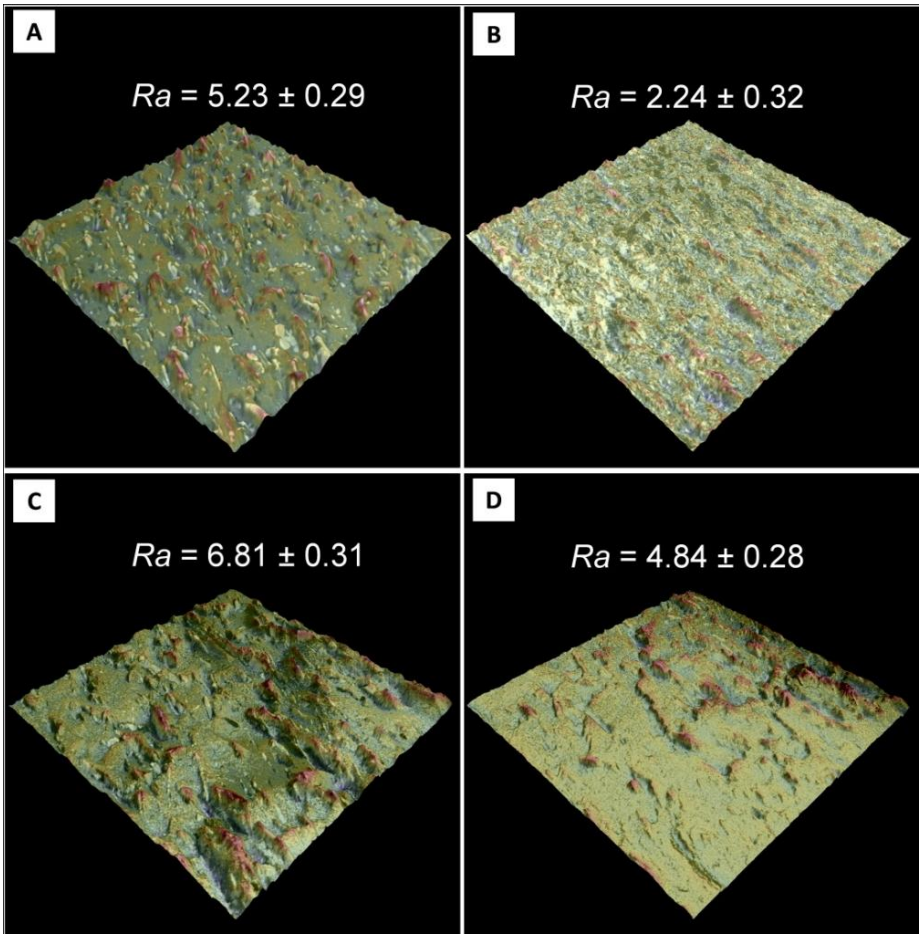

Fig.3.2-15. Composites' fracture surface 3D roughness images after biaxial flexure (A – 3Y-TZP/Ta and C – 3Y-TZP/Nb) and fatigue (B – 3Y-TZP/Ta and D – 3Y-TZP/Nb) tests

The roughness of the fracture surface of the 3Y-TZP/Nb composite reported to be higher than the one corresponding to 3Y-TZP/Ta. On the other hand, both niobium and tantalum metallic particles showed lower level of plastic deformation under fatigue load than under bending stress and hence, lower roughness. Moreover, niobium metallic particles show higher level of plastic deformation under fatigue load than tantalum metallic particles. It is assumed that a steady state is reached resulting from equilibrium between the shielding accumulation due to crack growth and the cyclic-induced degradation. In the 3Y-TZP/Ta composite case, since this energy was not used to plastically deform the metal particles, the crack propagation resistance is attributed to crack-particle interaction mechanisms,

including crack renucleation (in the matrix and/or particle), crack branching, crack blunting, limited interface debonding and discontinuous (out-of-plane) crack bridging.

In order to predict fatigue life of indented material with equivalent initial flaw size, indentation load of 98 N and 294 N was chosen for monolithic ceramic and for ceramic-metal composites, respectively. Initial flaw size was about 335 μm for all studied compositions. The indentation fatigue live for disk specimens are presented in semi logarithmic form as peak stress versus cycles to failure (Fig.3.2-16).

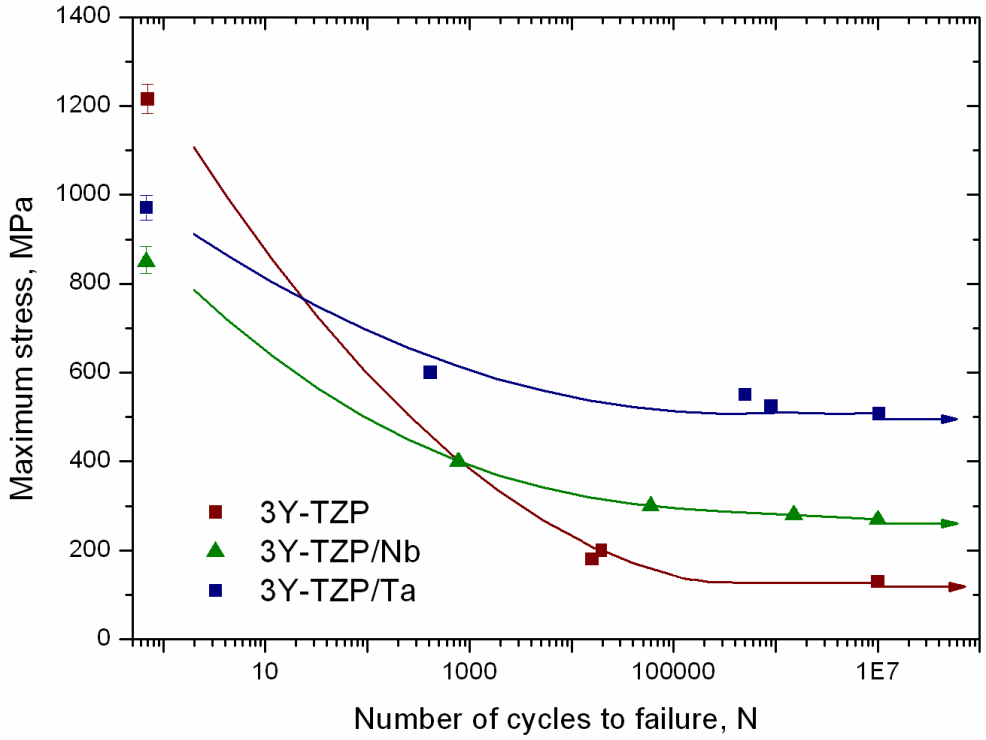

Fig.3.2-16. S–N plot of the cycles to failure (N) of indented 3Y-TZP, 3Y-TZP/Ta and 3Y-TZP/Nb composites. Ultimate flexural strength of un-indented specimens is plotted as well

The indented specimens were tested under the same cyclic conditions as the un-indented ones.

It has been shown that fatigue life of well-polished ceramic-metal composites without any artificial produced flaw is reduced when compared with monolithic zirconia (Fig.3.2-14). However results from Fig.3.3-16 indicate that the situation changes dramatically for the

indentation fatigue. In this particular case, it was found that fatigue limit for 3Y-TZP/Ta, 3Y-TZP/Nb and 3Y-TZP is around 500 MPa, 270 MPa and 130 MPa, respectively.

In Table 3.2-4, the fatigue performance of all materials tested in the study is compared by the fatigue ratio (the ratio of the fatigue limit to the static tensile strength). For the monolithic ceramic, the ratio shows a significant decrease between un-indented and indented specimens. Therefore, the fatigue ratio of zirconia is extremely sensitive to surface condition and the presence of defects, that act as stress concentrations and consequently the chances of failure of monolithic ceramic is higher than in ceramic-metal composites.

Table 3.2-4. Fatigue ratio of all tested materials

Composition	Flexural strength σ_f, [MPa]	Fatigue limit [MPa]	Fatigue ratio
Specimens without artificial flaws			
3Y-TZP	1217	1200	0.98
3Y-TZP/Ta	970	860	0.88
3Y-TZP/Nb	850	370	0.43
Artificially-flawed samples			
3Y-TZP	312	130	0.41
3Y-TZP/Ta	710	500	0.70
3Y-TZP/Nb	642	270	0.42

On the other hand, it has long been known that the ratio of fatigue limit to strength, fatigue ratio, is consistently higher for Ta (0.86) than for Nb (0.77) [44]. The ability to continue well-dispersed dislocation mobility, even after prolonged fatigue cycling, may be the most important characteristic of the Ta for fatigue resistance. A second reason for their superiority is the larger stress needed to move dislocations [34]. Hence, the yield stress of

Ta will always be correspondingly higher which, together with the lower rate of work hardening in these metals, will place the fatigue limit closer to the strength.

The strength and reliability of monolithic zirconia are significantly decreased when compared with composites. Meanwhile less sensitivity of ceramic-metal composites, especially 3Y-TZP/Ta materials, to defects under cyclic loading allows to visualize the growth of defects before reaching critical size and prevent sudden fracture. In order to observe crack propagation test was stopped at various stages of cycling tests. At each stop, for SEM observation, the test specimen was dismounted from the servo-hydraulic machine. After crack length measurements the test was continued until the specimen fractured or reached the final number of cycles. The combination of this information with the test load is showed in graphics of crack lengths depending on the number of cycles (Fig.3.2-17). In this figure vertical black arrows correspond to the number of cycles of stress to cause complete fracture of the specimen. It has been found that zirconia ceramic with artificially produced flaws shows fatigue crack growth when the applied load is only ~ 7% (80 MPa) of the flexural strength value of un-indented specimens. In other words, any flaw in zirconia monolithic material under very low subcritical loading can lead to catastrophic failure. In the case of 3Y-TZP/Nb cermets for load levels of ~ 17% (150 MPa) of flexural strength value of un-indented specimens cracks start to growth.

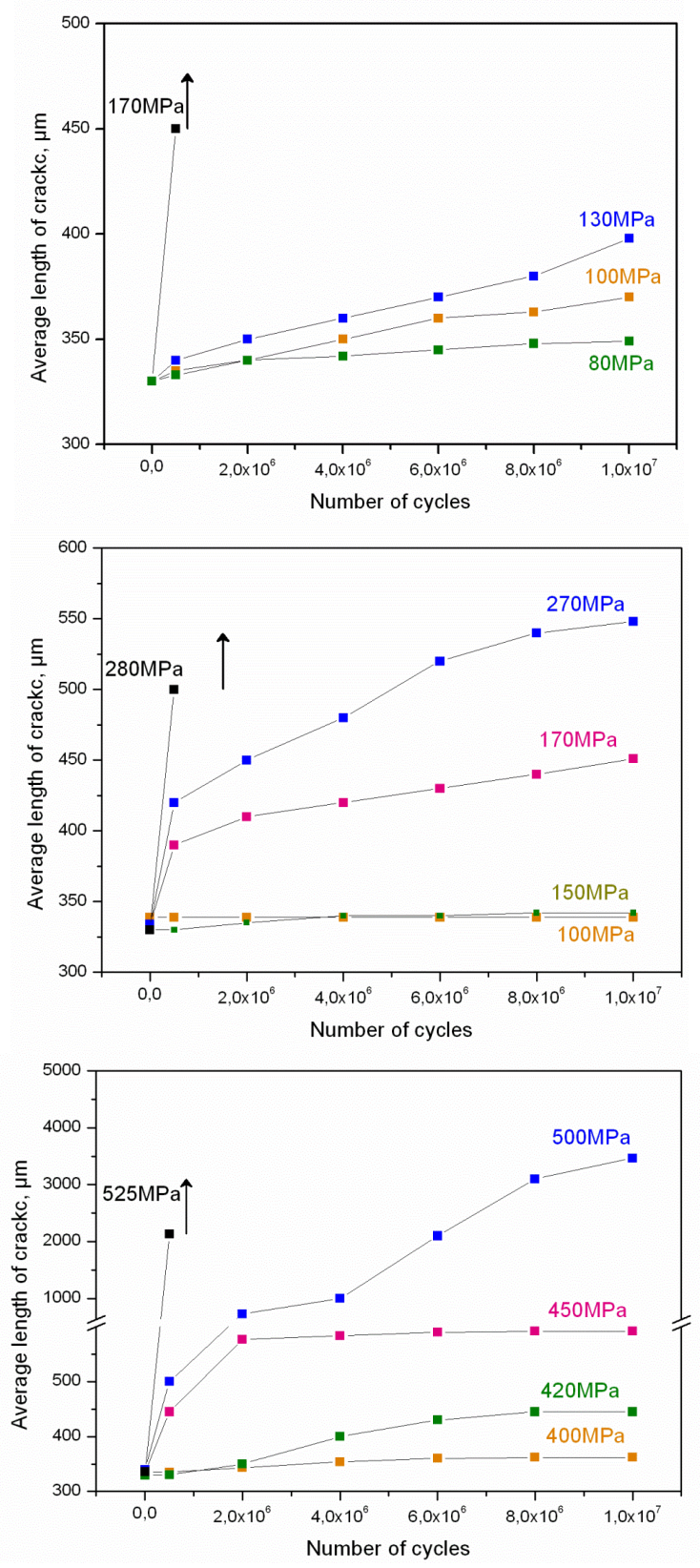

Fig.3.2-17. The number of cycles with crack length depending on the load applied for 3Y-TZP ceramic (top), 3Y-TZP/Nb (middle) and 3Y-TZP/Ta (bottom) cermets

For load levels as high as ~ 41% (400 MPa) of flexural strength value of un-indented specimens, the 3Y-TZP/Ta composites show subcritical crack growth resistance and the cracks do not propagate. Moreover, fatigue crack length propagation for maximum stress under which the specimens never fracture (fatigue limit) is ~ 550 μm and ~ 398 μm for 3Y-TZP/Nb and 3Y-TZP, respectively. However, 3Y-TZP/Ta composites show infinite fatigue life even being in high damaged state (crack length of ~ 3500 μm) and therefore excellent flaw tolerance fatigue behavior.

It was established that in contrast to fracture toughness, fatigue crack growth values do not exhibit a monotonic correlation with microstructural aspects. Zirconia-metal cermets reinforced with more ductile metal (Nb), were found to be more fatigue sensitive in terms of crack growth resistance. Moreover, these materials are more fatigue susceptible with artificial induced flaws (indentation) under cyclic loading. The experimental fact that failure under cyclic loading of zirconia-metal cermets is controlled by subcritical growth of preexisting flaws shows that a damage tolerance analysis for structural design involving these materials is difficult to apply in practice. In the case of ZrO_2-Ta composites, there is a way to avoid the conflicts between mutually exclusive properties of toughness and fatigue resistance through the presence of multiple mechanisms acting on different length scales decreasing locally stresses through limited plastic deformation to provide for intrinsic toughness and further extrinsic mechanisms, such elastic bridging of the tantalum particles. This investigation suggests that ductile phases are associated with multiple and competing mechanisms operating under fatigue loading and being sensitive to elastic properties of the reinforcement. Cracks propagate only when the crack tip energy reaches a threshold that corresponds to the bond failure energy. If the metal particle-matrix bonds are both, strong and weak or the interface cleaves easily, the crack tip surface is multiplied (for instance by

a particle circumference) and propagation stops since the stress intensity falls instantaneously below the above-mentioned threshold. In the case of Ta particle embedded in a zirconia matrix this threshold is much higher than in the case of more plastic Nb particles. In a sense, then, the effects of elastic properties in the cavity growth in isolated ductile particles bridging a brittle matrix crack provide a facet of fatigue theory which is predictive. That is, the effects allow one to predict those classes of ceramic-metal composite materials which are more likely to be fatigue resistance.

3.2.3.2 Wear behaviour

Fig.3.2-18 represents the friction coefficient as a function of the sliding distance registered during the wear test for the UHMWPE under dry and wet conditions, when worn against SPS sintered 3Y-TZP ceramic and 3Y-TZP/Ta ceramic-metal composite. As can be observed, the friction coefficient has different values under dry conditions, but no significant differences were found in the case of the SBF lubricating conditions. The friction coefficient increases rapidly throughout the first meters of sliding and then stabilizes in dry conditions. This behavior can be attributed to a wear process of the UHMWPE during the first 200 m. As the wear proceeds further, the surface of pin becomes smoother and the friction coefficient settles to a steady level.

According to Equation 8.5-17 (Chapter 8), the UHMWPE wear rate (W) against 3Y-TZP/Ta and 3Y-TZP rises from 25 x 10^{-6} to 42 x 10^{-6} mm^3/m under dry conditions, respectively. Reduction of the UHMWPE wear rate as well as the friction coefficient under dry conditions are observed in case of ceramic-metal composite (Table 3.2-4).

This behavior can be attributed to the characteristic of the formed debris film that may act as lubricant. The origin of this film is the metal particles that have been plastically deformed and then smeared on the surface.

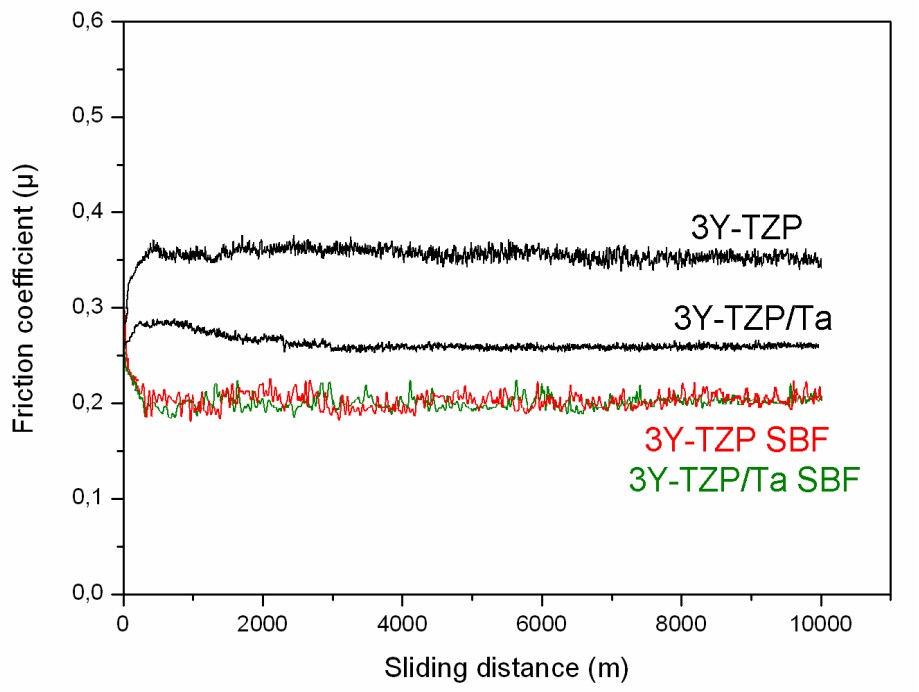

Fig.3.2-18. Friction coefficient as a function of sliding distance corresponding to 3Y-TZP ceramic and 3Y-TZP/Ta ceramic-metal composite plate against UHMWPE pin under dry and wet conditions

It is well known that tantalum is a ductile and soft metal, moreover, when applying a bearing load in the tribological system, the friction between the materials becomes more intensive producing a higher contact temperature, increasing the tantalum plasticity and in

Table 3.2-4. Friction coefficient, volume loss and wear rate of UHWMPE pins after testing against 3Y-TZP ceramic and 3Y-TZP/Ta ceramic-metal composite under dry and wet conditions

	Friction coefficient (μ)	**Volume loss of UHWMPE pin, *V* (mm^3)**	**Wear rate, *W* (mm^3/m)**
3Y-TZP	0.35	4.2	42×10^{-6}
3Y-TZP/Ta	0.26	2.5	25×10^{-6}
3Y-TZP SBF	0.21	1.9	19×10^{-6}
3Y-TZP/Ta SBF	0.21	1.8	18×10^{-6}

consequence promoting the formation of the lubricating layer. Furthermore, due to elongated plate-like morphology of the metal particles, the improved plastic deformation contributes to a more easy formation of the auto-lubricating layer. To study the effect of microstructural changes of the plate surface, SEM observations of the worn surface of a 3Y-TZP/Ta composite after sliding against UHMWPE pin were performed. In Fig.3.2-19 it can be observed that the metal grains on the surface deform plastically and creates an interfacial layer in the contact. A patchy layer is formed during sliding and a selflubrication mechanism is generated [15].

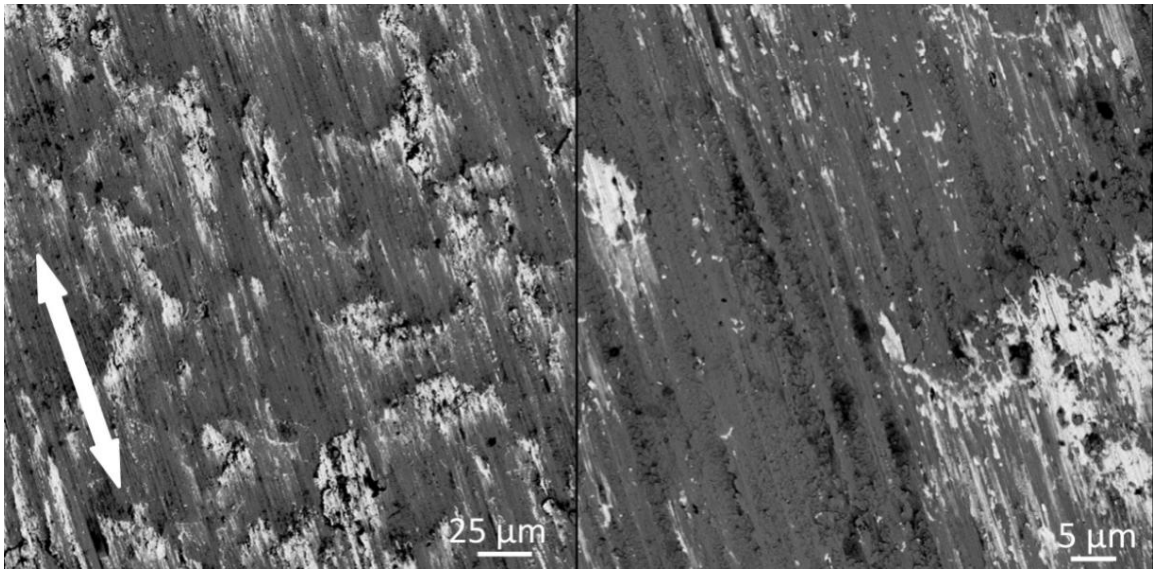

Fig.3.2-19. Scanning electron micrograph of the worn surface of a 3Y-TZP/Ta composite after sliding against UHMWPE pin (double pointed arrow indicates the sliding direction)

In wet condition, the initial friction coefficients are all higher than their stead-state friction coefficients and similar to that in dry sliding of monolithic zirconia, because the state of water absorption of UHMWPE is low at the first meters of sliding. Nevertheless, the friction coefficients decreased with increasing sliding distance, and steady-state friction coefficients are about 0.2 for both compositions. The UHMWPE absorbs water in SBF, thus, the friction coefficient decreases with increasing sliding distance. After sufficient

sliding distance, the water absorption rate of UHMWPE pin surfaces reaches steady state and thus the friction coefficients enter steady state as well. Under wet conditions, the wear rate was 18 x 10^{-6} to 19 x 10^{-6} mm^3/m for 3Y-TZP/Ta and 3Y-TZP, respectively.

3.2.3.3 Low temperature degradation (LTD)

Fig. 3.2-20 shows the results of the aging experiments. At the beginning of the aging the polished surfaces of the 3Y-TZP and 3Y-TZP/Ta SPS sintered ceramics contained 1 and 2.1%, monoclinic zirconia, respectively. After 15 h of aging at 134°C, the difference between these materials becomes more significant. At this point, the amount of transformed zirconia is almost 8 times higher for the monolithic material (7.4%), while in the tantalum-reinforced material only 2 times (4.3%). At the end of the experiment the content of the monoclinic phase in the 3Y-TZP ceramic increased to 27% but only to 11.1% in the 3Y-TZP/Ta ceramic-metal composite.

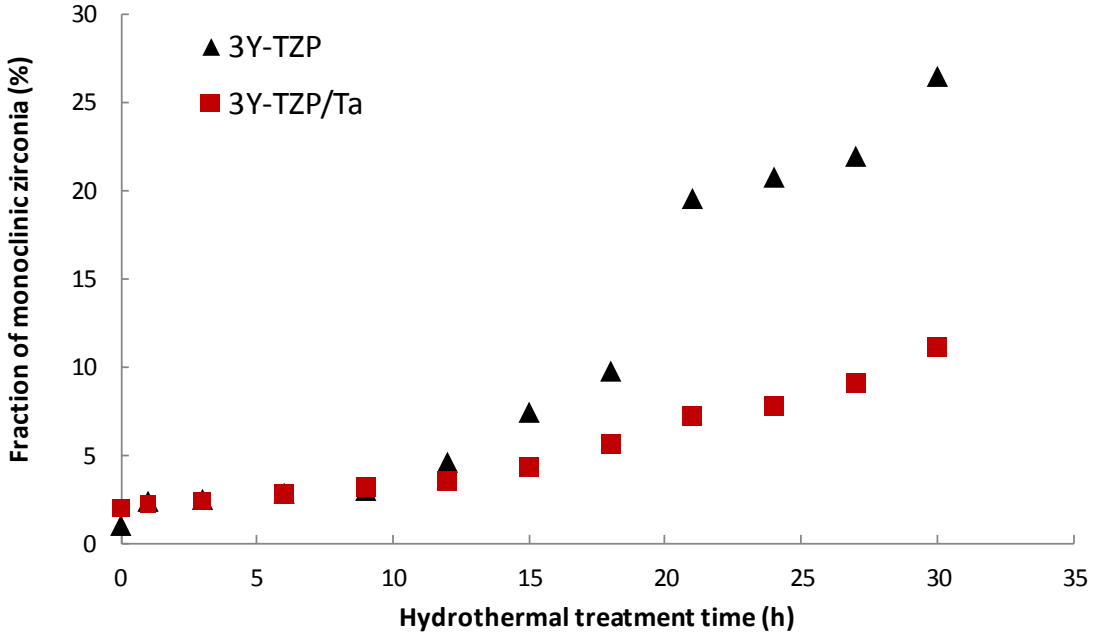

Fig.3.2-20. LTD – evolution of the volume fraction of monoclinic transformed zirconia in dependence of the aging treatment time

It has been proved that tantala (Ta_2O_5) plays a very important role in the aging process of yttria-doped zirconia. In yttria-stabilized TZPs (Y-TZPs), the substitution of Y^{3+} (ionic radius of 0.97 Å) for Zr^{4+} (ionic radius of 0.79 Å) causes the distorted fluorite structure and charge imbalance due to the larger ionic size of $Y^{3+}$and the charge deficiency, resulting in the formation of internal strain and oxygen vacancy, as depicted by the following equation represented using the Kröger–Vink notation [45]:

$$yY_2O_3 \xrightarrow{ZrO_2} 2yY'_{Zr} + V_O^{\bullet\bullet} + 3yO_O$$

where Y'_{Zr} represents a Y^{3+} ion occupying a Zr^{4+} lattice site in a perfect ZrO_2 crystal and $V^{\bullet\bullet}_O$ stands for an oxygen vacancy. However, when Y_2O_3 and Ta_2O_5 are simultaneously incorporated into ZrO_2, the following reaction occurs:

$$yY_2O_3 + xTa_2O_5 \xrightarrow{ZrO_2} 2yY'_{Zr} + 2xTa^{\bullet}_{Zr} + (5x+3y)O_O + (y-x)V_O^{\bullet\bullet}$$

Hence, the incorporation of Ta_2O_5 (cationic radii in the +5 oxidation state of ~ 0.68Å) partially eliminates oxygen vacancies originally existing in the Y_2O_3 stabilized t-ZrO_2, because charge compensation between $Y^{3+}$and Ta^{5+}. As oxygen vacancy diffusion rate is proposed as the mechanism that governs the tetragonal to monoclinic transformation during aging at low temperatures, because water molecules can be incorporated into the ZrO_2 lattice by filling oxygen vacancies, generating nucleation and growth of the transformation [46], it appears that the reduction of these vacancies, are responsible for the reduction of the LTD rate in the 3Y-TZP/Ta composite material.

3.2.3.4 Magnetic resonance imaging (MRI)

Depending on MRI sequence protocols the biocermet showed a range of distortion degrees. Distortions are related to non-uniformity and noise of signal, repetition time (TR) and the echo time (TE) of MRI protocol. Compared to the other techniques, gradient echo

sequences (GRE) methods are more versatile and allow one to variate flip or tip angle of the spins in addition to the usual TR and TE parameters and, consequently, lead to clear image. Echo planar (EPI) is the fastest acquisition method in MRI, but with the limited spatial resolution and therefore with higher distortion. The spin echo pulse sequence (SE) is the most commonly used pulse sequence. The pulse sequence timing can be adjusted to give T1-weighted and T2-weighted images. A short TR and short TE will give a T1-weighted image and a long TR and long TE will give a T2-weighted image. None of the (GRE) in ceramic-metal composites studied caused any detectable distortions (Fig. 3.2-21A).

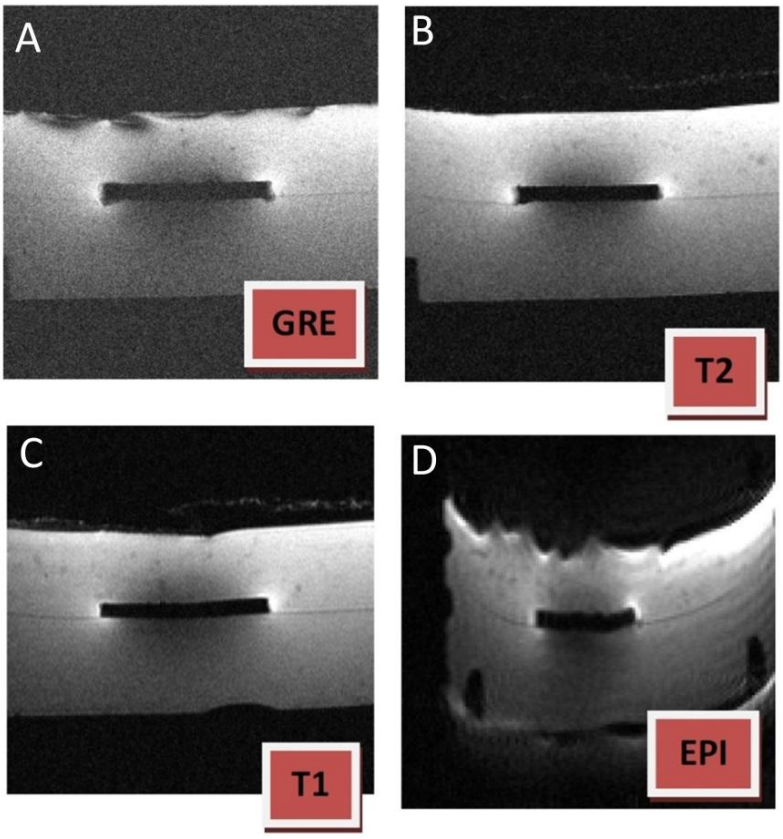

Fig.3.2-21. Gradient echo (A), spin echo (B, C) and echo planar (D) images of biocermet

Spin echo pulse sequences (SE) showed negligible distortions, especially in T2-weighted images (Fig. 3.2-21B), while in T1-weighted images distortion is little bit higher. In echo planar (EPI) the highest image distortion was observed (Fig. 3.2-21D).

Thereby, MRI testing results showed no image artifacts and consequently confirm compatibility of newly developed cermets with MRI examination technique. This diagnostic procedure provides the necessary information about potential treatment options that could allows to avoid surgical revision or replacement of the implants.

3.3 SUMMARY

The new 3Y-TZP/Ta ceramic/metal systems with enhanced mechanical properties have been first developed and fabricated by three technological routes: pressureless sintering, hot press, and spark plasma sintering. The use of pressure-assisted techniques, especially spark plasma sintering, were adequate to perform 3Y-TZP/20 vol.% Ta composites of high density, which had not been achieved by pressureless sintering.

The 3Y-TZP/20 vol.% Ta composites produced by HP and SPS, exhibit a higher toughness value (16 MPa·$m^{1/2}$) than the ZrO_2 (6 MPa·$m^{1/2}$). The increase of toughness is explained mainly by crack bridging of the elastic–plastic deformations of ductile metal particles associated with the transformation toughening mechanism in zirconia matrix. This toughening mechanism agrees with the theoretical simulation which indicates the presence of both strong and weak interfaces depending on the ZrO_2 orientation rather than on the metal. The fatigue crack growth influences the bridging actions, and causes significant changes in the mechanical properties of the composite materials. The fatigue crack growth resistance of 3Y-TZP/Ta composite is superior to the one corresponding to the Nb reinforced composite. The fatigue limit was 860 MPa at 10^7 cycles, with a rather flat *S*–*N* curve. This value is more than twice that obtained for the 3Y-TZP/Nb composite (370 MPa). Such enhanced fatigue performance is related to the lower plastic deformation under cyclic load of tantalum than niobium particles. The crack can be arrested at the Ta particle such that it must renucleate on the other side. This toughening mechanism will not necessarily degrade under cyclic loads. However, if the ductility of the trapping phase is sufficiently high to remain intact in the wake of the crack tip, as in the case of the Nb particles, it can additionally act as a crack bridge. These plastic bridges can be considered to be susceptible to premature failure by fatigue. Moreover, the fatigue crack flaw tolerance

of 3Y-TZP/Ta composite is much higher than for 3Y-TZP/Nb composite. The present study has demonstrated the unique and unpredicted, simultaneous enhancement in toughness and strength with very high flaw tolerance of zirconia–Ta composites. In addition to their excellent static strength properties, these composites also have exceptional resistance to fatigue loading. To our knowledge, the ability of tantalum metal to dramatically improve the fatigue resistance and flaw tolerance of a ceramic material has not been previously reported in the literature, and was discovered here only because the particular microstructural feature of this ceramic-metal composite.

Moreover, according to the results of pin-on-flat wear test using UHMWPE pins under dry condition, ceramic–metal composite exhibited a higher wear resistance and lower friction coefficient, related both to the high toughness and the presence of an autolubricating phase. Besides exceptional mechanical and tribological properties, 3Y-TZP/Ta composites also showed high resistance to low temperature degradation.

Preliminary MRI results revealed that the abiding by the MRI protocol parameters avoids the image artifacts and consequently ensured compatibility of this noninvasive technique for medical revision of newly developed biocermet.

3.4 REFERENCES

[1] Bartolomé JF, Gutiérrez-González CF, Pecharromán C, Moya JS. Synergistic toughening mechanism in 3Y–TZP/Nb composites. *Acta Materialia*, 2007; 55:5924-5933.

[2] Bartolomé JF, Beltrán JI, Gutiérrez-González CF, Pecharromán, Muñoz MC, C, Moya JS. Influence of ceramic–metal interface adhesion on crack growth resistance of ZrO_2–Nb ceramic matrix composites. *Acta Materialia*, 2008; 56:3358-3366.

[3] Park YB, Lee DN, Gottstein G. The evolution of recrystallization textures in body centered cubic metals. *Acta* Materialia, 1998; 46:3371-3379.

[4] Díaz M, Bartolomé JF, Requena J, Moya JS. Wet processing of mullite/molybdenum composites. *J. Eur. Ceram. Soc*., 2000; 20:1907-1914.

[5] Koch W, Holthausen MC. Chemist's guide to density functional theory. Wiley-VCH; (2001)

[6] J. M. Soler JM, E. Artacho E, J.D. Gale JD, A. Garcia A, J. Junquera J, P. Ordejon P, Sanchez. The SIESTA method for ab initio order-N materials simulation. *J Phys Condens Matter,* 2002*;* 14: 2745-2779.

[7] Perdew JP, Burke K, Ernzerhof M. Generalized Gradient Approximation Made Simple. *Phys Rev Lett*., 1996;77:3865.

[8] Beltrán JI Muñoz MC. Ab-initio study of the decohesion properties in oxide/metal. *Phys. Rev. B,*2008; 78: 245417.

[9] ASTM C1161-02c(2008)e1, Standard Test Method for Flexural Strength of Advanced Ceramics at Ambient Temperature.

[10] ASTM C1421-01b, Standart test methods for determination of fracture toughness of advanced ceramics at ambient temperature.

[11] ISO 6872-2015 Dentistry – Ceramic materials.

[12] ASTM F732-00 (2011), Standard Test Method for Wear Testing of Polymeric Materials Used in Total Joint Prostheses.

[13] Daniel M, Herman S, Dolinar D, Iglic A, Sochor M, Kralj-Iglic V. Contact stress in hips with osteonecrosis of the femoral head. *Clinical Orthopaedics and Related Research, 2006;* 447:92–99.

[14] Smirnov A, Gutiérrez-González CF, Bartolomé JF. Cyclic fatigue life- and crack-growth behavior of zirconia-niobium composites. *J. Am. Ceram. Soc.*, 2013; 96:1709-1712.

[15] Bartolomé JF, Moya JS, Couceiro R, Gutiérrez-González CF, Guitián F, Martinez-Insua A. In-vitro and in-vivo evaluation of a new zirconia/niobium biocermet for hard tissue replacement. *Biomat,*. 2016; 76:313-20.

[16] Gutiérrez-González CF, Bartolomé JF. Tribological behavior of a novel alumina/nano-zirconia/niobium biocomposite against ultra high molecular weight polyethylene. *Wear*, 2013; 303:211-215.

[17] Gutiérrez-González CF, Smirnov A, Bartolomé JF. Aging effect on the tribological behavior of a novel 3Y-TZP/Nb biocomposite against ultra high molecular weight polyethylene. *J. Am. Ceram. Soc.*, 2012; 95:851-854.

[18] PH100, ACerS-NIST Phase Equilibria Diagrams CD-ROM Database Version 3.1, 2005.

[19] Bhattacharya AK, Shklover V, Steurer W, Witz G, Bossmann H-P, Fabrichnaya O. Ta_2O_5–Y_2O_3–ZrO_2 system: experimental study and preliminary thermodynamic description. *J. Eur. Ceram. Soc*., 2011; 31:249-257.

[20] Kim DJ. Effect of Ta_2O_5, Nb_2O_5, and HfO_2 Alloying on the Transformability of Y_2O_3-Stabilized Tetragonal ZrO_2. *J. Am. Ceram. Soc.*,1990; 73:115–120.

[21] Kim DJ, Tien TY. Phase stability and physical properties of cubic and tetragonal ZrO_2 in the system ZrO_2-Y_2O_3-Ta_2O_5. *J. Am. Ceram. Soc.*, 1991; 74:3061-3065.

[22] Smirnov A, Bartolomé JF. Mechanical properties and fatigue life of ZrO_2–Ta composites prepared by hot pressing. *J. Eur. Ceram. Soc*., 2012;32:3899–3904.

[23] Déve HE, Evans AG, Odette GR, Mehrabian R, Emiliani ML, Hecht RJ. Ductile reinforcement toughening of γ-TiAl: effects of debonding and ductility. *Acta metall. mater*., 1990; 38:1491-1502.

[24] Zimmermann A, Hoffman M, Emmel T, Gross D, Rödel J. Failure of metal-ceramic composites with spherical inclusions. *Acta Mater*., 2001; 49:3177-3187.

[25] Raddatz O, Schneider GA, Claussen N. Modelling of R-Curve Behaviour in Ceramic/Metal Composites. *Acta mater*., 1998; 46:6381-6395.

[26] Sbaizero O, Pezzotti G, Nishida T. Fracture energy and R-curve behavior of Al_2O_3/Mo composites. *Acta mater*., 1998; 46:681-687.

[27] Lu TC, Evans AG, Hecht RJ, Mehrabian R. Toughening of $MoSi_2$ with a ductile (niobium) reinforcement. *Acta Metall Mater*., 1991; 39:1853-1862.

[28] Torres Y, Anglada M, Llanes L, Bartolomé JF, Díaz M, Moya JS. Fracture and fatigue behaviour of mullite/molybdenum composites. *Key Engineering Mat*., 2005; 290:110-120.

[29] Venkateswara Rao KT, Odette GR, Ritchie RO. On the contrasting role of ductile-phase reinforcements in the fracture toughness and fatigue-crack propagation resistance of TiNb/γ-TiAl intermetallic-matrix composites. *Acta Metall et Mater*., 1192; 40:353–361.

[30] Murugesh L, Venkateswara Rao KT, Ritchie RO. Crack growth in a ductile-phase-toughened Nb/Nb3Al in situ intermetallic composite under monotonic and cyclic loading. *Scripta Metall. Mater*., 1993; 29:1107–1112.

[31] Badrinarayanan K, McKelvey AL, Venkateswara Rao KT, Ritchie RO. Fracture and fatigue crack growth in ductile-phase toughened molybdenum disilicide: effects of niobium wire vs particulate reinforcements. *Metall Mater Trans.*, 1996:27:3781–3792.

[32] Shen Y, Clarke DR. Resistance to Low-Temperature Degradation of Equimolar $YO_{1.5}$–$TaO_{2.5}$ Stabilized Tetragonal ZrO_2 Ceramics in Air. *J. Am. Ceram. Soc*., 2010; 93:2024–2027.

[33] Raghavan S, Wang H, Porter WD, Dinwiddie RB, Mayo MJ. Thermal Properties Of Zirconia Co-Doped With Trivalent And Pentavalent Oxides. *Acta mater*., 2001; 49:169–179.

[34] Bieler TR, Sutton SC, Dunlap BE, Keith ZA, Eisenlohr P, Crimp PA, Boyce BL. Grain Boundary Responses to Heterogeneous Deformation in Tantalum Polycrystals *JOM*, 2014; 66:121-128.

[35] Boyce BL, Clark BG, Lu P, Carroll JD, Weinberger CR. The Morphology of Tensile Failure in Tantalum. *Metall Mater Trans.,* 2013; 44:4567-4580.

[36] Gerberich WW, Moody NR, Jatavallabhula K. A proposed cyclic cleavage crack growth model for fatigue of BCC iron and its alloys. *Scripta Metall.,* 1980; 14:113-118.

[37] Gerberich WW, Jatavallabhula K Quantitative fractography and dislocation interpretations of the cyclic cleavage crack growth process. *Acta Metall*, 1983; 31:241-255.

[38] Fariabi S, A. L. W. Collins ALW, Salama K. Effects Of Hydrogen On Near-Threshold Crack Propagation In Niobium. *Metall. Trans,*.1983;14:701-707.

[39] Dickson I, Uribe-Perez I, Geckinli E. Fractographic aspects of cyclic cleavage. *Mater. Sci. Eng.*,1983; 60:231-240.

[40] Murugesh L, Venkateswara Rao KT, Ritchie RO. Crack Growth in a ductile-phase-toughened Nb/Nb_3Al in situ intermetallic composite under monotonic and cyclic loading, *Scripta Metall Mater.*, 1993; 29:1107-1112.

[41] Chan KS. Influence of microstructure on intrinsic and extrinsic toughening in an alpha-two titanium aluminide alloy. *Metall Trans A*, 1992; 23:183-199.

[42] Ritchie RO, Gilbert CJ, McNaney JM. Mechanics and mechanisms of fatigue damage and crack growth in advanced materials. *Inter J Solids and Structures*, 2000; 37:311-329.

[43] Emsley J. "The Elements", Oxford University Press, Oxford, UK, 3rd edition, 1997.

[44] Buck A. Fatigue properties of pure metals. *Inter J Fract Mec*., 1967; 3:145-152

[45] Kröger FA. The Chemistry of Imperfect Crystals. North Holland Publishing Co, Amsterdam, 1964.

[46] Gutiérrez-González CF, Moya JS, Palomares FJ, Bartolomé JF. Low-temperature aging degradation-free 3Y-TZP/Nb composites. *J. Am. Ceram. Soc.*, 2010; 93:1842-1844.

4

2Y-TZP/Ta System: Ceramic matrix optimization by Laser vaporization (LAVA)

4.1 INTRODUCTION

It is known that the monolithic zirconia fracture toughness has its highest values at the yttria molar percent concentration equal to two, or 2Y/TZP zirconia [1, 2]. Co-precipitation and gas phase reaction–plasma coating methods are generally utilized in the large-scale production of doped zirconia powders for the fabrication of TZP ceramics. However, these routes do not allow obtaining a homogeneous yttria distribution in 2Y/TZP powders and consequently provoke the degradation of mechanical properties during low temperature aging because of spontaneous tetragonal to monoclinic phase transformation [3-7]. In order to prevent this spontaneous transformation the manufacturers of TZP powders only introduce partially-stabilized zirconia powder with 3 mol% yttria onto the market. However, even zirconia ceramics with 3 mol% yttria suffer from LTD [8-10].

In order to achieve simultaneously the lessened degree of low temperature degradation and enhanced mechanical reliability of the monolithic zirconia, specific studies should be completed on the different factors influencing its microstructure, properties and performance. These are, for example, the preparation method of the starting powder, its impurity content, the presence of dopants, yttria content and distribution, and sintering temperature [11-19].

In this context, a new reliable powder processing route (LAVA) to avoid inhomogeneity in the yttria distribution and to engineer the microstructure and mechanical properties of Y-TZP ceramics was chosen. The principle of LAVA function is described in Chapter 8 section 8.2.2.3. Fig.4.1-1 shows Strategy II on zirconia powder homogenization and manufacturing route of zirconia-tantalum composites.

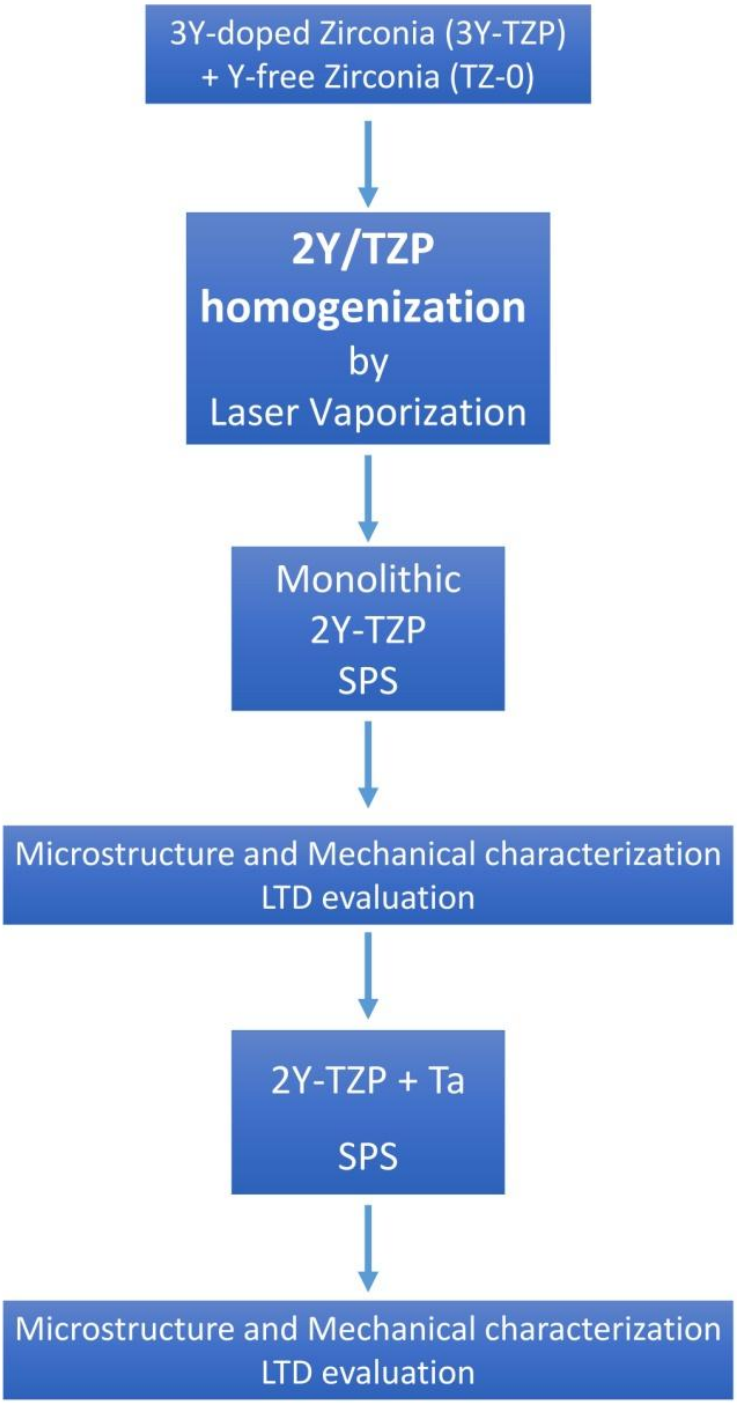

Fig.4.1-1. Strategy II on fabrication of 2Y-TZP ceramic and 2Y-TZP/Ta composite

4.2 2Y-TZP SYSTEM

4.2.1 Raw Materials

The following commercial available powders were used for CO_2 laser vaporization homogenization:

- Tetragonal zirconia polycrystals (3Y-TZP, 3 mol.% Y_2O_3; TZ-3YS-E, Tosoh Corp.), with an average particle size of d_{50} = 0.26 ± 0.05 µm, with specific surface area of 16 ± 3 m^2/g.
- Y_2O_3-free monoclinic zirconia powder (TZ-0 Tosoh Corp., Tokyo, Japan) with an average particle size of d_{50} = 0.3 µm.

4.2.2 Fabrication and processing of powders

Zirconia raw powders with an overall Y_2O_3 content of 2 mol% (2Y/TZP) were prepared by dry mixing of corresponding portions of 3Y/TZP and TZ-0 grades in a polyethylene bottle with zirconia balls in a multidirectional mixer for 24 hours. The obtained 2Y/TZP raw powder mixture was used as starting material for the preparation of nanoparticles with LAVA. The mixture was vaporized using pulsed CO_2 laser radiation (wavelength 10.59 µm, pulse length 1 ms, pulse frequency 200 Hz, average radiation power 730W, pulse peak power 3.5 kW, focus diameter 1 mm) and air as the process gas (flow rate in the zone of vaporization 2 m^3/h, total flow rate 14.5 m^3/h). Pulsed laser radiation was applied in order to reduce the width of the particle size distribution and to minimize the fraction of primary particles firmly bonded by solid-state bridges. At these conditions the production rate of the nanopowder was 10 grams per hour in a continuously running process [20]. For comparison reasons 2Y-TZP mixture were performed at wet conditions of corresponding portions of

3Y/TZP and TZ-0 grades in a polyethylene bottle with zirconia balls in a multidirectional mixer for 24 h as described in Chapter 8, section 8.8.2.1. Commercially available 3Y-TZP powder was used as reference material as well. Powders prepared by wet mixing, LAVA, and the commercially available zirconia powder are designated as WP, LAVA, and 3Y-TZP, respectively.

4.2.3 X-Ray diffraction (XRD) of powder mixtures

X-ray diffraction were conducted in a step scanning mode at diffraction angles 2θ ranging from 10° to 70°, as explained in Chapter 8, Section 8.5.1, for the 2Y/TZP starting powder mixture and for the 2Y/TZP nanopowder prepared from this mixture by LAVA. According with the information provided by the International Center of Diffraction Data (ICDD), the position and intensity of the peaks found in the tested materials corresponded with the characteristic peaks of zirconia (monoclinic, 24-1165 and tetragonal, 83-0113).

4.2.4 TEM investigation of the LAVA nanopowder

Morphologic properties of the LAVA nanoparticles were evaluated by transmission electron microscopy at accelerating voltage 300 kV. For this purpose nanoparticles were deposited on a TEM grid (perforated carbon film on copper mesh, Plano GmbH, Wetzlar, Germany) which was placed momentarily into the flowing particle aerosol in the LAVA laboratory setup. The particle diameter distribution of the LAVA nanopowder was determined from TEM micrographs by measuring the diameters of about 1200 nanoparticles [21].

4.2.5 Spark plasma sintering

The sintering experiments were carried out at a temperature of 1150°C and 1300°C in vacuum. Specimens were maintained at the maximum sintering temperature 3 minutes with

pressure 80 MPa. As a result discs of 20 and 50 mm diameter and thickness about 2-4 mm were obtained.

4.2.6 Characterization of dense material

The choice of the methods applied for the materials microstructural and mechanical characterization was in correspondence to the Chapter 3. This characterization includes X-ray diffraction (XRD), scanning electron microscopy (SEM) as well as tests for assessing the mechanical properties such as biaxial flexural strength and hardness. However, beside them, the below described techniques were additionally used.

In order to quantify the matrix average grain size, the sintered samples were thermally etched for 30 minutes at a temperature of 1250°C in air, and the linear intercept method (LIM) was used [22].

The microstructure of the sintered specimens was studied by FIB-SEM microscope with energy dispersive X-ray spectrometry (Chapter 8, Section 8.5.5.1). EDS spectra were conducted in specific regions at 20 kV voltage and 12μA beam current for 5 min to obtain well-resolved Y-Kα and Zr-Kα peaks. EDS measurements were performed to quantitatively examine the chemical composition of localized portions. Analyses of 100 random points were conducted to obtain a semi-quantitative basis for the yttria distribution in the sintered microstructures.

The toughness was measured by indentation. The applied load was 294 N with an indentation time of 10 s. The sizes of the corresponding indentation prints and cracks were evaluated by tabletop SEM. The results were averaged over 10 indentations per specimen. The fracture toughness was calculated using the formulations given by Miranzo and Moya (Chapter 8, Section 8.5.7.4.1) [23].

4.2.7 Results and discussion

4.2.7.1 TEM investigation of LAVA powder

The LAVA nanoparticles are predominantly spherically shaped with partially facetted surfaces (Fig.4.2-1, left and middle).The primary particles form soft agglomerates due to weak Vander Waals forces. Only a marginal fraction is bound to vicinal particles by sinter necks. The geometric mean diameter μ_g (q_0) of the particle size distribution (Fig.4.2-1, right) is 15.4 nm ± 0.8 nm, and the d_{10}, d_{50}, and d_{90} diameters are 4.6 nm, 13.1 nm, and 26.4 nm, respectively, with an uncertainty of ± 0.5 nm. From the geometric mean diameter $\mu_g(q_2)$ the specific surface area S_{TEM} of the nanopowder was calculated to be 39.6 m^2/g.

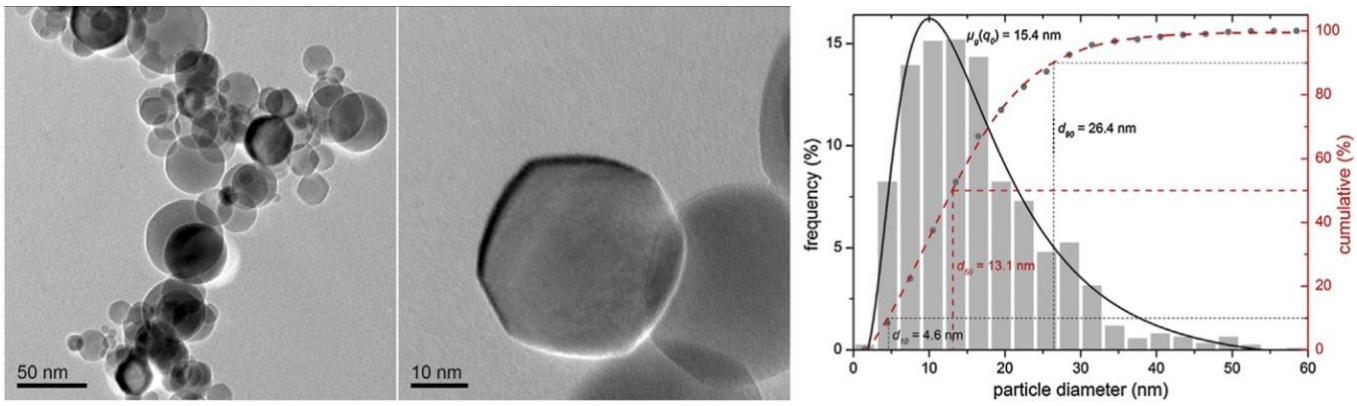

Fig.4.2-1. TEM micrographs (left and middle) and diameter distribution (right) of the LAVA prepared zirconia nanoparticles

4.2.7.2 XRD investigation of powder mixture

X-ray diffraction was carried out for the 2Y/TZP starting powder mixture and for the nanopowder prepared from this mixture by LAVA. XRD analysis revealed the complete conversion of the monoclinic ZrO_2 into tetragonal ZrO_2 (2θ between 10° and 70°) after the LAVA process, as shown in Fig. 4.2-2. Thus, the LAVA technique proved to be suitable to prepare 2Y/TZP nanopowders from a mixture of monoclinic zirconia and 3Y/TZP raw

powders. However, it is worth mentioning that the average size of the LAVA nanoparticles (d_{50}= 13.1 nm ± 0.5 nm) is below the threshold down to which m-ZrO_2 can exist whereas the average particle size of the mixed powders is significantly higher (d_{50}= 300 nm).

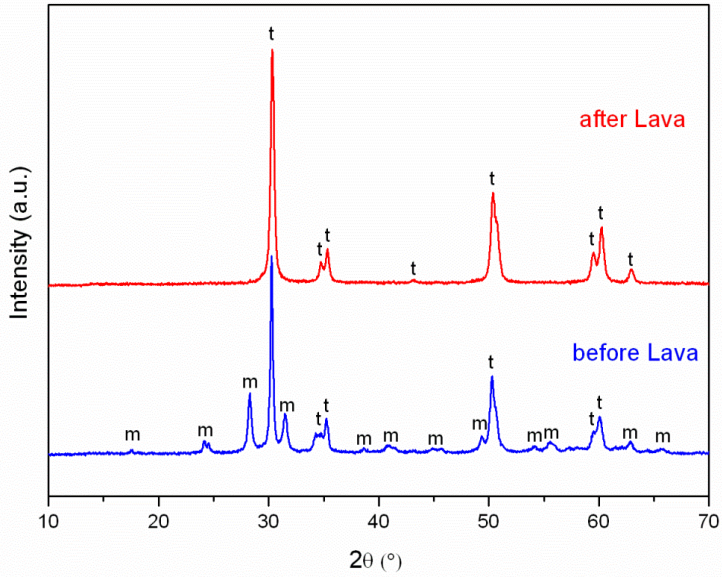

Fig.4.2-2. XRD patterns of the 3Y/TZP-TZ-0 (monoclinic) zirconia powder mixture before and after the LAVA process. Labelling "t" and "m" denote tetragonal and monoclinic zirconia, respectively

4.2.7.3 Characterization of sintered composites

First of all it should be noted that 2Y-TZP powders obtained by LAVA were SPS sintered at 1150 °C. However, at this temperature only the density of 85% of theoretical was reached (Table 4.2-1).

Table 4.2-1. Archimedes densities of sintered ceramics

Composition	Density
2Y-TZP LAVA 1150 °C	85% th.
2Y-TZP LAVA 1300 °C	99% th.
2Y-TZP wet mixing 1300 °C	98% th.
3Y-TZP 1300 °C	99% th.

This was also confirmed by the presence of black-coloured spots (pores) in the SEM images (Fig. 4.2-3). Meanwhile, materials sintered at 1300°C show the density close to the theoretical (Table 4.2-1). Thus, the 1300 °C was chosen as the temperature providing full densification of compacts.

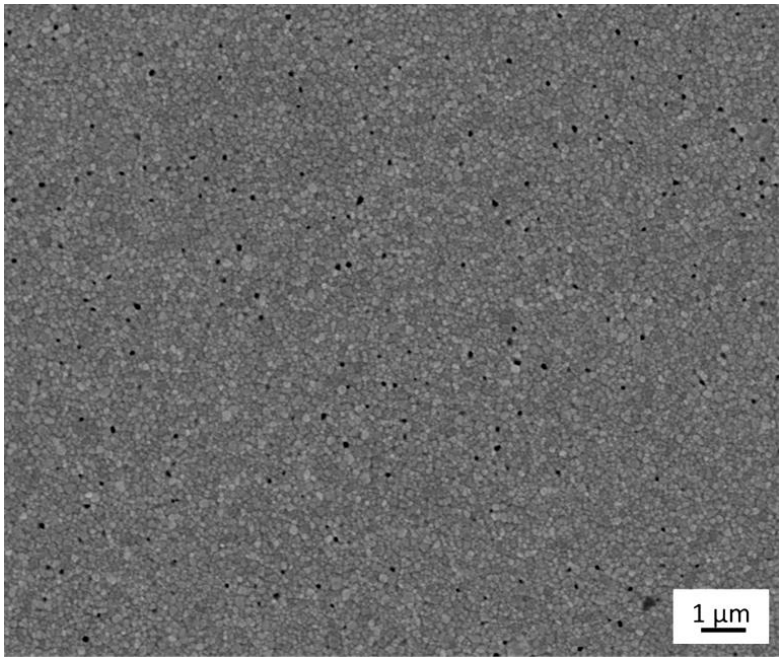

Fig.4.2-3. SEM images of sintered, polished and thermally etched LAVA ceramic sintered at 1150°C

4.2.7.3.1 Microstructures

Typical thermally etched microstructures of the SPSed ceramics are shown in Fig.4.2-4, left column. The grains in all the investigated materials have fairly equiaxed shapes, although in the WP and 3Y-TZP ceramics few coarse grains can be observed (Fig.4.2-4, left column, top and middle, respectively). The average grain size was determined using the linear intercept method and was found to be 305 ± 0.5 nm, 285 ± 0.2 nm and 310 ± 0.3 nm for 2Y-TZP wet mixing, 2Y-TZP LAVA and 3Y-TZP ceramics, respectively. The average grain size of the LAVA ceramic is smaller and exhibits a narrower grain size distribution as well (Fig.4.2-4, middle column). The semi-quantitative microanalyses were performed on

polished and thermally etched surfaces at three different points of each sample. The results were analyzed in terms of mol% of yttria for comparison with the 3Y-TZP raw powder. The yttria distribution in the ceramic samples is presented in Fig.4.2-4, right column. Due to the different processing of the starting powders the yttria distribution in the 3Y-TZP and WP ceramics is not as narrow as in the LAVA ceramic. The LAVA process allows to prepare 2Y/TZP nanopowders with the most homogeneous yttria distribution and therefore with the most homogeneous Y^{3+}distribution in the corresponding ceramic.

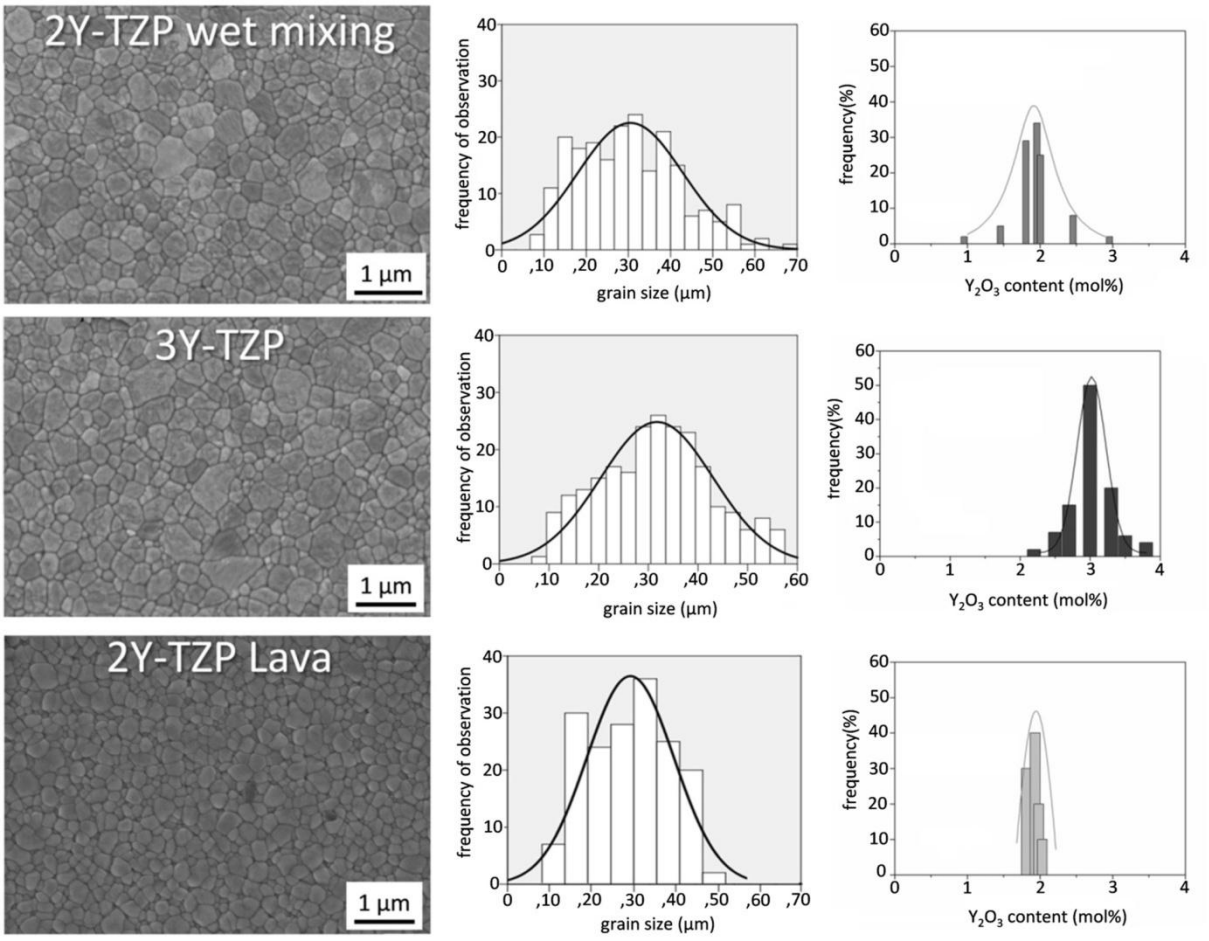

Fig.4.2-4. SEM images of polished and thermally etched sections of 2Y-TZP wet mixing, 3Y-TZP, and 2Y-TZP LAVA ceramics (left column) together with the corresponding grain size distributions (middle column) and the semi-quantitative Y_2O_3 distributions (right column) obtained from EDS measurements

4.2.7.3.2 Mechanical properties

The evaluation of mechanical properties is summarized in Table 4.2-2. All sintered ceramics show comparable hardness and elastic moduli. A maximum strength of 1380 MPa and a maximum fracture toughness of 13 MPa $m^{1/2}$ was obtained for the LAVA ceramics.

Table 4.2-2. Densities and mechanical properties of the ceramic specimens sintered by SPS from the ceramic nanopowders as well as volume fractions of tetragonal (t) and monoclinic (m) zirconia in polished and fractured surfaces of the ceramic specimens and the resulting transformabilities of tetragonal zirconia

Specimen	Elastic modulus E [GPa]	Flexural strength σ_f [MPa]	Hardness HV [GPa]	Fracture toughness K_{Ic} [MPa·$m^{1/2}$]	Volume fractions of t- and m-ZrO_2 [vol%]				Transformability of t-ZrO_2 V_{trans}
					Polished		Fractured		
					t	m	t	m	
2Y-TZP wet mixing	187	1070±70	11.2±0.4	10±0.8	90	10	38	62	52
2Y-TZP LAVA	194	1380±30	11.6±0.3	13±0.3	93	7	16	84	77
3Y-TZP	197	1060±107	11.3±0.1	5±0.6	99	1	97	3	2

Table 4.2-2 shows the transformability (V_{trans}) determined as the difference of the contents of monoclinic zirconia in the polished and in the fractured surfaces of all studied samples. XRD analyses of the polished surfaces revealed the predominant presence of the t-ZrO_2 phase in 2Y-TZP wet mixing, 2Y-TZP LAVA, and 3Y-TZP samples. Additionally, these data proved that the fraction of the zirconia transformation in the ceramic samples considerably increases during the fracture process. It was found that the transformability in 2Y/TZP ceramics is around 52% for wet mixing and 77% for LAVA. However, in the 3Y-TZP ceramic only 2% of the available tetragonal zirconia transformed to monoclinic

symmetry during the fracture process. Therefore, the fracture toughness (5 ± 0.8 MPa·m$^{1/2}$) of the 3Y-TZP ceramic is comparatively small. On the other hand, the presence of the t→m transformation in the 2Y-TZP LAVA ceramic together with the high transformability causes the increase of the average fracture toughness to a value as high as 13 MPa·m$^{1/2}$ which significantly exceeds the values for 2Y-TZP wet mixing composition.

4.2.7.3.3 Low temperature degradation

Fig.4.2-5 shows the results of the aging experiments. At the beginning of the aging the polished surfaces of the 3Y-TZP, LAVA, and wet mixing ceramics contained 1%, 7%, and 10% monoclinic zirconia, respectively.

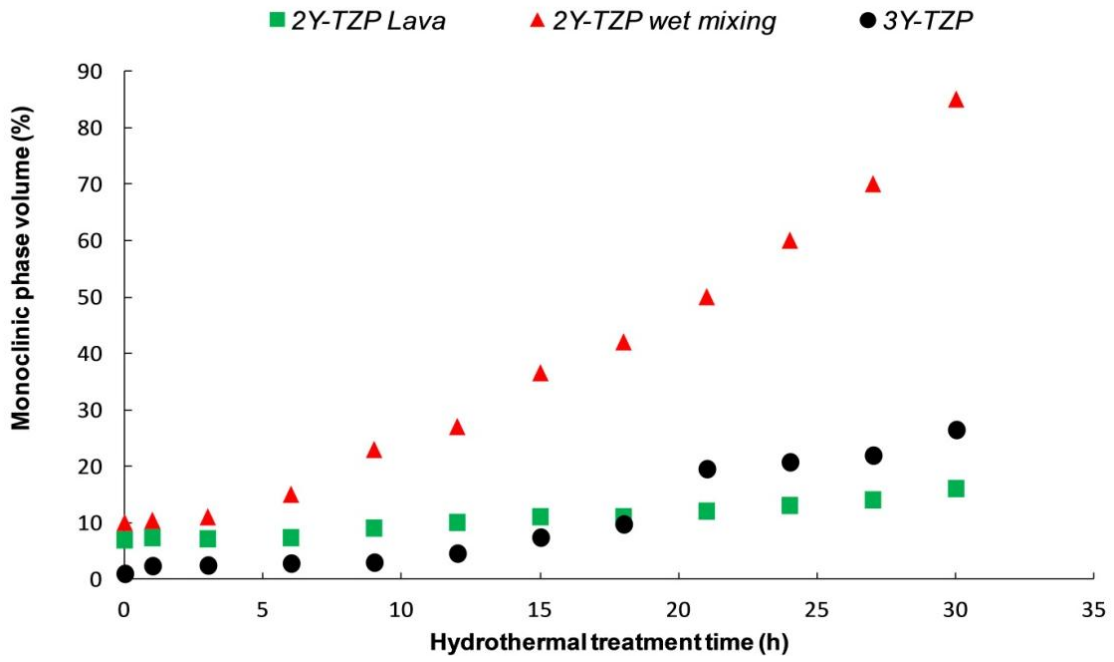

Fig.4.2-5. X-ray diffraction data of monoclinic-transformed zirconia as a function of the aging treatment time for all zirconia ceramics

After 10 h of aging at 134°C, the difference between these materials becomes more significant. At this point, the amount of transformed zirconia is almost three times higher for the wet mixing ceramic (23%), while in the 3Y-TZP and the LAVA ceramics the

amount of transformed zirconia (3% and 9%, respectively) remains almost equal when compared to the starting values. At the end of the experiment (after 30 h at 134°C) the content of the monoclinic phase in the WP and 3Y-TZP ceramic increased to 60% and 27%, respectively, but in the LAVA ceramic increased only to 16%. However, for up to 18 h of aging the amount of transformed zirconia was negligible lower in conventional 3Y-TZP ceramics than in the LAVA ceramic.

4.3 2Y-TZP/Ta CERAMIC-METAL SYSTEM

2Y-TZP ceramic powder was processed by LAVA resulting with nanostructure and further used as the raw powder for sintering zirconia based composite with milled tantalum metal. (Chapter 3, Section 3.1.3.2).

4.3.1 Processing and Fabrication

The resulting ceramic nanopowder/milled tantalum suspension was prepared and then sintered at 1400°C using Spark Plasma Sintering with the same parameters as for 3Y-TZP/Ta composite (Chapter 3, Section 3.1.4.3).

4.3.2 Characterization of sintered composites

The experimental attempt to add the reinforcing Tantalum to 2Y-TZP ceramic matrix obtained by LAVA would not be entitled as successful. As mentioned earlier, the presence of Ta_2O_5 decreases the stability of ZrO_2 lattice and consequently increases transformability of zirconia. However, this high level of transformability provokes the degradation of mechanical properties due to spontaneous tetragonal to monoclinic phase transformation.

In order to visualize microcracks produced by spontaneous transformation on the polished surface of 2Y-TZP/20 vol.% Ta composite SEM photo was produced in topographic mode (Fig.4.3-1). For this reason metallic particles are not presented on the image.

Even though it was possible to retain the tetragonal zirconia phase in 3Y-TZP/Ta ceramic-metal composite with 3 mol% (Chapter 3), but nonetheless it was not succeed in the composition with less yttria content.

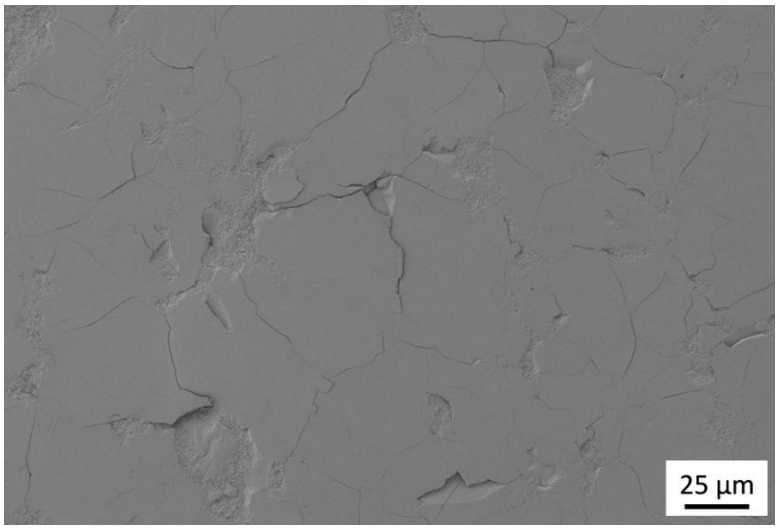

Fig.4.3-1. Polished surface of 2Y-TZP/Ta ceramic-metal composite with microcracking induced by spontaneous transformation of zirconia

4.4 SUMMARY

4.4.1 2Y-TZP system

The LAVA process proved to be a highly suitable method to prepare 2Y/TZP nanopowders with a homogeneous yttria as well as particle size distribution by simultaneously vaporizing of 3Y/TZP and monoclinic ZrO_2 raw powders at a certain ratio. Spark plasma sintering of these nanopowders led to the manufacturing of 2Y/TZP ceramics with high indentation toughness (13 $MPa \cdot m^{1/2}$) in combination with high flexural strength (1380 MPa).

The t→m transformability of the LAVA 2Y/TZP ceramic during the crack propagation is around 77%. In addition to high transformability, LAVA ceramic was highly resistant to hydrothermal degradation in comparison with commercially available 3Y-TZP powder and 2Y-TZP ceramic performed by wet mixing.

4.4.2 2Y-TZP/Ta system

The presence of Ta_2O_5 oxide in ceramic matrix with low content of yttria leads to spontaneous transformation of zirconia and, consequently, to degradation of mechanical properties.

In order to retain more metastable tetragonal phase particles, one effective way is to decrease the starting powder particle size [24] and the other is to increase the elastic modulus of the composite matrix [25]. Al_2O_3, with a modulus of elasticity twice of that ZrO_2, is considered as a suitable additive. Alumina grains acts as a constraint to the zirconia particles, retaining the tetragonal zirconia in a metastable state, toughening the ceramic material. It leads to the next systems, Alumina Toughened Zirconia (ATZ) and ATZ/Ta composites.

4.5 REFERENCES

[1] Sakuma T, Eda H, Sato H. Composition optimization of ZrO_2–Y_2O_3 alloys to improve the fracture toughness. Science and technology of Zirconia III. *Adv Ceram.*, 1988; 24:357–63.

[2] Masaki T, Sinjo K. Mechanical properties of highly toughened ZrO_2–Y_2O_3.*Ceram Int.*, 1987; 13:109–12

[3] Lange FF. Transformation-toughened ZrO_2: Correlations between grain size control and composition in the system ZrO_2–Y_2O_3. *J Am Ceram Soc*., 1986:69:240–2.

[4] Lee JK, Kim H. Surface crack initiation in 2Y-TZP ceramics by low temperature aging. *Ceram Int.*, 1994; 20:413–8.

[5] Kubo T, Machida N, Sakai H, Shigematsu T. Isothermal tetragonal to monoclinic phase transition around room temperature in 2.0 mol.% yttria-doped zirconia ceramics. *J Jap Soc Powder Powder Metall.*, 1999; 46:496–501.

[6] Yasuda K, Arai S, Itoh M, Wada K. Influence of Y_2O_3 distribution on the rate of tetragonal to monoclinic phase transformation of yttria-stabilized zirconia during hydrothermal aging. *J Mater Sci.*, 1999; 34:3597–604.

[7] Li JF, Watanabe R, Zhang BP, Asami K, Hashimoto K. X-ray photoelectron spectroscopy investigation on the low-temperature degradation of 2 mol.% ZrO_2–Y_2O_3ceramics. *J Am Ceram Soc.*, 1996; 79:3109–12.

[8] Chevalier J, Gremillard L, Deville S. Low-temperature degradation of zirconia and implications for biomedical implants. *Annu Rev Mater Res*., 2007; 37:1–32.

[9] Gutiérrez-González CF, Moya JS, Palomares FJ, Bartolomé JF. Low-temperature aging degradation-free 3Y-TZP/Nb composites. *J Am Ceram Soc.*, 2010; 93:1842–4.

[10] Bartolomé JF, Montero I, Díaz M, López-Esteban S, Moya JS, Deville S, et al. Accelerated aging in 3-mol.%-yttria-stabilized tetragonal zirconia ceramics sintered in reducing conditions. *J Am Ceram Soc*., 2004; 87:2282–5.

[11] Masaki T. Mechanical properties of toughened ZrO_2–Y_2O_3 ceramics. *J Am Ceram Soc*., 1986; 69:638–40.

[12] Schmauder S, Schubert H. Significance of internal stresses for the martensitic transformation in yttria-stabilized tetragonal zirconia polycrystals during degradation. *J Am Ceram Soc*., 1986; 69:534–40.

[13] Chevalier J, Deville S, Münch E, Jullian R, Lair F. Critical effect of cubic phase on aging in 3 mol% yttria-stabilized zirconia ceramics for hip replacement prosthesis. *Biomaterials*, 2004; 25:5539–45.

[14] Matsui K, Yoshida H, Ikuhara Y. Nanocrystalline, ultra-degradation-resistant zirconia: its grain boundary nanostructure and nanochemistry. *SciRep* 2014; 4:1–6.

[15] Zhang F, Vanmeensel K, Inokoshi M, Batuk M, Hadermann J, Van Meerbeek B, et al. Critical influence of alumina content on the low temperature degradation of 2–3 mol% yttria-stabilized TZP for dental restorations. *J Eur Ceram Soc.,* 2015; 35:741–50.

[16] Yamashita I, Tsukuma K. Phase separation and hydrothermal degradation of 3 mol% Y_2O_3–ZrO_2 ceramics. *J Jap Ceram Soc.,* 2005; 113:530–3.

[17] Basu B, Vleugels J, Van Der Biest O. Toughness tailoring of yttria-doped zirconia ceramics. *Mater Sci Eng*., 2004; 380:215–21.

[18] Basu B, Vleugels J, Van Der Biest O. Microstructure–toughness–wear relationship of tetragonal zirconia ceramics. *J Eur Ceram Soc*., 2004; 24:2031–40.

[19] Basu B, Vleugels J, Van Der Biest O. Transformation behaviour of tetragonal zirconia: role of dopant content and distribution. *Mater Sci Eng*., 2004; 366:338–47

[20] Kurland HD, Grabow J, Müller FA. Preparation of ceramic nanospheres by CO_2 laser vaporization (LAVA). *J Eur Ceram Soc*., 2011; 31:2559–68.

[21] Kurland HD, Stötzel C, Grabow J, Zink I, Müller E, Staupendahl G, et al. Preparation of spherical titania nanoparticles by CO_2 laser evaporation and process-integrated particle coating. *J Am Ceram Soc.,* 2010; 93:1282–9.

[22] Wurst JC, Nelson JA. Lineal intercept technique for measuring grain size in two-phase polycrystalline ceramics. *J Am Ceram Soc.,* 1972; 55:109.

[22] Miranzo P, Moya JS. Elastic/plastic indentation in ceramics: a fracture toughness determination method. *Ceram Int*., 1984; 10:147–52.

[24] Lange FF, Green DJ, in "Advances in Ceramics", Vol. 3, edited by A. H. Heuer and L. W. Hobbs (The American Ceramic Society, Columbus, OH, 1981) p. 217.

[25] Lange FF. Transformation toughening *J. Mater. Sci.*, 1982*;* 17:255-262.

5

ATZ/Ta System: Ceramic matrix optimization by Laser Co-vaporization (CoLAVA)

5.1 INTRODUCTION

The combination of alumina and zirconia materials in so-called alumina toughened zirconia (ATZ) and zirconia toughened alumina (ZTA) aims on combining the high strength and toughness of ZrO_2 with the excellent tribological properties and aging resistance of α-Al_2O_3 [1, 2]. In addition, the mechanical properties of ZrO_2/Al_2O_3 dispersion ceramics could be considerably increased by reducing the corresponding grain sizes and by improving the homogeneity of the phase dispersion [3-7]. Furthermore, these factors are critical under hydrothermal conditions. In ZTA ceramics the spontaneous transformation of tetragonal to monoclinic ZrO_2 grains in a humid environment and in the temperature range 20 °C to 300 °C, i.e. low temperature degradation (LTD), occurs more readily if the grain size is below a critical value (500 nm) [8]. Additionally, their narrow size distribution as well as their concentration and isolation, i.e. the absence of aggregates, are important for the inhibition of intergranular water diffusion which would lead to a premature transformation [8]. For this purpose ZrO_2/Al_2O_3 nanoparticles with an intraparticular phase dispersion instead of just mixing different portions of raw materials might be desirable. Therefore, this Chapter examined the Co-Laser vaporization (CoLAVA) opportunities to obtain the ZrO_2/Al_2O_3 nanoparticles with an intra-granular phase dispersion instead of just mixing different portions of raw materials. It was also expected that the homogeneously distributed alumina grains acts as a constraint to the zirconia particles, retaining the tetragonal zirconia in a metastable state, toughening the ceramic material and, consequently, allows to avoid spontaneous transformation of zirconia in ceramic-metal composite. Fig.5.1-1 illustrates the idea of the manufacturing Strategy III where ceramic powders are homogenized by CoLAVA process.

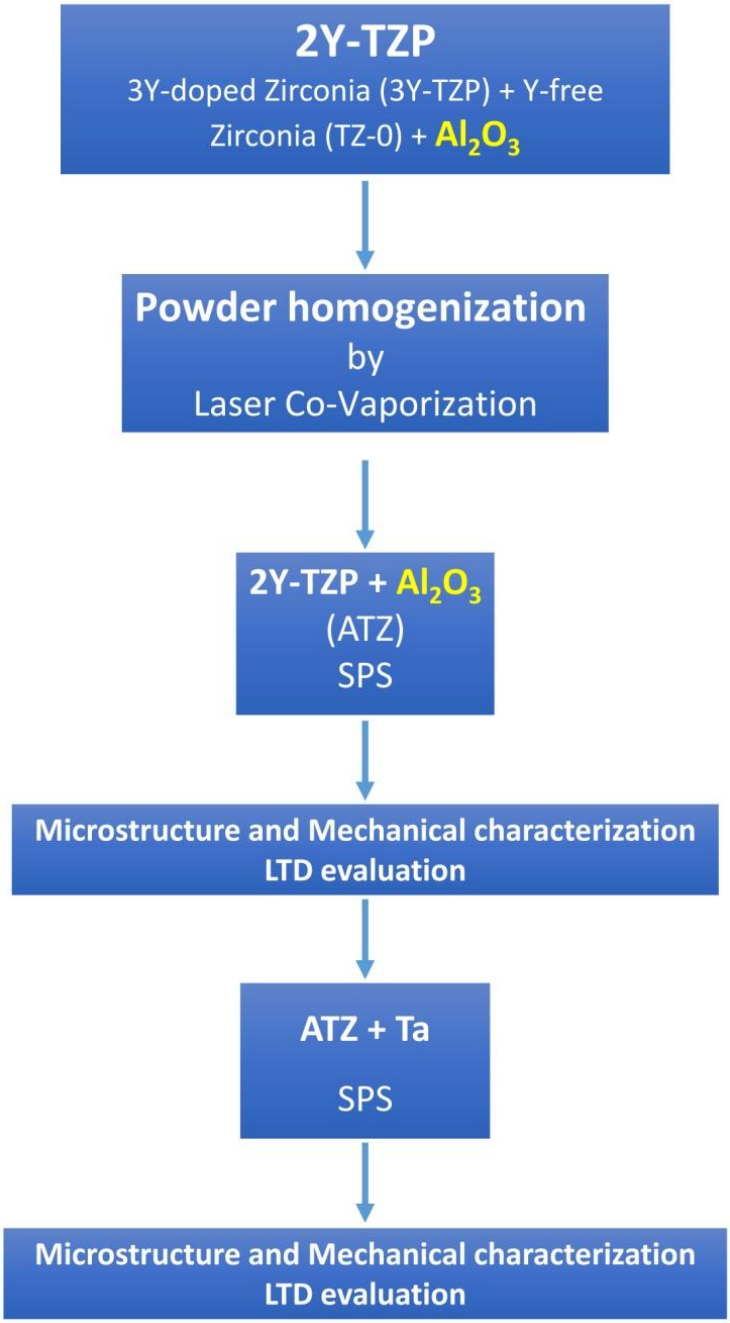

Fig.5.1-1. Strategy III on manufacturing of ATZ and ATZ/Ta composites

5.2 ZIRCONIA/ALUMINA (ATZ) SYSTEM

5.2.1 Raw Materials

The starting materials were previously fabricated 2Y-TZP Lava nanopowder and alumina commercial powder:

- 2Y-TZP LAVA nanopowder (Chapter 4, Section 4.2.2)
- Corundum (α-Al_2O_3, Alcoa, A16SG), average grain size of d_{50} = 0.53 µm.

5.2.2 Processing of ATZ mixture

Appropriate quantities of 2Y/TZP powder fabricated earlier and α-Al_2O_3 raw powder were mixed in order to obtain a powder mixture containing 20 mass.% of corundum. Mixing was conducted in a polyethylene bottle with zirconia balls (diameter 1 mm, volume fraction 10%) in a multidirectional mixer (24 h at 150rpm). The obtained zirconia-alumina powder mixture was used as starting material for the preparation of nanoparticles with the CoLAVA process (Chapter 8, Section 8.8.2.3). The CoLava processing parameters were kept on the same level as in LAVA (Chapter 4, Section 4.2.2). For comparison purposes ATZ mixture has been fabricated by wet mixing route as well.

5.2.3 Characterization of ATZ CoLAVA powder

5.2.3.1 X-Ray diffraction (XRD)

XRD measurements of the CoLAVA powder was performed at diffraction angles 2θ ranging from 20° to 70° (step scanning mode, step size 0.03°, scan speed 3.46° min^{-1}). Qualitative analyses of the crystal phases were conducted using the following powder diffraction files: ICDD-PDF 01-083-0113 (t-ZrO_2), ICDD-PDF 00-024-1165 (m-ZrO_2), ICDD-PDF 00-046-1212 (α-Al_2O_3), ICDD-PDF 00-023-1009 (θ-Al_2O_3), ICDD-PDF 00-

046-1215 (δ-Al_2O_3), and ICDD-PDF 00-050-0741 (γ-Al_2O_3). The mass fraction X_m and volume fraction V_{mtot} of m-ZrO_2 was evaluated using Equations 8.5-2 and 8.5-3, respectively.

5.2.3.2 TEM investigation

Morphologic properties of the CoLAVA nanoparticles were evaluated by transmission electron microscopy at accelerating voltage 300 kV. For this purpose nanoparticles were deposited on a TEM grid (perforated carbon film on copper mesh, Plano GmbH, Wetzlar, Germany). The particle diameter distribution was determined from TEM micrograph by measuring the diameters of about 900 nanoparticles [9].

5.2.3.3 Differential thermal analyses

The phase transformations of the CoLAVA nanopowder were examined using DTA technique (Chapter 8, Section 8.5.2.1). For this purpose the nanopowder (170 mg) and a reference corundum powder (NETZSCH alumina, NETZSCH-Gerätebau GmbH, Selb, Germany) were filled into alumina crucibles. Both crucibles were heated up in air from room temperature to 1445 °C applying a heating rate of 5 °C min^{-1}.

5.2.3.4 Dilatometry

Shrinkage behaviour and dynamic sintering of green compacts of the CoLAVA nanopowder were investigated using a high-temperature horizontal dilatometer at a heating rate of 5 °C min^{-1} in air up to 1500 °C. The dwelling time at maximum temperature was 2 h (Chapter 8, Section 8.5.2.2).

5.2.3.5 Fourier transform infrared (FTIR) spectroscopy

FTIR spectra of the CoLAVA nanopowder as-prepared as well as calcined at different temperatures from 500 °C to 1350 °C were measured in the wavenumber range 200 cm^{-1} to

1200 cm^{-1} (transmission mode, resolution 2 cm^{-1}, 120 scans per sample) (Chapter 8, Section 8.5.3). For this purpose potassium bromide pellets of each powder sample were prepared using a uniaxial press. The vibrational bands of the FTIR spectra were assigned according to Boumaza *et al.* [10].

5.2.3.6 Inductively coupled plasma-optical emission spectroscopy (ICP-OES) analyses of calcined nanopowders

The distribution of Al, Zr, Y, and Hf in the CoLAVA nanopowder after calcination at 1350 °C was characterized by ICP-OES analyses after leaching in HCl (Chapter 8, Section 8.5.4). A custom designed charge-coupled detector (CCD) provided true simultaneous measurement, full wavelength coverage from 167 nm to 770 nm and fast read-out enabling short sample analysis times. The CCD detector has pixels arranged in continuous angled arrays that are matched exactly to the two-dimensional image from the Echelle polychromator. The source was powered by a radiofrequency generator operating at 40.48 MHz. The analyses were repeated five times. The results are given with their standard deviations.

5.2.4 Spark plasma sintering

The sintering experiments were carried out at 1400°C in vacuum (Chapter 3, Section 3.1.4.3). Specimens were maintained at the maximum sintering temperature 3 minutes with applied pressure 80MPa. As a result discs of 20 and 50 mm diameter and thickness about 2-4 mm were obtained.

5.2.5. Characterization of dense material

For the materials' microstructural and mechanical characterization the same methods as in Chapter 3 and Chapter 4 were chosen. This includes X-ray diffraction (XRD), scanning

electron microscopy (SEM), transition electron microscopy (TEM), energy-dispersive X-ray Spectroscopy (EDS), density and low temperature degradation measurements as well as tests for assessing the mechanical properties such as biaxial flexural strength, SENB fracture toughness and hardness.

5.2.6 Results and discussion

5.2.6.1 TEM investigation of ATZ CoLAVA nanoparticles

Fig.5.2-1 shows TEM images and the size distribution of the hybrid nanoparticles obtained from CoLAVA of the Al_2O_3/Y_2O_3-ZrO_2 raw powder mixture.

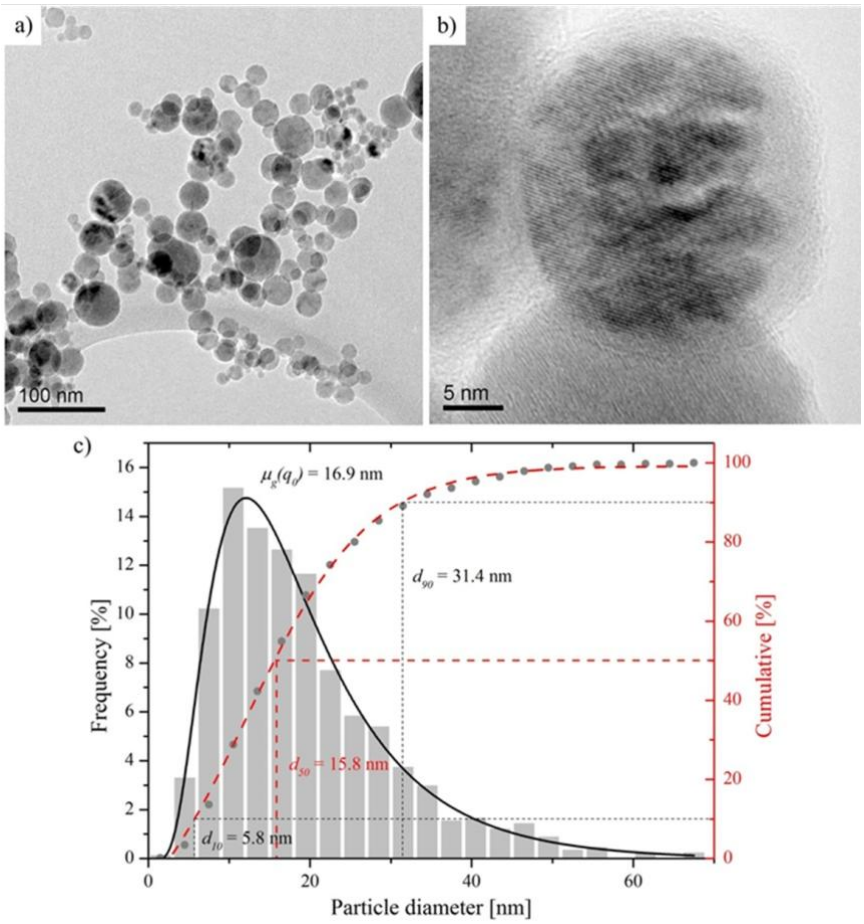

Fig.5.2-1. TEM investigation of the CoLAVA nanoparticles: (A) survey and (B) high resolution micrographs, (C) frequency based particle diameter distribution of the CoLAVA nanopowder (log normal (—) and cumulative (----) distribution) with the geometric mean diameter $\mu_g(q_0)$ and the characteristic diameters d_{10}, d_{50}, and d_{90}

The particles are spherically shaped (Fig. 5.2-1A and B), and their diameters follow a log normal distribution (Fig. 5.2-1C) with an average diameter d_{50} of 15.8 nm and a specific surface area S_{BET} of 49.7 m^2 g^{-1}. The particles appear crystalline with visible lattice planes. However, in high resolution micrographs some of the particles show a core/shell structure (Fig. 5.2-1B) where the core consists of crystalline phases and the shell seems to be amorphous. The thickness of the shell is generally below 1 nm and reaches up to 5 nm in very few cases as illustrated in Fig. 5.2-1B. The rate of production of the Al_2O_3/ZrO_2 nanopowder was 10.2 g h^{-1} under the applied CoLAVA process conditions.

5.2.6.2 Thermal behaviour of the CoLAVA nanopowder

Heating the CoLAVA nanopowder to 1445°C results in two exothermic peaks in the differential thermal analysis (DTA) curve at 1097°C and 1340°C (Fig.5.2-2). The dilatometry curve (Fig.5.2-2) reveals that under conventional conditions the powder starts to sinter at a temperature around 900°C and reaches its maximum sintering rate above 1200°C. Above 1300°C the densification slows down immediately and the shrinkage rate drops to a minimum. After sintering at 1500°C for 2 h the samples reached 88% of their theoretical density φ_{th} which is equivalent to a porosity of 12%.

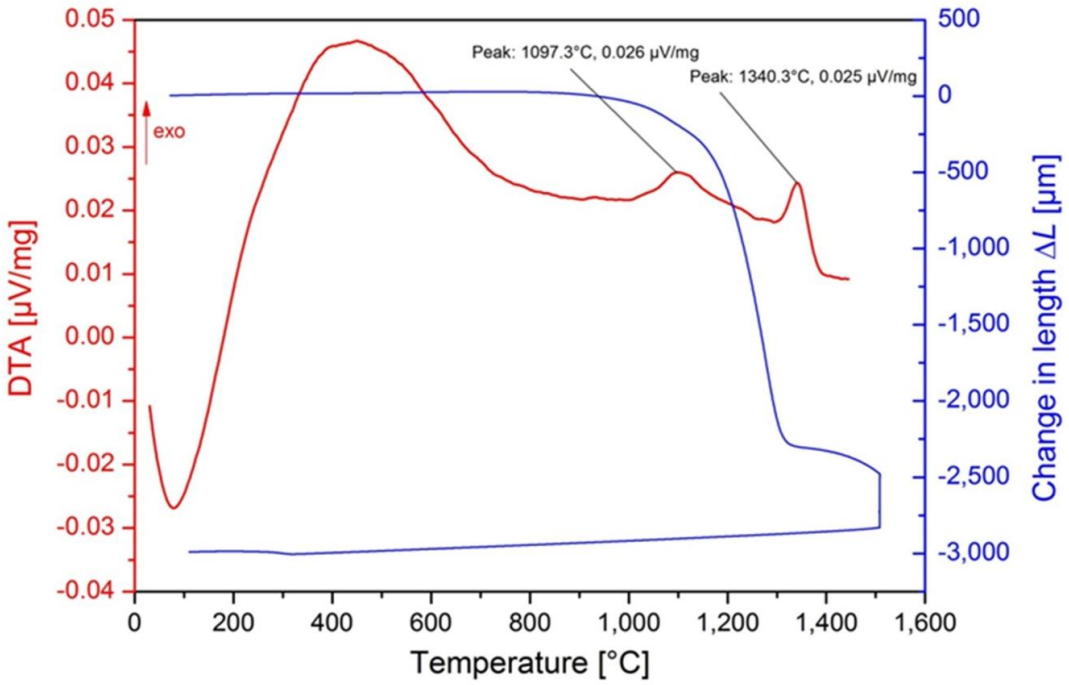

Fig.5.2-2. Thermoanalyses of the CoLAVA nanopowder: differential thermal (DTA —) and dilatometric measurements (absolute change in length —)

5.2.6.3 X-ray diffraction and Fourier transform infrared analyses of the CoLAVA nanopowder

The as prepared CoLAVA nanopowder consists of tetragonal zirconia (Fig. 5.2-3A) and amorphous or low crystalline transition alumina phases like γ-Al_2O_3 or δ-Al_2O_3 (Fig. 5.2-3B). The domain size $d_{(101)}$ of t-ZrO_2 calculated from the Scherrer equation amounts to 5 nm. The X-ray diffraction (XRD) reflections of t-ZrO_2 (Fig. 5.2-3A) are slightly shifted towards higher diffraction angles 2θ. Heating the powder to 500 °C and 900 °C, respectively, has no influence on the composition or on the domain size. Heating the powder to 1100 °C which is the temperature of the first exothermic peak in the DTA curve (Fig.5.2-3) results in a phase transition of the γ- and δ-alumina phases to θ-Al_2O_3 (Fig. 5.2-3B). The t-ZrO_2 domains grow to $d_{(101)}$ = 19 nm and the XRD reflections (Fig. 5.2-3A) shift

back to the original angular positions of t-ZrO_2 found in the Powder Diffraction File (PDF) 01-083-0113 from the International Centre for Diffraction Data (ICDD). At a temperature of 1350°C which is in the range of the second exothermic peak in the DTA curve (Fig.5.2-3) θ-Al_2O_3 transforms to highly crystalline α-Al_2O_3 (Fig. 5.2-3A and B) with a domain size of $d_{(10\text{-}2)}$ = 49 nm, and the domains of t-ZrO_2 grow to $d_{(101)}$ = 48 nm.

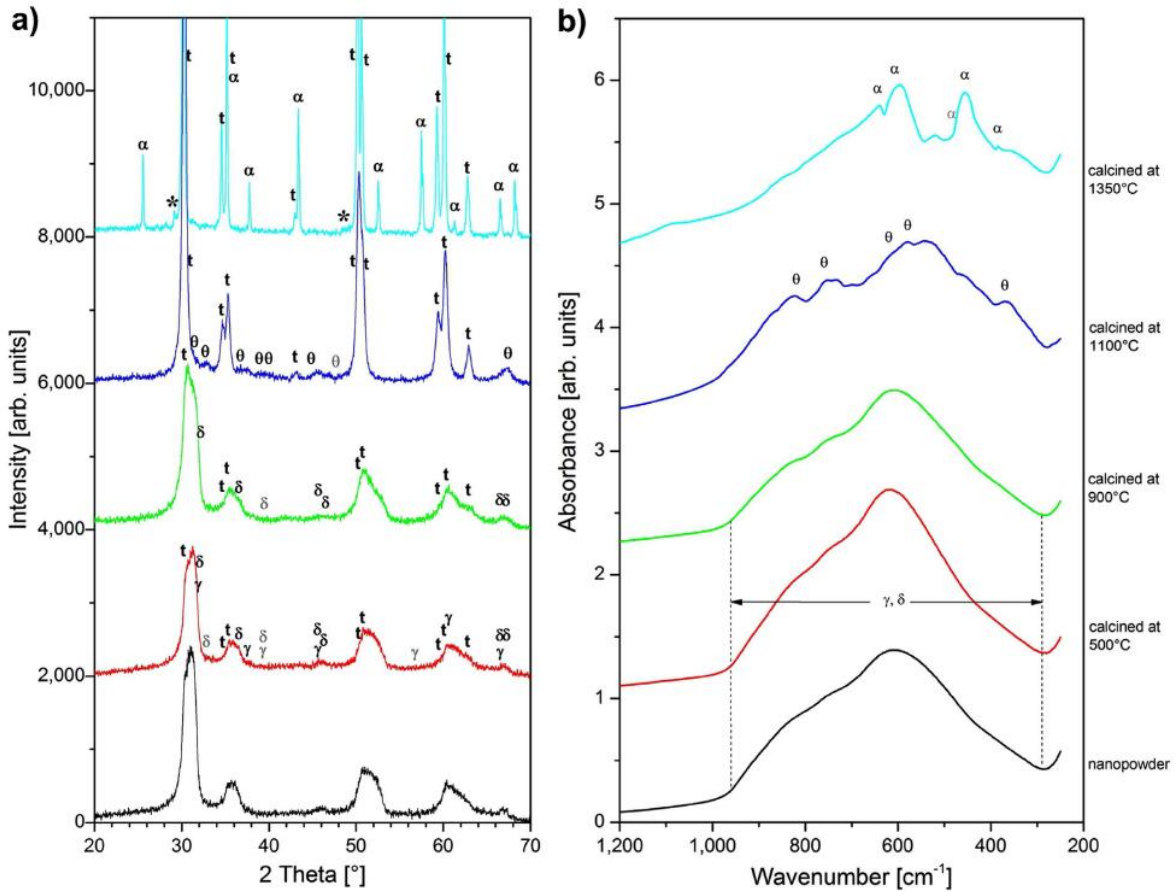

Fig.5.2-3. Evolution of the crystal phases in the CoLAVA nanopowder with increasing sintering temperatures: a) XRD analyses and b) FTIR spectrometry of the nanopowder as prepared (—) as well as calcined at 500 °C (—), 900 °C (—), 1100 °C (—), and 1350 °C (—), labelling "t" denotes tetragonal zirconia, "γ", "δ", "θ", and "α" denote the alumina phases, and "*" marks yttria reflections

Moreover, at 1350°C small additional reflections appear at 2θ angles of 29.2° and 48.6°. They represent the two most intense reflections of yttria and were assigned to its (222) and (440) planes, respectively, according to the ICDD-PDF 00-41-1105.

Results from thermoanalyses, Fourier transform infrared (FTIR) spectroscopy, XRD, and TEM reveal that the CoLAVA nanoparticles mainly consist of t-ZrO_2 and a small amount of transition alumina phases. Some of the particles exhibit a core/shell structure with a crystalline core and an amorphous shell. Heating the nanoparticles to 1100 °C leads to a phase transformation of the γ- and δ-alumina transition phases to θ-alumina which is in agreement with literature [11]. The $Zr_{(1-x)}Al_xO_{(2-x/2)}$ defect structure seems to remain stable up to a temperature of 900°C as can be seen by its constant domain size. Between 900 °C and 1100 °C the zirconia domains start to grow, and the thermal energy is finally used to separate θ-Al_2O_3 and t-ZrO_2 (Fig.5.2-4).

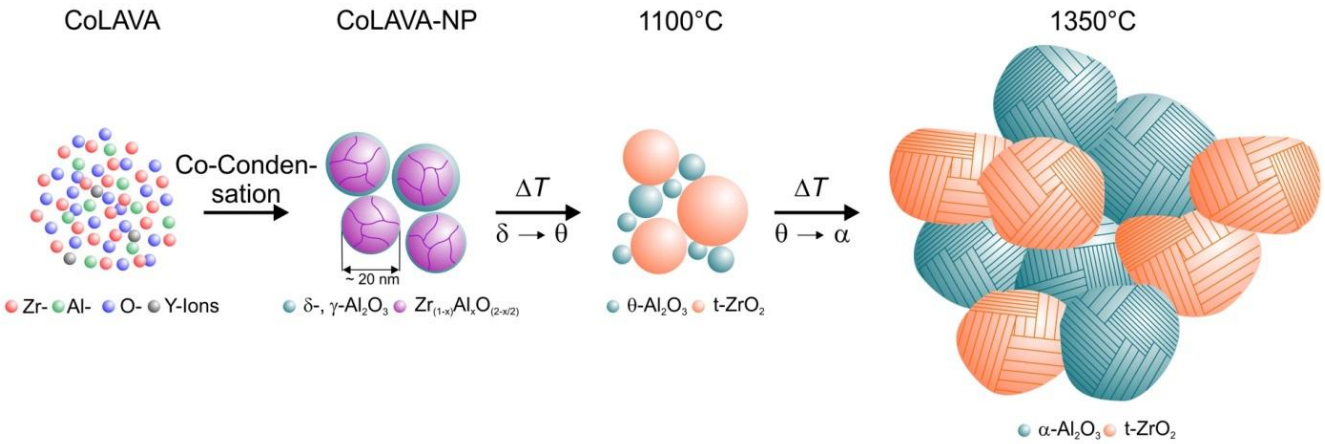

Fig.5.2-4. Gas phase condensation of alumina/zirconia hybrid nanoparticles in the CoLAVA process and their stepwise evolution at increasing sintering temperatures up to 1350 °C

Consequently, the XRD reflections of t-ZrO_2 shift towards smaller diffraction angles. Only a small amount of alumina (< 3 mol%) remains dissolved in the t-ZrO_2 crystals [12]. Above 1300 °C θ-Al_2O_3 transforms to α-Al_2O_3. In pure alumina the θ to α transformation usually

occurs at temperatures ranging from 1000 °C to 1200 °C [13-15]. The shift towards higher temperatures observed here is a consequence of the nanocrystallinity of the CoLAVA powder and is additionally supported by the stabilizing effect of zirconia. The θ- to α-Al_2O_3 transformation is considered to occur through a nucleation and growth process [16]. During thermal treatment the θ-Al_2O_3 crystallites grow and exceed a critical size of approximately 20 nm necessary for the exothermic formation of stable α-Al_2O_3 [14, 17, 18]. Subsequently, the α-Al_2O_3 nuclei grow rapidly and form polycrystalline α-Al_2O_3 with crystallite sizes around 50 nm [17, 19]. The phase transformation also attends a volume shrinkage (densities: $\rho_{\theta\text{-}alumina}$ = 3.60 g cm^{-3} and $\rho_{\alpha\text{-}alumina}$ = 3.99 g cm^{-3}) [20]. However, under conventional sintering conditions it is hardly possible to obtain fully dense polycrystalline α-Al_2O_3 ceramics because the θ to α transformation is accompanied by the formation of vermicular microstructures consisting of a network of large pores [16, 21, 22]. This explains the residual porosity of 12% after conventional sintering at 1500 °C for 2 h.

5.2.6.4 Characterization of sintered Al_2O_3/ZrO_2 ceramics

First of all it must be noticed that, the components of the raw powder mixture have different rates of vaporization due to their different melting (T_m) and vaporization temperatures (T_b) (Al_2O_3: T_m = 2015 °C, T_b = 2980 °C; ZrO_2: T_m = 2700 °C, T_b = 5155 °C), absorption coefficients at the CO_2 laser wavelength (Al_2O_3: 3556 cm^{-1}; ZrO_2: 1185 cm^{-1}) [23, 24], and thermal conductivities (Al_2O_3: 37.0 W $m^{-1}K^{-1}$ at 25°C, 5.7 W $m^{-1}K^{-1}$ at 1600 °C; ZrO_2: 1.7 W $m^{-1}K^{-1}$ at 25 °C, 2.3 W $m^{-1}K^{-1}$ at 1600 °C) [25]. Therefore, it is not possible to map the mixing ratio of the raw components onto the phase composition of the resulting nanoparticles. To obtain defined phase ratios in the nanopowder, the mixing ratio of the raw powders has to be determined experimentally. However, at this point it is

important to mention that the reproducibility of the CoLAVA method is very high. Under the same experimental conditions (e.g. raw powder ratio, laser parameters, and process gas flows) the obtained results (e.g. composition, phase distribution, particle size and size distribution) are always exactly the same.

To determine Al_2O_3 and ZrO_2 fractions, SPS-sintered (from CoLAVA nanopowders), polished, and thermally etched specimens were analysed by SEM micrography (program ImageJ 1.48v, W. Rasband, National Institutes of Health, USA) (Fig.5.2-5A).

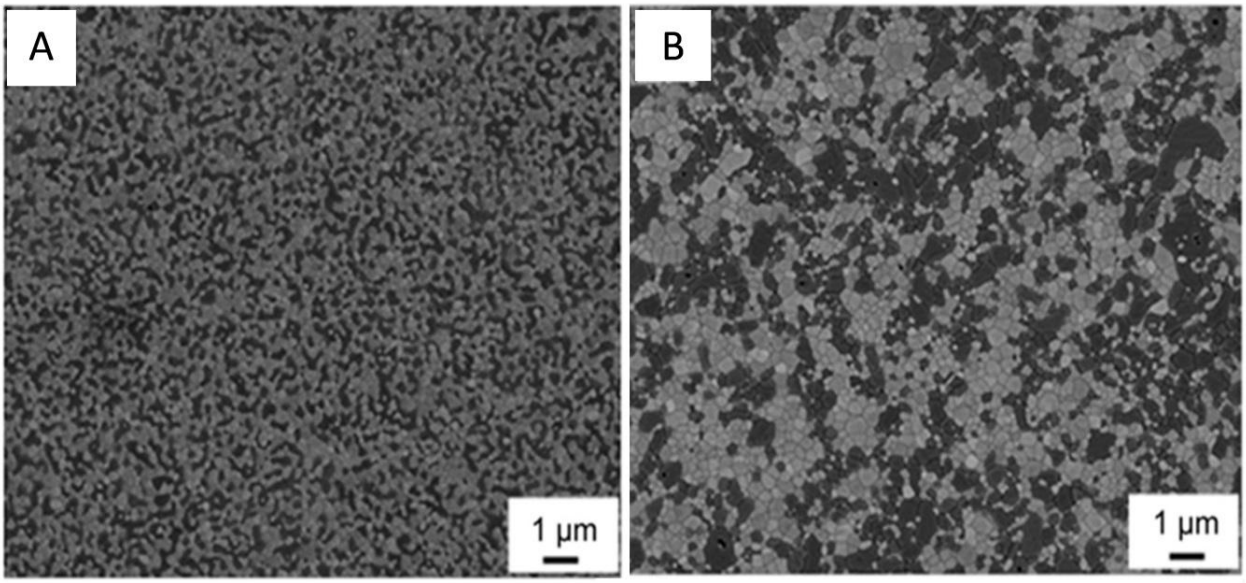

Fig.5.2-5. SEM micrographs of sintered, polished, and subsequently thermally etched surfaces of ATZ CoLAVA nanopowder (A) and from ATZ wet mixing reference powder (B) (bright phase t-ZrO_2, dark phase α-Al_2O_3)

It was found that the resulting alumina content after CoLAVA exceeds the one of the raw powder mixture and amounts to 47.6 vol% (i.e. 37.4 mass%). In addition, ICP-OES analyses reveal that CoLAVA nanoparticles calcined at 1350 °C consist of 60.4 ± 0.6 mass% ZrO_2, 37.5 ± 0.3 mass% Al_2O_3, 1.3 ± 0.03 mass% Y_2O_3, and 0.8 ± 0.02 mass% HfO_2. The latter represents an impurity that is usually present in ZrO_2 raw powders. Therefore, a mixture of 63.4 mass% 2Y-TZP and 37.4 mass% alumina raw powders was

wet processed by a conventional method in distilled water adding an alkali-free organic polyelectrolyte as surfactant for comparison reasons and sintered under the same conditions (Fig. 5.2-5B).

5.2.6.4.1 X-ray diffraction

Fig.5.2-6 shows diffractograms obtained from polished surfaces of ceramics sintered from the wet mechanically mixed Al_2O_3/ZrO_2 reference powder (WM) and from the CoLAVA nanopowder by SPS. The diffraction patterns are almost identical, and they reveal that the surfaces of both specimens mainly consist of tetragonal zirconia, α-alumina, and a minor amount of monoclinic zirconia.

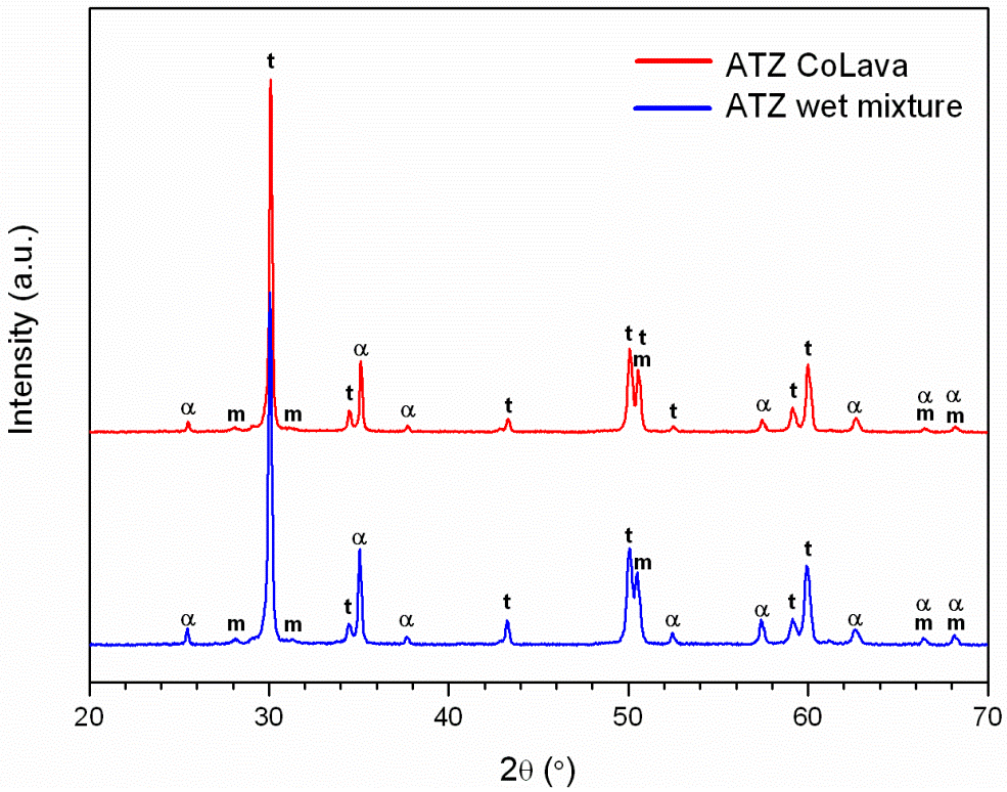

Fig.5.2-6. XRD analyses of polished surfaces (labelling "t" and "m" denote tetragonal and monoclinic zirconia, respectively, labelling "α" denotes α-alumina)

Sintered samples of the CoLAVA nanopowder consist of 47.6 vol% α-Al_2O_3 and 52.4 vol% t-ZrO_2 of high crystallinity. This means that according portions of Al^{3+} and Zr^{4+} ions

must have been present in the nanoparticles already after the CoLAVA process. Under thermodynamic equilibrium conditions there is no evidence for the formation of a solid solution in the zirconia-alumina system [26].

Alper presented a ZrO_2-Al_2O_3 phase diagram according to which Al_2O_3 has a maximum of 7 mol% solubility in ZrO_2 at 1885°C [27]. However, in gas phase condensation processes like CoLAVA or flame pyrolysis the particle formation occurs within milliseconds [28], i.e. far from thermodynamic equilibrium. For these conditions it was reported that a huge amount of up to 40 mol% Al_2O_3 can be incorporated into a t-ZrO_2 defect crystal structure with the composition $Zr_{(1-x)}Al_xO_{(2-x/2)}$ [29, 30]. It was suggested that Al^{3+} ions substitute Zr^{4+} ions by creating oxygen vacancies to maintain local charge balance [29]. At higher alumina concentrations the exceeding alumina might form an amorphous shell around the defect crystals [31]. Due to the significantly higher melting and vaporization temperatures of zirconia compared with alumina, ZrO_2 should condense and nucleate first from the gas phase followed by Al_2O_3 [32, 33]. The pre-condensed zirconia crystals subsequently act as nuclei for the heterogeneous nucleation of alumina. Fig.5.2-7 schematically illustrates the phase distribution within these nanoparticles. As mentioned earlier the difference in the alumina/zirconia ratio of raw powders and nanoparticles is reproducible and results from the higher vaporisation rate of alumina when compared to zirconia.

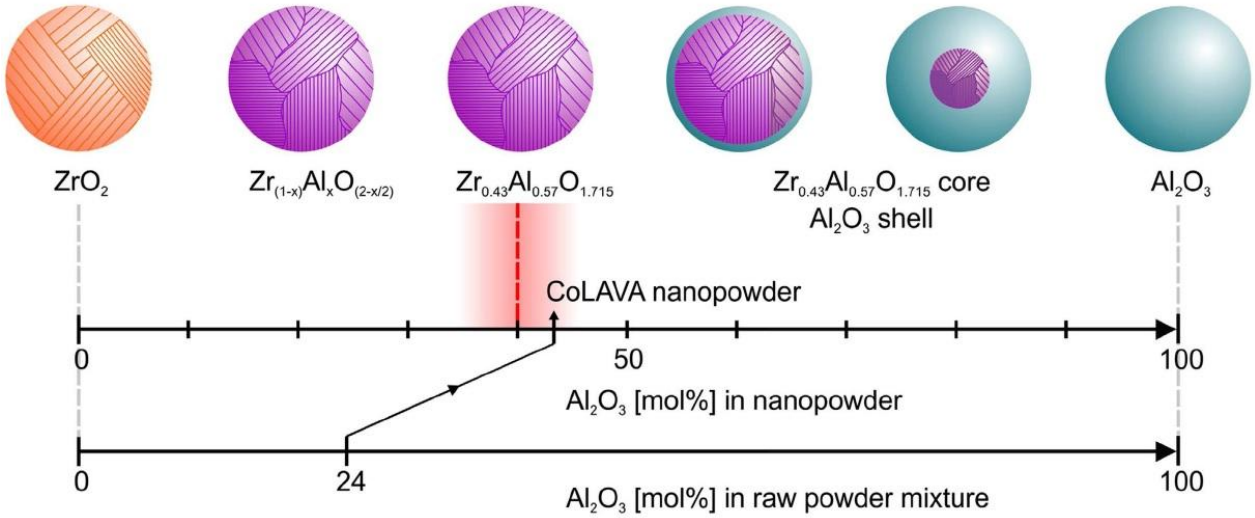

Fig.5.2-7. Composition and phase distribution of CoLAVA alumina/zirconia nanoparticles in dependence on the alumina content of the raw powder mixture

5.2.6.4.2 Microstructural characterization

The scanning electron microscope (SEM) images in Fig.5.2-8 show the microstructure of the sintered Al_2O_3/ZrO_2 specimens.

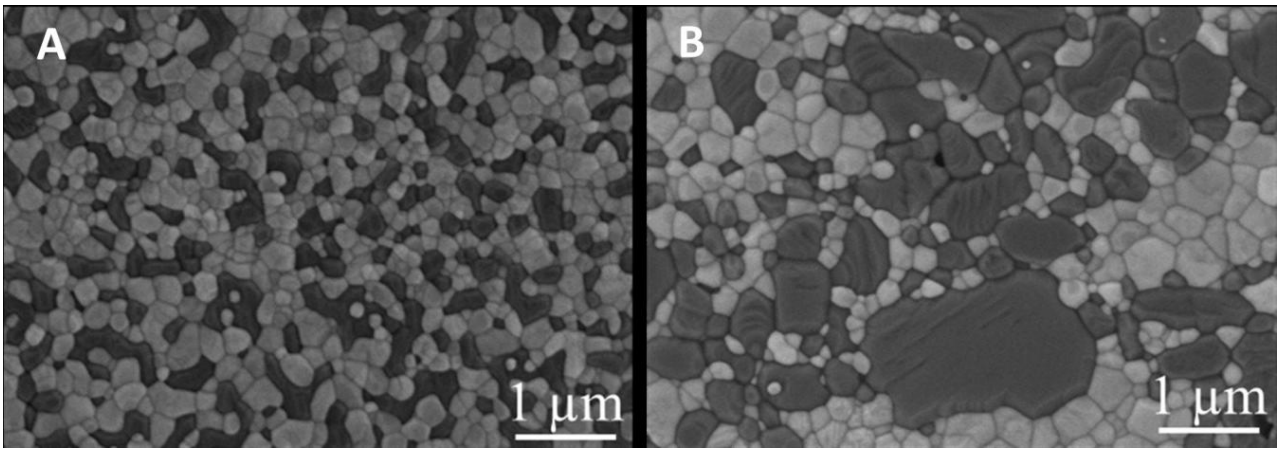

Fig.5.2-8. SEM micrographs of sintered, polished and thermally etched surfaces of ATZ CoLAVA nanopowder (A) and ATZ wet mixing reference powder (B) (bright phase t-ZrO_2, dark phase α-Al_2O_3)

The specimens sintered from the CoLAVA and from the wet mixed powder reached a density of 99% φ_{th} and 98% φ_{th}, respectively, due to high pressure of 80 MPa that was applied during SPS cycle. In both cases both phases are clearly separated. However, the grain sizes of both specimens differ. In the wet mixed composites the average grain sizes of ZrO_2 and Al_2O_3 were 403 ± 3 nm and 981 ± 5 nm, respectively, whereas they were 216 ± 2 nm and 270 ± 3 nm in the CoLAVA composites, respectively. Beyond that, the dispersion of the ZrO_2 and Al_2O_3 grains in the CoLAVA composite (Fig. 5.2-5A and Fig.5.2-8A) is much more homogeneous compared with the WM composite (Fig. 5.2-5B and Fig.5.2-8B). Therein both the ZrO_2 grains and also the Al_2O_3 grains are clustered together forming voluminous aggregates with maximum sizes exceeding 2 µm. Semi-quantitative microanalyses using energy dispersion spectroscopy (EDS) were conducted to determine the mean yttria content of the ZrO_2 grains in the sintered specimens. It was found that the ZrO_2 grains in the CoLAVA ceramic contain significantly less yttria (≈ 0.5 mol%) than in the case of the WM ceramic (≈ 2 mol%). On the other hand, in Chapter 4 (Section 4.2) was demonstrated that the homogeneity of the yttria distribution in zirconia ceramics depends on the type of preparation of the Y_2O_3/ZrO_2 starting powder mixture.

So a wet mechanically mixed starting powder generally leads to a less homogeneous yttria distribution when compared with a CoLAVA nanopowder prepared from the same conventionally mixed starting powder [34].

5.2.6.4.3. Mechanical properties

The complete densification, comparatively small sizes of the ZrO_2 (216 nm) and Al_2O_3 (270 nm) grains and a very homogeneous distribution of the dispersed phases explain the outstanding mechanical properties, especially flexural strength, of ZrO_2/Al_2O_3 ceramics

sintered from the CoLAVA nanopowder (Table 5.2-1). The flexural strength σ_f, Vickers hardness *HV*, and fracture toughness K_{Ic} of the CoLAVA composite significantly exceed the ones of the WM composite by 36%, 8%, and 45%, respectively, and reaches levels of 1500 MPa, 14.9 GPa, and 6.8 MPa $m^{1/2}$, respectively. Meanwhile the elastic modulus *E* of both specimens is in the same range.

Table 5.2-1. Densities and mechanical properties of the ceramic specimens sintered by SPS from the WM powder and the CoLAVA nanopowder as well as volume fractions of tetragonal "t" and monoclinic "m" zirconia in polished and fractured surfaces of the ceramic specimens and the resulting transformabilities of tetragonal zirconia

Specimen	Density [% φ_{th}]	Elastic modulus *E* [GPa]	Flexural strength σ_f [MPa]	Hardness *HV* [GPa]	Fracture toughness K_{Ic} [MPa $m^{1/2}$]	Volume fractions of t- and m-ZrO_2 [vol%]				Transformability of t-ZrO_2 V_{trans}
						Polished		Fractured		
						t	m	t	m	
WM	98	278	1100±70	13.8±0.4	4.7±0.3	94	6	85	15	9
CoLAVA	99	279	1500±30	14.9±0.3	6.8±0.2	98	2	64	36	34

The volume fractions of monoclinic zirconia (Table 5.2-1) on polished and on fractured surfaces of the ceramic specimens were calculated from XRD data using Equations 8.5-2 and 8.5-3. It was found that the transformability V_{trans} of t-ZrO_2, determined as the difference of the contents of m-ZrO_2 in the polished and in the fractured surfaces of the specimens, is around 34% for the CoLAVA ceramic and only 9% for the WM ceramic (Table 5.2-1).

The lower coefficient of thermal expansion α of α-Al_2O_3 ($\alpha_{(300\ K\ -\ 800\ K)}$ = 6.6 × 10^{-6} K^{-1}) compared with yttria stabilized ZrO_2 ($\alpha_{(300\ K\ -\ 2000\ K)}$ = 9.8 × 10^{-6} K^{-1}) is the reason for the tensile residual stress in ZrO_2/Al_2O_3 ceramics. In the WM ceramic this stress acts non-

uniformly due to the aggregation of the ZrO_2 grains causing an increased partial transformation of t-ZrO_2 during cooling down from the sintering temperature. Consequently, this reduces its transformability during the fracture process compared with the CoLAVA ceramics (Table 5.2-1). The superior transformability of the CoLAVA ceramic (Table 5.2-1) is also related to the reduced content of Y_2O_3 in the zirconia grains as measured by EDS. This could be due to the formation of the CoLAVA nanoparticles from the gas phase. During their condensation yttria is incorporated into the transition alumina phases. Heated above 1300°C these alumina phases transform to α-Al_2O_3. However, yttria is not soluble in corundum and is segregated again. Actually, two weak reflections appear at 2θ = 29.2° and 48.6° in the diffractogram of the CoLAVA nanopowder calcined at 1350°C (Fig. 5.2-3A) which correspond to the most intense reflections of Y_2O_3.

5.2.6.4.4 Low temperature degradation

The LTD resistance of sintered specimens was evaluated under hydrothermal conditions (Fig.5.2-9). After 30 h at 134 °C the volume fraction of monoclinic zirconia increased from 2% to 5% in the CoLAVA ceramic and from 6% to 40% in the WM ceramic. LTD resistance of the CoLAVA nanopowder derived ZrO_2/Al_2O_3 ceramics is excellent and far beyond the levels that have been achieved for typical 3Y-TZP (3 mol% yttria stabilised tetragonal zirconia polycrystals) ceramics [34] and yttria stabilised ZrO_2/Al_2O_3 composites with a zirconia content beyond 25 wt% [35]. Significant ageing followed by microcracking was noted at Al_2O_3 grain boundaries for ZrO_2 contents exceeding a percolation limit of 16 vol% causing pathways for water diffusion from the surface towards the bulk [36]. For WM ceramics a first gradual increase up to 10 vol% of the monoclinic zirconia phase was observed after two hours and they exhibited a more rapid increase up to 40 vol% m-ZrO_2

after 20 h of ageing treatment time. A degradation plateau was observed after 25 h. This behaviour was related to the presence of aggregated zirconia grains which act as further nucleation sites for the tetragonal-to-monoclinic transformation.

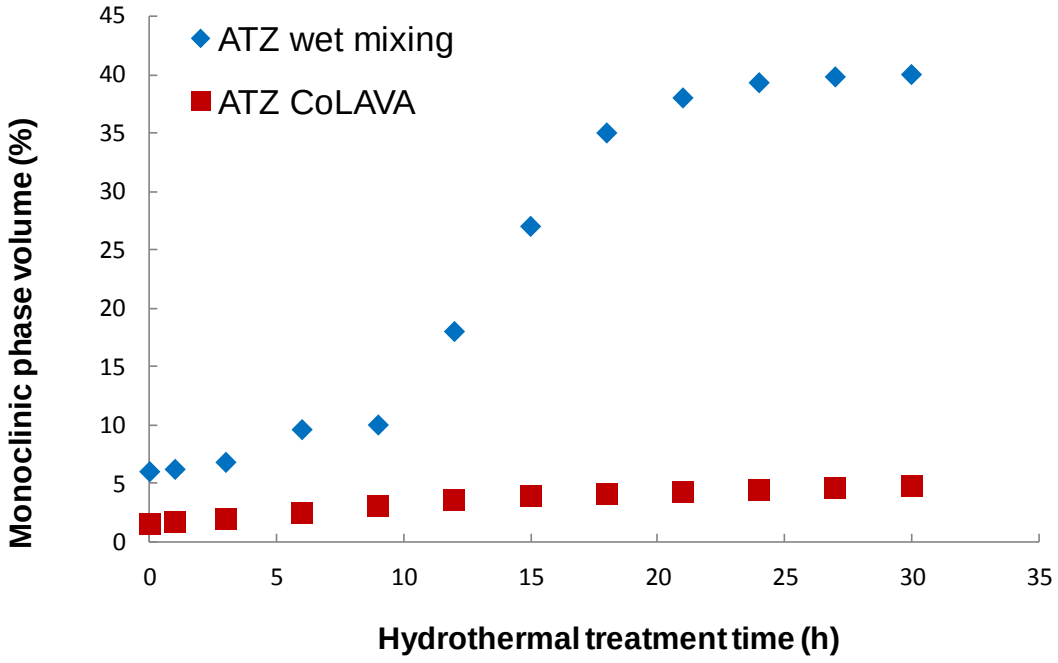

Fig.5.2-9. LTD – evolution of the volume fraction of monoclinic transformed zirconia in dependence of the aging treatment time

However, a very limited ageing was observed for Al_2O_3/ZrO_2 ceramics derived from the CoLAVA powder. There are several factors that might retard the degradation: The gas phase condensation of the CoLAVA nanoparticles proceeds fast and far from thermodynamic equilibrium. Hence, alumina is incorporated into zirconia during their co-condensation resulting in the formation of the defect structure $Zr_{(1-x)}Al_xO_{(2-x/2)}$. Even after sintering some Al^{3+} remain dissolved in zirconia. These Al^{3+} ions now directly stabilize the tetragonal structure of zirconia instead of the Y^{3+} ions. Furthermore, Al_2O_3 that was initially dissolved segregates at the zirconia grain boundaries during sintering. Thus, it can effectively contribute to the improved degradation resistance as it was observed for Al_2O_3

doped Y-TZP ceramics [37]. Additionally, the homogeneously distributed alumina grains act as a constraint to the zirconia grains, retaining t-ZrO_2 in a metastable state and making the material highly resistant to hydrothermal degradation.

5.3 ZIRCONIA/ALUMINA – TANTALUM (ATZ/Ta) SYSTEM

5.3.1 Raw materials, processing, fabrication and characterization

Previously fabricated ATZ CoLAVA powder (Chapter 5, Section 5.2.2) and lamellar Ta metal particles (Chapter 3, Section 3.1.3.1) were wet mixed (Chapter 3, Section 3.1.3.2) and subsequent sintered by SPS at 1400 °C under applied pressure of 80 MPa in vacuum (Chapter 3, Section 3.1.4.3). The sintered specimens had diameters of 20 and 50 mm with a thickness of 2 – 4 mm. Microstructural investigations of this novel ATZ/20 vol.% Ta sintered composite was carried out using a SEM microscopy (Chapter 3, Section 3.1.5.3). Materials' mechanical properties test methods are referred to the Chapter 3, Section 3.1.5.6. LTD behaviour of composite was investigated as well (Chapter 3, Section 3.1.5.8). Earlier obtained 3Y-TZP/Ta composite (Chapter 3, Section 3.2.3), 2Y-TZP LAVA ceramic (Chapter 4, Section 4.2), and ATZ CoLAVA (Chapter 5, Section 5.2) composite were used as reference materials.

5.3.2 Results and discussion

5.3.2.1 Microstructural characterization

An electron scanning micrograph of typical fracture surface from specimen broken during flexural strength is shown in Fig.5.3-1. Grey phase is zirconia, black is alumina and elongated inclusion is tantalum. Analyses of the post-mortem fracture surfaces reveal that failure mechanisms were complete or partial plastic deformation and debonding of lamellar tantalum particles.

It is important to mention that no difference has been found between the ceramic matrix grain sizes of the ATZ CoLAVA (Chapter 5, Section 5.2.6.4.2) and ATZ CoLAVA/Ta

composites. Consequently, the presence of the tantalum particles has not affected grain growth of ceramic.

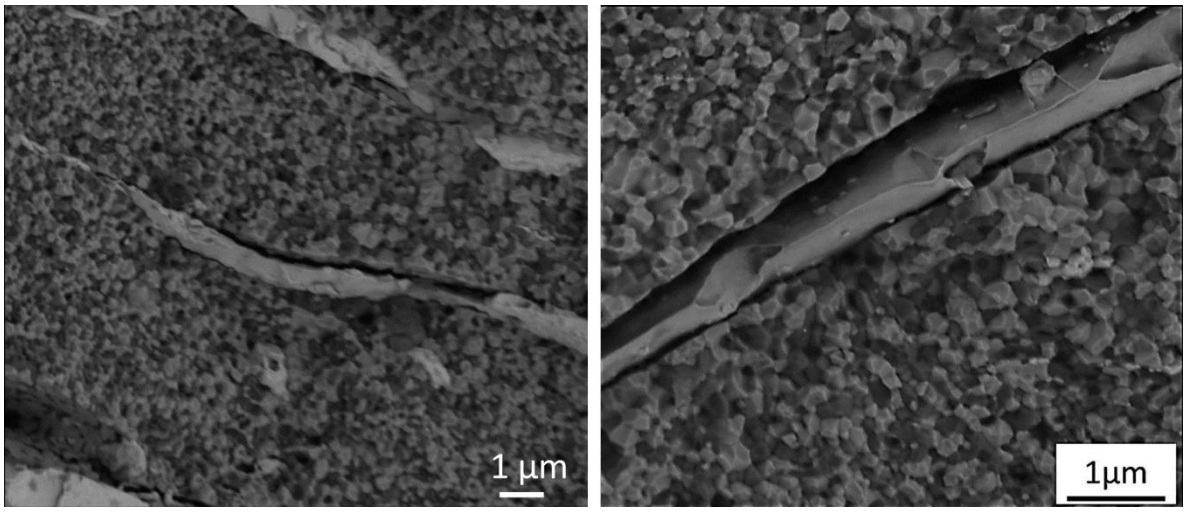

Fig.5.3-1. SEM micrographs of the fracture surface of micro-nano biocomposite

5.3.2.2 Mechanical properties

The mechanical properties of studied materials are presented in Table 5.3-1. A maximum values of flexural strength and Vickers hardness were obtained for ATZ composite (Chapter 5, section 5.2.6.4.3). However the highest values of fracture toughness corresponded to ATZ/Ta composite. Crack bridging and plastic deformation of the ductile Ta phase are two phenomena by which the energy of crack propagation during failure is absorbed. This could enhance crack deflection and bridging as well as stress relaxation near the crack tip and become the primary source of the increased toughness.

Table 5.3-1. Densities and mechanical properties of the ceramic and ceramic-metal specimens sintered by SPS from the 2Y-TZP, ATZ, and ATZ/Ta powders as well as volume fractions of tetragonal (t) and monoclinic (m) zirconia in polished and fractured surfaces of the specimens and the resulting transformability of tetragonal zirconia

Specimen	Density [% φ_{th}]	Elastic modulus E [GPa]	Flexural strength σ_f [MPa]	Hardness HV [GPa]	Fracture toughness K_{Ic} [MPa m$^{1/2}$]	Volume fractions of t- and m-ZrO_2 [vol%]				Transformability of t-ZrO_2 V_{trans}
						Polished		Fractured		
						t	m	t	m	
3Y-TZP/Ta*	98	194	970±18	9±0.7	16±0.9	94	6	77	23	17
2Y-TZP**	99	194	1380±70	11.6±0.1	13±0.3	93	7	16	84	77
ATZ***	99	279	1500± 30	14.9±0.3	6.8±0.2	98	2	64	36	34
ATZ/Ta	98	256	1300±70	10.4±0.4	17±1	95	5	28	72	33

*Chapter 3, section 3.2.3 ** Chapter 4, section 4.2.7.3.2 ***Chapter 5, section 5.2.6.4.3

The transformability of ATZ/Ta composite is 33% higher than in ATZ and only 10% lower than in case of 2Y-TZP monolithic zirconia (Table 5.3-1). As discussed earlier, tantala is strong destabilizer which enhances the transformability of zirconia matrix and additional resource of the enhanced fracture toughness (Chapter 3, Section 3.2.1). At the same time addition of Al_2O_3 levels off the influence of Ta_2O_5 solid solution on the transformability of 2Y-TZP matrix and allows to avoid the spontaneous transformation of zirconia in ceramic-metal composite (Chapter 4, Section 4.3). Therefore, the interactions between t→m transformation of zirconia and crack bridging of metal particles causes the increase of the average fracture toughness of ATZ/Ta composite to values as high as 16 ± 0.3 MPa·m$^{1/2}$ that is in the same range of 3Y-TZP/Ta composites' values.

5.3.2.3 Low temperature degradation

The monoclinic ZrO_2 phase content measured by XRD as a function of the increasing hydrothermal treatment time on the surface of ATZ/Ta composite are presented in Fig.5.3-2.

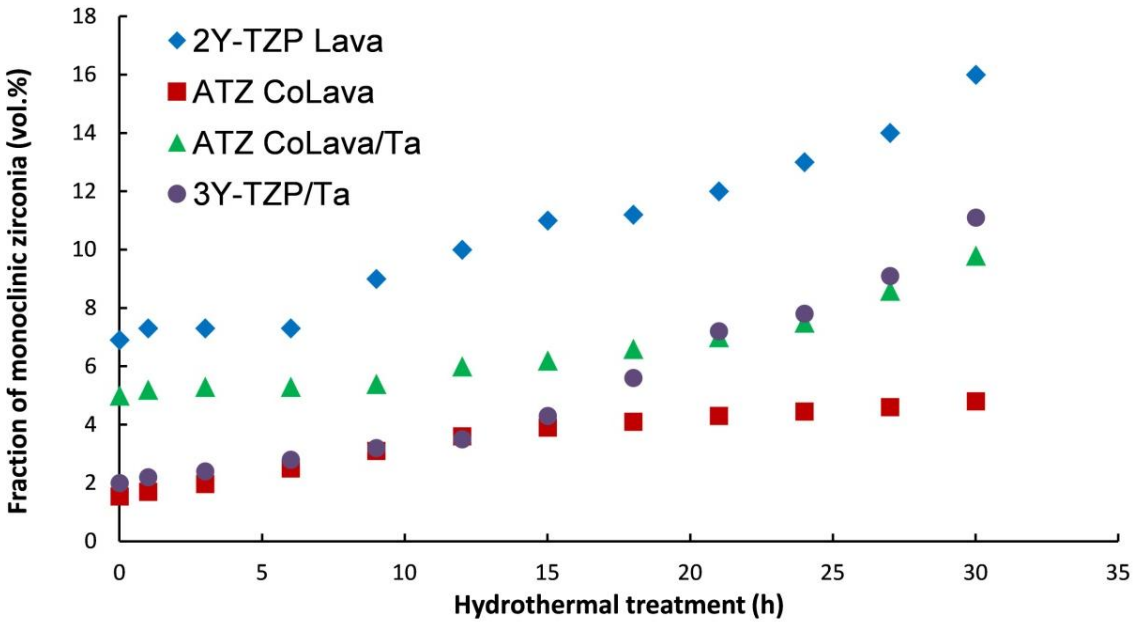

Fig.5.3-2. X-ray diffraction data of monoclinic-transformed zirconia as a function of the aging treatment time for all studied materials

At the beginning of the aging process the polished surfaces of the 3Y-TZP/Ta, 2Y-TZP, ATZ and ATZ/Ta composition contained about 2%, 7%, 2% and 5% monoclinic zirconia, respectively. With increasing aging time the monoclinic volume fraction slightly increasing. At the end of the experiment (after 30 h at 134 °C) the content of the monoclinic phase in the 3Y-TZP/Ta, 2Y-TZP, ATZ and ATZ/Ta composition increased to 11%, 16%, 4.8% and 10%, respectively. ATZ/Ta composite showed little enhancement resistance to LTD than 3Y-TZP/Ta, but for up to 18 h of aging the amount of transformed zirconia was negligible lower in 3Y-TZP/Ta material than in the ATZ/Ta composite.

5.4 SUMMARY

5.4.1 Zirconia/Alumina (ATZ) system

The mechanical properties of ZrO_2/Al_2O_3 dispersion ceramics were considerably increased by reducing the corresponding grain sizes and by increasing the homogeneity of the phase dispersion. In this study, $Zr_{x-1}(Al_x)O_{2-x/s}/(\gamma,\delta)Al_2O_3$ nanoparticles were prepared by a laser induced gas phase condensation process, then sintered resulting an intra-particular phase distribution. During subsequent spark plasma sintering the zirconia defect structures and transition alumina phases transfer to a homogeneously distributed dispersion of tetragonal ZrO_2 (52.4 vol. %) and α-Al_2O_3 (47.6 vol. %). Outstanding mechanical properties (σ = 1500 MPa, K_{Ic} = 6.8 $MPam^{1/2}$) together with a high resistance against low temperature degradation make these materials promising candidates for next generation bioceramics in total hip replacements and for dental implants. This high strength value was attributed to comparatively small sizes of the ZrO_2 (216 nm) and Al_2O_3 (270 nm) grains and a very homogeneous distribution of the dispersed phases after sintering.

The obtained results suggest that for CoLAVA nanopowder derived Al_2O_3/ZrO_2 dispersion ceramics a further yttria stabilization could be omitted because the t-ZrO_2 phase is stabilized by the incorporation of Al^{3+} ions in addition to strain effects of the alumina matrix due to the homogeneous distribution of the alumina and zirconia grains and their narrow size distribution.

5.4.2 Zirconia/Alumina – Tantalum (ATZ/Ta) system

New zirconia-alumina-Ta hierarchical micro-nano biocomposites were successfully fabricated using advanced powder processing technique (i.e., CoLAVA) and consolidated using SPS. It was shown that this ceramic-metal composite with nanostructured matrix

reinforced with lamellar metallic particles exhibit a high value of toughness (16 MPa·$m^{1/2}$) and strength (1300 MPa). It can be concluded that the large toughness values found in new multi-scale composites are a consequence of the strong interaction between the transformation of zirconia and bridging mechanisms of metallic particles. In addition, the zirconia-alumina-tantalum composite has low susceptibility to low temperature degradation. Because of its outstanding mechanical properties and phase stability, we consider this composite to be an excellent alternative for medical implants.

5.5 REFERENCES

[1] Chevalier J, Gremillard L. Ceramics for medical applications: A picture for the next 20 years. *J. Eur. Ceram. Soc*., 2009; 29:1245-1255.

[2] Kirsten A, Begand S, Oberbach T, Telle R, Fischer H. Subcritical crack growth behavior of dispersion oxide ceramics. *J.Biomed. Mater. Res. B* 2010; 95:202-210.

[3] Vasylkiv O, Sakka Y, Skorokhod VV. Low-temperature processing and mechanical properties of zirconia and zirconia–alumina nanoceramics. *J Am Ceram Soc.,* 2003; 86:299–304

[4] Nevarez-Rascon A, Aguilar-Elguezabal A, Orrantia E, Bocanegra-Bernal M. On the wide range of mechanical properties of ZTA and ATZ based dental ceramic composites by varying the Al_2O_3 and ZrO_2 content. *Int. J Refract Met H.*,2009; 27:962-970.

[5] Sommer F, Landfried R, Kern F, Gadow R. Mechanical properties of zirconia toughened alumina with 10–24 vol% 1.5 mol% Y-TZP reinforcement. *J. Eur. Ceram. Soc.,* 2012; 32:3905-3910.

[6] Tang D, Lim HB, Lee KJ, Lee CH, Cho WS. Evaluation of mechanical reliability of zirconia-toughened alumina composites for dental implants. *Ceram. Int.*,2012; 38:2429-2436.

[7] Zhan GD, Kuntz J, Wan J, Garay J, Mukherjee AK. A Novel Processing Route to Develop a Dense Nanocrystalline Alumina Matrix (< 100 nm) Nanocomposite Material. J. *Am. Ceram. Soc.,* 2003; 86:200-202.

[8] Deville S. *et al.* Microstructural Investigation of the Aging Behavior of (3Y-TZP)-Al_2O_3 Composites. *J. Am. Ceram. Soc.,* 2005; 88:1273-1280.

[9] Kurland HD. *et al.* Preparation and process integrated surface modification of spherical titania nanoparticles by CO_2 laser evaporation. *J. Am. Ceram. Soc.,* 2010; 93:1282-1289.

[10] Boumaza A. *et al.* Transition alumina phases induced by heat treatment of boehmite: An X-ray diffraction and infrared spectroscopy study. *J. Solid State Chem.*, 2009; 182:1171-1176.

[11] Macedo MIF, Bertran CA, Osawa CC. Kinetics of the γ - to α -alumina phase transformation by quantitative X-ray diffraction. *J. Mater. Sci.*, 2007; 42:2830-2836.

[12] Lakiza SM, Lopato LM. Stable and metastable phase relations in the system alumina–zirconia–yttria. *J. Am. Ceram. Soc.*, 1997; 80:893-902.

[13] Pach L, Roy R, Komarneni S. Nucleation of alpha alumina in boehmite gel. *J. Mater. Res.*,1990; 5:278-285.

[14] Wen HL, Yen FS. Growth characteristics of boehmite-derived ultrafine theta and alpha-alumina particles during phase transformation. *J. Cryst. Growth.*, 2000; 208:696-708.

[15] Wang Y, Suryanarayana C, An L. Phase transformation in nanometer-sized γ -alumina by mechanical milling. *J. Am. Ceram. Soc.*, 2005; 88:780-783.

[16] Dynis FW, Halloran W. Alpha alumina formation in alum-derived gamma alumina. *J. Am. Ceram. Soc.*,1982; 65:442-448.

[17] Chang PL, Yen FS, Cheng KC, Wen HL. Examinations on the critical and primary crystallite sizes during θ - to α –phase transformation of ultrafine alumina powders. *Nano Lett.*, 2001; 1:253-261.

[18] Yen FS, Wang MY, Chang JL. Temperature reduction of θ - to α -phase transformation induced by high-pressure pretreatments of nano-sized alumina powders derived from boehmite. *J. Cryst. Growth*, 2002; 236:197-209.

[19] Bagwell RB, Messing GL, Howell PR. The formation of α -Al_2O_3 from θ -Al_2O_3: The relevance of a “critical size” and: Diffusional nucleation or “synchro-shear”? *J. Mater. Sci.*,2001; 36:1883-1841.

[20] Yen FS, Wen HL, Hsu YT. Crystallite size growth and the derived dilatometric effect during θ - to α -phase transformation of nano-sized alumina powders. *J. Cryst. Growth*, 2001; 233:761-773.

[21] Badkar PA, Bailey JE. The mechanism of simultaneous sintering and phase transformation in alumina. *J. Mat. Sci*., 1976; 11:1794-1806.

[22] Legros C, Carry C, Bowen P., Hofmann H. Sintering of a transition alumina: Effects of phase transformation, powder characteristics and thermal cycle. *J. Eur. Ceram. Soc.*, 1999; 19:1967-1978.

[23] Kischkat J. *et al.* Mid infrared optical properties of thin films of aluminum oxide, titanium dioxide, silicon dioxide, aluminum nitride, and silicon nitride. *Appl. Opt.,* 2012; 51:6789-6789.

[24] Folks WR, Ginn J, Shelton D, Tharp J, Boreman G. Spectroscopic ellipsometry of materials for infrared micro-device fabrication. *Phys. Status Solidi C,* 2008; 5:1113-1116.

[25] Kingery WD, Brown HK, Uhlmann DR. Introduction to ceramics. John Wiley & Sons, New York, 1976.

[26] Gevales G. Phase-equilibrium of alumina-zirconia and examination of new phase 99% Al_2O_3-1% ZrO_2 (ε -Al_2O_3). *Ber. Dtsch. Keram.Ges*., 1968; 45:216-219.

[27] Alper AM. Science of ceramics, Vol. 3 [Stewart, G. H. (ed.)] [339] (Academic Press, London, 1967).

[28] Kurland HD, Grabow J, Müller FA. Preparation of ceramic nanospheres by CO_2 laser vaporization (LAVA). *J. Eur. Ceram. Soc*., 2011; 31:2559-2568.

[29] Balmer ML, Lange FF, Levi CG. Metastable phase selection and partitioning for $Zr_{(1-x)}Al_xO_{(2-x/2)}$ materials synthesized with liquid precursors. *J. Am. Ceram. Soc.,* 1994; 77:2069-2075.

[30] Inamura S. *et al.* Formation and hot isostatic pressing of ZrO_2 solid solution in the system ZrO_2-Al_2O_3. *J. Mater. Sci.,* 1994; 29:4913-4917.

[31] Suffner J, Wang D, Kübel C, Hahn H. Metastable phase formation during flame spray pyrolysis of ZrO_2 (Y_2O_3)–Al_2O_3 nanoparticles. *Scripta Mater.,* 2011; 64:781-784.

[32] Müller E. *et al.* Zirconia-alumina nanoparticles prepared by laser evaporation: Powder characterisation by TEM and Al MAS NMR. *Part. Part. Syst. Charact.*, 2002; 19:169-175.

[33] Kim M, Laine RM. Liquid-feed flame spray pyrolysis (LF-FSP) for combinatorial processing of nanooxide powders along the $(ZrO_2)1-x(Al_2O_3)x$ tie-line. Phase segregation and the formation of core-shell nanoparticles. *J. Ceram. Proc. Res.*, 2007; 8:129-136.

[34] Smirnov A, Kurland HD, Grabow J, Müller FA, Bartolomé JF. Microstructure, mechanical properties and low temperature degradation resistance of 2Y/TZP ceramic materials derived from nanopowders prepared by laser vaporization. *J. Eur. Ceram. Soc.*, 2015; 35:2685-2691.

[35] Deville S. *et al.* Low-temperature ageing of zirconia-toughened alumina ceramics and its implication in biomaterial implants. *J. Eur.Ceram. Soc.*, 2003; 23:2975-2982.

[36] Pecharroman C. *et al.* Percolative Mechanism of Aging in Zirconia-Containing Ceramics for Medical Applications. *Adv. Mater.*, 2003; 15:507-511.

[37] Zhang F. *et al.* Y-TZP ceramics with improved hydrothermal degradation resistance and fracture toughness. *J. Eur. Ceram. Soc.*, 2014; 34:2453-2463.

6

Biocompatibility of 3Y-TZP/Tantalum cermets

6.1 INTRODUCTION

The chemical, physical and mechanical characterization of all materials intended to be used in biomedical applications is essential, but the evaluation of other different aspects such as their behaviour in the biological environment or biocompatibility is also crucial; the improvement of mechanical properties of an implantable device would be useless if it does not possess a suitable biocompatibility once implanted. There are many reports about the *in vitro* and *in vivo* biocompatibility of ZrO_2 and Ta in their monolithic form [1-7], but the biological response to ZrO_2/Ta composites has never been studied yet. Thereby, the aim of this chapter is *in vitro* and *in vivo* evaluation of a novel 3Y-TZP/Ta biocermets for hard tissue replacement.

6.2 *IN VITRO* STUDY

As animal cells are in a complex dynamic environment in the whole animal (*in vivo*), their regulatory processes are more readily examined in a more simplified external environment (*in vitro*). Animal cells that are removed from the body can be maintained (or cultured) for prolonged periods in an appropriate environment [8]. The cell culture approach treats mammalian cells virtually like bacterial cultures and this allows to study the cells' intrinsic functions like adhesion, migration, proliferation, differentiation, matrix synthesis, and death; as well as their interactions with each other and with their environment [9, 10]. These studies were carried out at the Health Research Institute of Santiago (Santiago de Compostela, Spain) by Dr. Ramiro Couceiro Otero.

6.2.1 Materials

Dense SPS sintered zirconia/tantalum composites with 20 vol. % of Ta developed in Chapter 3, Section 3.2.3 were used in this investigation. Commercial available 20 mm of diameter and 50 mm of length pure Tantalum rod (TA007950, 99.9% purity, Goodfellow, Huntingdon, England) and SPS sintered zirconia (Chapter 3, Section 3.2.3) were used as reference materials.

6.2.2 Microstructure and surface characterization

The microstructure of specimens was studied on surfaces polished down to 1 μm by tabletop SEM (Chapter 8, Section 8.5.5.1). Roughness measurements of 3Y-TZP/Ta composites were carried out by using surface profilometer (Chapter 8, Section 8.5.9).

6.2.3 Isolation and culture of Human Mesenchymal Stem Cell (HMSCs)

For investigating the cellular responses to the developed biocermet, mesenchymal stem cells derived from human bone marrow were used (hBMSCs). hBMSCs were obtained by the Department of Orthopedic Surgery (University of Santiago de Compostela Clinical Hospital) during routinely hip prosthesis surgeries by ethically approved protocols. Bone marrow was stored in heparin coated tubes and taken to the cell culture laboratory for proceeding with mesenchymal stem cell isolation (Fig.6.2-1). A Ficoll protocol as described by Yeo et al. was used [11]. Briefly, cells are separated through a density gradient where an intermediate band is formed after a 2000 rpm centrifugation. This band is washed with DMEM (10%, Strep, Gibco) centrifuged for a second time and cultured in 75cm^2 flasks (Corning). Cultures are kept at a temperature of 37ºC and 5% CO_2 in an incubator until a 90% confluence is reached. Cells are tripsinised and subcultured on the

surface of the assayed materials at a density of 60 x 10^3 cells/cm^2. Cultured materials are assayed for different parameters after 2, 7 and 10 days.

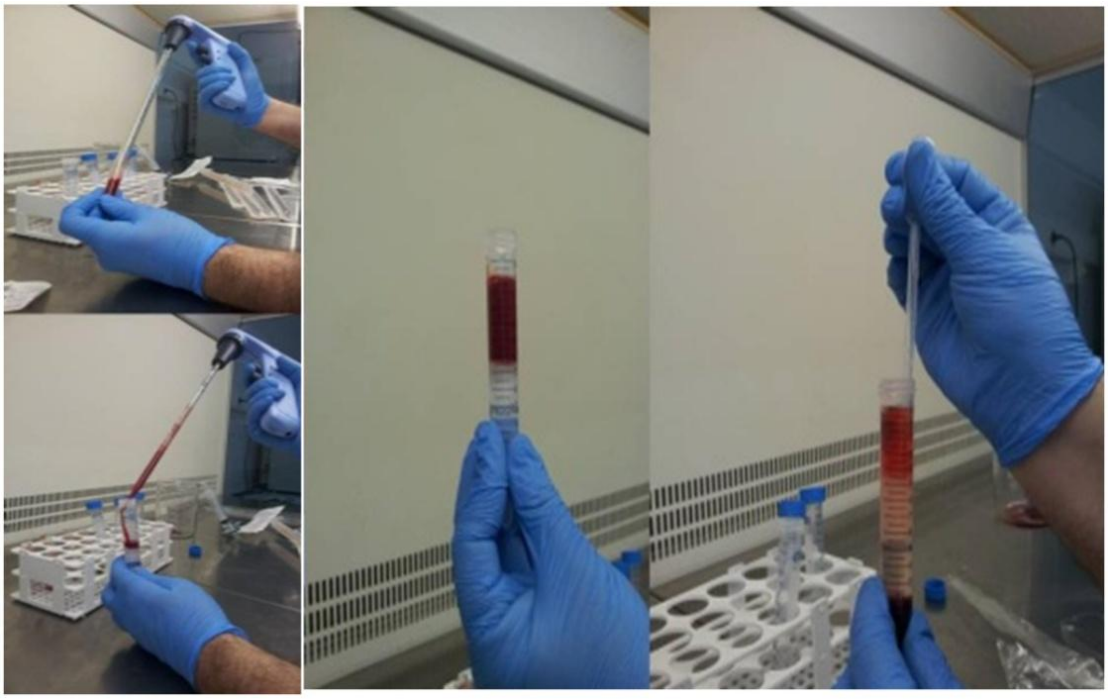

Fig.6.2-1. HMSCs Isolation

6.2.4 Biocompatibility tests

6.2.4.1 Cell Proliferation by MTT assays

The survival and proliferation of hBMSCs on pure tantalum, zirconia and biocermet discs was examined with a colorimetric MTT assay after 2, 7 and 10 days of culture. The MTT assays were carried out as per manufacturer's protocol (Sigma-Aldrich, St. Louis, MO, USA). Briefly, hBMSCs were seeded on the sample discs at a density of 25 x 103 cells per well in a 24-well plate. At each time point, the medium were removed, MTT solution was added, and cells were incubated overnight. After removal of the MTT solution, the purple formazan crystals were dissolved in 100 mL of dimethyl sulphoxide (DMSO) by shaking the plate for 15 min, and 50 mL solution of each well was added into a new 24-well plate.

The optical density value was quantified by measuring the absorption at 570 nm using an automatic plate reader (PerkinElmer, Boston, MA, USA).

6.2.4.2 Apoptosis: caspase activity assay

Caspase-3 activity wasmeasured in supernatants by a Quantikine immunoassay (ELISA) active caspase-3 kit (R&D Systems, Minneapolis, MN, USA). Briefly, cytoplasmic protein extract was incubated with biotin-ZVKD-fluoromethyl ketone inhibitor, which covalently binds and makes detectable the active caspase-3. A monoclonal antibody specific for active caspase-3 was precoated onto a microplate, and active protease concentrations were assessed in cell lysates, according to the manufacturer's instructions.

6.2.4.3 Cell morphology

Cell morphology was assessed under tabletop SEM. Human bone marrow derived mesenchymal stem cells were cultured on metallic Ta, zirconia and biocermet substrates (DMEM+FCS 20%+Gent) at a density of 250 x 103 cell/cm^2. Cultures were kept in a CO_2 incubator for 48 hours (5% CO_2, 37 ºC). After this period, culture media was removed and cells were washed twice with PBS. Immediately after the last wash, a fixing solution (1% Glutaraldehyde , 1% Paraformaldehyde) was added to the culture wells and kept at 25 ºC for 48 h. Once cells were fixed a dehydratation process took place by means of serial dilutions of EtOH.

6.2.4.4 Confocal microscopy. Live/dead staining

Calcein-AM and propidium iodide were used to stain the hBMSCs cultured on the glass ceramic pellets. After 48 h of incubation the samples were gently washed with D-MEM. The viable and non-viable cells were visualized by using a confocal laser scanning

microscope (CLSM-SP2, Leica, Wetzlar, Germany), the viable cells appear fluorescent green, whereas nonviable cells appear fluorescent red.

6.2.5 Statistical analysis

Minitab 16 statistical software (Minitab INC, PA, USA) was used for the statistical data analysis. T-student tests were carried out with an α=0.05.

6.2.6 Results and discussion

6.2.6.1 Microstructure and roughness

Microstructure characterization was presented in Chapter 3 (Section 3.1.5.3). In order to estimate average surface roughness, the samples were analyzed with a 3D surface profilometer (Chapter 8, Section 8.5.9) that maps the surface by putting a stylus in mechanical contact with the sample. Profilometer was used to determine three dimensional surface topographic maps (Fig.6.2-2). The results of average surface roughness (*Ra*) were obtained: 0.01 ± 0.005 µm, 0.05 ± 0.01 µm and 0.12 ± 0.04 µm for 3Y-TZP, Ta and 3Y-TZP/Ta, respectively.

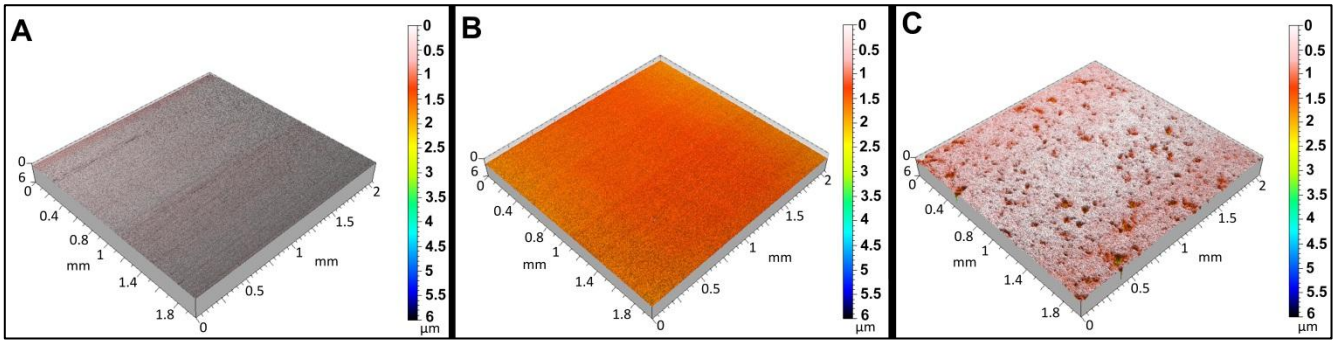

Fig.6.2-2. 3D topographies images of 3Y-TZP (a), Ta (b) and 3Y-TZP/Ta (c) disks

6.2.6.2 *In vitro* cytocompatibility of discs

Mesenchymal cells were chosen in this experiment as it was considered as an important approach for testing the new materials. It is known that a primary cell will not have its cytoskeleton or proliferation patterns modified if compared to cell lines such as SAOS-2 [12].

Proliferation of mesenchymal stem cells to substrates is show in Fig.6.2-3. Cells were plated onto each of the substrates and incubated on the various substrates for 2 days, 7 days or 10 days. MTT assay results are presented as mean ± standard deviation

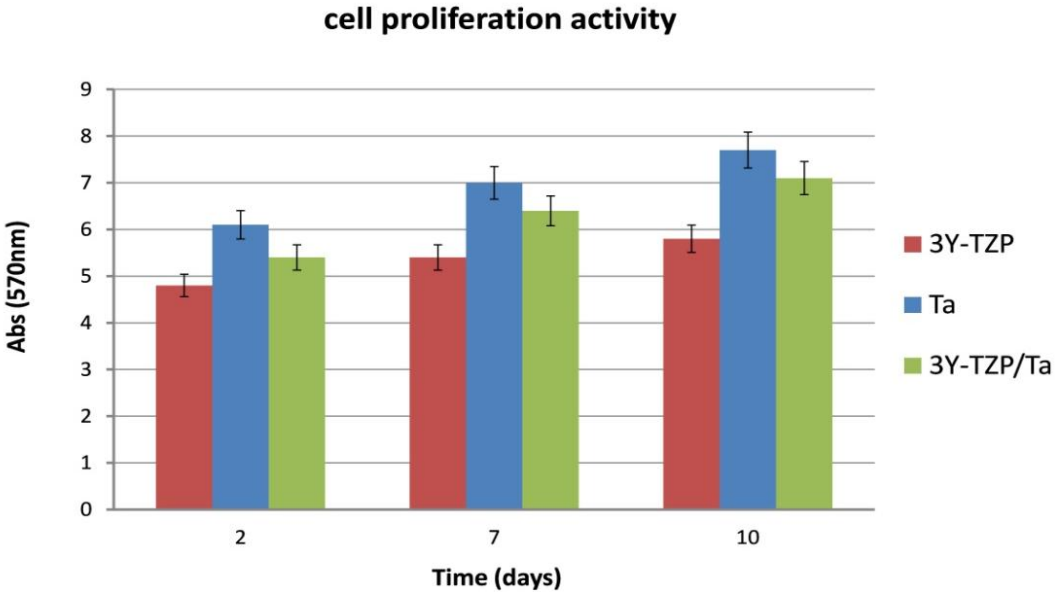

Fig.6.2-3. MTT assay of cells on 3Y-TZP, Ta and 3Y-TZP/Ta substrates after 2, 7 and 10 days of culture

Fig.6.2-3 shows higher cell proliferation for pure Ta and 3Y-TZP/Ta materials than for 3Y-TZP monolithic ceramic, and consequently, more prone for cell colonization. Fig.6.2-4 shows there is a steady increase of Caspase 3 activity in all samples, this is due to the intrinsic apoptosis rate in a culture.

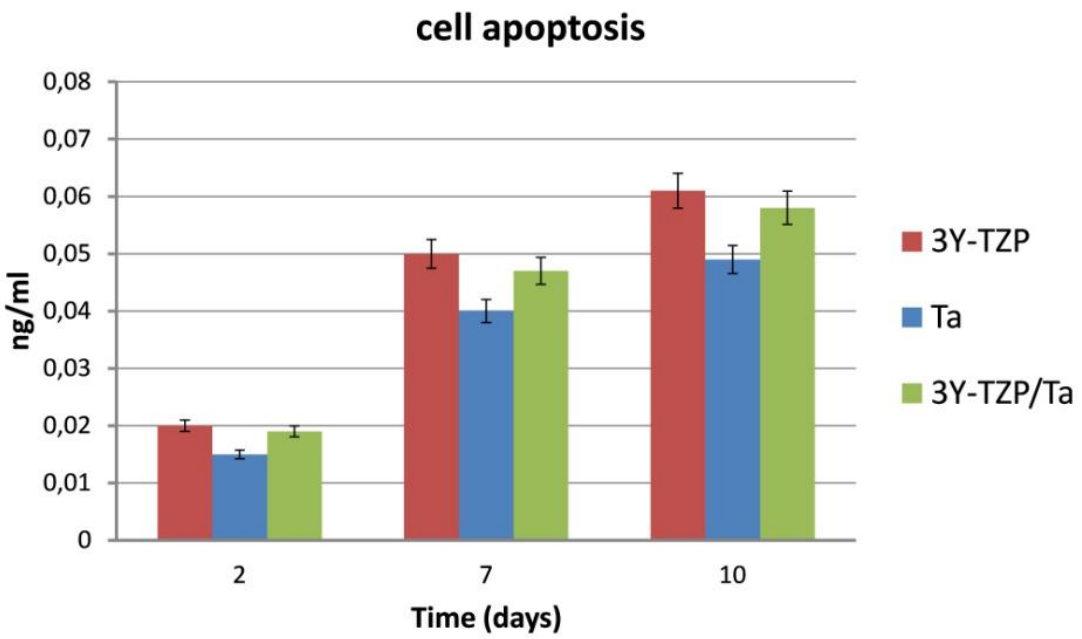

Fig.6.2-4. Caspase assay results for all studied materials

3Y-TZP shows however a somehow larger apoptosis rate for the long term group. Caspase 3 activity is low in both Ta and 3Y-TZP/Ta materials proving the biocompatibility of Ta and the newly described biocermet.

Fig.6.2-5 shows the SEM study of cell morphology after 48 hours of incubation. Cell spreading and proliferation is observed clearly in all the samples.

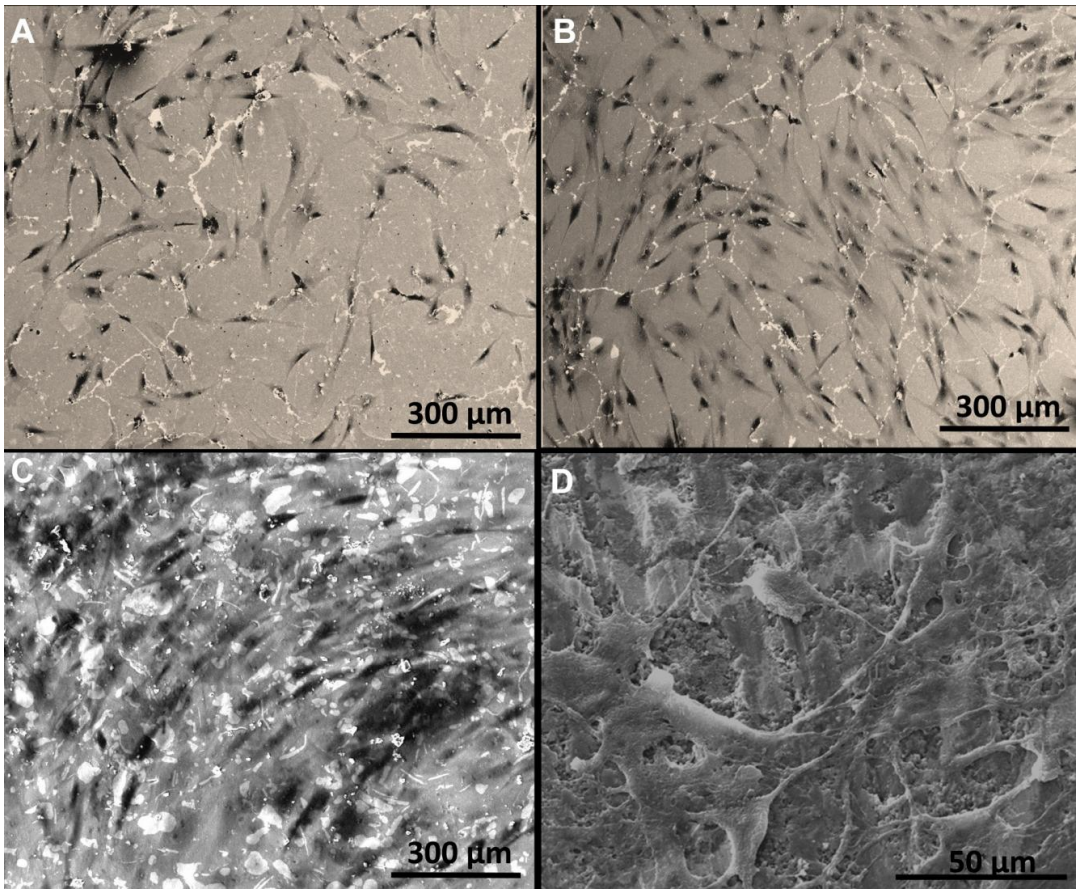

Fig.6.2-5. Scanning electron micrographs of mesenchymal stem cells plated onto the 3Y-TZP (A), Ta (B) and 3Y-TZP/Ta (C,D) substrates

Almost the whole surface is covered with cells at this stage, and a large amount of Extracellular matrix (ECM) is now visible (Fig. 6.2-5D). Human Mesenchymal cell have already undergone through an attachment process and spreading is clearly taking place. The morphology of the cells was not obviously different when adherent to any of the materials and the surface roughness did not markedly influence cell adherence or shape. This might have been expected because all the surfaces were relatively smooth whether polished.

Cell proliferation and viability is optimal for both Ta and 3Y-TZP/Ta surfaces when observed in a confocal microscope (Fig.6.2-6). After 10 days of culture, the biocermet sample appears to show a greater concentration of cells on the surface and even some

alignment patterns. The zirconia samples on the other hand is not as colonized, supporting the observations from the ELISA essays.

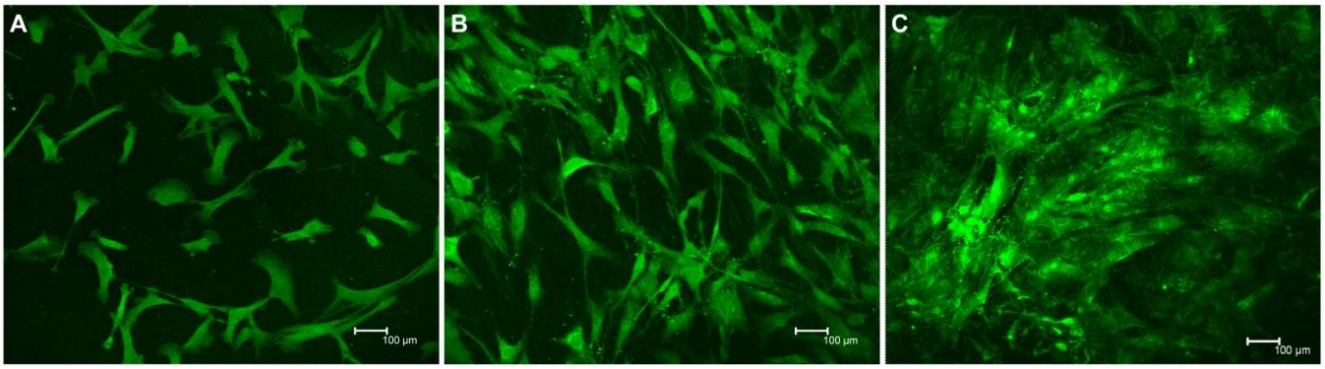

Fig.6.2-6. Confocal laser scanning microscope image of the hBMSCs grown on: A) Zr surface B) Ta and C) 3Y-TZP/Ta surface during culture for 10 days. hBMSCs were stained with green fluorescent calceim-AM

6.3 *IN VIVO* STUDY

The implant surgery in rabbits was carried out in the Instituto de Cerámica de Galicia, Universidad de Santiago de Compostela (Santiago de Compostela, Spain) by Dr. A. Martinez Insúa. The implantation procedure in beagle dog was performed at the Minimally Invasive Surgery Center (Cáceres, Spain) by Dr. Roberto López-Píriz.

6.3.1 Study in rabbits

6.3.1.1 Materials and methods

Details of the starting ceramic and metallic powders and the processing of the composites have been described previously in Chapter 3, Section 3.1.3. Implanted cylinders (∅ 2 mm) were produced from SPS sintered and well-polished 3Y-TZP/Ta ceramic-metal composite by means of diamond drill tool. Cylinders 2 mm in diameter of commercially Tantalum rod (TA007920, 99.9% purity, Goodfellow, Huntingdon, England) were implanted as a reference material as well.

6.3.1.2 Microstructure and surface characterization

The microstructure of sintered specimens was studied on surfaces polished down to 1 µm by tabletop SEM. Roughness measurements of cylinders were carried out by using SEM with the 3D Roughness Reconstruction application (Chapter 8, Section 8.5.5.1). The cut-off filter was 0.03 mm and the evaluation length was 500 µm per measurement. Three samples of each surface type were scanned to evaluate the average surface roughness (*Ra*) of the surfaces at ten different locations. General view, microstructure and roughness measurements (*Ra*) of 3Y-TZP/Ta and Ta cylinders are shown in Fig.6.3-1 and Fig.6.3-2, respectively.

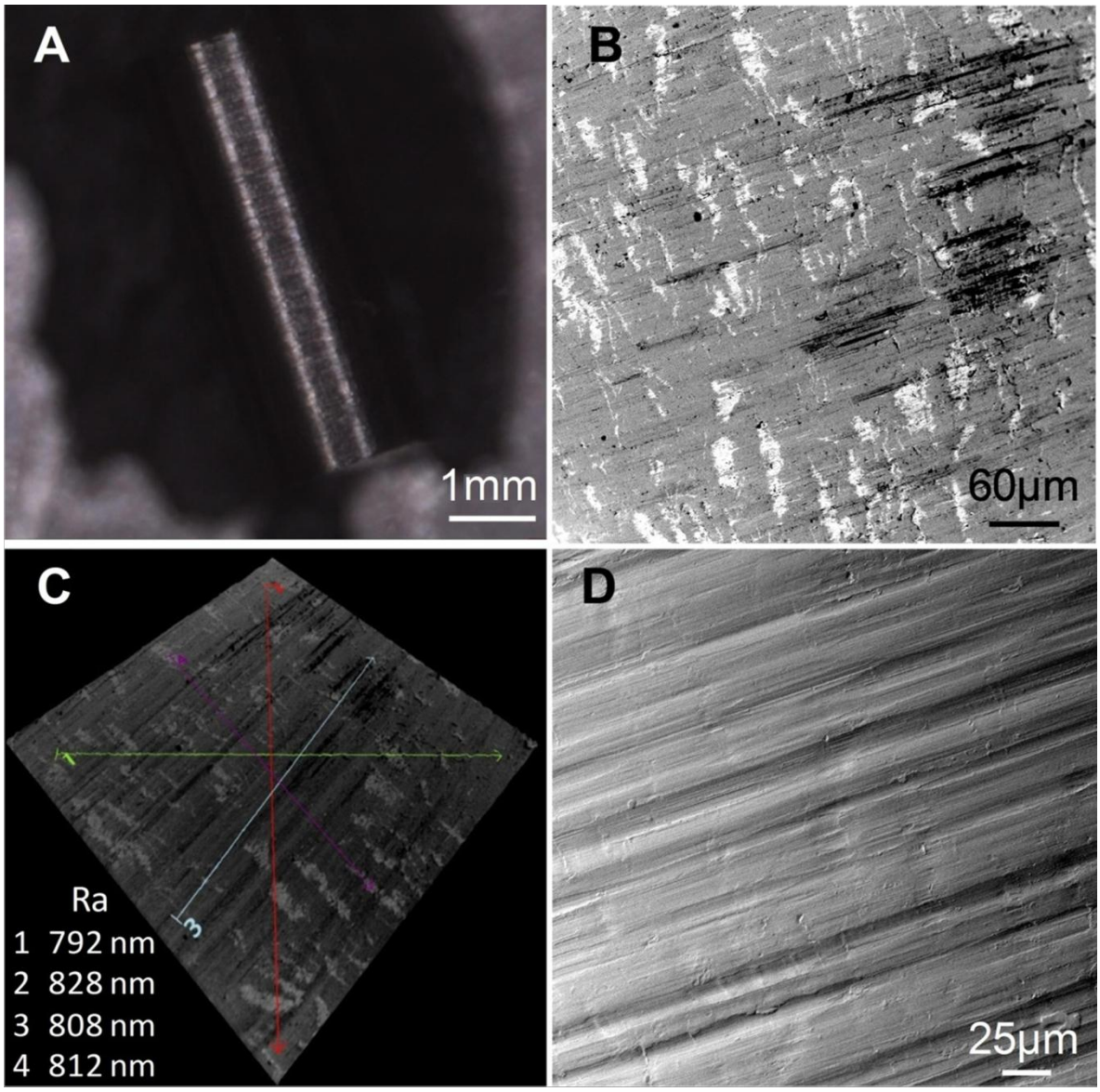

Fig.6.3-1. General view (A), microstructure (B, D) and roughness measurements (C) of 3Y-TZP/Ta cylinders

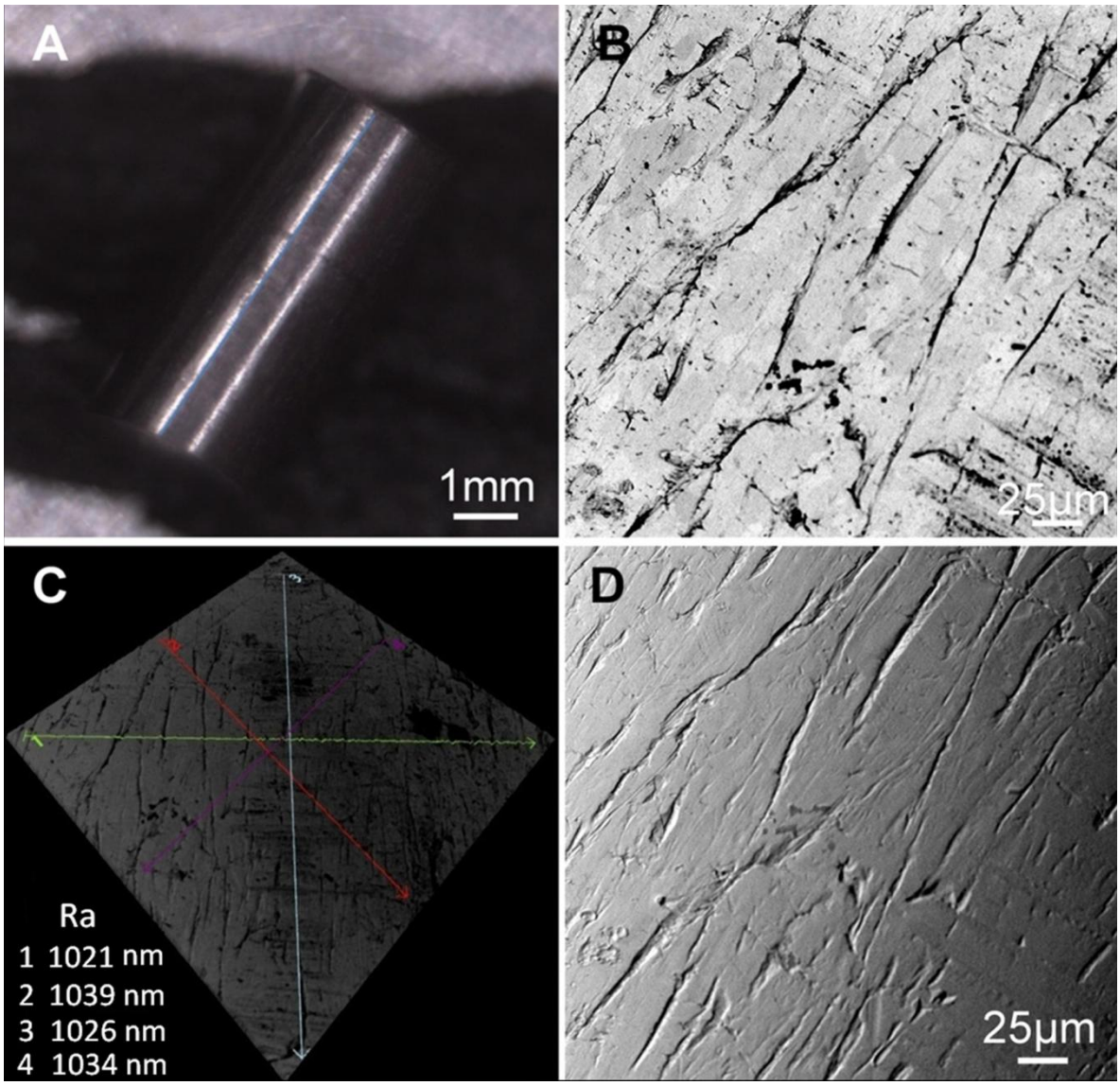

Fig.6.3-2. General view (A), microstructure (B, D) and roughness measurements (C) of Ta cylinders

6.3.1.3 Animals and surgical technique

Biocermet cylinders were placed into each medial proximal tibia of three adult New Zealand white rabbits (Charlie Rivel, France), aged from 9 to 10 months with weight about 3.5 kg (Fig.6.3-3).

Fig.6.3-3. Implantation of cylinders in the medial proximal tibia of New Zealand white rabbits

All animals experiments and procedures were conducted following protocol № 01/2007A that received institutional authorization by Scientific Council of the Institute of Ceramics of Galicia, Santiago de Compostela, Spain (January 26, 2009).

The animals were premedicated with diacepam 0.2 ml/kg (Valium 10, Roche), and anaesthetized with ketamine 10 mg/kg (Imalgene 1000, Merial, Lyon, France) and medetomidina (0.1 mg/kg) (Domitor, Orion, Espoo, Finland) injected intramuscularly in the hind leg. The animal tibialis anterior face was shaved. The skin was disinfected with a povidone-iodine solution 10% (Betadine, Medapharma, San Fernando de Henares, Spain). Infiltrative Articaine (1.5 ml) anesthesia (Ultracain 40/0.005, Normon, Tres Cantos, Spain) was employed injected subcutaneously in the anterior tibialis face. Three cylindrical bars with a length of 5 mm and diameter of 2 mm, were placed in each animal, two in each medial proximal tibia. Surgical preparations for the cylinders were done using first a pilot drill (Precision drill 33071 Nobel Biocare, Barcelona, Spain), and then a 2 mm twist drill (Twist Drill 32296 Nobel Biocare, Barcelona, Spain). Careful drilling was done with a low rotary hand piece (KaVo Intrasurg 300, Madrid, Spain) never exceeding 2000 rpm and

under profuse saline cooling. Metallic bars were placed on the right tibia, while biocermets were placed on the left tibia. All cylinders were more than 10 mm apart. The cylinders were impacted using hammer-impacting method and the surface end was placed floss with bone. The periosteum was sutured with continuous monofilament resorbable suture (3-0 Monocryl, Ethicon, Madrid, Spain). The skin was sutured with interrupted threaded resorbable sutures (Vicryl 3-0, Ethicon, Madrid, Spain). Skin was again soaked with a povidone-iodine solution. After three months, rabbits were euthanized with a lethal dose of ketamine/diazepam injection.

6.3.1.4 Histological preparation and examination

After euthanized the entire tibias were removed and the exact position of the implants was located via radiologic examinations. The tibiae were fixed in buffered formalin (10%) for one week. The size of each sample was reduced by separating the two implants of each tibia. Following Donath and Breuner method [13], dehydration of the samples was achieved by immersion in increasing concentration of alcohol solutions. The samples were infiltrated with Technovit 7200 resin (Kulzer, Madrid, Spain). After photopolymerization of the infiltrated blocks, thin ground slides were obtained. The preparations were dyed with Papanicolau Harris Hematoxyline (Merck, Darmstadt, Germany) and Wheatley's modification of thrichrome stain (Chromotrope 2R, Newcommersupply, Middleton, WI, USA) and preserved with Canada balsam solution (Fluka Biochemika, Alcobendas, Madrid, Spain). Preparations were examined by using a transmitted light microscope (Optiphot, Nikon, Tokyo, Japan) equipped with a digital Camera (DP-12, Olympus, Tokyo, Japan).

6.3.1.5 Histomorphometric evaluation

Histomorphometry was done employing an Olympus SZX12 microscope equipped with a Olympus DP12 camera. Images obtained were processed with image J-1.46r software (NIH, Bethesda, MD, USA) to measure the bone-to-implant contact (BIC) ratio, defined as the proportion of bone in direct contact with the implant surface. When necessary, polarized light microscope was employed to determine the boundaries of the newly formed bone. All measurements were taken by the same investigator and boundaries were revised by a different one. To determine the reproducibility and the measurement error, five randomly selected slides where measured three times, in three different days [14]. BIC evaluations were performed by the eight measurements per cylinder.

6.3.1.6 Statistical analysis

The normality of the histomorphometry data was tested with a K–S test and then with Wilcoxon signed-rank test was employed to compare the means. The statistical package employed was the IBM-SPSS 18.0 (Chicago, IL, USA). The level of significance was set at P=0.05.

6.3.1.7 Results and discussion

6.3.1.7.1 Surface roughness

The machined process resulted in a different mean surface roughness values (*Ra*) between pure tantalum and 3Y-TZP/Ta cylinders. It was found that Ra_{Ta} and $Ra_{3Y\text{-}TZP/Ta}$ cylinders is around 1.03 ±0.2 µm and 0.81 ± 0.1 µm, respectively.

6.3.1.7.2 *In vivo* biocompatibility

The growing status of newborn bones in defective bone region around the implants and the interfacial morphology between the implant and newborn bone was observed by light microscopic as shown in Fig.6.3-4 and Fig.6.3-5 for biocermet and Ta metal, respectively.

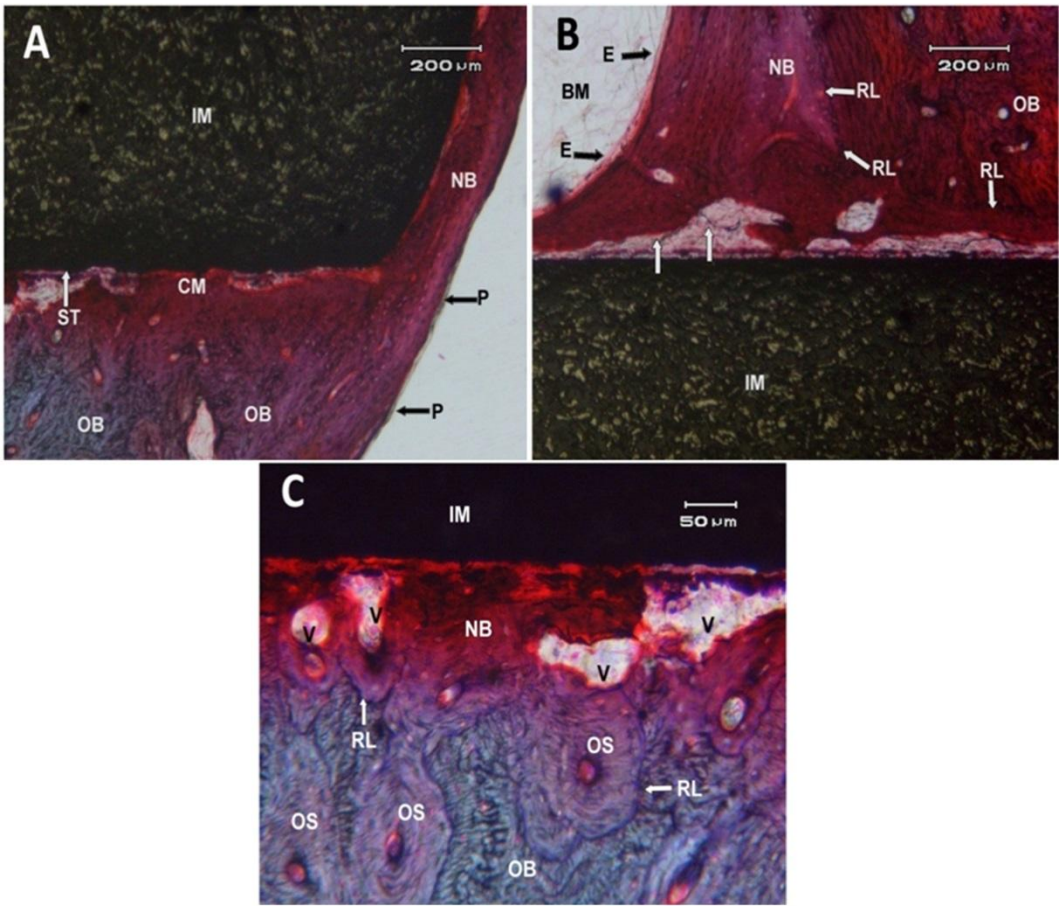

Fig.6.3-4. A) Surface end of the biocermet implant rod (IM). The new bone (NB) formed from the adjacent diaphysal old bone (OB) and from periosteum (P). At the implant-tissue interface the direct contact zones: mineralized (CM) and unmineralized (ST) matrix were observed. B) Surface of the biocermet rod in the entrance of the cavitas medullaris tibiae (BM). The endosteum (E) stimulates formation of new bone (NB) along the surface of the stabilized implant (IM). Cement reversal lines (RL) are recognized between the compact Harvesian old bone (OB) and neoformed bone with lamellar structure with plexiform features. Note: the intense vascularization of the new bone coming from the adjacent diaphysal old bone (OB). The lack of mineralization in some points at interface was observed (vertical white arrows) C) Close-up of the bone-implant interface. Note: bone remodeling (NB) in bone-implant contact proceeds with vascular structures (V) and separated from Haversian systems (osteons) (OS) of old bone (OB) by cemental lines (RL)

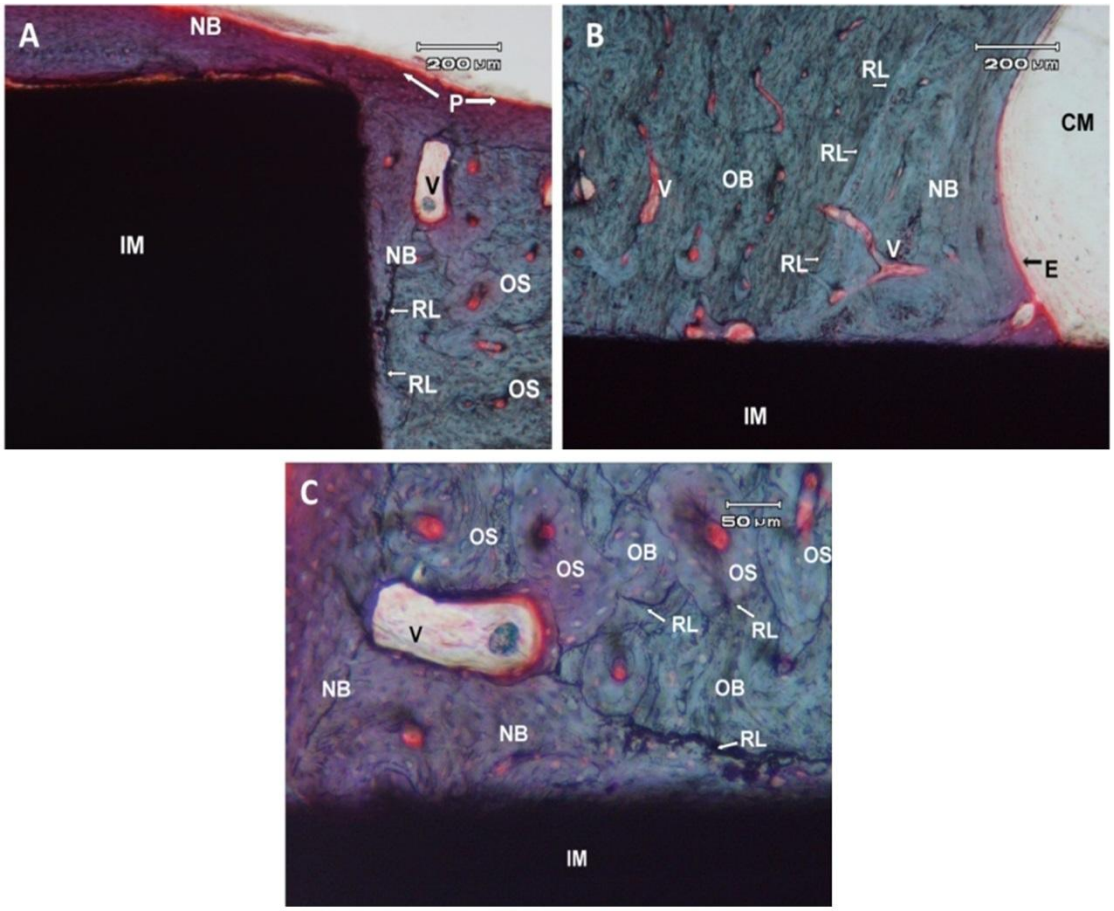

Fig.6.3-5. A) Surface end of a Tantalum rod (IM). New bone (NB) formation was seen from the periosteal (P) antero-internal surface of the diaphysis of the tibia. Old compact bone consisting of Haversian structure (OS), vascular space (V) and cemental lines (RL) were observed. B) Interphase zone of the Implant (IM) at the cavitas medullaris (CM). Cemental line (RL) separates endosteal (E) new bone formation (NB) from compact old bone (OB). Note the new-vascularization passing through the cemental lines (V). C) Close-up of the bone-implant interface shows close apposition of neoformed bone (NB) highly vascularized (V) to the implant surface. Cemental lines (RL) as boundaries between the old (OB) and new bone (NB) and between Haversian systems (OS) of old bone (OB) as well

Histological observations after three months of the implantation show that some immature newborn osteons could be found in new bone (NB) regions for both materials, biocermet and pure Ta metal as shown in Fig. 6.3-4C and Fig. 6.3-5C. These new bone tissues can contact directly with the Ta metal and biocermet and no fibrous tissue was observed at the interface between the implants and new bones. No inflammatory response was observed in

the histological examination of these implants. The complete stabilization of the biocermet cylinder in the tibial diaphysis is observed (Fig.6.3-4). The superficial end and apical end of the implant is totally covered by neoformed bone. Moreover, the implanted cylinder shows also osteoconductive properties because some of new formed bone grows from the endosteum on the implant surface. However, this newly formed bone show irregular lamellae structure. At the bone/implant interface neoformed bone shows immaturity and lower structuring. The osteocyte lacunae are occupied by typical osteocytes cells, but present nonuniform distribution around the neoformed vascular strucrures close to the implant. This difference reduces contact area between implant and mineralized matrix interface and, consequently, produces immaturity of the newly formed bone. Inflammatory response could not be seen in any part of the preparations and the implant surface is well tolerated for the bone marrow found in the medullary cavity.

A continuous apposition of mineralized bone matrix in direct contact with the tantalum rod surface was clearly observed (Fig.6.3-5). Stabilization of tantalum implant in diaphysis of the tibia is due to close contact between surfaces of compact bone and metal rod. The new formed bone occupies scar tissue around an implant contact zone and shows highly vascularized plexiform structure appeared from old bone, periosteum and endosteum. The newly formed bone covers the surface end and the apical end of the rod. New bone layers, formed from the endosteum, stabilizes the implant through the cavitas medullaris. This bone is highly vascularized and have woven and lamellar structure. In the implant contact are, neoformed bone has a low degree of mineralization Cement lines delineate the boundaries of new formed bone. Osteocytes occupying lacunae show uniform distribution at the bone/implant interface. Evidence of atypia and dysplasia or interposition of inflammatory tissue or connective tissue at the interface were not observed. Bone marrow is

strongly vascularized and in close contact with the implant without signs of inflammatory response.

The amount of bone and bone-to-implant contact area was higher for the tantalum metal rod compared to the biocermet. The mean contact index (BCI) presented the following values: biocermet: 55.3 ± 6.3 and tantalum rod: 80.4 ± 5.2, with a significant difference between the groups for $p<0.04$. The high BCI values of tantalum rod verify the result obtained in vitro and consequently confirm the outsanding biocompatibility of tantalum metal. On the other hand, the value obtained for biocermet is in good agreement with values reported for zirconia-niobium system [15]. Therefore it could be found that 3Y-TZP/Ta biocermet is a biocompatible material that can be osteointegrated.

6.3.2 Study in dogs

For present research the SPS sintered 3Y-TZP/Ta composites were used (Chapter 3, Section 3.1.4.3). The samples were prepared in the form of cylinders of ~ 2 mm diameter from well-polished disks by means of diamond drill tool.

6.3.2.1 Animal Study Design

One year old Beagle dog (12-15 kg) was purchased from Minimally Invasive Surgery Centre, Caceres, Spain. The study protocol was approved by their Ethics Committee for Animal Research Welfare. The outline of the experiment is presented in Fig.6.3-6.

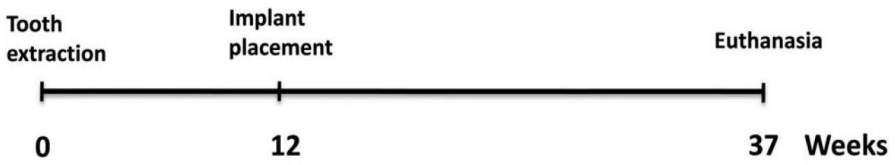

Fig.6.3-6. Outline of the study

During all procedures veterinary assistance was mandatory. General anesthesia was induced with intravenous injected propofol 10 mg/kg (Propofol Hospira, Hospira Productos Farmaceuticos y Hospitalarios, Madrid, Spain). A n°7 endotracheal tube with a balloon cuff was placed and connected to a circular anesthesia circuit (Leon Plus, Heinen & Löwenstein, Bad Ems, Germany). The anesthesia was sustained with sevofluorane (Sevorane, Abbott Laboratories, Madrid, Spain). Multimodal analgesia was employed in the perioperative (ketorolac 1 mg/kg (Toradol 30 mg, Roche); - tramadol 1.7 mg/kg (Adolonta inyec., Grünenthal); y – buprenorfine 0,01 mg/kg (Buprex, Reckitt Benckiser Pharmaceuticals Limited, Berkshire, UK). All mandibular premolars and the first molar were extracted. After three months of healing cylinders were installed in the edentulous region on both sides of the mandible (Fig.6.3-7).

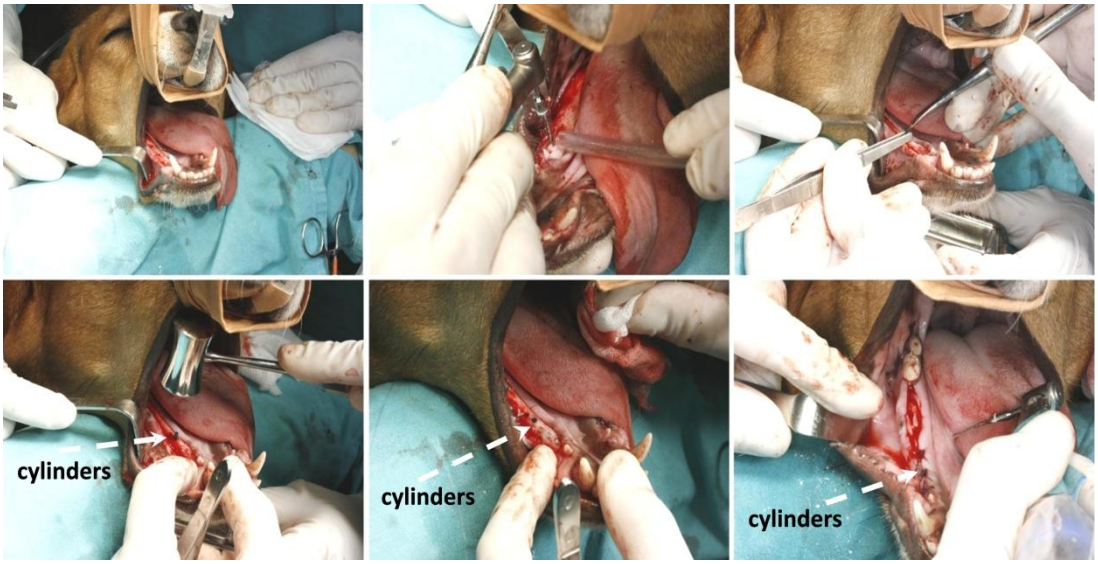

Fig.6.3-7. Implantation of cylinders in the mandible of beagle dogs

A total of 10 implants were placed in one dog. During this period animal was feed with a soft diet. After 6 months animal was euthanized with a lethal dose of Sodium-Penthotal®.

6.3.2.2 Histological preparation and examination

Mandibular blocks containing implants were retrieved from the jaw bone using an

oscillating autopsy saw (Exakt, Kulzer, Germany) and stored in a 5% formaldehyde solution (pH 7). The position of the implants was located via radiologic examinations (Fig.6.3-8).

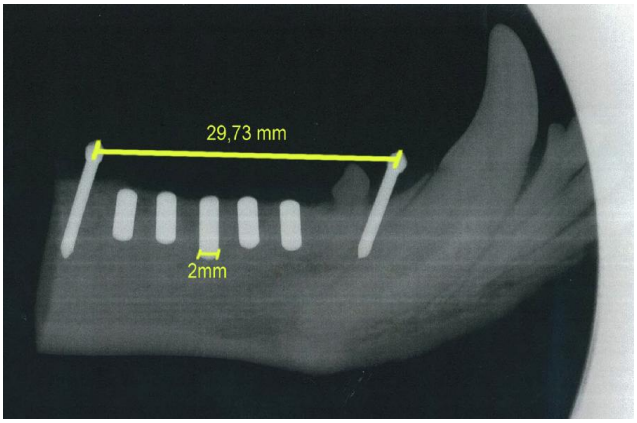

Fig.6.3-8. X-Ray of mandibular block with implanted cylinders

The dissected specimens were immediately immersed in a solution of 4% formaldehyde and 1% calcium and processed for ground sectioning following the Donath & Breuner methods [13]. Each implant block was individualized, embedded in methyl-methacrylate and stained with combined Harris Haematoxyline and Wheatley. Two central bucco-lingual ground slides of about 25 mm were obtained from each implant. The histological analysis was performed by using a transmitted light microscope (Optiphot, Nikon, Japan) equipped with a digital camera (DP-12, Olympus, Japan).

6.3.2.3 Results and discussion

Radiographic examination shows that implants have integrated with the surrounding bone (Fig.6.3-9). Moreover, in radiological analysis no signs of lack of osseointegration around implants after six months implantation appear. The *in vivo* tests have clearly show a perfect osseointegration after six months of implantation without any sign of inflammation.

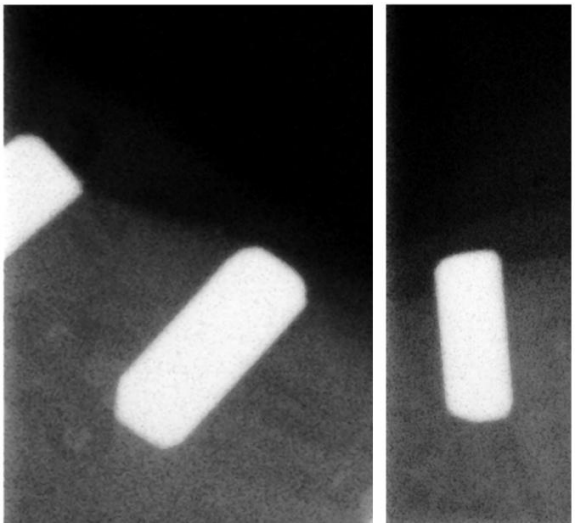

Fig.6.3-9. X-Ray of implanted cylinders after six month of implantation

Histological observations after six months of the implantation show that some immature newborn osteoids could be found in LB and BB regions (Fig.6.3-10). These new bone tissues can contact directly with the composite and no fibrous tissue was observed at the interface between the implants and new bone. No inflammatory response such as the presence of foreign body giant cells and infiltration of inflammatory cells were observed in the histological examination of these implants.

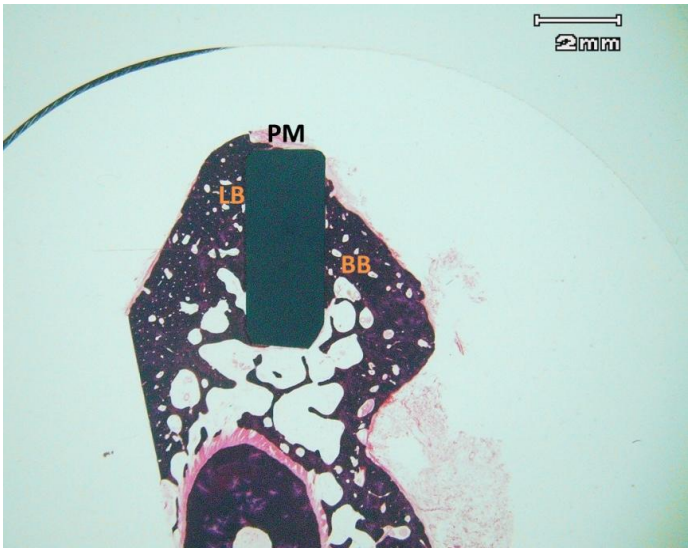

Fig.6.3-10. Representative buccal-lingual section of implanted rod (**PM**: peri-implant mucosa; **BB**: buccual bone; **LB**: lingual bone)

6.4. SUMMARY

6.4.1 *In vitro* study

All the samples were found to be biocompatible, but 3Y-TZP/Ta biocermet and pure Ta metal show higher cell viability when compared to monolithic zirconia. Biocermet showed no deleterious effect on cell proliferation, extra-cellular matrix production or on cell morphology. Therefore, biocermet and tantalum pure metal create a more cell friendly surface.

6.4.2 *In vivo* study

Observations during *in vivo* study have confirmed effectiveness of osseointegration within this period of time. The surfaces of biocermet implants appeared to be highly biocompatible and no gaps, fibrous tissue, multinucleated cells, or inflammatory cell infiltrate were found at the bone-implant interface. These results for the *in vivo* studies are largely consistent with the *in vitro* studies. The results obtained here indicate that biocermets are suitable for orthopedic and dental applications and have large clinical potential.

6.5 REFERENCES

[1] Piconi C, Maccauro G. Zirconia as a ceramic biomaterial. *Biomat*., 1999; 20:1-25.

[2] Hisbergues M, Vendeville S, Vendeville P. Review Zirconia: Established Facts and Perspectives for a Biomaterial in Dental Implantology. *J Biomed Mater Res Part B*., *Appl Biomater*, 2009; 88:519–529.

[3] Möller B, Terheyden H, Acil Y, Purcz NM, Hertrampf K, Tabakov A, Behrens E, Wiltfang J. A comparison of biocompatibility and osseointegration of ceramic and titanium implants: an *in vivo* and in vitro study. *Int. J. Oral Maxillofac. Surg*., 2012; 41:638–645.

[4] Park JB. Biomaterials science and engineering. New York: Plenum Press 1984; 217.

[5] Plenk Jr.H, Danhel-Mayrhauser M, Reichsthaler J, Schuh E. The bone-tantalum interface in the double blade implant ‘‘Implandent Austria’’. A clinical and histomorphometrical evaluation. In:Biomaterial-tissue interfaces. Doherty PJ, Ed Oxford: Elsevier Science 1992; 73

[6] Black J. Biological performance of tantalum. *Clin Mater*., 1994; 16:167-173.

[7] Stackpool GJ, Kay AB, Morton P, Harvey EJ, Tanzer M, Bobyn JD. Bone ingrowth characteristics of porous tantalum: A new material orthopaedic implant. Orthopaedic research society, editor. *Proceedings of Combined Orthopaedic Research Societies Meeting*. Chicago: Rider Dickerson Inc 1995; 45.

[8] Taub ML. Cell culture. Chapter 14, In: Bittar EE, Neville B, editors. Principles of Medical Biology: Elsevier; 1996. p. 463-83.

[9] Majeska RJ, Gronowicz GA. Chapter 89 - Current Methodologic Issues in Cell and Tissue Culture. In: Bilezikian JP, Raisz LG, Rodan GA, editors. Principles of Bone Biology (Second Edition). San Diego: Academic Press; 2002. p. 1529-41.

[10] Freshney RI, Obradovic B, Grayson W, Cannizzaro C, Vunjak-Novakovic G. Chapter 12 - Principles of tissue culture and bioreactor design. In: Lanza R, Langer R, Vacanti J, editors. Principles of Tissue Engineering (Third Edition). Burlington: Academic Press; 2007. p. 155-83.

[11] Yeo C. et al., Ficoll-Paque versus Lymphoprep: a comparative study of two density gradient media for therapeutic bone marrow mononuclear cell preparations, *Regen. Med*., 2009; 4:689-696.

[12] Cy L, Gao S, Terashita T, Shimokawa T, Kawahara H, Matsuda S, Kobayashi N. In vitro assays for adhesion and migration of osteoblastic cells (Saos-2) on titanium surfaces. *Cell Tissue Res*., 2006; 324:369-375.

[13] Donath K, Breuner GA. A method for the study of undecalcified bones and teeth with attached soft tissues. The Säge-Schliff (sawing and grinding) technique. *J. Oral Pathol*., 1982; 11:318-326.

[14] Yezerinac SM, Lougheed SC, Handford P. Measurement error and morphometric studies: statistical power and observer experience. *Syst. Biol*., 1992; 41:471-482.

[15] Bartolomé JF, Moya JS, Couceiro R, Gutiérrez-González CF, Guitián F, A. Martinez-Insua A. *In vitro* and *in vivo* evaluation of a new zirconia/niobium biocermet for hard tissue replacement. *Biomaterials*, 2016; 76:313-320.

7

Conclusiones / Conclusions

7.1 CONCLUSIONES

- Se han obtenido materiales compuestos de circona/Ta (con un de 5, 10, 15 y 20% en volumen) mediante una ruta de procesamiento de polvos por vía líquida y sinterizados sin aplicar presión. Estos materiales presentan microestructuras con una distribución uniforme de partículas metálicas en una matriz de circona. Todos los materiales compuestos, excepto la composición con un 20% en volumen de Ta, muestran un aumento de tenacidad debido al anclaje elástico-plástico que desarrollan las partículas metálicas dúctiles asociado a la transformación martensítica de la matriz de circona. El menor valor de resistencia mecánica y tenacidad en el material 3Y-TZP/20 vol.% Ta está relacionado con la porosidad en la interfase cerámica-metal y su baja densidad (90% de la teórica).
- Se han obtenido materiales completamente densos con composición 3Y-TZP/20 vol.% Ta con valores de tenacidad muy superiores a los correspondientes a los monolíticos de circona mediante prensado en caliente y sinterización mediante descarga de plasma. Estos elevados valores de tenacidad han sido alcanzados por la interacción entre la transformación de la fase tetragonal a monoclínica de la matriz de circona y el anclaje de los granos de Tántalo. Además se ha comprobado que estos materiales son muy tolerantes a los defectos y muestran un excelente comportamiento frente a la fatiga cíclica.
- Los materiales 3Y-TZP/20 vol.% Ta sinterizados mediante descarga de plasma exhiben una gran resistencia frente al desgaste asociado a un bajo coeficiente de fricción. Este comportamiento está relacionado con su alta tenacidad y la presencia

de una capa interfacial en la superficie de metal deformado que actúa como capa autolubricante.

- Además estos materiales 3Y-TZP/20 vol.% Ta sinterizados mediante descarga de plasma también muestra un excelente comportamiento frente al envejecimiento acelerado, debido fundamentalmente a la reducción del número de vacantes en la matriz de 3Y-TZP producida por la presencia de una solución sólida de Ta_2O_5 en dicha matriz.
- Los materiales 3Y-TZP/20 vol.% Ta son compatibles con las pruebas de diagnóstico realizadas por resonancia magnética nuclear (RMN) debido a la baja susceptibilidad magnética del Ta.
- Los resultados de los ensayos *in vitro* de los compuestos 3Y-TZP/20 vol.% Ta han mostrado que no existe ningún efecto de deterioro en la proliferación celular, en la producción de la matriz extracelular o en la morfología de las células. Por tanto, se puede concluir que estos materiales compuestos cerámica-metal son completamente biocompatibles.
- Los estudios realizados *in vivo* en conejos New Zealand y perros Beagles han puesto de manifiesto que los materiales 3Y-TZP/20 vol.% Ta implantados son completamente biocompatibles. No se observaron separaciones en la interfase material-hueso, tejido fibroso, células multinucleadas o inflamación.
- Se han obtenido polvos nanoestructurados de 2Y-TZP mediante la técnica de vaporización por laser de CO_2 (LAVA) y se han sinterizado mediante descarga de plasma. Los materiales resultantes tienen una combinación única de alta tenacidad, alta resistencia mecánica y al envejecimiento debido a una homogénea distribución de la itria y del tamaño de grano.

- Los materiales compuestos con una matriz de 2Y-TZP obtenidos a partir de polvos fabricados por el proceso LAVA y reforzados con partículas de Ta no son estables mecánicamente debido a la transformación espontánea de la matriz de circona. Esta degradación mecánica es debida a la presencia de Ta_2O_5 en solución sólida en la circona aumentando la transformabilidad de esta de forma descontrolada.
- Se han obtenido materiales compuestos de ZrO_2/Al_2O_3 (ATZ) a partir de nanopartículas de $Zr_{x-1}(Al_x)O_{2-x/s}/(\gamma,\delta)Al_2O_3$ preparadas por vaporización por laser y condensación (CoLAVA) y sinterizados mediante descarga de plasma con unas elevadas propiedades mecánicas y gran resistencia al envejecimiento. Estas propiedades se deben principalmente a una reducción del tamaño de partícula en el material sinterizado y a una distribución muy homogénea de ambas fases.
- Se han desarrollado materiales jerárquicos micro-nanoestructurados ATZ/Ta con alta resistencia mecánica y tenacidad a partir de nanopolvos híbridos 2Y/TZP-Al_2O_3 y partículas micrométricas de Ta sinterizados mediante descarga de plasma. Las elevadas propiedades mecánicas obtenidas junto a una excepcional resistencia al envejecimiento son debidas a la interacción de esta microestructura jerarquizada entre la matriz cerámica nanoestructurada junto al reforzamiento de la fase metálica microestructurada.
- El conjunto de propiedades de los materiales compuestos cerámica-Ta presentadas en este trabajo de investigación multidisciplinar abren la posibilidad del uso de los diferentes materiales desarrollados en un gran abanico de aplicaciones biomédicas, como son las aplicaciones ortopédicas, dentales y otro tipo de implantes

estructurales donde se requieran tanto propiedades estructurales como biofuncionales.

7.2 CONCLUSIONS

- Homogeneous zirconia/tantalum composites (with 5, 10, 15 and 20 vol.% Ta) fabricated by wet-processing route and pressureless sintering exhibited microstructures with uniformly distributed metallic particles into zirconia matrix. All composites, except the composition with 20 vol.% Ta, showed increase in toughness due to crack bridging of the elastic–plastic deformations of ductile metal particles associated with the transformation toughening mechanism in zirconia matrix. The lower value in strength and fracture toughness of 3Y-TZP/20 vol.% Ta composite is related to ceramic–metal interface porosity and low density (90% th.).
- Fully dense 3Y-TZP/20 vol.% Ta cermets with toughness much higher than monolithic zirconia, were manufactured for the first time using Hot Pressing Sintering (HP) and Spark Plasma Sintering (SPS) as sintering techniques. Extremely high toughness was engineered by the interactions between tetragonal to monoclinic transformation in zirconia matrix and crack bridging of Tantalum metal particles. This fracture toughness was accompanied by an excellent damage tolerance and performance under subcritical loading conditions.
- SPS sintered 3Y-TZP/20 vol.% Ta composite exhibited a higher wear resistance and lower friction coefficient, related both to the high toughness and the presence on the surface an interfacial layer (autolubricating phase) of plastically deformed metal grains.
- Besides exceptional mechanical and tribological properties, SPS sintered 3Y-TZP/Ta composites also showed high resistance to low temperature degradation (LTD) due to

reduction of oxygen vacancies in the 3Y-TZP matrix because the presence of solid solution of Ta_2O_5.

- Magnetic Resonance Imaging (MRI) results ensured compatibility of this diagnostic technique with the new developed biocermet due to low magnetic susceptibility of Tantalum.
- *In vitro* studies of 3Y-TZP/Ta biocermet showed no deleterious effect on cell proliferation, extra-cellular matrix production or on cell morphology. Thereby, biocermet was found to be biocompatible.
- *In vivo* studies in New Zealand white rabbits and Beagle dogs, revealed that implanted biocermets appeared to be highly biocompatible, and no gaps, fibrous tissue, multinucleated cells, or inflammatory cell infiltrate were found at the bone-implant interface.
- SPS sintering of 2Y-TZP nanopowders prepared by CO_2 laser vaporization (LAVA) method led to the manufacturing of monolithic ceramics with high indentation toughness in combination with high flexural strength and high resistant to hydrothermal degradation due to homogeneous yttria as well as particle size distribution in sintered ceramic.
- The attempt to add Tantalum metal particles to 2Y-TZP ceramic matrix obtained from LAVA powders led to spontaneous transformation of zirconia and, consequently, to degradation of mechanical properties of composite. This degradation is due to presence of Ta_2O_5 in SPS sintered composite which increase the transformability in the less stable zirconia matrix with 2 mol.% Y_2O_3 and provokes spontaneous tetragonal to monoclinic phase transformation.

- Outstanding mechanical properties together with a high resistance against LTD of SPS sintered ZrO_2/Al_2O_3 (ATZ) ceramics, manufactured from $Zr_{x-1}(Al_x)O_{2-x/s}/(\gamma,\delta)Al_2O_3$ nanoparticles prepared by a laser induced gas phase and condensation process (CoLAVA), were obtained by reducing the corresponding grain sizes and by increasing the homogeneity of the phase dispersion.
- SPS sintered ATZ/Ta hierarchical micro-nano biocomposites with high strength and enhanced intrinsic fracture toughness, were achieved from the mixture of 2Y/TZP-Al_2O_3 hybrid nanoparticles, prepared by CoLAVA, and Tantalum metal particles. These mechanical properties obtained due to the homogeneity of the 2Y/TZP-Al_2O_3 nanocomposite matrix and the reinforcement with a micrometer-sized ductile phase, were accompanied by an LTD resistance as well.
- The properties presented in this thesis could stimulate multidisciplinary applied research on ceramic-tantalum composites, which open up the possibility of using these materials in large panoply in orthopaedics, dentistry and other hard tissue replacement applications where biofunctional and structural properties are required.

8

Experimental setup and data analysis

8.1 INTRODUCTION

Present chapter describes the experimental setup and data analysis techniques used in the research. This includes:

- Powders mixture preparation by traditional wet mixing route and by new versatile laser vaporization method
- Forming and sintering of powders without and with externally applied pressure
- Characterization techniques

8.2 POWDERS MIXTURE PROCESSING

8.2.1 Attrition milling of tantalum raw powder

The attrition mill or attritor is a device for mechanically reducing solid particle size by intense agitation of slurry of material being milled and coarse milling media. Attritor consists of a cylindrical grinding chamber with a drive shaft having multiple impellers sticking out from the rotating shafts. Both cylindrical grinding chamber and drive shaft with impellers were made from teflon (Fig.8.2.-1).

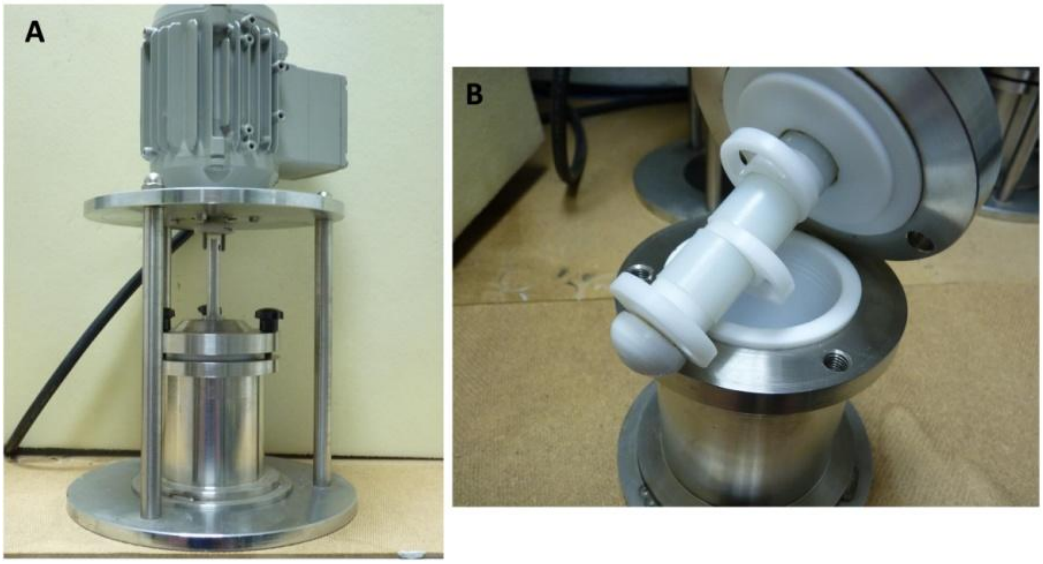

Fig.8.2-1. Overal view of attrition mill (A). Grinding chamber and drive shaft with impellers (B)

Tantalum raw powder has been multi directionally milled in an attritor using isopropyl alcohol as the process control agent and zirconia balls as grinding media during 4 hours with ball-to-powder ratio 10:1. After milling the slurry was removed and oven dried.

8.8.2 Powder's mixture preparation

In order to prepare the mixtures for sintering, two processing methods were used: powder mixing and laser vaporization. The powder wet mixing route was applied for further

manufacturing of all studied compositions while laser vaporization was used only for fabrication of ceramic.

8.8.2.1 Wet mixing route

Stepwise wet mixing process is shown schematically in Fig.8.2-2. Slurries of powders were prepared using distilled water as liquid media and a 3 wt.% addition of an alkali-free organic polyelectrolyte (Dolapix CE-64) as surfactant. The mixture was homogenized by milling with zirconia balls in polyethylene containers at 150 rpm during 24 h and then dried at 90 ˚C during 12 h. The resulting powders were ground in an agate mortar and subsequently passed through a 75 µm sieve in order to avoid agglomeration.

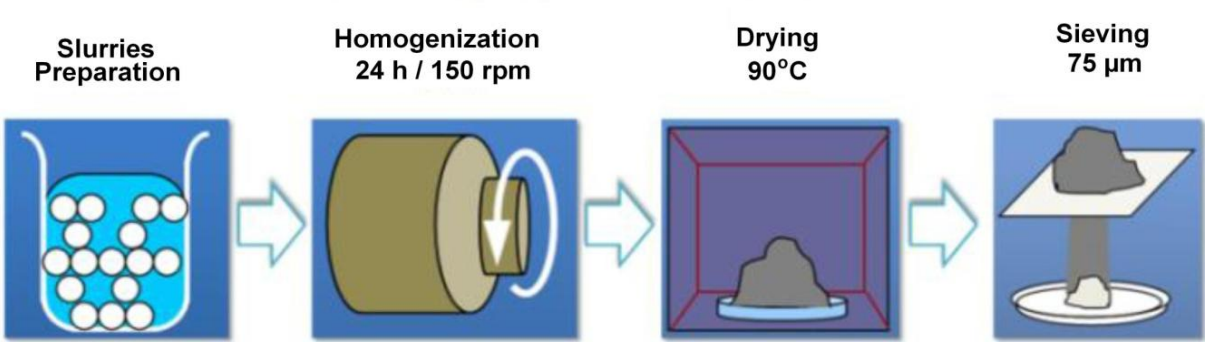

Fig.8.2-2. General scheme of wet processing route

8.2.2.2. Dry mixing

Starting mixture for the preparation of nanoparticles with laser vaporization process was fabricated by dry mixing of ceramic commercial powders in a polyethylene bottle with zirconia balls in a Turbula T2F (Glen Mills Inc., Clifton, NJ, USA) multidirectional mixer for 24 h (Fig.8.2-3).

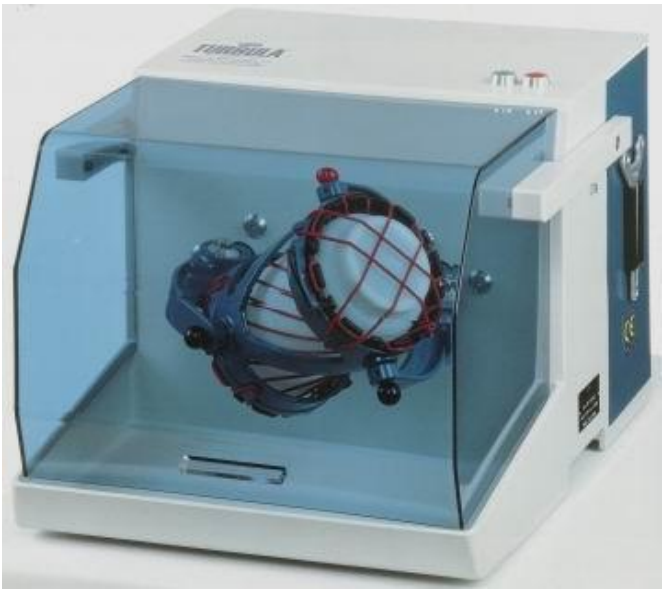

Fig.8.2-3. Turbula T2F multidirectional mixer

8.2.2.3 Laser vaporization (LAVA) / Laser Co-vaporiazation (CoLAVA)

This technique was developed by the research group of the Otto Schott Institute of Materials Research (Jena, Germany) and was used for fabrication zirconia and alumina-zirconia nanoparticles in Chapter 4 and Chapter 5, respectively [1]. This method allows to prepare ceramic nanopowders with enabling microstructural homogeneity and therefore optimized mechanical properties and low temperature degradation resistance of ceramic and ceramic-metal composites. The principle of Lava function allows the continuous production of nanopowders under well-defined and stable process conditions. The only difference between LAVA (Fig. 8.2-4A) and CoLAVA (Fig. 8.2-4B) is that for CoLAVA homogeneous mixtures of at least two ceramic raw powders are laser evaporated in one single process.

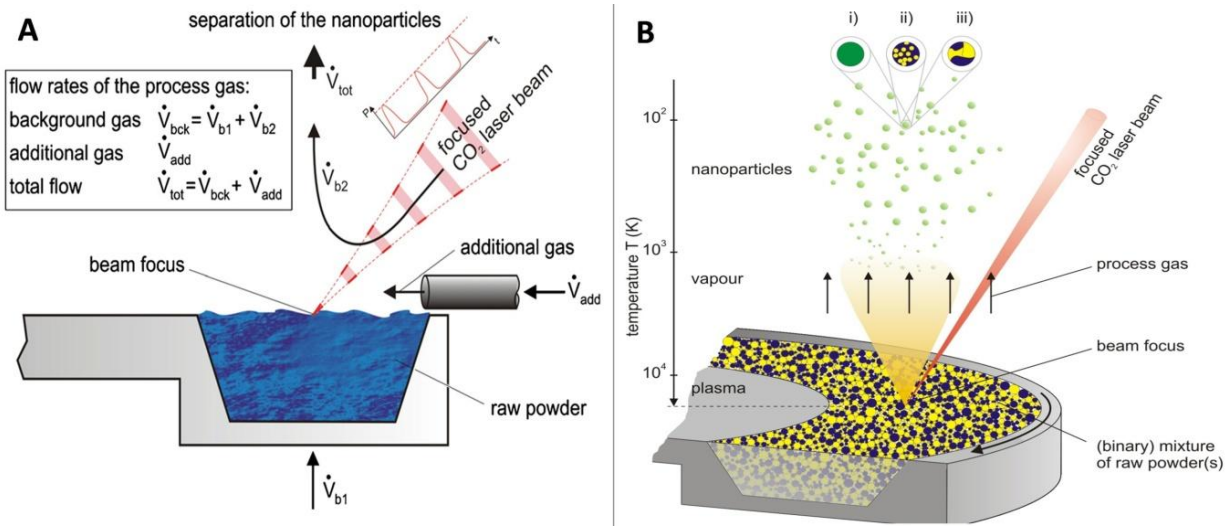

Fig.8.2-4. Principle of the laser (A) – and Co-laser (B) vaporization process

For the preparation of nanoscaled ceramic particles with the LAVA process coarse ceramic powders with grain sizes ranging from µm to mm are used as raw materials. In order to vaporize the provided raw powder a laser beam is focused onto its surface (Fig.8.2-4). Absorbing the high-intensity laser radiation within the beam focus, the raw material heats up, vaporizes, and forms plasma. Vaporization and plasma formation proceed in a continuously flowing aggregation (process) gas under normal pressure. For the processing of oxidic ceramic materials air is used as process gas. During expansion into the flowing aggregation gas, plasma and vapor instantly cool down. Subsequently, gas phase condensation leads to the formation of an ultra-fine particle aerosol. Finally, the process gas transports the resulting aerosol towards the particle separation. This principle of function was implemented in the Lava laboratory system (Fig.8.2-5), which allows the continuous production of nanopowders under well-defined and stable process conditions. In order to achieve high vaporization rates (mass of vaporized raw material per time unit), a high power CO_2 laser was chosen as the beam source.

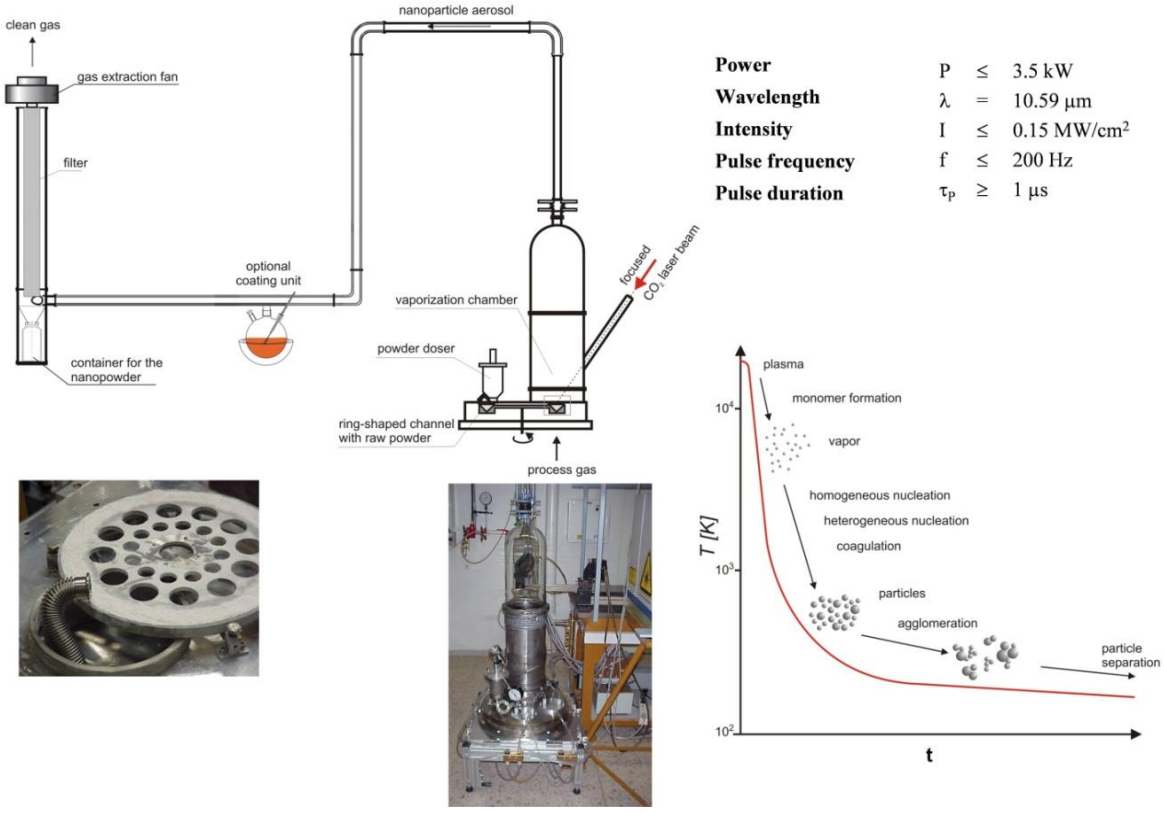

Fig.8.2-5. Schematic representation of the LAVA laboratory system

The CO_2 laser radiation in the middle infrared part of the electromagnetic spectrum is absorbed to a high degree by the ceramic raw materials. The laser can be operated in a continuous beam mode as well as in a variable pulsed mode. Vaporization and particle formation proceed in a stainless-steel chamber. The main part of the vaporization chamber is a motor-driven revolvable disc (maximum rotational frequency 15 rpm) with a ring-shaped channel along its rim. The ceramic raw powder is filled in to this channel. The CO_2 laser beam is focused on to the continuously revolving powder surface through an inlet tube in the chamber and vaporizes the raw powder. During the rotation of the disc, the vaporized material is automatically refilled by a variable powder doser. A doctor blade continuously planishes the surface of the refilled powder. Thereby, an incessantly regenerated powder surface is fed to the focus of the laser beam, ensuring stable and reproducible process

conditions. The vaporization chamber is connected to the filtering chamber through a system of hermetically sealed glass tubes. The total flow rate of the process gas V_{tot} is comprised of two variable gas flows (Fig.8.2-4), the background gas flow (flow rate $V_{bc}k$) through the evaporation chamber that is provided by a gas extraction fan and an additional jet of gas (flow rate V_{add}) that is conducted through the zone of particle condensation. The process gas flow transports the nanoparticles out of the vaporization chamber towards the filtering chamber where they are separated from the aerosol by a filtering unit. During the process of vaporization, the transmission of the filter continuously decreases due to the accumulation of nanopowder on its surface. In order to keep the process gas flow constant, the power of the gas extraction fan has to be adjusted. For this purpose the differential pressure between the filtering chamber and the ambient laboratory atmosphere is used as a control. Once the maximum power of the fan is achieved, the filter is regenerated by mechanically stripping off the nanopowder. The LAVA process and thereby the quality of the ceramic nanopowders is controlled by the relevant process parameters laser power, continuous or pulsed laser operation, and also volume flow and thermal conductivity of the process gas within the zone of particle condensation.

8.3 FORMING AND SINTERING

Consolidation of samples prepared by a wet mixing and Lava was fulfilled by pressureless sintering (PS), hot press sintering (HP) and spark plasma sintering (SPS). The spark plasma sintering technique was shown to be superior to the other methods giving dense materials with uniform morphology and decreasing grain size at lower temperatures and shorter sintering time.

8.3.1 Basics of sintering

Sintering is a thermal treatment of powder bodies which change their dimensions and physical-mechanical properties as a result of the diffusion flow (redistribution) of the material under the action of alloy formation and capillary forces. During sintering, the areas of the solid-vapor interface begin to decrease while the solid-solid interface is simultaneously formed; the motive force is the reduction of the free energy in the system [2]. The sintering temperature is usually between 70% and 90% of the melting point of the material and generally higher than Tamman temperature, which can be estimated as half the melting temperature and is considered the point at which sintering begins in ceramics material. This will cause bonding mechanisms to occur between powders particles pressed together in the compact. Bonding within the green compact is weak and this pressed unsintered part usually has just enough structural integrity to be handled. Bonding that occurs during sintering greatly strengthens the part. Bonding mechanisms during sintering are complicated and different, however the main driving force that enacts this particle bonding is considered to be a reduction of energy due to a reduced surface area. This decreasing corresponds to (1) the curvature of the surface of the particles, (2) the external pressure and (3) the chemical reaction. In the absence of external pressure and chemical

reaction, the surface curvature provides the necessary motive force for sintering. As schematically shown in Fig.8.3-1, the reduction in total energy in a sintering system can be obtained by densification and grain growth. The elimination of porosity leads to as densification or sintering. When the pores change shape without an increase in density, coarsening take place.

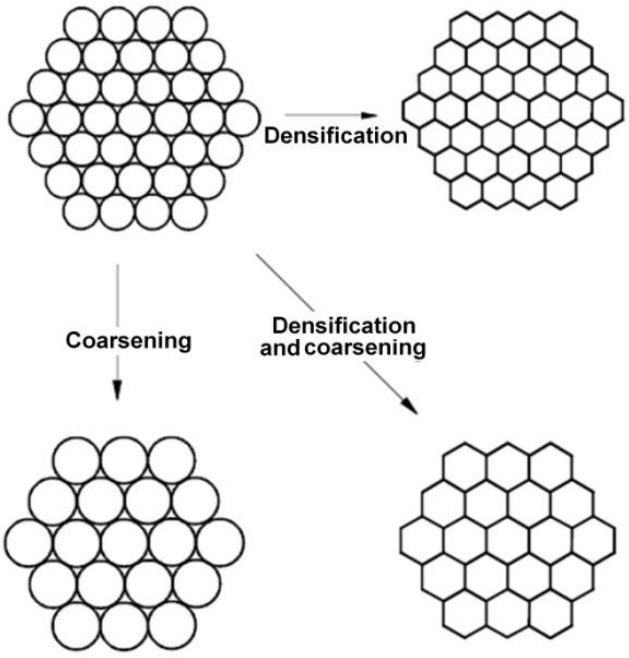

Fig.8.3-1. Basic phenomena occurring during sintering under the driving force for sintering

The development of microstructure and densification during sintering is a direct consequence of mass transport through several possible paths (one of these paths is usually predominant at any given stage of sintering):

- gas phase (evaporation/condensation)
- liquid phase (solution/precipitation)
- solid phase (lattice diffusion)
- interfaces (surface diffusion, grain boundary diffusion)

- viscous or plastic flow, under capillary pressure (internal) or externally applied pressure (pressure-sintering, hot-pressing, hot-isostatic-pressing)

Mechanisms leading to particle joining and neck growth and which can affect the kinetics of densification and grain growth but cannot cause the densification are surface diffusion and evaporation-condensation. Grain boundary diffusion, volume diffusion, and plastic flow are directly involved in densification. Fig.8.3-2 schematizes those mechanisms.

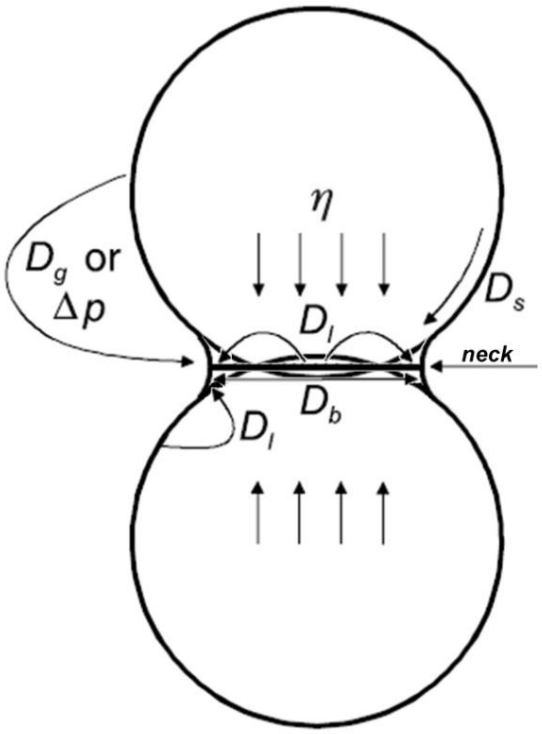

Fig.8.3-2. Material transport paths during sintering in the Two-Particle Model. (D_g) gas diffucion; (Δp) evaporation/condensation; (η) viscous flow; (D_l) lattice diffusion; (D_b) grain boundary diffusion; (D_s) surface diffusion

Since certain mechanisms of mass transport can be dominant in some systems, two broad categories of sintering are recognized: solid state sintering (where all densification is achieved through changes in particle shape, without particle rearrangement or the presence of liquid) and liquid phase sintering (where some liquid phase that is present at sintering

temperatures aids compaction). In this work ceramic and metallic powders are not bonded by the particle-dissolving action of glassy liquids that appear at high temperatures. Therefore, solid-state sintering predominates. Solid state sintering is usually divided into three overlapping stages — initial, intermediate and final. Initial stage of sintering, involving:

- local point of contact formation or "fusion", without shrinkage of compact. This is accompanied by smoothing of the free surface of particles
- neck formation at the contact point, with the resulting concave curvature at the neck

As sintering proceeds, the growing necks merge and the intermediate stage begins. At this stage the porous phase is continuous and intersected by grain boundaries. Many concurrent phenomena govern the microstructural evolution. Grain boundary migration, that is, grain growth begins when the porosity is sufficiency low. Pores may migrate with advancing boundaries and, therefore, the average pore size may increase through pore coalescence. Surface diffusion may increase the average pore size by locally redistributing material from regions of convex curvature to regions of concave curvature. Ultimately, during the final stage of sintering, the pore space is broken-up into isolated pores. Those may all remain on grain boundaries, and theoretically disappear after a heat treatment sufficiency long, or, alternatively, they can become isolated from the grain boundaries during discontinuous grain growth.

8.3.2 Pressureless Sintering (PS)

The terminology ‘pressureless sintering’ is used for atmospheric pressure sintering without an external pressure. Pressureless sintering is a more affordable manufacturing technology than alternative powder processing techniques, like Hot Press Sintering (HP) or Spark Plasma Sintering (SPS). However, many of these techniques are not economically viable

depending on the use of the final product. Thus, conventional sintering is still a more attractive sintering method to produce ceramic products, mainly due to its simplicity and cost compared to other methods.

Prior the Pressureless sintering, the mixtures of ceramic and ceramic-metal powders were placed into a flexible mold and immersed in an oil (Fig. 8.3-3B) and then were compressed to a high pressure. In other words, were cold isostatically pressed using Astursinter equipment (Oviedo, Spain) (Fig.8.3-3). The most attractive thing about isostatic pressing is that the powder is compacted with the even for all directions pressure magnitudes. The high and uniform density can be achieved without any specific binder or lubricant addition to the powder mixture. The green samples then were extracted from the mold and ready for sintering.

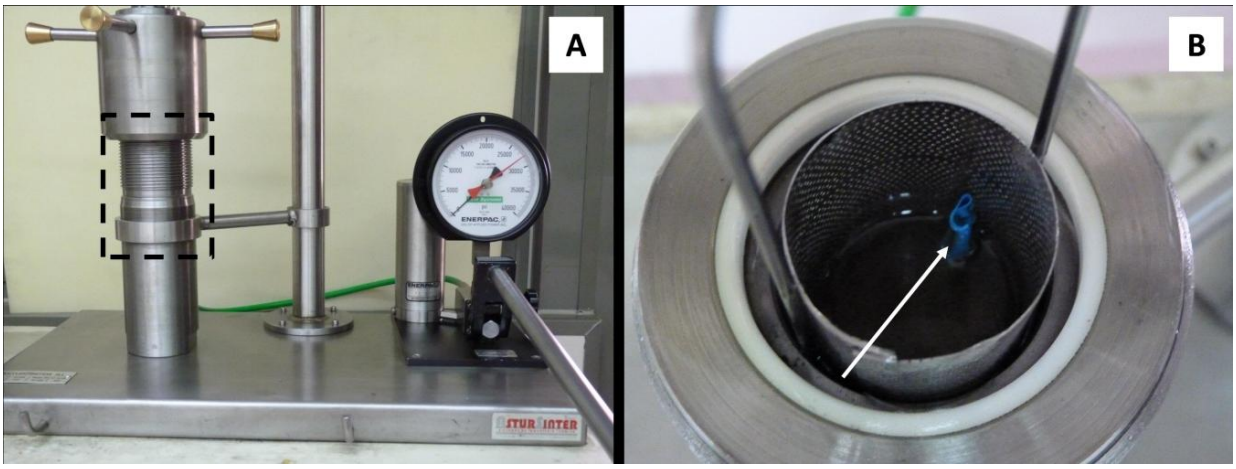

Fig.8.3-3. Cold Isostatic Press (A). Dashed area denotes where close-up of pressure vessel (B) was taken. The arrow shows rubber mold dipped into oil

Obtained cylinders were placed into a Hobersal tube furnace (Barcelona, Spain) shown in Fig.8.3-4 and sintered under flowing argon that prevent oxidation.

Fig.8.3-4. Hobersal tube furnace

Sintering of oxide ceramics require relatively long time and high temperature because the diffusion proceeds in solid state. Applying pressure decreases sintering time and the resulted porosity. Consequently, in order to enhance the final density pressure-assisted sintering Hot Press and Spark Plasma Sintering were chosen.

8.3.3 Hot Press Sintering (HP)

Hot pressing is the simultaneous application of external pressure and temperature to enhance densification. It is conducted by placing powder into a graphite die, and applying uniaxial pressure while the entire system is held at an elevated temperature. An example of a HP sintering cycle is plotted in Fig.8.3-5. Temperature-pressure related processing parameters such as heating rate, dwelling time and temperature as well as pressure have a strong effect on the specimen's final microstructure.

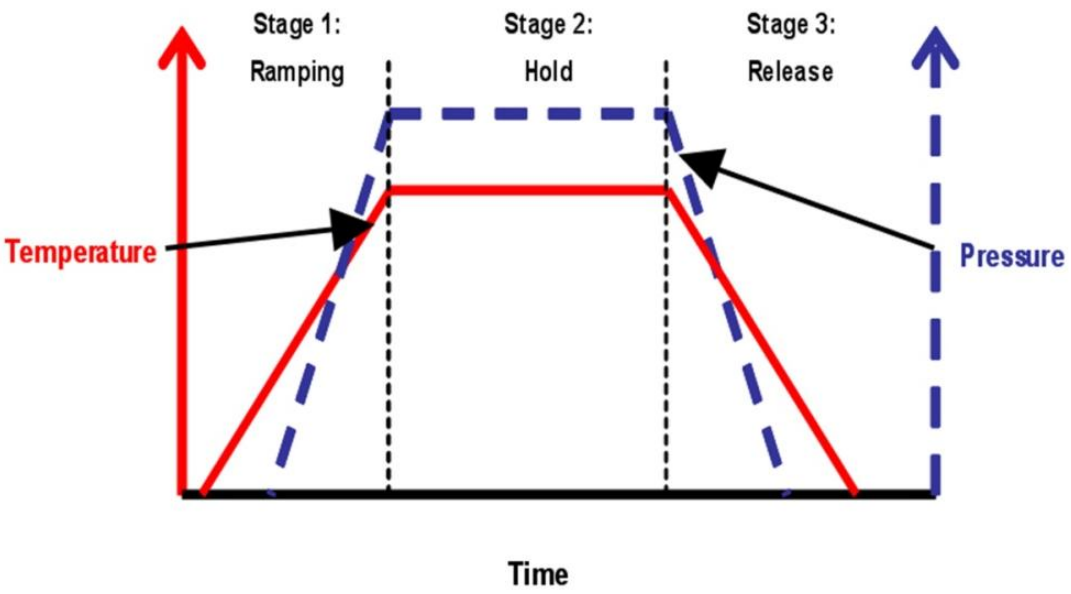

Fig.8.3-5. Hot Press sintering cycle

Before HP the mixed powder were slightly uniaxially cold pressed in graphite die. Then this graphite die was placed in the hot press, where electromagnetic field induces a current in the work piece, which generates heat in the work piece. The coil, which is water-cooled is placed around to the graphite piece (Fig. 8.3-6B). It does not touch the work piece, and the heat is only generated by the induced current flowing in the work piece.

The experiments were conducted in a FCT Systeme Gmbh (HT W5, Rauenstein, Germany) hot press in a reducing environment (Fig. 8.3-6A). The chamber was evacuated and purged with argon to remove contaminants. The desired temperature-pressure-time cycles were programmed into the controller which were then executed and plotted automatically. The chamber temperature was measured with a thermocouple and was also cross-checked with an optical pyrometer. The pressure was calculated based on the applied load by the hydraulic pump on the ram and the cross-sectional area of the die. The vertical movement of the ram was monitored by a micrometer. The chamber was connected to a mechanical

pump to obtain the desired chamber pressure. Argon was backfilled to create an approximately inert atmosphere in the chamber when required.

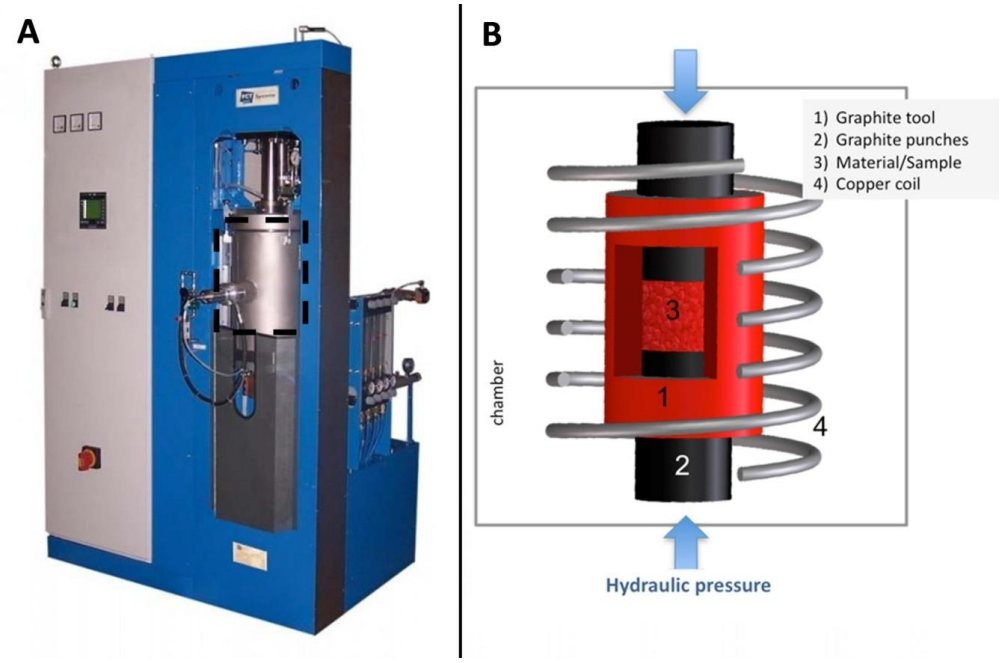

Fig.8.3-6. Hot Press Furnace (A). Dashed area denotes where schematic close-up of chamber with graphite die and punches as well as material was taken (B)

8.3.4 Spark Plasma Sintering (SPS)

Spark Plasma Sintering (SPS), also known as Pulsed Electric Current Sintering (PECS), Plasma Activated Sintering (PAS) or Field Assisted Sintering Technology (FAST), is a sintering technique that uses a high pulsed DC current to heat up a powder compact that is loaded into a die/punch set-up. The SPS furnace is used for sintering ceramic, cermet and metallic materials. Its main technical advantages are the high heating and cooling rates, hereby shortening processing times, while the high pulsed current enhances densification in electrically conductive materials.

Sintering by SPS takes place in a wide range of temperature, which is controlled by the electric current [3, 4]. The pulsed discharge can produce spark plasmas and pressure due to

its impact, heating by Joule effect, and also an effect of diffusion of electric field [5, 6]. Therefore, a significantly lower temperature as well as significantly lower mould pressure is needed than is used for hot press sintering. The FCT Systeme Gmbh (HPD25, Rauenstein, Germany) SPS furnace is shown in Fig.8.3-7.

Fig.8.3-7.SPS furnace (A) and close-up of vacuum chamber with red-hot graphite mold (B)

In this apparatus compressive forces up to 250 kN can be applied, while a maximum output voltage of 10 V and current up to 10 kA can be generated by the transformer. The applied pulsed DC current patterns can be varied with both ON and OFF segments ranging between 0 and 255 ms. Since the die and powder compact act as the actual heating elements, very high heating and cooling rates up to 1000 °C/min and 400 °C/min, respectively, can be achieved, depending on the tool size and design. This offers advantages such as the minimization of coarsening processes at low temperatures and maintaining intrinsic nanostructures after full densification. The temperature is controlled using a central pyrometer focusing on the bottom of a borehole inside the upper punch, 5 mm above the

top of the sintering compact. This guarantees a correct temperature measurement, independent of the sample properties or size. An external pyrometer, focusing on the die wall, as well as four additional flexible thermocouples, can be used to measure the temperature at different locations. The sintering was conducted in vacuum atmosphere ($1 \cdot 10^{-2}$ mbar). Different process parameters such as temperature, applied force, piston travel, piston speed, current, voltage and internal vessel pressure are logged automatically and are continuously displayed. A touch screen facilitates the process control and sinter cycle programming. However, in order to obtain homogeneous sintered materials it is necessary to achieve homogeneous temperature distribution as well, which is nonuniform due to high heating rate. The sample material's electrical and thermal properties; the size, shape, thickness of the die/punch set; the pressure and speed heating are influencing factors to the temperature distribution during the sintering. SPS sintering cycle is presented in Fig.8.3-8. The first stage is performed to remove gases and create vacuum. Then pressure is applied in the second stage followed by resistance heating in the third stage and finally cooling in the fourth stage.

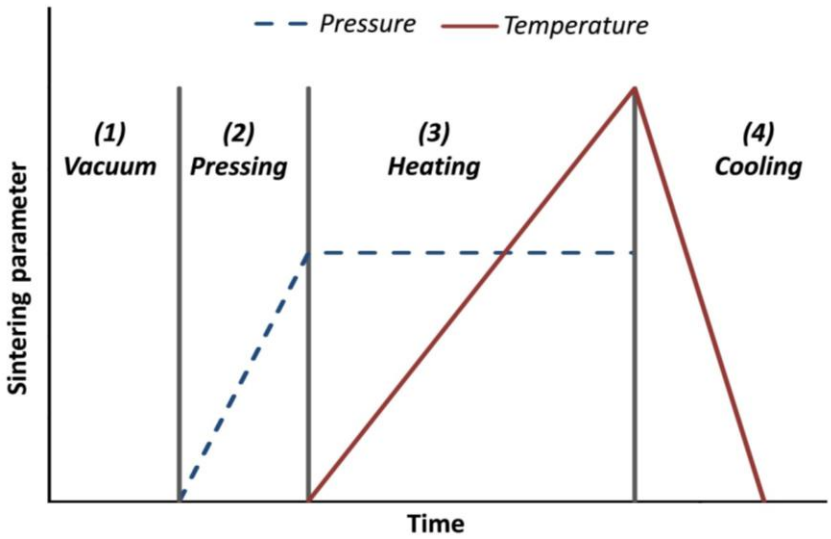

Fig.8.3-8. Spark plasma sintering stages

8.4 DENSE SAMPLE'S GRINDING AND POLISHING

Prior to characterization, the sintered samples require mounting and polishing. In this work mounting of samples was realized by means of hot mounting technique. Automatic hot mounting press Remet IPA (Casalecchio di Reno, Bologna, Italy) is shown in Fig. 8.4-1A. During hot mounting, the samples are placed in a mounting mould which is then filled with thermoplastic resin granules. With the controlled application of pressure and heat, the resin granules are melted and cured to fill in the cavities of the specimen and mould. Then the sample is cooled under pressure with water to prevent cracking and shrinkage of resin (Fig. 8.4-1B and C). The sample is then ready for grinding and polishing.

Fig.8.4-1. Automatic hot mounting press (A). Dashed area denotes where close-up (B,C) was taken

Both grinding and polishing operations (down to 1 μm) were carried out using the polishing machine RotoPol-22 (Struers, Copenhagen, Denmark) at a speed of 150 rpm and a force of

30 N. Fig.8.4-2 shows polishing machine (left) and close-up of sintered samples mounted into a resin with revolver head (right).

Fig.8.4-2. Polishing machine RotoPol-22

8.5 CHARACTERIZATION TECHNIQUES

8.5.1 X-Ray Diffraction (XRD)

X-ray diffraction (XRD) is a versatile, non-destructive technique that reveals detailed information about the chemical composition and crystallographic structure of natural and manufactured materials. It can be used not only to determine the separations of layers of atoms but also to determine the locations of the atoms.

Crystal lattice

A crystal lattice is a regular three-dimensional distribution (cubic, rhombic, tetragonal etc.) of atoms in space (Fig.8.5-1). These are arranged so that they form a series of parallel planes separated from one another by a distance, which varies according to the nature of the material. For any crystal, planes exist in a number of different orientations - each with its own specific spacing.

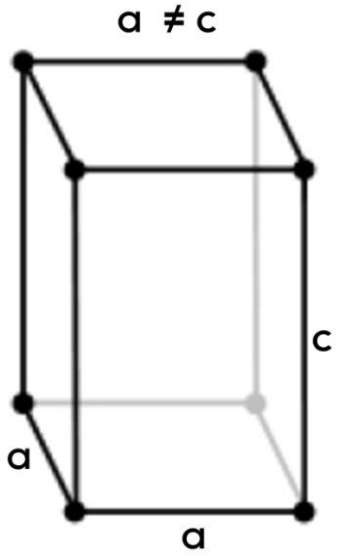

Fig.8.5-1. Example of one crystal form called tetragonal structure

Bragg's law and basic geometry of x-ray diffraction

X-rays are electromagnetic radiation similar to light, but with a much shorter wavelength. They are produced when electrically charged particles of sufficient energy are decelerated. In an X-ray tube, the high voltage maintained across the electrodes draws electrons toward a metal target (the anode). X-rays are produced at the point of impact, and radiate in all directions. Tubes with copper targets, that produce their strongest characteristic radiation (Kα1) at a wavelength of about 1.5 angstroms.

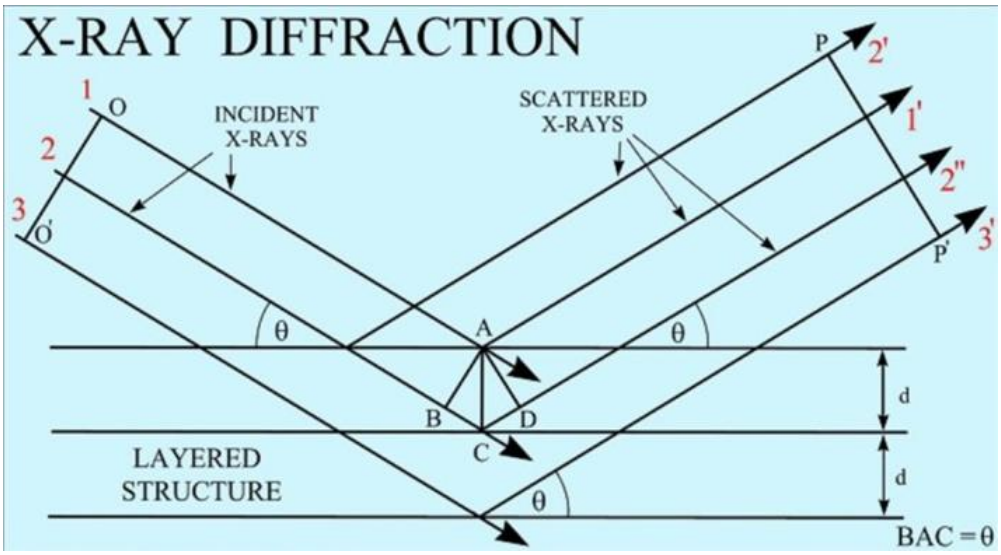

Fig.8.5-2. The proof of Bragg's law [7]

If an incident X-ray beam encounters a crystal lattice, general scattering occurs. Although most scattering interferes with itself and is eliminated (destructive interference), diffraction occurs when scattering in a certain direction is in phase with scattered rays from other atomic planes. Under this condition the reflections combine to form new enhanced wave fronts that mutually reinforce each other (constructive interference). The relation by which diffraction occurs is known as the Bragg's law or equation. Because each crystalline material has a characteristic atomic structure, it will diffract x-rays in a unique characteristic pattern. The Bragg's law equation is given as follow:

$$2d \sin\theta = \eta\lambda \qquad (8.5\text{-}1)$$

where η is an integer, λ is the wavelength of incident wave, d is the spacing between the planes in the atomic lattice, and θ is the angle between the incident ray and the scattering planes.

The basic geometry of an X-ray diffractometer involves a source of monochromatic radiation and an X-ray detector situated on the circumference of a graduated circle centered on the powder specimen. Divergent slits, located between the X-ray source and the specimen, and divergent slits, located between the specimen and the detector, limit scattered (non-diffracted) radiation, reduce background noise, and collimate the radiation. The detector and specimen holder are mechanically coupled with a goniometer so that a rotation of the detector through 2θ degrees occurs in conjunction with the rotation of the specimen through θ degrees, a fixed 2:1 ratio (Fig.8.5-3).

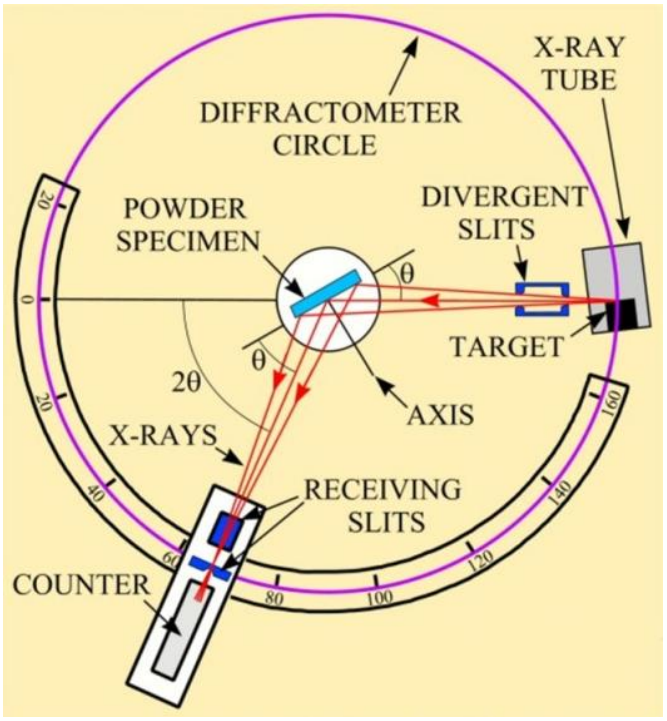

Fig.8.5-3. Schematic of x-ray diffractometer [7]

In this thesis all XRD analyses were carried out using Bruker D8 Advance X-ray diffractometer (Bruker AXS Inc., Madison, Wisconsin, USA) with Cu-Kα radiation, wavelength 1.5405981 Å, accelerating voltage of 40 kV and beam current of 30 mA (Fig.8.5-4).

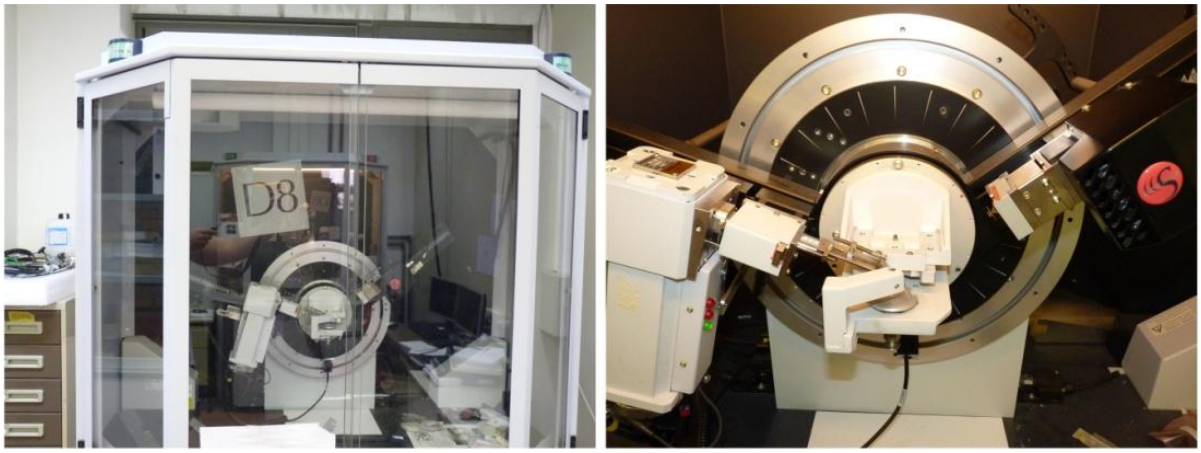

Fig.8.5-4. Bruker D8 Advance X-ray diffractometer

The monoclinic phase X_m content in the different zirconia-based materials were measured on ground as well as fractured surfaces and was calculated using the method of Garvie and Nicholson [8]:

$$X_m = \frac{I_m(111) + I_m(\bar{1}11)}{I_m(111) + I_m(\bar{1}11) + I_t(101)} \qquad (8.5\text{-}2)$$

Where, I_t and I_m represent the integrated intensities (areas under the peaks) of the tetragonal $(101)_t$ and monoclinic $(111)_m$ and $(\text{-}111)_m$ reflections. The monoclinic volume fraction V_{mtot} was calculated using equation proposed by Toraya et al. [9]:

$$V_{mtot} = \frac{1.311X_m}{1 + 0.311X_m} \qquad (8.5\text{-}3)$$

8.5.2 Thermal analysis techniques

Thermal analysis is a group of techniques that study the properties of materials as they change with temperature and includes several different methods: Thermogravimetric analysis (TGA), Differential thermal analysis (DTA), Differential scanning calorimetry (DSC), Dilatometry (DIL), and etc. In this work DTA and DIL techniques were used to study phase transformations of ceramic nanopowders.

8.5.2.1 Differential thermal analysis (DTA)

The basic principle involved in DTA is the temperature difference between the test sample and an inert reference sample under controlled and identical conditions of heating or cooling is recorded continuously as a function of temperature or time, thus the heat absorbed or emitted by a chemical system is determined. If any phase transitions takes place in the sample, then the temperature difference will occur between the sample and reference material (endothermic or exothermic reactions).

Typical DTA apparatus consist of the following basic components: (1) furnace sample and reference holder with thermocouple assembly, (2) sample holder furnace, (3) furnace temperature controller, (4) furnace atmospheric control system, (5) amplifier, and (6) recorder (Fig.8.5-5).

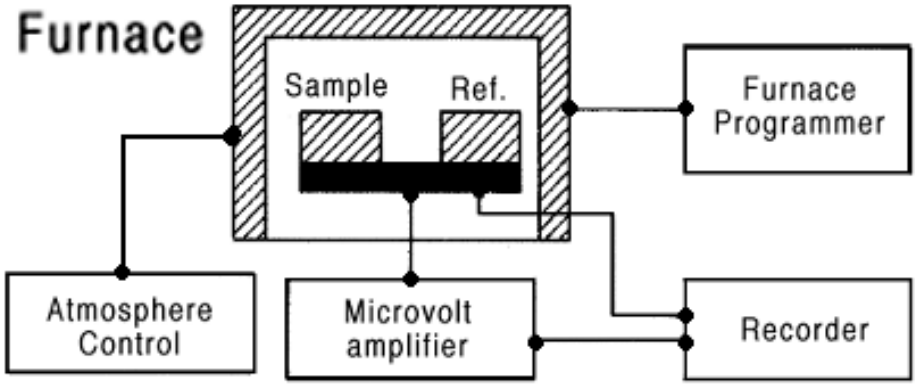

Fig.8.5-5. Scheme of DTA appartus

Overall view and cross-sectional cut of NETZSCH STA 409 C/CD (NETZSCH-Gerätebau GmbH, Selb, Germany) apparatus which was used for analysis of zirconia-alumina nanopowder phase transformations is presented in Fig.8.5-6.

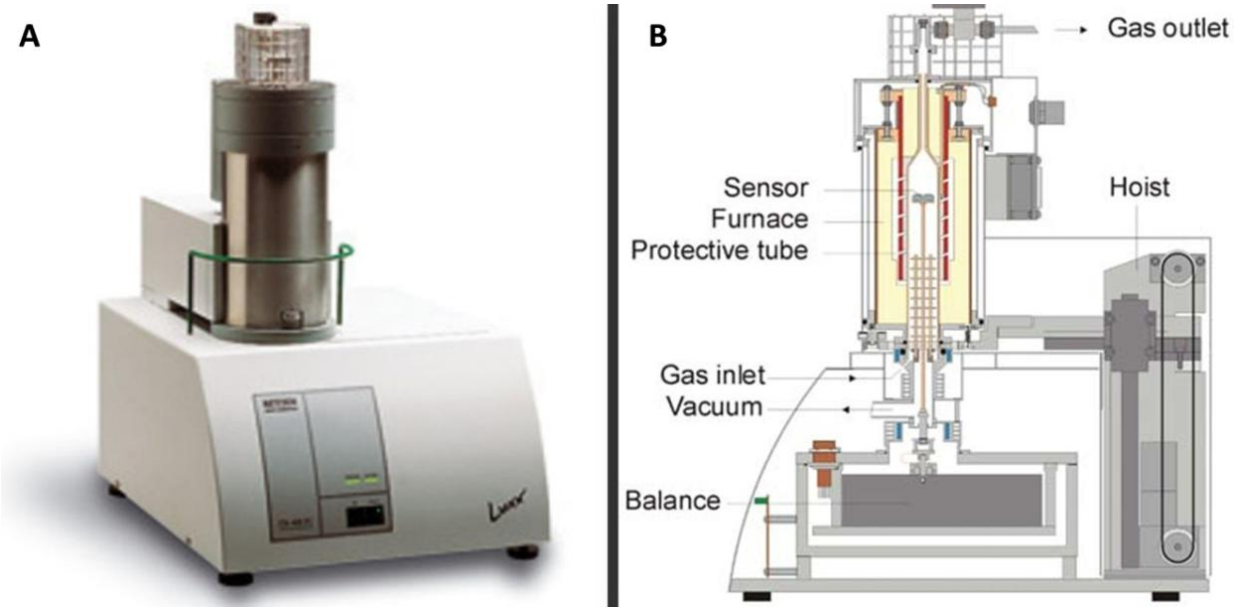

Fig.8.5-6. Overall view (A) and cross-sectional cut (B) of Netzsch STA apparatus

The vertical design with top-loaded samples ensures total protection of the balance, which is on the bottom, through accurate flow of the purge and protective gases in a natural vertical path to the top.

8.5.2.2 Dilatometry (DIL)

Dilatometry is a method by which the thermal expansion of a material may be measured. There are many types of dilatometers. Dilatometers may use a pushrod, capacitor, or optical system to sense expansion and may be configured in horizontal, vertical, or in-between configurations. A schematic of the type of pushrod dilatometer used in this work can be seen in Fig.8.5-7.

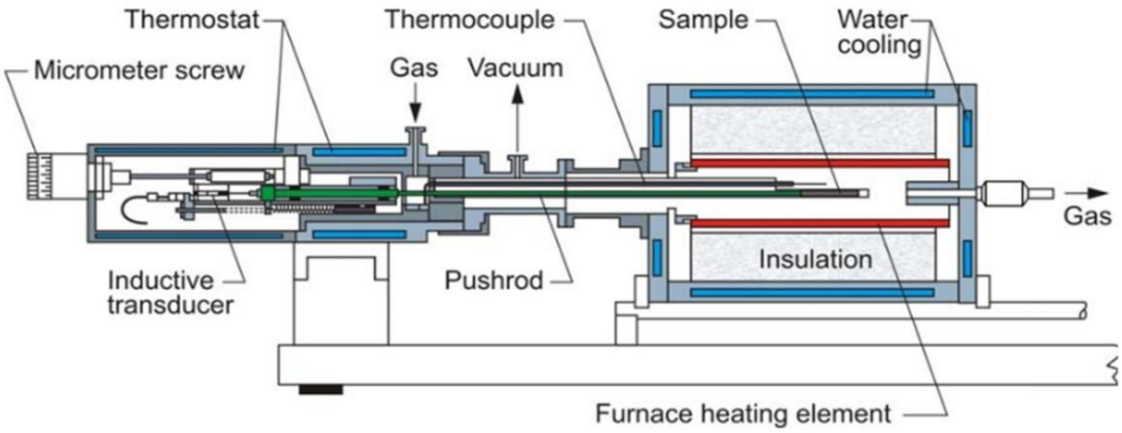

Fig.8.5-7. Schematic of dilatometer in horizontal configuration

Shrinkage behaviour and dynamic sintering of green compacts of the zirconia-alumina nanopowder were investigated using a high-temperature horizontal dilatometer (DIL 802, BÄHR-Thermoanalyse GmbH, Hüllhorst, Germany) which is plotted in the Fig. 8.5-8.

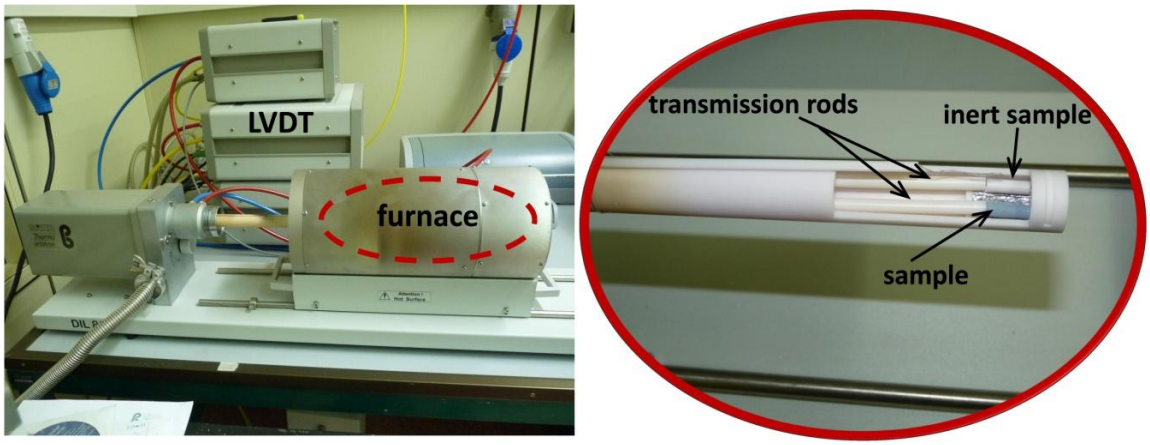

Fig.8.5-8. DIL 802 system and close-up of sample holder

To perform a dilatometric analysis, cold-pressed green cylindrical body with diameter 4 mm and length 14 mm of ceramic powders was placed in a special holder inside a moveable furnace. A pushrod is connected to a linear variable displacement transducer (LVDT) on one side, and on the other, it is in close contact with a sample in order to register any length change in the sample material during heating or cooling. As sample length changes during the temperature program, the LVDT core is moved, and an output signal proportional to the displacement is recorded. The temperature program is controlled using a thermocouple located next to the heating element or next to the sample. The measured length change of the sample includes both the sample holder expansion and the length change of the sample itself. The measurement is automatically corrected against the expansion behavior of a suitable standard reference material under identical conditions as the sample. The coefficient of thermal expansion (CTE) is determined by comparing the sample length change with the initial length over a temperature range.

8.5.3 Fourier transform infrared spectroscopy (FTIR)

It is known that the precisely characterization the transition alumina structures cause difficulties for classic methods [10]. In particular, X-ray diffraction provides similar

patterns for various transition aluminas and does not allow to unambiguously characterizing the phases. Therefore FTIR was chosen as extra technique for evolution of the crystal phases in zirconia-alumina nanopowder with increasing sintering temperatures. In infrared spectroscopy, IR radiation is passed through a sample. Some of the infrared radiation is absorbed by the sample and some of it is passed through (transmitted). The obtained spectrum represents a fingerprint of a sample with absorption peaks which correspond to the frequencies of vibrations between the bonds of the atoms making up the material. Because each different material is a unique combination of atoms, no two compounds produce the exact same infrared spectrum. Measurement procedure with main parts of equipment is shown in Fig.8.5-9.

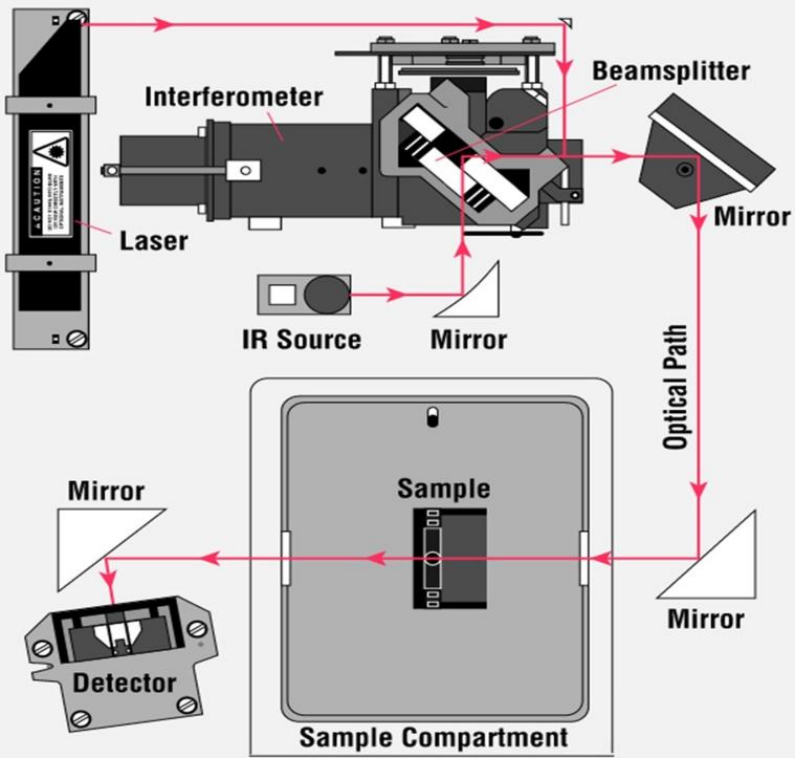

Fig.8.5-9. The layout of spectrometer

Infrared energy is emitted from a glowing black-body source. This beam enters the interferometer where the "spectral encoding" takes place. The interferometer consists of a beam splitter, a fixed mirror, and a mirror that translates back and forth, very precisely. The beam splitter is made of a special material that transmits half of the radiation striking it and reflects the other half. Radiation from the source strikes the beam splitter and separates into two beams. One beam is transmitted through the beam splitter to the fixed mirror and the second is reflected off the beam splitter to the moving mirror. The fixed and moving mirrors reflect the radiation back to the beam splitter. The resulting interferogram signal then exits the interferometer. Then the beam enters the sample compartment where it is transmitted through or reflected off of the surface of the sample. This is where specific frequencies of energy, which are uniquely characteristic of the sample, are absorbed. Finally, the beam passes to the detector for final measurement. After measured signal is digitized and sent to the computer and presented for interpretation.

In this investigation, IFS 66v/S spectrometer (Bruker AXS Inc., Madison, WI, USA) was used (Fig.8.5-10).

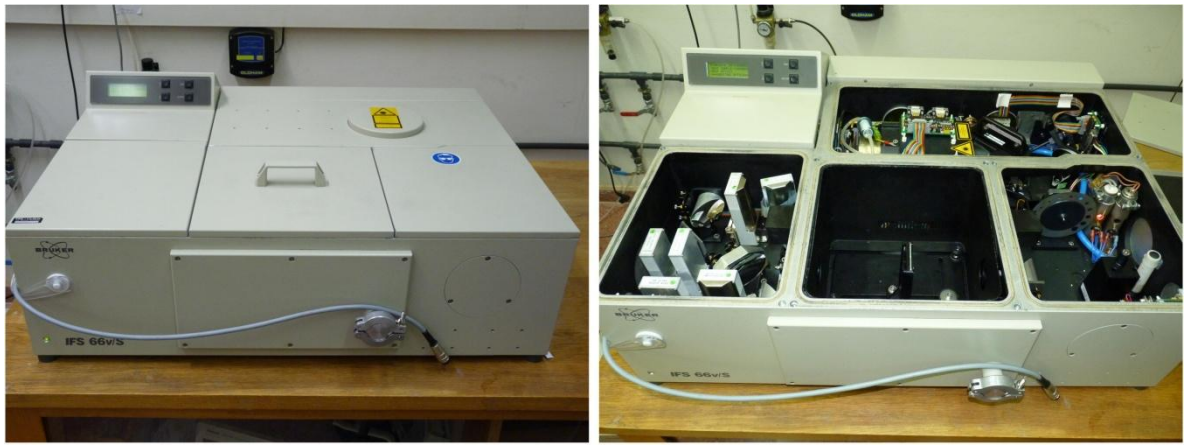

Fig.8.5-10. Bruker IFS 66v/S spectrometer

FTIR spectra of ATZ nanopowders were measured as-prepared as well as calcined at different temperatures from 500 °C to 1350 °C. The as-prepared and calcined powders were mixed in agate mortar with potassium bromide (KBr) and after uniaxial pressed into 13 mm diameter pellets. KBr compound was chosen because does not have any peaks in the range of IR spectrum of ATZ ceramic. Obtained bands were compared with alumina reference spectra.

8.5.4 Inductively coupled plasma-optical emission spectroscopy (ICP-OES)

ICP-OES is designed to determine the composition of a wide variety of materials, with excellent sensitivity. An ICP is an Inductively Coupled Plasma, which is the excitation source used in Optical Emission and Mass Spectrometry instruments (Fig.8.5-11)

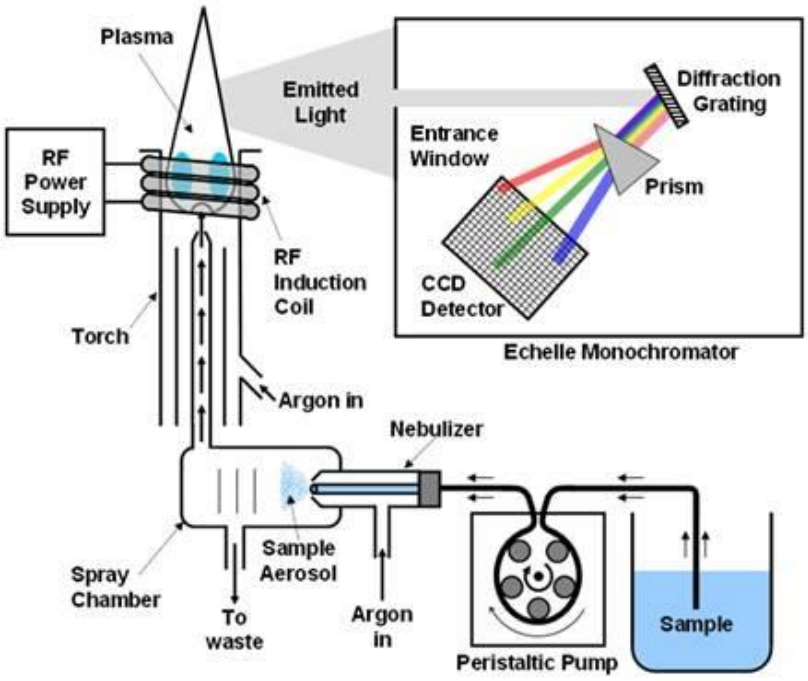

Fig.8.5-11. Basic design of the ICP-OES instrument

The ICP source consists of a quartz torch inside a radio frequency (RF) coil. Argon is passed through the torch and RF energy is applied to the coil. When a spark is added to the

highly energized argon atoms, electrons are stripped from the argon, and the plasma is formed. The argon ions and free electrons are further agitated by the RF field, causing the temperatures within the plasma to reach approximately 8000-10000 Kelvin. In most analyses using ICP techniques, the sample is introduced in liquid form, meaning solid materials will need to be dissolved in an aqueous solution prior to analysis. The liquid is converted to an aerosol using a nebulizer and is then sprayed into the center of the plasma. Very quickly (in both distance and time), the particles within the aerosol are dried, atomized, ionized, excited and relaxed.

The ICP-Optical Emission Spectrometer separates the light emitted from the plasma into its discrete component wavelengths using a diffraction grating (Fig.8.5-12).

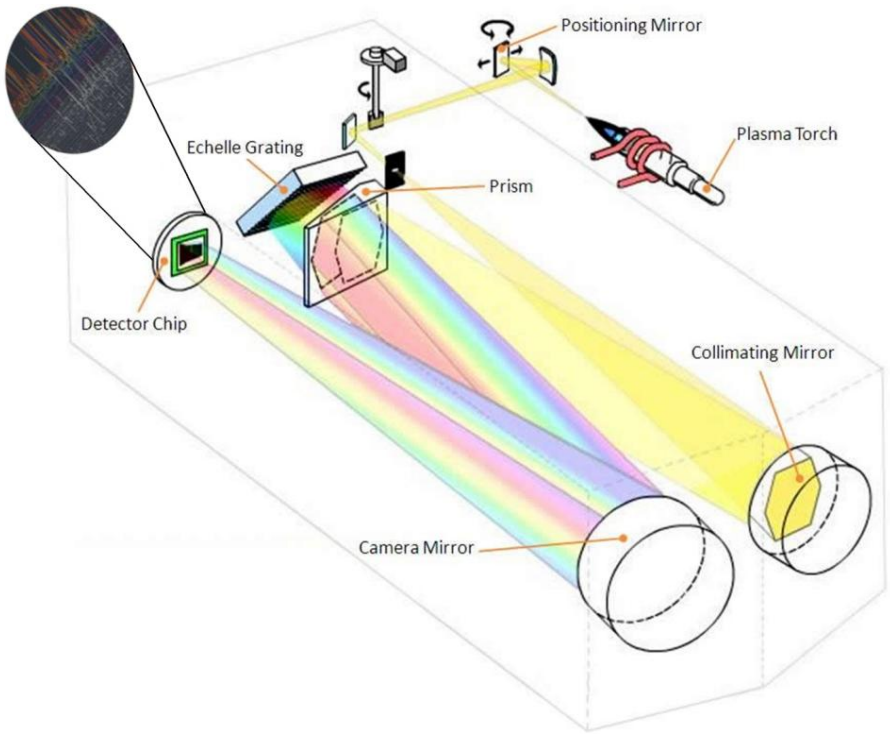

Fig.8.5-12. Optical layout of ICP-OES spectrometer

Each element in the periodic table has its own distinct set of emission wavelengths. Charge-coupled detectors (CCD) are used to quantify the amount of light at a given wavelength. Within the calibration range of the instrument, the amount of light on a given wavelength is proportional to the concentration of the corresponding element in the solution presented to the instrument. Once this concentration is known, the mass fraction of the element in the material being tested can be calculated.

In this work the distribution of elements in nanopowders was characterized by ICP-OES equipment (Agilent 720, Agilent Technologies, Santa Clara, CA, USA) (Fig.8.5-13).

Fig.8.5-13. General view of ICP-OES Agilent 720 equipment

8.5.5 Microscopy

Microscopy implies obtaining magnified images to study the morphology, structure, and shape of various features, including grains, phases, embedded phases, embedded particles, and so on. For small features, electron microscopy techniques such as scanning electron microscopy (SEM) and transmission electron microscopy (TEM) are the tools of choice.

8.5.5.1 Scanning Electron Microscopy (SEM)

The SEM is an instrument that produces a largely magnified image by using electrons instead of light to form an image. As shown in Fig.8.5-14 the electron beam goes across different lenses in the scanning electron microscope, crosses the copper coils and scans the sample while a secondary electrons detector collects those secondary electrons that are emitted from each surface point.

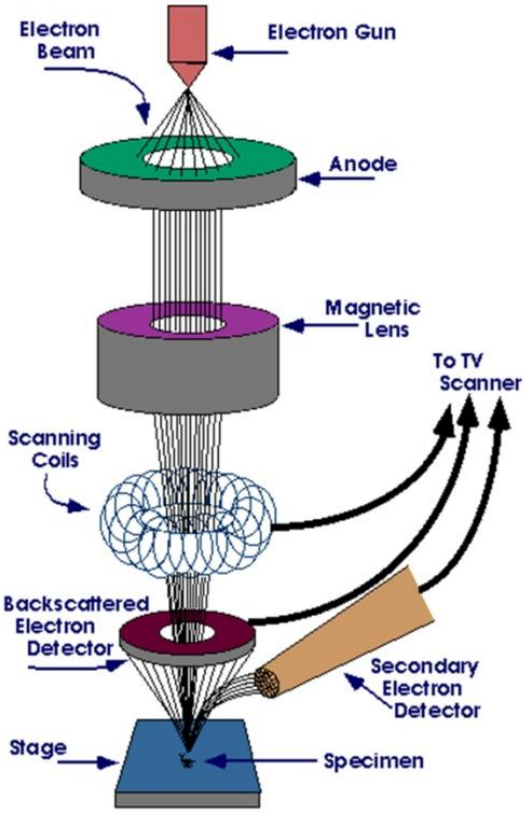

Fig 8.5-14. Diagram of a scanning electron microscope

Simultaneously, the focus of a cathode-ray-tube provides contrast at the image. The current through the coils generates a strong sweeping magnetic field, that acts as a convex lens deflecting the axial rays towards the focus [11, 12]. A beam of electrons is produced at the top of the microscope by an electron gun. The electron beam follows a vertical path through the microscope, which is held within a vacuum. The beam travels through electromagnetic

fields and lenses, which focus the beam down toward the sample. The diameter of the electron beam limits the image resolution, and the final current in the probe determines the intensity of secondary and backscattered electrons, and X-ray signals [13]. The angle of the conical beam impinging on the specimen governs the range of heights on the specimen that will simultaneously be in focus. The acceleration voltage (kV) determines the reliability degree on the image of the sample surface. The standard accelerating voltage of a scanning electron microscope ranges from 2 kV to 50 kV, whilst the resolution goes from 20 to 50 Angstroms [14, 15].

The SEM versatility for the study of solids is derived from the variety of interactions that the electron beam undergo within the specimen. As seen in Fig. 8.5-15A, these interactions can be divided into two classes: (1) elastic events, which affect the trajectories of the beam electrons within the specimen without significantly altering the energy, and (2) inelastic events, which result in a transfer of energy to the solid that leads to the generation of secondary electrons, Auger electrons, characteristic X-rays, long-wavelength electromagnetic radiation in the visible, ultraviolet, and infrared regions, electron-hole pairs, lattice vibrations (phonons), and electron oscillations (plasmons) [16]. All these interactions derive information about the solid's nature, shape, composition, crystal and electronic structure, internal electric or magnetic fields, etc [17]. Due to the Coulomb force, the electrons are backscattered when they interact with the atomic core. Only a small amount of energy is lost in this interaction, so electrons may reach the surface of deep areas. The backscattered electrons vary with the type of core, providing information about elemental composition in the material. Furthermore, both incident electrons and backscattered electrons can interact with atomic electrons, ejecting secondary electrons of

low-energy of outer layers. Because secondary electrons are released in all directions, they allow to study topography [18].

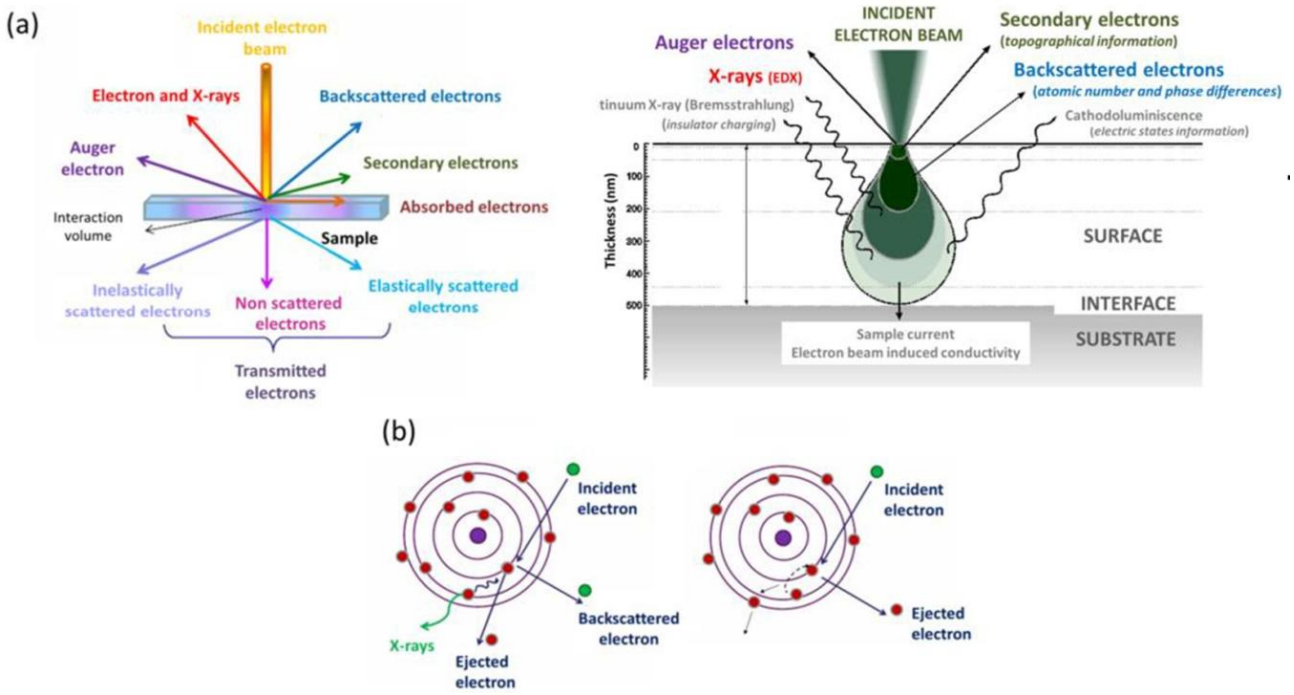

Fig.8.5-15. Interactions of an incident electron beam with the solid surface (A); electrons and X-rays (B)

An alternative interaction of electrons with matter involves a high energetic incident beam that ejects other electrons of inner atomic layers, resulting into ionized atoms (Fig. 8.5-15B). This unstable system will return to the minimum energy state; if taking place the emission process, and an electron of higher orbit occupies the vacant space, the excess of energy would be emitted as a photon of X-rays. Their detection is the base of the X-ray Analysis Energy Dispersive (EDS) or Wavelength (WDS) technique, a chemical analysis that takes place by measuring the energy and the intensity distribution of the X-ray signals associated with the focused electron beam. When the energy excess is yielded to a third

electron into an upper layer, this may be released as an auger electron. Unlike photons of X-rays, the low-energetic auger electrons can only be detected near the surface [18, 19].

The focused ion beam (FIB) instrument is similar to a scanning electron microscope, except that the beam that is rastered over the sample is an ion beam rather than an electron beam. Secondary electrons are generated by the interaction of the ion beam with the sample surface and can be used to obtain high-spatial-resolution images. In most commercially available systems, Ga ions are used, and their sputtering action enables precise machining of samples (Fig.8.5-16).

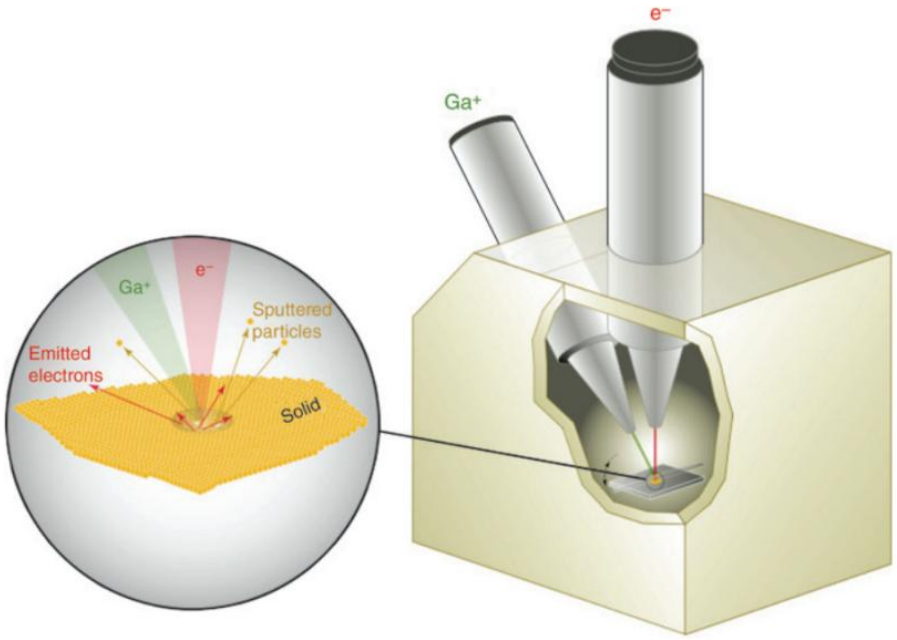

Fig.8.5-16. Schematic illustration of a dual-beam FIB–SEM instrument. Expanded view shows the electron and ion beam sample interaction.

Most widespread FIB instruments are using liquid-metal ion sources (LMIS). Source ions are then generally accelerated to an energy of 1–30 kV, and focused onto the sample by electrostatic lenses. At low primary FIB currents, very little material is sputtered. At higher primary currents, a great deal of material can be removed by sputtering. A FIB is nowadays

usually incorporated into a scanning electron microscope – often called a dual-beam microscope. This combination of imaging and sample treatment techniques allows the same feature of the sample to be investigated and/or manipulated using either one of the beams. A FIB is therefore used as a precision micro-machining tool, to modify or machine materials at the microscale, including transmission electron microscope sample preparation. Combined with the SEM, slice-and-view techniques have become commonplace procedures. In FIB Slice-and-View mode the FIB is being used to remove sample material in slices such that after every slice a new surface of the sample is seen, revealing new features and details of the sample interior. This can be viewed with the SEM beam. This mode of slicing a sample allows for a 3D-reconstruction and successive view of the sample. However, it is clear that FIB is inherently destructive to the specimen. Gallium ions are larger and heavier than electrons. When accelerated, they (brown spheres in Fig.8.5-17) impinge on a surface and their interaction with the outmost atoms on the substrate will result in atomic ionization and breaking of chemical bonds.

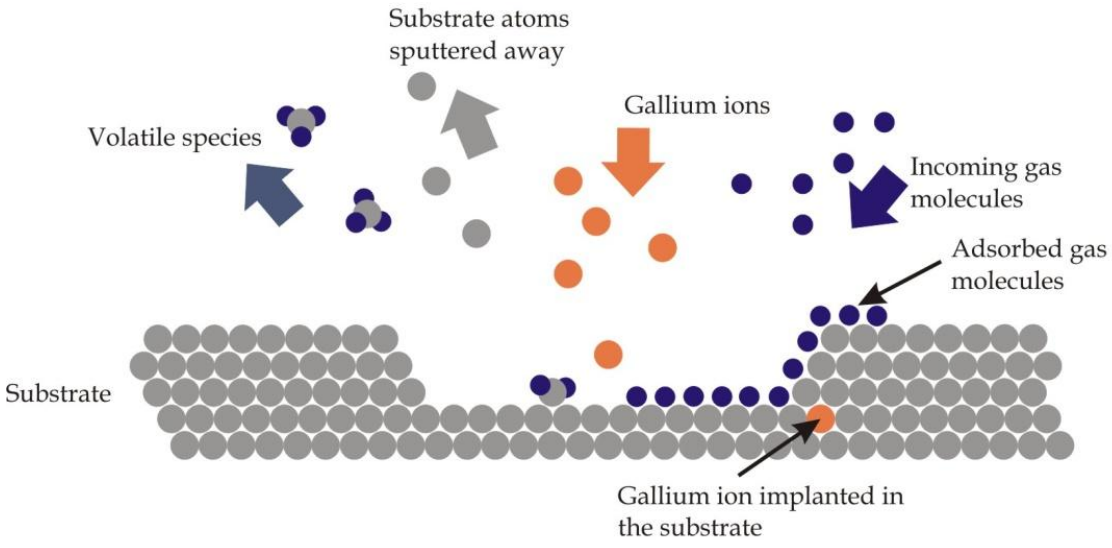

Fig. 8.5-17 Schematic describing atomic processes during ion beam-promoted sputtering

As a result, outer atoms in the substrate are sputtered away, as seen in the grey spheres in Fig.8.5-17. The availability of gas injectors in the FIB chamber can actually assist the atom ejection process by first adsorbing, and then chemically etching the targeted surface (blue spheres in Fig.8.5-17). The use of gases can accelerate milling in large regions and facilitate etching through deep trenches. In addition, gallium ions are likely to be unintentionally implanted during etching. Unintentional gallium ions will also be implanted into the top few nanometers of the surface, and the surface will mostly be made amorphous.

The characterization of materials involved in this work was made with tabletop SEM microscope Phenom G2Pro (Phenom-World, Eindhoven, The Netherlands) and Focused Ion Beam Scanning Electron Microscope (FIB-SEM) AURIGA 60 CrossBeam Workstation (Carl Zeiss Microscopy, Jena, Germany), which integrates an Energy Dispersive X-ray spectrometer (EDS) Noran 6 system (Thermo Electron Corporation, Waltham, Massachusetts, USA) for full-scale elemental analysis of samples.

The Tabletop SEM is designed for easy operation and maintenance and also enables the characterization of micro scale samples with high quality imaging at magnifications up to 20kX. The touch screen feature that allows users to navigate the entire sample makes the characterization process easier and requires considerably less time (Fig. 8.5-18A). In addition, 3D Roughness reconstruction application (Phenom TM Pro Suite) is able to generate three-dimensional images and submicrometer roughness measurement.

Meanwhile analyses at high magnification and spot chemical analyses using EDS were carried out by FIB-SEM microscope (Fig. 8.5-18B). The FIB-SEM uses the electron GEMINI e-beam column which includes the combination of the source and the magnetic or electrostatic lens elements. The main advantage of such a design is that there is virtually no magnetic field on the specimen that could distort the imaging if the specimen is magnetic.

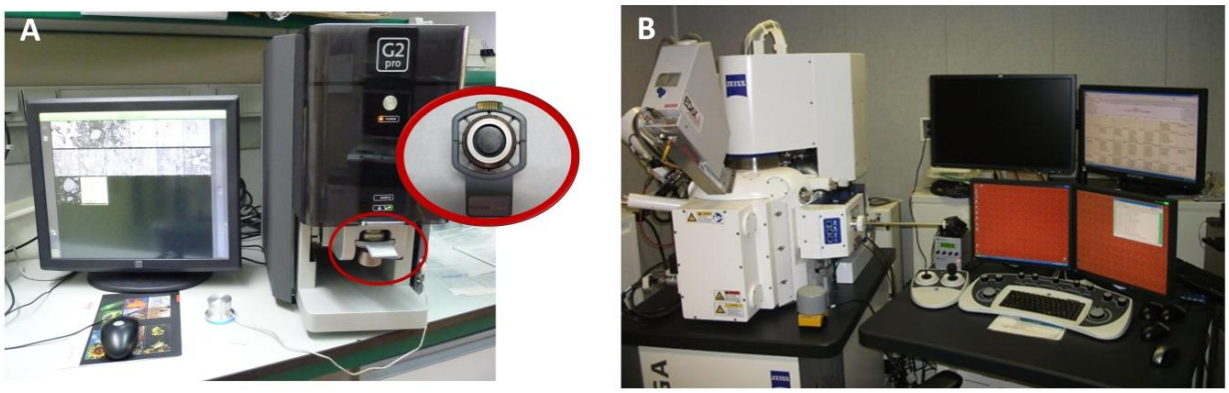

Fig.8.5-18. Tabletop SEM with sample holder (A) and FIB-SEM workstation (B)

For investigations by FIB-SEM polished and thermally etched (50 °C below the sintering temperature, with 30 min dwell time at maximum temperature) ceramic samples were coated with a thin layer of gold. Sputter coating makes the surface of samples electrically conductive; allowing them to be imaged with a SEM. Sputter coater is presented below (Fig.8.5-19). Because cermets could not be thermally treated, they microstructures were studied from polished and fractured surfaces that were visualized by FIB-SEM.

Fig.8.5-19. Sputter coater

8.5.5.2 Transmission Electron Microscopy (TEM)

There are a variety of similarities between SEM and TEM. Both are types of electron microscopes and both use electrons. However, the method used in TEM is based on transmitted electrons. In TEM the source of illumination is a beam of electrons of very short wavelength, emitted from a tungsten filament at the top of a cylindrical column of about 2 m high. When a beam of electrons is transmitted through an ultrathin specimen, interacting with the specimen as it passes through it. Thus, another point of difference is the sample preparations.

In order to evaluate morphologic properties of nanoparticles they were collected during the LAVA process for TEM investigations by positioning sample grid (perforated carbon film on copper mesh, Plano GmbH, Germany) directly into the flowing particles aerosol at the beginning of the tube system. By diffusion randomly distributed particles were deposited on the TEM grids, thus unaffected by an otherwise necessary later preparation. Meanwhile for the microstructure and composition study the sintered sample must be electron transparent (~ 100-150 nm thick). The steps which were used for sintered sample preparation for TEM investigations are described below.

Firstly, the sintered and polished sample was cut into thin slices with thickness of the order of 250 μm using IsoMet 5000 precision cutter (Buehler, Lake Bluff, IL, USA) (Fig.8.5-20).

Fig.8.5-20. IsoMet 5000 precision cutter

Then, from the slices the discs with diameter of 3 mm are punched by using an ultrasonic disc cutter. And lastly, for final thinning of discs ion milling method was used. Fig.8.5-21 exhibits disk specimen ready for TEM observation.

Fig.8.5-22. Disc with a diameter 3 mm for TEM investigation

Electromagnetic lenses allow the beam to be focused and magnification to be modulated. The imaging system also consists of electromagnetic lens system and a screen which has a fluorescent plate. The plate glows when hit by the electrons after passing through the specimen. Diagram of a transmission electron microscope is shown in Fig.8.5-23.

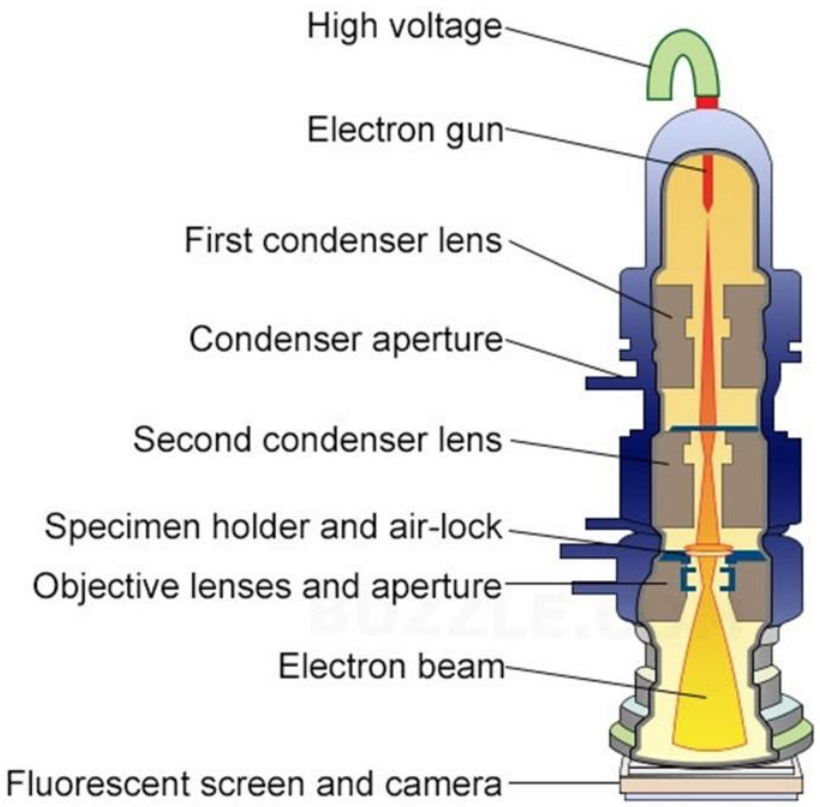

Fig.8.5-23. Diagram of a transmission electron microscope

In terms of magnification and resolution, TEM has an advantage compared to SEM. TEM has up to a 50 million magnification level while SEM only offers 2 million as a maximum level of magnification. In addition, only small amount of sample can be analyzed at a time with TEM. Additionally, if SEM focuses on the sample's surface and its composition, whereas TEM provides the details about internal composition. Therefore TEM is used for imaging of dislocations, tiny precipitates, grain boundaries and other defect structures.

In this work the images obtained by the transmission electron microscopy (JEOL 4000-EX, Tokyo, Japan) which is shown below (Fig.8.5-24), were analysed in order to evaluate morphological properties of nanoparticles and perform efficient electronic structure and density functional ab-initio calculations for 3Y-TZP/Ta interfaces as well.

Fig.8.5-24. Transmission electron microscope JEOL 4000-EX

8.5.6 Density

Density measurements were performed on each sintered specimen using the Archimedes principle. The measurements were carried out in distilled water on a Sartorius YDK01 (Goettingen, Germany) balance and associated density kit (Fig.8.5-25). Since there was no

reaction between ceramic matrix and metallic particles, the theoretical density of the composites was calculated according to the rule of mixtures.

Fig.8.5-25. Density kit with a SPS sintered sample immersed to distilled water

The mass in of each specimen was measured three times. The mean values of these air and water masses were used as actual and suspended weights, respectively, and the density was calculated using the equation:

$$\rho = W_a \cdot (\rho_{fl} - 0.0012) / (0{,}99983 \cdot G) + 0{,}0012 \qquad (8.5\text{-}4)$$

Where *Wa* is weight of sample in air (*g*), *G* weight of sample immersed in water (*g*) and p_{fl} is the density of water (g/cm^3). Water temperature (°*C*) was recorded and p_{fl} obtained from the chart.

8.5.7 Mechanical properties

8.5.7.1 Vickers Hardness

Hardness is defined as resistance to surface indentation or penetration by applied mechanical load. There are a number of tests available for hardness testing. In this work the hardness of ceramics and ceramic-metal composites was measured using the Vickers indentation (H_v) method that involves the application of a load via a square pyramid diamond indenter. The methodology used for the determination of Vickers hardness, H_V, was in accordance with ASTM C 1327-9925 specifications [20].

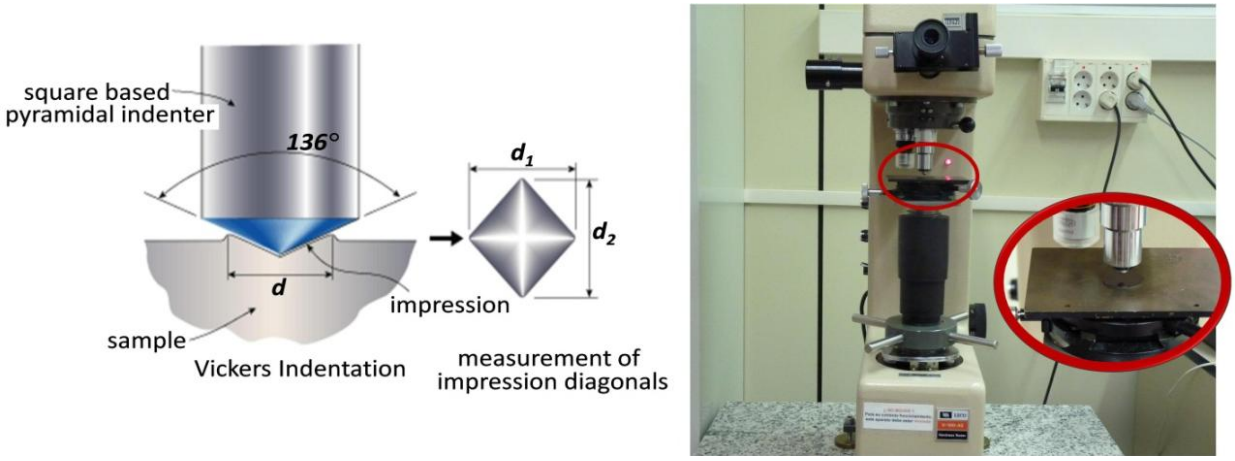

Fig.8.5-26. Diagram of the Vickers indenter and measurement of the impression diagonals (left) and LECO indenter (right)

The suitable load was applied during ten seconds by a Vickers diamond indenter (Leco 100-A, St. Joseph, MI, US) with a diamond-tip of pyramidal geometry and an apex of 136°, such as shown in Fig.8.5-26. Ten Vickers impressions were carried out in the polished surfaces of each one of the tested samples.

The indentation diagonal lengths were measured using a scanning electron microscopy (SEM Phenom G2, Eindhoven, The Netherlands). Then the mean result calculated, and this

value employed to calculate a hardness number which is equivalent to the mean force per actual unit area of indenter surface contacting the test surface using equation:

$$HV = 0.1891\ P/d^2 \qquad (8.5\text{-}5)$$

where, P is the applied load (N) and d is the average length of the two diagonals (mm).

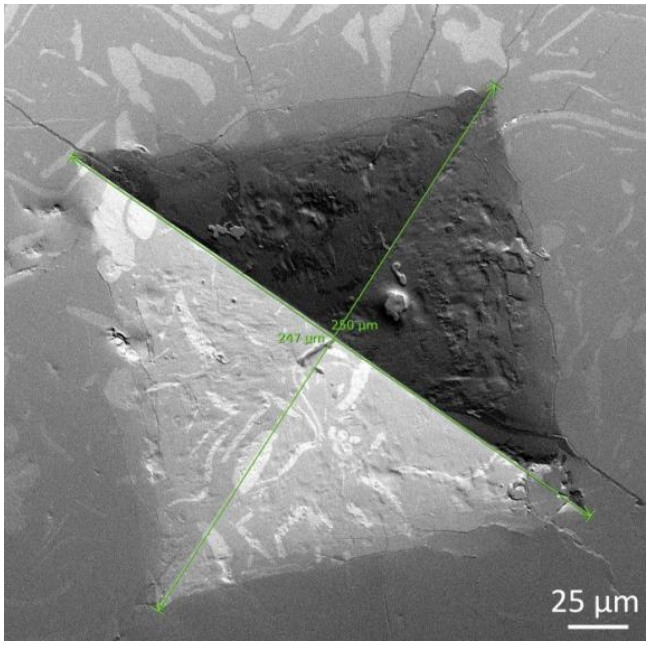

Fig.8.5-27. SEM photo of indentation print of ceramic-metal composite with measured diagonals

8.5.7.2 Three point bending test

Extremely low ductility of ceramic materials does not allow measuring their mechanical properties by conventional tensile test, because specimens can be easily broken during alignment, gripping or testing. Therefore, the most commonly performed tests on ceramic materials is a test of flexural strength and performance. Flexural bend tests help determine the tensile properties of ceramics, without encountering the difficulties of a uniaxial tension test. This test produces an inhomogeneous stress distribution in the specimen, with the

maximum tensile and compressive stresses arising on opposing surfaces, and with a zero-stress axis in the specimen center. Fig.8.5-28 shows a schematic of a three point bend test used in this work. The sample is placed on two supporting points a set distance apart and a third loading pin is lowered from above at a constant rate until sample failure.

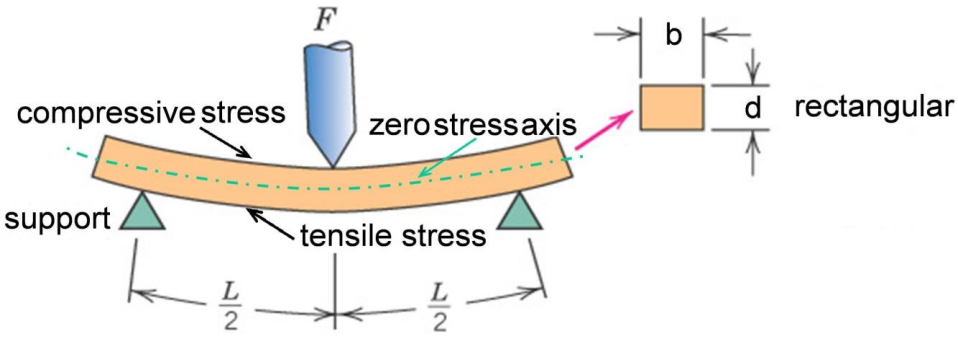

Fig.8.5-28. Schematic of three point bending test

A bending load provides values for highest stress experienced within the material at its moment of rupture and is called flexural strength (σ_f) or modulus of rupture. Flexural testing is performed according to ASTM C1161-13 [21]. Shimadzu Autograph AG-X (Kyoto, Japan) universal testing machines which was used to determine the strength is presented in Fig.8.5-29.

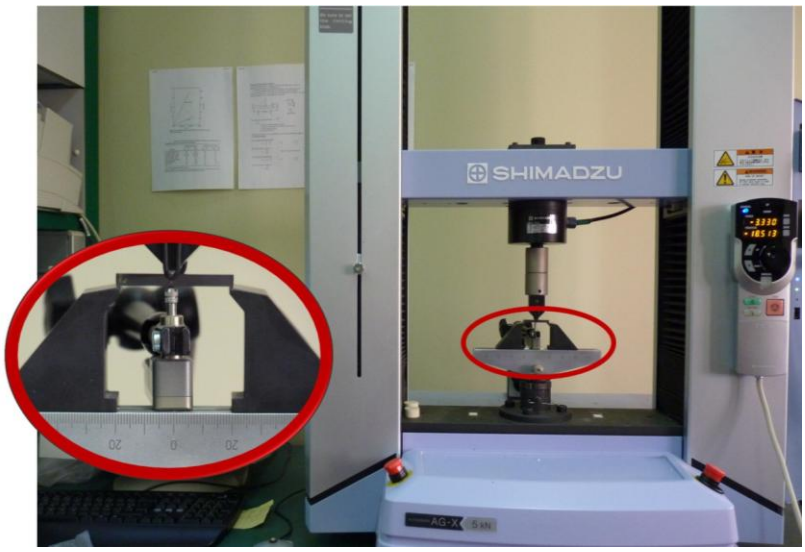

Fig.8.5-29. Shimadzu universal testing machine with prismatic specimen

The strengths, σ_f, were calculated from the failure loads, F (N), and the specimen dimensions, using the following equation:

$$\sigma_f = \frac{3FL}{2bd^2} \quad \textbf{(8.5-6)}$$

where L is the distance between support points (mm), b is the width (mm) and d is the height (mm) of the specimen. The Young modulus (E) was obtained from the slopes of stress-strain plot of three point bending tests as well. A typical plot for a homogeneous ceramic that was tested to failure is shown in Fig.8.5-30. A static extensometer was used to measure the deflection with an error in the measurement of 0.1%.

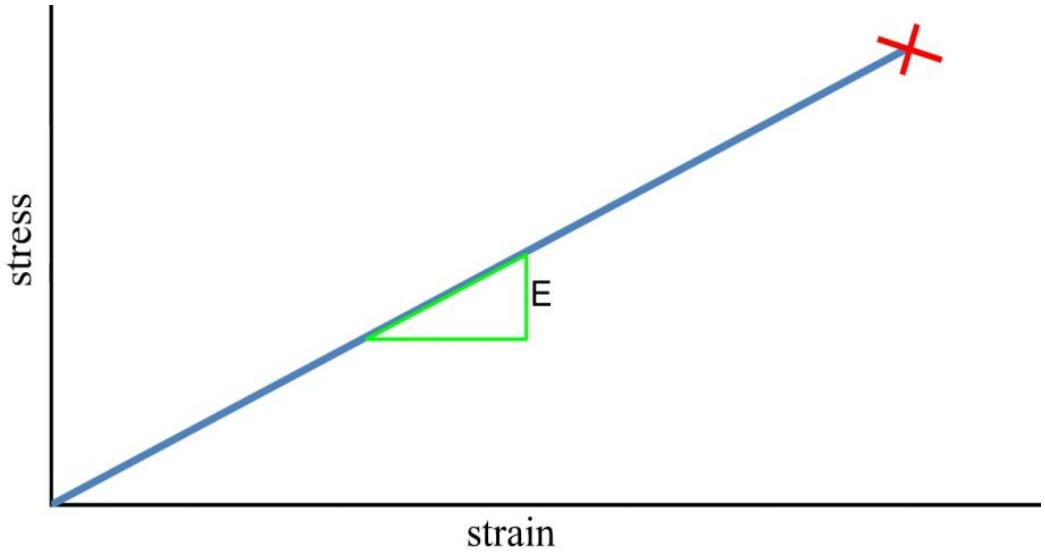

Fig.8.5-30. A typical stress-strain curve for a homogeneous ceramic tested until fracture (***X***). The slope of the curve represents the Young's Modulus (E).

8.5.7.3 Biaxial flexure strength and Young modulus (for the disk-shaped specimens)

As was mentioned above, due to the inherent brittleness, strength of ceramics are normally measured in 3- or 4-point uniaxial bending tests by using prismatic specimens. However, the disadvantage of this method is the specimen preparation; rectangular bars have to be cut from the bulk material and the tensile surface of the test specimens has to be defect free, i.e., surface and edge preparations should be performed. Alternative to 3- or 4-point bending tests is biaxial flexure test. The advantage of this test is that the central portion of the specimen is subjected to a uniform biaxial state of stress. The test is independent of edge conditions and accounts for all flaws regardless of direction. The technique is simple, low cost, and does not require rigorous sample preparation.

The method determines the strength utilizing the exact elastic solutions for small deflections. For mechanical testing, ceramics can be produced in cylindrical shape and the discs can be cut from the green body or sintered part. There are different loading fixtures are commonly used to examine the biaxial flexure strength ceramics disk-shaped specimens: piston-on-three-balls test, ball-on-three-balls test, ring-on-ring test, and ball-on-ring test. The differences between them are how the load to the specimen is applied and the support configuration. Load to the disc can be applied at the center by a single ball or a flat surface piston/punch or the disc can be concentrically loaded by a ring or ring of balls, i.e. equally spaced balls on a ring (circle). Supporting of the disc can be made by a concentric ring or concentric ring of balls. The piston-on-three-balls test method was standardized in ASTM F 394 [22] and ISO 6872 [23], therefore this loading scheme has have been selected for evaluation of mechanical properties of composites (Fig.8.5-31).

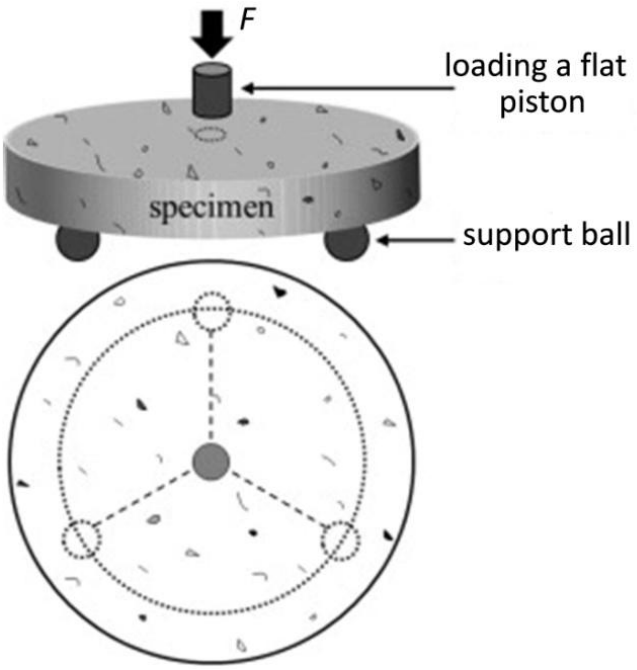

Fig.8.5-31. Schematic drawing of piston-on-three-balls test method for biaxial tensile strength

The same universal testing machine as in three point bending test was used to determine flexural strength (Fig.8.5-32).

Fig.8.5-32. Universal testing machine with biaxial configuration

Each disc-shaped polished specimen with thickness 1.3 – 1.5 mm, was placed centrally on three hardened steel balls (with the diameter of 3mm, positioned 120° apart on a support circle with a diameter of 10 mm). The polished surface of the specimen was the tension side while the unpolished surface was loaded with a flat punch with a diameter 1.2 mm at the center of specimen with a cross head speed of 1 mm/min until failure occurred. The load to failure (*N*) of each specimen was recorded and the biaxial flexural strength (MPa) was calculated using the following equation:

$$S = -0.2387\,P(X - Y)/d^2 \qquad (8.5\text{-}7)$$

Where *S* is the maximum tensile stress (MPa), *P* the total load causing fracture (*N*) and *d* is the specimen thickness at fracture origin (mm). *X* and *Y* were determined as follows:

$$X = (1+\nu)\ln(r_2/r_3)^2 + [(1-\nu)/2](r_2/r_3)^2 \qquad (8.5\text{-}8)$$

$$Y = (1+\nu)[1+\ln(r_1/r_3)^2] + (1-\nu)(r_1/r_3)^2 \qquad (8.5\text{-}9)$$

Where ν is Poisson's ratio; r_1 is the radius of the support circle, r_2 is the radius of the loaded area (mm), r_3 is the radius of the specimen (mm), *d* is the specimen thickness at the origin of fracture (mm).

Determination of flexural strength of indented specimens was based on the same protocol as in the biaxial test. Indentation prints were obtained on finely polished surface. The mechanical tests were performed immediately after indentation to avoid any subcritical crack growth due to stress corrosion effects. Special effort was made to examine all specimens after testing using scanning electron microscopy, to verify that the indentation contact site acted as the origin of failure.

The elastic modulus of composite was calculated using the equation:

$$E = \frac{\beta P a^2}{\omega h^3} \qquad (8.5\text{-}10)$$

E – Elastic Modulus, MPa; β– center deflection function; P – load, N; ω – center deflection, mm; a – radius of support points, mm; h – thickness of sample, mm.

The centre of deflection function given by Equation 8.5-11 is dependent upon the number of supports (m), Poisson's ratio (ν), and the ratio (t) of the radius of the support circle to the radius of the disc.

For this study, $\nu = 0.25$, and $r_1 = 5$ mm.

$$\beta = -0.0642 - 2.1900\,m^{-3} + (0.5687 + 3.254\,m^{-3})(1-\nu^2) + \\ + \left[-0.3793 + 11.0513\,m^{-3} + (0.5223 - 7.8535\,m^{-3})(1-\nu^2)\right] t^3 \qquad (8.5\text{-}11)$$

8.5.7.4 Toughness

Fracture toughness describes a material's resistance to brittle fracture when a crack is present. Low fracture toughness values increase the risk of catastrophic failure of a ceramic component. In ceramics fracture starts from any type of bulk discontinuities or tiny defects which act as a localized stress concentrators. This may occur due to bad or incomplete mechanical design, insufficient surface finish, cracks introduced during service and mishandling. Thus, at certain stress levels these defects might lead to catastrophic failure in non-ductile materials. There are several methods to determine fracture toughness of brittle materials. In this work Vickers indentation fracture toughness (VIF) for monolithic ceramics and single-edge-notch-beam (SENB) techniques for ceramic-metal composites has been selected.

8.5.7.4.1 Indentation toughness

Indentation techniques for assessing fracture toughness are attractive due to the simplicity and expediency of experiments, and because they potentially allow the characterization of both local and bulk fracture properties. Such tests can be relatively quick and easy to perform, require little specialized equipment, and can allow probing of localized microstructural features. The Vickers indentation fracture (VIF) test has been selected to determine fracture toughness of ceramics. The indentation and measured techniques were the same as for Hardness measurement. Only difference that for VIF were measured cracks instead of diagonals of indentation print. The Vickers indentation print of ZrO_2 with measured diagonals is plotted in Fig.8.5-33.

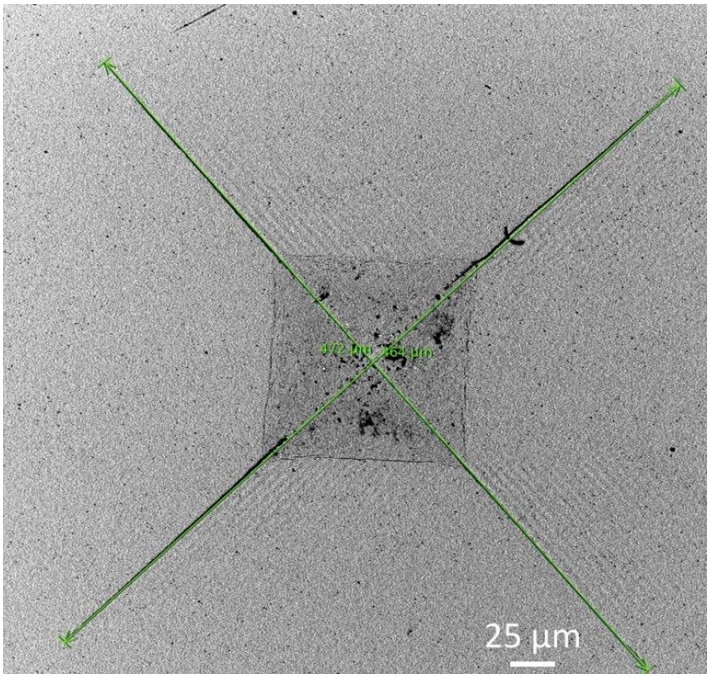

Fig.8.5-33. Measured cracks after Vickers indentation of ZrO_2

The fracture toughness was calculated using the formulations given by Miranzo and Moya [24].

$$K_{IC} = \frac{0.047 \cdot P}{\left(d^{0,42} \cdot c^{1,08}\right)\left[f\left(E/H_v\right)\right]} \quad ; \quad c/d > 2.8 \qquad \textbf{(8.5-12)}$$

$$K_{IC} = \frac{0.0232 \cdot P}{\left(d \cdot c^{1/2}\right)\left[f\left(E/H_v\right)\right]} \quad ; \quad c/d < 2.8 \qquad \textbf{(8.5-13)}$$

Where

$$\left[f\left(E/H_v\right)\right] = \frac{0.768 \cdot \left(E/H_v\right)}{0.05 + 0.612 \cdot Ln\left(E/H_v\right)} - 2 \qquad \textbf{(8.5-14)}$$

where, *Hv* isVickers hardness of material (GPa), *P* is the applied load (N), *d* is the average length of the two diagonals (mm) and *c* average length of cracks (mm).

Vickers indentation technique is appropriate testing method to measure the fracture toughness of monolithic ceramic. It is necessary to mention that the VIF test was used not only of its simplicity and to obtain results which are comparable with previous investigations as well. However despite of all advantages, the VIF results were disappointing primarily because of the high scatter. The cracks are very complex and often are not the idealized. A practical problem is that it is difficult to determine the type of cracks and to precise measure the crack lengths. The strong dependence of the computed fracture toughness upon the crack length, and the difficulty in measuring such combined to cause high scatter. Variations in values arise depending on the particular laboratory and the observer. Sometimes a plausible estimate of fracture toughness is obtained, but just as often an incorrect estimate is obtained. Even if one settled on one equation, the calculated

fracture toughness often depends upon the indentation load [25]. In addition, 3Y-TZP/Ta cermets show little evidence of cracking which demonstrated that this method is not suitable for measuring fracture toughness of these composites. This is why alternate method was carried out to determine fracture toughness of composites. This method is called Single Edge Notch Beam (SENB).

8.5.7.4.2 Single Edge Notch Beam (SENB)

In order to determine fracture toughness of a material SENB technique has been selected. The sintered and polished samples with the same dimensions as in three point bending test (Section 8.5.7.3) were prenotched in the center using diamond saw blade and then pre-crack was introduced by tapping on a razor blade placed in the root of a previously machined notch. The SENB testing installation has been performed as per instructions [26] according to three point bending test. The specimen was placed with the notch face down and loaded at a constant rate of stress. The values of fracture toughness, K_{IC}, were estimated by Equation 8.5-15 from the maximum load (F), as well as the dimensions of the specimen and notch such as shown in Fig.8.5-34.

$$K_{1C} = g\left[\frac{F\,S\,10^{-6}}{BW^{3/2}}\right]\left[\frac{3[a/W]^{1/2}}{2[1-a/W]^{3/2}}\right] \qquad (8.5\text{-}15)$$

where F is maximum failure force (N), B is the specimen thickness (mm), W is the sample width (mm), S is the distance between supports (mm), a is the length of notch (mm) and g function of the ratio a/W for three-point flexure is calculated as below:

$$g = \frac{1.99 - [a/W][1-a/W][2.15 - 3.93[a/W] + 2.7[a/W]^2]}{1 + 2[a/W]} \qquad (8.5\text{-}16)$$

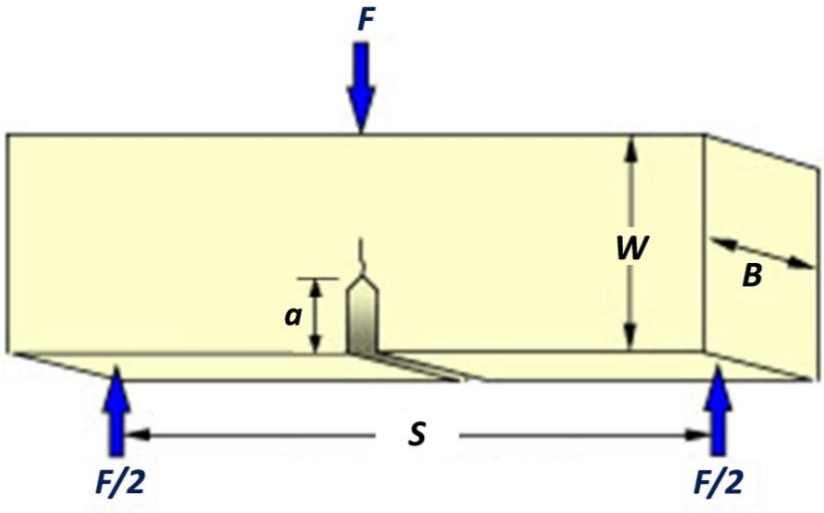

Fig.8.5-34. Schematic of test specimen geometry for SENB test

All experiments were carried out in a Shimadzu AG-X universal testing machine (Fig.8.5-35).

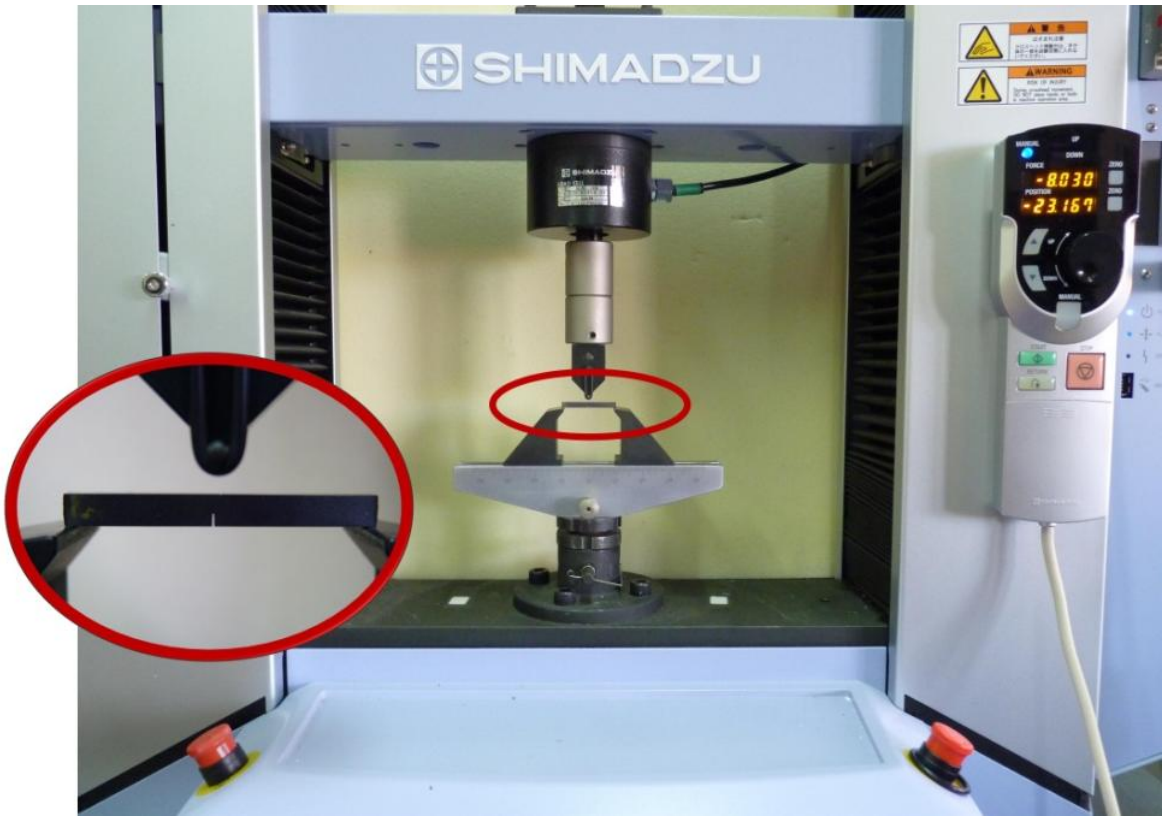

Fig.8.5-35. Shimadzu testing machine with notched specimen

The advantages of this testing method are: simple loading configuration, well-defined notch and easy measurement of the precrack length. Additionally this technique avoids the main problem in *VIF* method, i.e. a scatter in the measurement values.

8.5.7.5 Fatigue testing

Fatigue is the condition whereby a material cracks or fails because of repeated (cyclic) stresses applied below the ultimate strength of the material. Fatigue failure often occurs quite suddenly with catastrophic result. Therefore, fatigue analysis and fatigue strength prediction are highly required especially for the case of fail-safe or damage tolerance design. Accurate prediction of fatigue life is a challenge in ceramic-metal composites due to the complicated nature of fatigue crack initiation and propagation, the interfaces' properties and complex material behavior under loading and unloading regimes. There are many factors influencing the fatigue behaviour, such as the material type, structural geometry, loading and working conditions, etc. The fatigue generally divided into three stages (Fig.8.5-36)

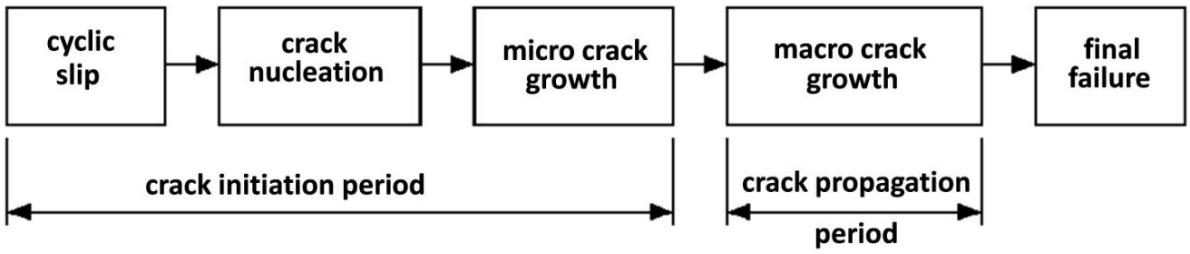

Fig.8.5-36. Different phases of the fatigue life

In fatigue testing, a specimen is subjected to periodically varying constant amplitude stress. The applied stresses may alternate between equal positive and negative value from zero to maximum positive or negative value, or between equal positive and negative values or

between unequal positive and negative values. Various parameters of interest in fatigue are shown in Fig.8.5-37.

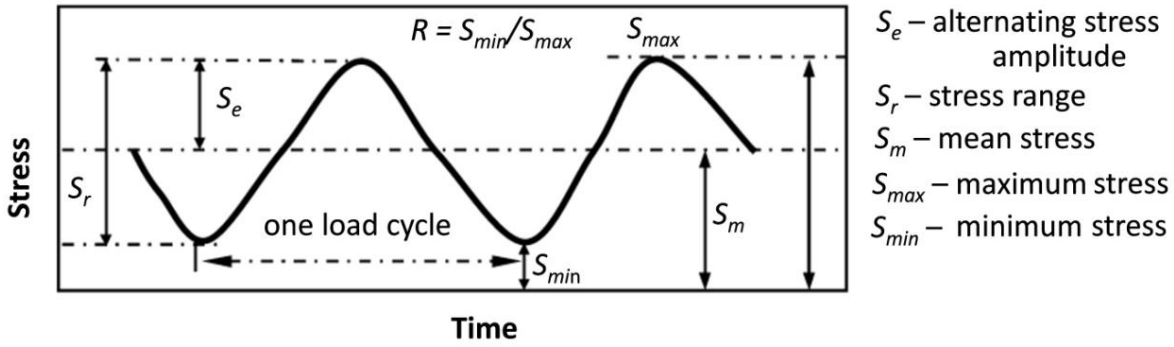

Fig.8.5-37. Various parameters in fatigue

A series of fatigue tests are made on a number of specimens of the different materials at different stress levels. The stress endured is then plotted against the number of cycle sustained. By choosing lower and lower stresses, a value may be found which will not produce failure, regardless of the number of applied cycle. This stress value is called the fatigue limit of the material or the endurance limit. The plot of the Stress amplitude (*S*) versus logarithm of the number of cycles to fatigue failure (*N*) is called stress-cycle diagram or *S*-*N* diagram (Fig.8.5-38).

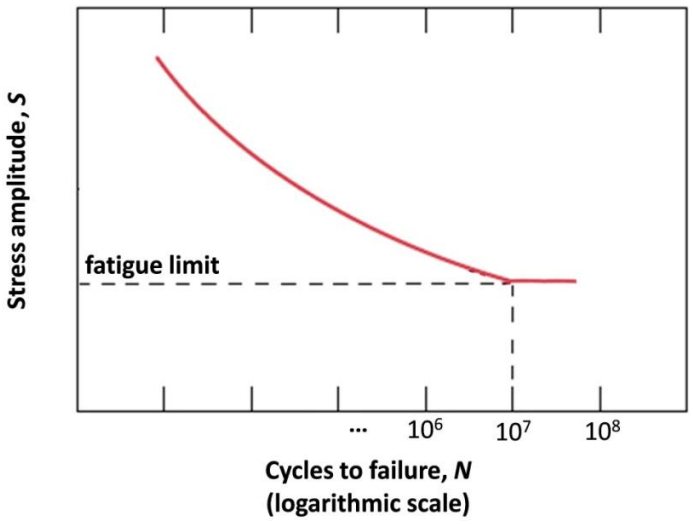

Fig.8.5-38. *S–N* diagram

In order to determine fatigue limit of composites series of similar specimens have been tested. Each sample with the polished surface as the tensile face was placed onto device with three balls which was used in biaxial bending test. The sinusoidal cyclic load at 20Hz was applied with a SHIMADZU electromagnetic testing machine (EMT-1kNV-30, Kyoto, Japan) and the number of loading cycles required to produce failure in each specimen is recorded. Initial stress value for each test was calculated using Equation 8.5-7. The experiments were interrupted at $N = 10^7$ cycles, for samples without failure.

Fig.8.5-39. Electromagnetic fatigue testing machine with biaxial configuration

Indentation fatigue life was analyzed following the same protocol. Indentation prints have been introduced in the tensile surfaces of all of the test specimens. In order to observe crack propagation test was stopped at various stages of cycling tests. At each stop, for SEM

observation, the test specimen was dismounted from the servo-hydraulic machine. After crack length measurements the test was continued until the specimen fractured or reached the final number of cycles.

8.5.8 Tribological properties

In materials science, wear is the erosion of material from a solid surface by the action of another surface. It is about to surface interactions and more specifically the removal of material from a surface as a result of mechanical action. In order to evaluate wear rate of studied materials, reciprocating pin-on-plate friction test with a moving plate and static pin with dead loading arrangement have been carried out in a MT/60/NI tribometer (Microtest, Madrid, Spain) (Fig.8.5-40 A).

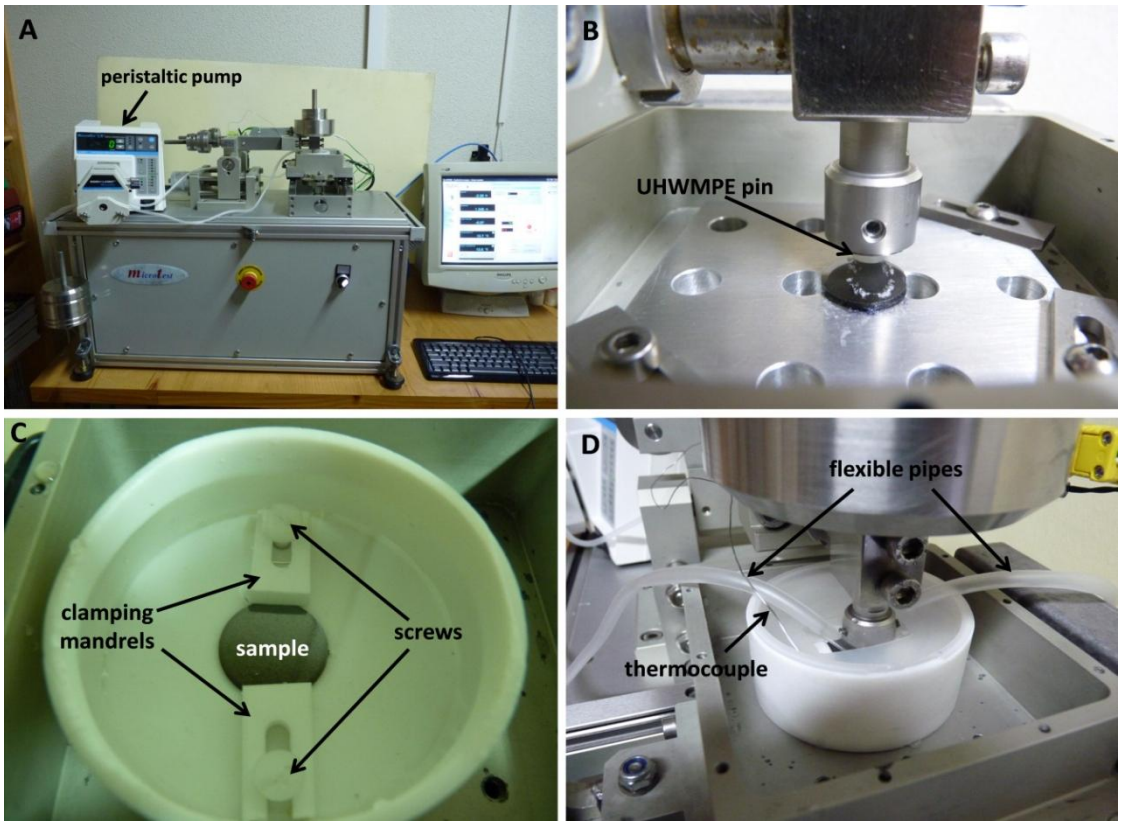

Fig.8.5-40. Configuration of linear reciprocating pin-on-flat apparatus

The following materials were used: flat-ended ultra-high molecular weight polyethylene (UHMWPE) circular cylinder (Fig.8.5-41) as the pin material and SPS sintered zirconia and zirconia-tantalum disks as the plate material (Fig.8.5-42). The measurements were carried out according to ASTM F732-00 (2011) [27].

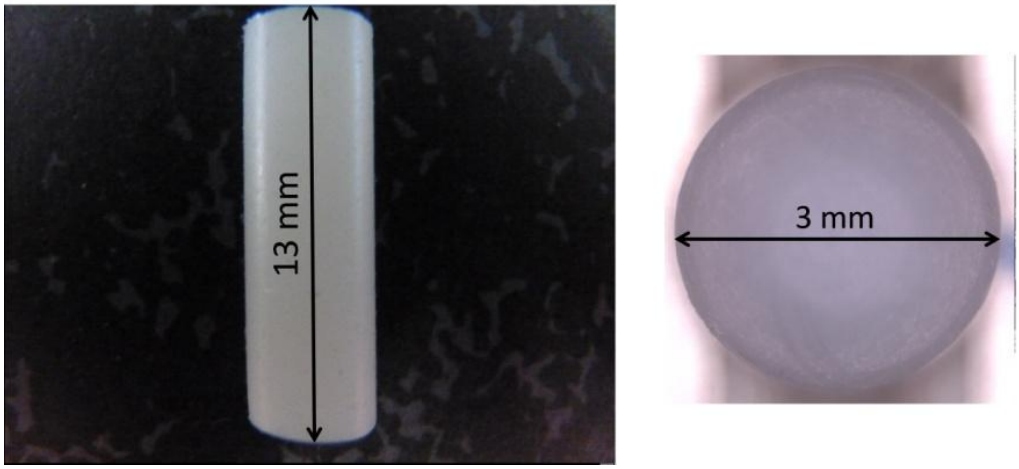

Fig.8.5-41. Flat-ended ultra UHMWPE circular cylinder

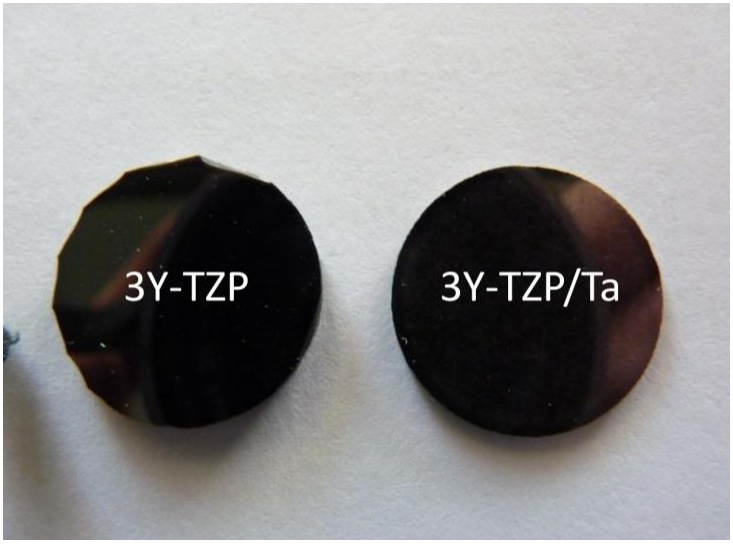

Fig.8.5-42. SPS sintered zirconia and zirconia-tantalum disks of diameter 20 mm

The specimens were rinsed in an ultrasonic cleaner in distilled water for 5 min and air-dried using compressed air before testing. After each sliding test, the worn surfaces were cleared by blowing pressurized air before post-mortem observations. Wear was calculated as

volume loss of the polymeric specimen as a function of sliding distance using the following equation:

$$W = \frac{V}{total \quad sliding \quad distance}\left(mm^3/m\right) \qquad (8.5\text{-}17)$$

Volume loss of the polymer specimen was determined by dividing the experimental weight loss by the density of the polymer.

The tribological tests were performed under dry conditions at room temperature (Fig. 8.5-40B) while under wet conditions the temperature of solution was controlled by heating source and thermocouple and was kept 37 ± 2 °C (Fig. 8.5-40D). The lubricated media, Simulated Body Fluid (SBF) was used as the prototype of the human body liquids that are the modelled bio-environment for the orthopedic implants (Table 8.5-1). SBF was prepared in laboratory according to the procedure for preparing Kokubo's solution while the ionic concentration was kept similar to that of human blood plasma [28, 29].

Table 8.5-1. Ion concentrations (mM) of SBF and human blood plasma

Ion	Simulated Body Fluid	Blood plasma
Na^+	142.0	142.0
K^+	5.0	5.0
Mg^{2+}	1.5	1.5
Ca^{2+}	2.5	2.5
Cl^-	148.8	103.0
HCO^{3-}	4.2	27.0
HPO_4^{2-}	1.0	1.0
SO_4^{2-}	0.5	0.5

For preparation of SBF, the ingredients were added in distilled water, containing in a beakers with continuous stirring. The addition sequence was strictly followed as written, otherwise common ion effect might cause problem. After adding $MgCl_2 \cdot 6H_20$, HCl was added to reduce the *pH*. Then after adding of Tris-buffered saline, 1 mole HCl was added till *pH* is strictly 7.4 ± 0.02. The sample was immersed in SBF during wear tests. In order to avoid corrosion, all parts (water bath, screws and clamping mandrels) of the equipment contacting with a SBF were made of Polytetrafluoroethylene (Fig. 8.5-40C). The SBF solution was pumped from the storage tank into the water bath with a volume of 100 mL and it passed the sample, and then recirculated through to the SBF storage tank back to the system. The peristaltic pump was used to control the rate at which the SBF solution was flowing through the water bath, which was set at 5 mL/min.

8.5.9 Surface roughness analysis

Surface roughness affects several functional attributes of parts, such as friction, wear and tear, light reflection, heat transmission, ability of distributing and holding a lubricant, coating etc. In medical fields the surface finish of machined components is of utmost importance. The desired surface finish is usually specified and appropriate processes are required to maintain the quality. Hence, the inspection of surface roughness of the work piece is very important to assess the quality of a component. Surface profilometer is one among many techniques to measure surface roughness. In contact profilometry methods a fine diamond tip travels in a line over a surface and in this way records a height profile. A variety of surface morphology parameters can be obtained from the height profile, such as, for example, roughness, waviness, the height histogram, skewness and steepness of height distribution , mean local surface slope, contact area percentages, and so on.

Besides tabletop SEM microscope (Section 8.5.5.1), the 3D surface profilometer (Talysurf CLI 500, Taylor Hobson, Leicester, UK) that maps the surface by putting a stylus in mechanical contact with the sample (Fig. 8.5-41) was used for surface roughness measurements. The stylus arm has a 90° diamond tip with a nominal radius of 2µm. The data sampling interval in X and Y was 0.5µm and 2.5µm respectively. The resolution of Z-scale was 32 nm. Fig.8.5-41 shows close-up of stylus arm with diamond tip during the measurement process of SPS sintered 3Y-TZP/Ta composite (B) and UHMWPE pin that was used in wear test (C). Data were analyzed using Talymap 3D Analysis Software.

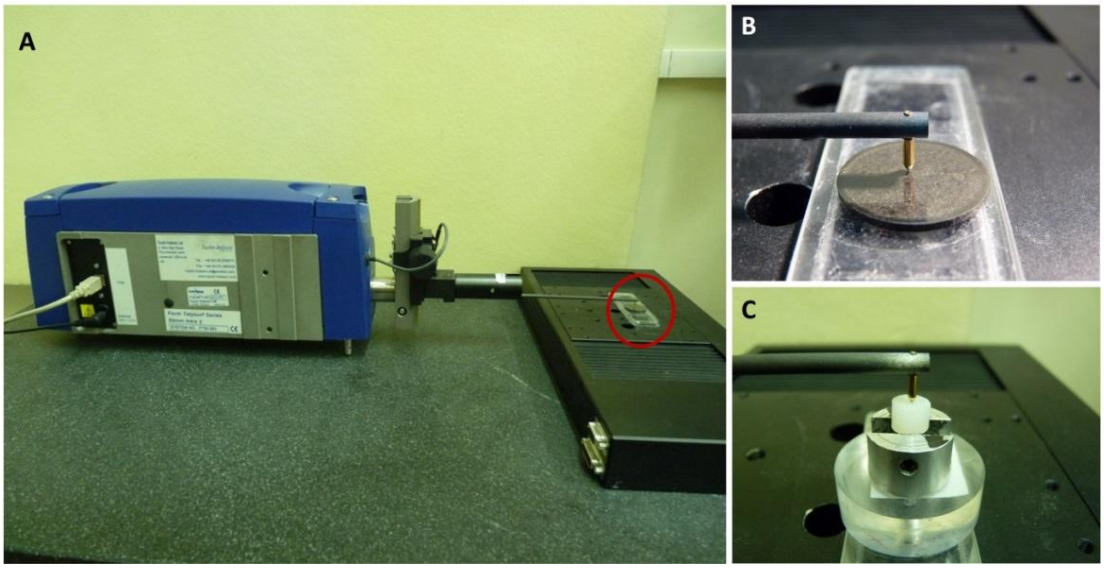

Fig.8.5-41. Talysurf profilometer (A) and close-up of stylus arm with diamond tip (B, C)

8.5.10 Low temperature degradation (LTD)

Accelerated aging tests under hydrothermal environment were conducted in autoclave (Microclave 4001404, J.P. Selecta, Barcelona, Spain) according to ISO 13356:2008 (Fig. 8.5-42A). This standard specifies the characteristics and the testing methods for ceramics based on yttria-stabilized tetragonal zirconia (Y-TZP) intended to be used in surgical implants [30]. The SPS sintered samples were placed into the autoclave (Fig. 8.5-42B) and

left in a steam atmosphere. At predefined times, the test was interrupted in order to measure the surface t–m transformation by means of XRD using Equations 8.5-2 and 8.5-3.

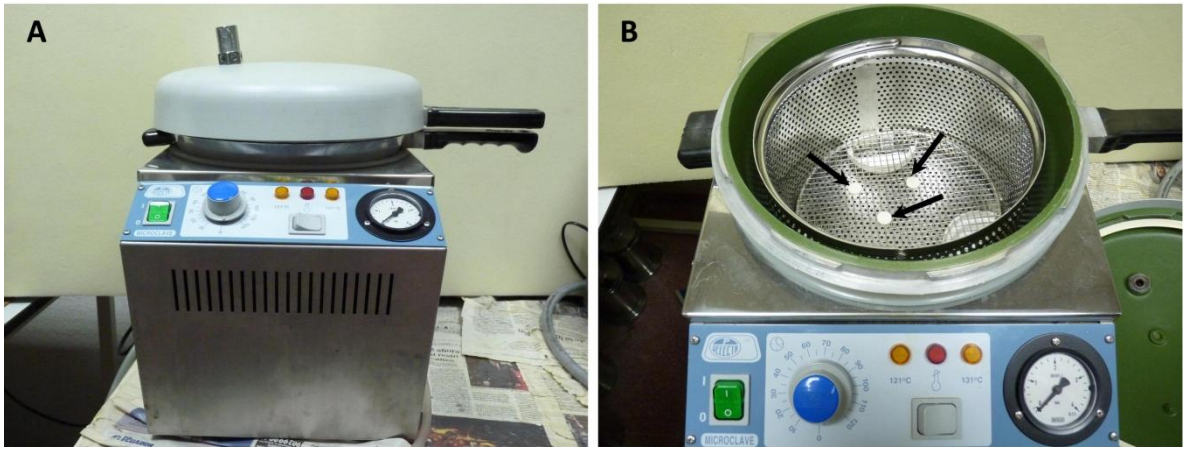

Fig.8.5-42. Autoclave general view (A) and samples placed into the autoclave (B)

8.6 REFERENCES

[1] Kurland HD, Grabow J, Müller FA. Preparation of ceramic nanospheres by CO_2 laser vaporization (LAVA). *J Eur Ceram Soc*., 2011; 31:2559–68.

[2] Moya JS, Baudín C, Miranzo P, "Sintering", Encyclopedia of physical science and Technology, Vol.15, Academic press, Inc. 1992

[3] Kim H-C, Shon I-J, Garay J, Munir ZA. Consolidation and properties of binderless sub-micron tungsten carbide by field-activated sintering. *Inter J Ref Met Hard Mater.*, 2004; 22:257-64.

[4] Anselmi-Tamburini U, Garay J, Munir Z. Fundamental investigations on the spark plasma sintering/synthesis process: III. Current effect on reactivity. *Mat Sci Engineering*, 2005; 407:24-30.

[5] Chen I-W, Wang X-H. Sintering dense nanocrystalline ceramics without final stage grain growth. *Nature*, 2000; 404:168-71.

[6] Suárez M, Fernández A, Menéndez JL, Torrecillas R, Kessel HU, Hennicke J, Kirchner R, Kesse T. Challenges and Opportunities for Spark Plasma Sintering: A Key Technology for a New Generation of Materials. *Sintering Applications*, 2013; 13:319-342.

[7] A Laboratory Manual for X-Ray Powder Diffraction
http://pubs.usgs.gov/of/2001/of01-041/htmldocs/xrpd.htm

[8] Garvie RC, Nicholson PS. Phase analysis in zirconia systems. *J Am Ceram Soc*., 1972; 55:303–5.

[0] Toraya H, Yoshimura M, Somiya S. Calibration curve for quantitative analysis of the monoclinic tetragonal ZrO_2 system by X-ray diffraction. *J Am Ceram Soc* 1984; 67:119–21.

[10] Chevalier S, Molins R, Heintz O, Larpin JP. *Mater. High Temp*., 2005; 22:365.

[11] Seiler H. Secondary electron emission in the scanning electron microscope. *J App Physics*,1983; 54:1-18.

[12] Todokoro H, Ezumi M. Scanning electron microscope. http://www.google.com/patents/US5900629

[13] Goldstein J, Newbury D, Echlin P, Joy D, Lyman C, Lifshin E, et al. Image Formation and Interpretation. Scanning Electron Microscopy and X-ray Microanalysis: Springer US; 2003; 99-193.

[14] Goldstein J, Newbury D, Echlin P, Joy D, Lyman C, Lifshin E, et al. The SEM and Its Modes of Operation. Scanning Electron Microscopy and X-ray Microanalysis: Springer US; 2003; 21-60.

[15] AMMRF. Australian Microscopy & Microanalysis Reserch Family. http://www.ammrf.org.au/myscope/xrd/background/machine/.

[16] Goldstein J, Newbury D, Echlin P, Joy D, Fiori C, Lifshin E. Electron-Beam Specimen Interactions. Scanning Electron Microscopy and X-Ray Microanalysis: Springer US; 1981; 53-122.

[17] Goldstein J, Newbury DE, Joy DC, Lyman CE, Echlin P, Lifshin E, et al. Scanning electron microscopy and X-ray microanalysis: Springer; 2003.

[18] Goldstein J, Newbury D, Echlin P, Joy D, Lyman C, Lifshin E, et al. X-Ray Spectral Measurement: EDS and WDS. Scanning Electron Microscopy and X-ray Microanalysis: Springer US; 2003; 297-353.

[19] Hayat MA. Principles and techniques of scanning electron microscopy. Bio applications. Volume 1: Van Nostrand Reinhold Company.; 1974.

[20] ASTM C1327 – 082008, Standard Test Method for Vickers Indentation Hardness of Advanced Ceramics.

[21] ASTM C1161 – 13, Standard Test Method for Flexural Strength of Advanced Ceramics at Ambient Temperature.

[22] ASTM F 394 Standard test method for biaxial flexure strength (modulus of rupture) of ceramic substrates.

[23] ISO 6872:2008, International standards for dental ceramics. Requirements and the corresponding test methods for dental ceramic materials for fixed all-ceramic and metal-ceramic restorations and prostheses.

[24] Miranzo P, Moya JS. Elastic/plastic indentation in ceramics: a fracture toughness determination method. *Ceram Int*., 1984; 10:147–52.

[25] Mechanical properties and performance of engineering ceramics and composites II, Ed. Tandon R, 2008.

[26] ASTM C1421-01b, Standart test methods for determination of fracture toughness of advanced ceramics at ambient temperature

[27] ASTM F732-00 (2011) Standard Test Method for Wear Testing of Polymeric Materials Used in Total Joint Prostheses

[28] Kokubo T, Kushitani H, Sakka S, Kitsugi T, Yamamuro T. Solutions able to reproduce *in vivo* surface-structure changes in bioactive glass-ceramic A-W. *J. Biomed. Mater. Res*., 1990; 24:721-734.

[29] Fan ZJ, Wang JQ, Wang ZF, Li ZP, Qiu YN, Wang HG, Yang SH. Casein phosphopeptide-biofunctionalized graphene biocomposite for hydroxyapatite biomimetic mineralization. *J. Phys. Chem. C*., 2013, 117:10375-10382.

[30] ISO 13356:2008 Implants for surgery - Ceramic materials based on yttria-stabilized tetragonal zirconia (Y-TZP).

List of publications

List of publications related to this thesis

1. J.F. Bartolomé, A. Smirnov, H-D. Kurland, J. Grabow, F.A. Müller. **New ZrO_2/Al_2O_3 Nanocomposite Fabricated from Hybrid Nanoparticles Prepared by CO_2 Laser Co-Vaporization**, *Scientific Reports* ***6*** Article number: 20589 (2016).

2. L. Esteban, A. Smirnov, C. Prado, J.S. Moya, R. Torrecillas, J.F. Bartolomé. **Multifunctional ceramic-metal biocomposites with Zinc containing antimicrobial glass coatings,** *Ceramics International* 42 (2016), pp.7023-7029.

3. A.Smirnov, H-D. Kurland, J. Grabow, F.A. Müller, J.F. Bartolomé. **Microstructure, mechanical properties and low temperature degradation resistance of 2Y-TZP ceramic materials derived from nanopowders prepared by laser vaporization**, *Journal of the European Ceramic Society* 35 (2015), pp.2685-2691.

4. A.Smirnov and J.F. Bartolomé. **Microstructure and mechanical properties of ZrO_2 ceramics toughened by 5–20 vol% Ta metallic particles fabricated by pressureless sintering**, *Ceramics International* 40 (2014), pp.1829-1834.

5. A.Smirnov, C.F. Gutiérrez-González, J.F. Bartolomé. **Cyclic fatigue life- and crack-growth behavior of zirconia-niobium composites**, *Journal of the American Ceramic Society* 96 (2013), pp.1709-1712.

6. A.Smirnov and J.F. Bartolomé. **Mechanical properties and fatigue life of ZrO_2 - Ta composites prepared by hot pressing**, *Journal of the European Ceramic Society* 32 (2012), pp. 3899-3904.

7. C.F. Gutiérrez-González, A. Smirnov and J.F. Bartolomé. **Aging effect on the tribological behavior of a novel 3Y-TZP/ Nb biocomposite against ultra high molecular weight polyethylene**, *Journal of the American Ceramic Society* 95 (2012), pp. 851–854.

8. A.Smirnov, J.F. Bartolomé H-D. Kurland, J. Grabow, F.A. Müller. **Design of a new zirconia-alumina-Ta micro-nanocomposite with unique mechanical properties,** *Journal of the American Ceramic Society* (submitted).

9. A.Smirnov, J.I. Beltrán, T. Rodriguez-Suarez, C. Pecharromán, M.C. Muñoz, J. S. Moya, J. F. Bartolomé. **Unprecedented simultaneous enhancement in flaw tolerance and fatigue resistance of zirconia–Ta composites** (submitted).

List of publications not related to this thesis

10. M.Antonov, J.Kers, L.Liibert, V.Shuliak, A. Smirnov, J.F. Bartolomé. **Effect of basalt reinforcement type and content on the abrasive wear behaviour of polymer composites**, *Key Engineering Materials* 674 (2016), pp 181-188.

11. M.I. Nieto, A. Cascales, N. Tabares, J.F. Bartolome, A. Cerpa, A. Smirnov, R. Moreno. **Processing and mechanical properties of mullite and mullite-alumina composites reinforced with carbon nanofibers**, *Journal of the European Ceramic Society* 35 (2015), pp.3613-3621.

12. J.F. Bartolomé, A. Smirnov, F. Sommer, R. Landfried, R. Gadow**. Sliding Wear Behavior of ZTA with Different Yttria Stabilizer Content**, *Journal of the American Ceramic Society* 98 (2015), pp.3981-3987.

13. C.F. Gutierrez-Gonzalez, A. Smirnov, A. Centeno, A. Fernández, B. Alonso, V.G. Rocha, R. Torrecillas, A. Zurutuza, J.F. Bartolome. **Wear behavior of graphene/alumina composite**, *Ceramics International* 41 (2015), pp.7434-7438.

14. T. Rodriguez-Suarez, J.F. Bartolome, A. Smirnov, S. Lopez-Esteban, R. Torrecillas and J.S.Moya. **Sliding wear behaviour of alumina/nickel nanocomposites processed by a conventional sintering route**, *Journal of the European Ceramic Society* 31 (2011), pp.1389-1395.

15. T. Rodriguez-Suarez, J.F. Bartolomé, A. Smirnov, S. Lopez-Esteban, L.A. Díaz, R. Torrecillas, J.S. Moya. **Electroconductive Alumina-TiC-Ni nanocomposites obtained by Spark Plasma Sintering**, *Ceramics International* 37 (2011), pp.1631-1636.

16. A. Smirnov, J.F. Bartolomé, J.S. Moya, F. Kern, R. Gadow. **Dry reciprocating sliding wear behaviour of alumina–silicon carbide nanocomposite fabricated by ceramic injection molding**, *Journal of the European Ceramic Society* 31 (2011), pp.469-474.

Appendix I

ELECTRICAL DISCHARGE MACHINING OF 3Y-TZP/Ta BIOCERMETS

A1.1 Introduction

In order to obtain sophisticated shaped implants advanced machining methods should be used instead of traditional machining techniques, because of associated advantages that include reduced processing costs, reduced waste, high precision, versatility and degree of automation [1]. Electrical discharge machining (EDM) is such a technique that can be successfully applied to machining of single-phase ceramics, cermets and ceramic/matrix composites [2]. An important feature to remember with EDM machining is that it will only work with materials that are electrically conductive. For being electrical descharge machinable, the materials' electrical resistivity should be lower than 100–300 Ω·cm [3]. In case of a composite, a mixture of conducting and insulating phases becomes conducting when the volume fraction of conducting phase exceeds a 'percolation threshold' of 16%, the minimum amount to give a continuous path across the whole sample. This threshold is independent of the size and shape of the conducting phase, as long as its particles are equiaxed. If the conducting phase consists of long thin particles, the chance of contact increases, this reduces the percolation threshold so that conduction occurs at much lower loading [4].

In comparison with conventional machinihg techniques, EDM achieves higher removal rates for these materials with respect of surface integrity and also tolerances of below 1 μm have been achieved [5]. However, difficulties also arise with respect to the surface finish conditions [6, 7], the corrosion of these materials during machining [8], and the influence

the machining parameters in the surface damage, i. e. cracks produced within the thermally affected zone (recast layer and adjacent regions) beneath the shaped surface.

The aim of this study was to assess the EDM machinability of 3Y-TZP/Ta biocermet and the surface microstructural quality obtained by the method. The EDM process was carried out at the A&R Wirecut SL company (Castell, Menorca, Spain).

A1.2 Materials characterization and results

The electrical resistance of SPS sintered 3Y-TZP/Ta biocermet was measured with a four-wire (Kelvin) connection method using a separate current source (Keithley 6220, Cleveland, OH, USA) and a two-channel nanovoltmeter (Keithley 2182A, Cleveland, OH, USA). The electrical resistivity of biocermet was equal to $2 \times 10^{-4} \pm 1$ Ω·cm. This value is about five orders of magnitude lower than the limit of 100–300 Ω·cm, which makes the material suitable for EDM.

Wire EDM experiments on the commercial machine (Agiecut 100D, AGIE SA, Losone, Switzerland) have been performed. The wire is usually made of brass or stratified copper with a diameter between 0.02 to 0.3 mm. Metallic wire and sintered disk are both electrodes separated by a dielectric liquid with conductivity of 10μS and subjected to an electric voltage (270 V). When the distance between electrodes is reduced, the discharge flows between the two electrodes. Once the discharge starts, plasma is formed in the neighbourhood of the machined front. Optical photos of EDM machined pieces with different geometries are presented in Fig.A1-1.

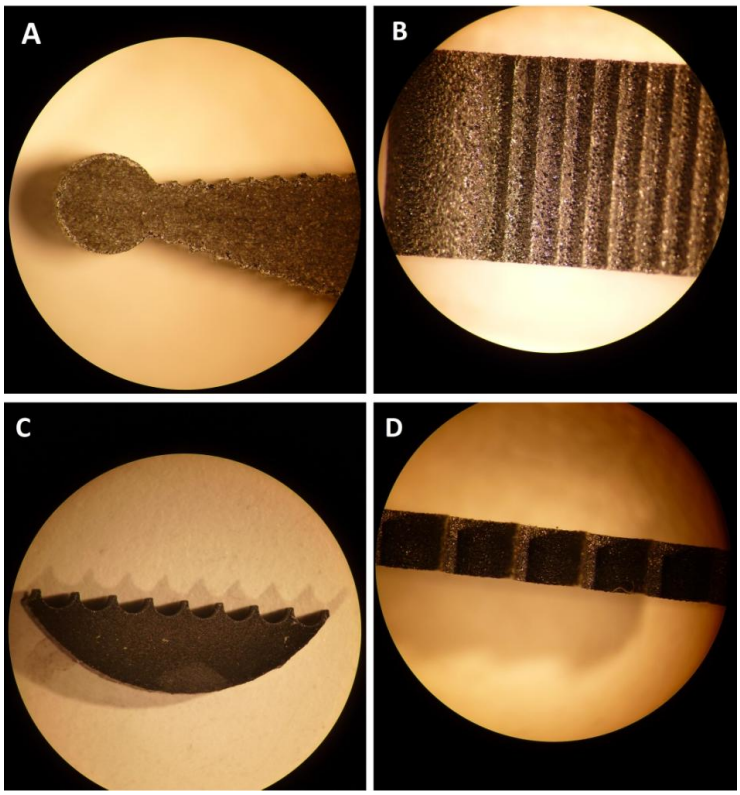

Fig.A1-1. Image showing front (A, B) and top (B, D) view of 3Y-TZP/Ta biocermet with different geometries after electroerosion process

Further the detailed analysis of heat affected regions has been done by using tabletop SEM. Fig.A1-2 shows the effects of the wire over the material surface after cutting. There are places where the wire has caused materials fusion. The surface topography of the machined biocermet is a recast layer with discharge craters of ~ 6.70 µm (Fig. A1-2D). In general terms, the final roughness (*Ra*) of the workpiece after cutting is about 1.1 µm. (Fig. A1-2D).

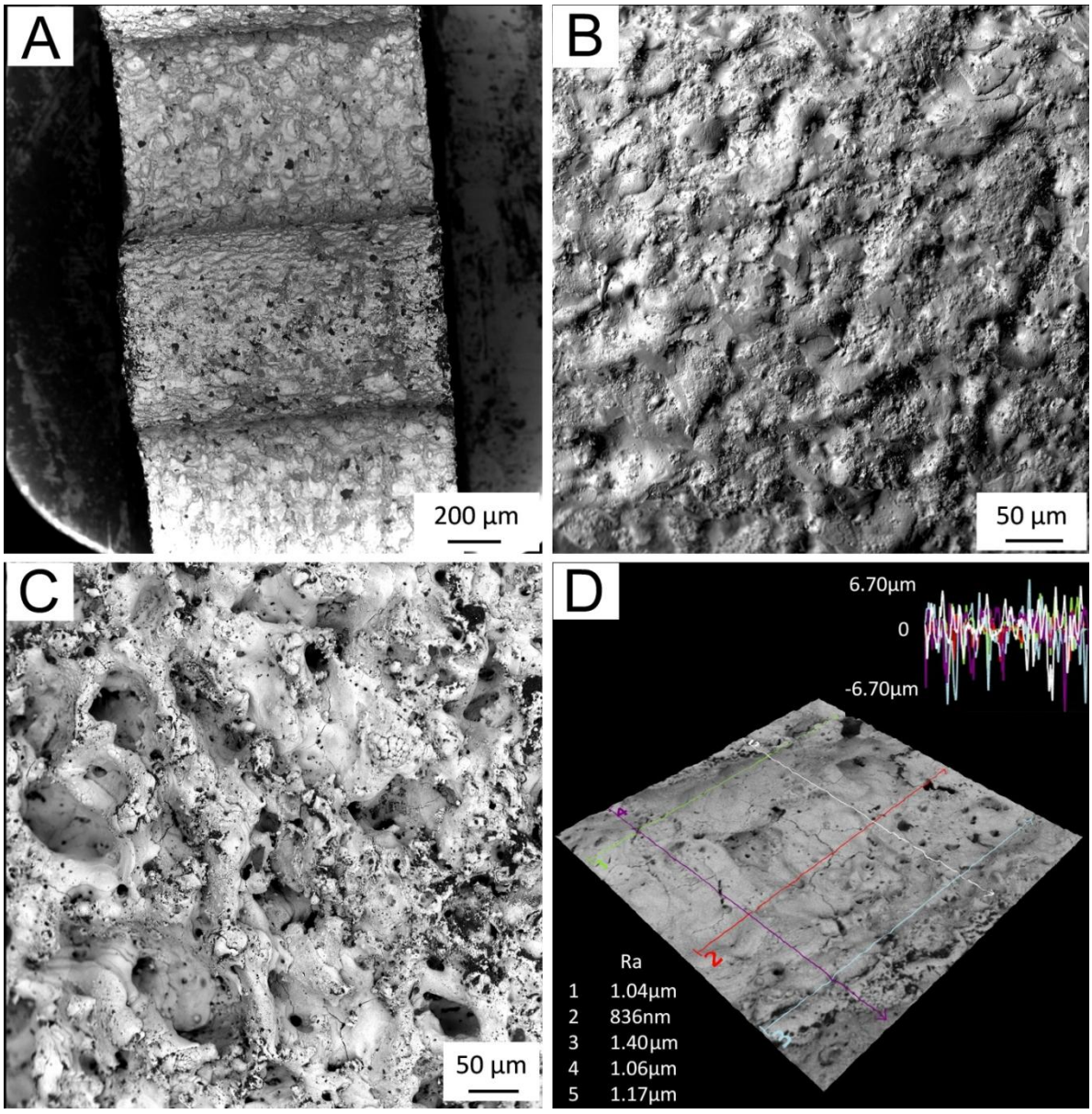

Fig.A1-2. SEM micrograph showing 3Y-TZP/Ta surface finishing (A, B, C) and roughness measurements (D) after EDM process

A1.3 Conclusions

The obtained results clearly point out that 3Y-TZP/Ta biocermet obtained by Spark Plasma Sintering possess the electrical conductivity and consequently is suitable for fabrication implants with sophisticated shapes by electrical discharge machining technique. Although the surface quality was modest after rough EDM cutting, with the formation of a thermally induced recast layer, exhibiting many resolidified droplets and voids as well as surface microcracks, the surface roughness (*Ra*) was about 1.1 µm.

A1.4 References

[1] Lauwers B, Kruth JP, Liu W, Eeraerts W, Schacht B, Bleys P. Investigation of material removal mechanisms in EDM of composite ceramic materials. *J. Mater. Process. Technol*., 2004; 149:347-352.

[2] König W, Dauw DF, Levy G, Panten U. EDM-Future Steps towards the Machining of Ceramics. *Ann. CIRP*, 1988; 37:623.

[3] Lopez-Esteban S, Gutierrez-Gonzalez CF, Mata-Osoro G, Pecharroman C, Diaz LA, Torrecillas R, Moya JS. Electrical discharge machining of ceramic/semiconductor/metal nanocomposites. *Scripta Mater*., 2010; 63:219-222.

[4] Robertson J. Realistic applications of CNTs. *Materials Today*, 2004; 10:46-52.

[5] Rodriguez-Suarez T, Bartolomé JF, Smirnov A, Lopez-Esteban S, Díaz LA, Torrecillas R, Moya JS. Electroconductive Alumina-TiC-Ni nanocomposites obtained by Spark Plasma Sintering. *Ceram Inter.*,2011; 37:1631-1636.

[6] Puertas I, Luis CJ, Álvarez L. Analysis of the influence of EDM parameters on surface quality, MRR and EW of WC–Co. *J Mater Processing Tech*., 2004; 154:1026-1032.

[7] Khan AA, Ali M, Shaffiar M. Relationship of surface roughness with current and voltage during wire EDM. *J Applied Sciences*, 2006; 6:2317-2320.

[8] Obara H, Satou H, Hatano M. Fundamental study on corrosion of cemented carbide during wire EDM. *J Mater Processing Tech*., 2004; 149:370-375

Appendix II

ANALYSIS OF THE *IN VITRO* ADHERENCE OF *STREPTOCOCCUS ORALIS* BIOFILM TO 3Y-TZP/Ta BIOCERMET

A2.1 Introduction

The human oral cavity is a complex ecological environment where microorganisms have access to both hard and soft tissue surfaces to adhere, hence to develop biofilms. Dental plaque is a complex biofilm that accumulates on the tooth surfaces in the oral cavity [1]. The development and maturation of dental plaque as a biofilm has profound implications in the etiology and progression of the most prevalent infections affecting humans, namely, dental caries and periodontal diseases [2]. *Streptococcus oralis* is one of the most commonly detected early colonizers of the tooth surface as it has been demonstrated *in vitro* and *in vivo* studies [3, 4]. Primary colonizers alter the surface not only by their physical presence but also they are likely to represent a new ‘‘surface-attached’’ phenotype with distinct metabolic activity and surface properties, thus altering their surroundings and creating new niches for other bacteria to colonize [5]. Titanium dental implants are widely used because of its excellent biocompatibility and outstanding mechanical properties [6, 7]. Exposure of the implant in the oral cavity presents a unique surface that can interact with native host bacteria, leading to plaque formation. The adhesion of oral microorganisms and the subsequent formation of pathogenic biofilms on the surface of dental implants result in infections of the peri-implant tissues and finally in implant failure. Therefore, inhibiting adherence has been considered an effective strategy for preventing infectious diseases. Many studies with different materials have been conducted on effective strategies in dental

hygiene practice to avoid biofilm formation and to prevent oral infectious diseases and the development of materials with the ability to inhibit bacterial growth has been of great interest in recent years [8]. Along with conventional material properties, bacterial colonization may be regarded as a further factor determining the clinical performance of dental materials. 3Y-TZP/Ta biocermet is a potential material for future implants and as such, its behavior with respect to microbial adhesion is of great interest. The aim of this study was to assess the *in vitro S. oralis* adhesion to a 3Y-TZP/Ta biocermet and compare with titanium alloy surface. These studies were carried out at the Department of Microbiology, School of Medicine, Universidad Complutense (Madrid, Spain) by group of Prof. Luís Alou.

A2.2 Materials and Methods

Dense SPS sintered (Chapter 3, Section 3.2.3) and polished (Chapter 3, Section 3.1.5.3) 3Y-TZP/20 vol.% Ta biocermets were used in this investigation.

Disks (20 mm diameter x 3 mm thickness) were saw cut from a Ti-Al6-V4 (90 wt.% Ti, 6wt.% Al, 4wt.% V) titanium alloy rod of 20 mm of diameter and 100 mm of length were used as reference material (Ti017950, 99.0% purity, Good fellow, Huntingdon, England). After cutting titanium alloy disks were mounted to epoxy resin and automated wet grinded using a polishing machine (Chapter 8, Section 8.4) with 240-grit size SiC paper (240 rpm, load 27N, complementary rotation) to obtain a flat surface free of cutting damage. Then, the rough polishing with 9-µm diamond paste on a hard-woven nylon cloth (120 rpm, load 27N, contra rotation) for 10-15 minutes with distilled water as lubricant was performed. Lastly, final polishing with 0.02-µm colloidal silica on a medium nap polishing cloth (120 rpm, load 30N, contra rotation) for 10 minutes was carried out. After polishing the samples

were ultrasonically cleaned using distilled water and acetone and subsequently dried with particle-free compressed air.

Bacterial Strains and Culture Conditions

Standard reference strain of *Streptococcus oralis* ATCC 35037 and two clinical isolates (CI-1 and CI-2) from a previous periodontal pathogen collection [14] were used in this study. Todd Hewitt Broth medium supplemented with 5% yeast extract (Difco; BD Diagnostics, Sparks, MD, USA) and 50 mM of glucose (Panreac, Barcelona, Spain) (THY-glucose) was the medium used in the biofilm experiements since in a preliminary study higher biofilms (data not shown) in THY-glucose than THY-saliva medium were observed in all strains.

Biofilm Formation Assays

Colonies of *S. oralis* strains from an overnight culture on Columbia sheep blood agar (Difco, BD Diagnostic Systems, Sparks, MD, USA) were allowed to grow in THY-glucose at 37 ºC in the presence of 5% CO_2 to a density of 0.5–1 x 10^8 colony forming units (CFU/mL) as measured by a UV-Visible spectrophotometer (GBC, Model Cintra 101, Australia). Samples were placed in 24-well culture plates and 100 µl of this inoculum suspension were inoculated in 900 µl (1:10 dilution) of THY-glucose. Plates were incubated at 37 ºC in the presence of 5% CO_2 for 24 h in a wet chamber.

Two methods were used to quantify biofilm formation abilities: i) crystal violet staining followed by measures of absorbance, and ii) determination of viable counts.

The crystal violet assay was performed to determine the total amount of biofilm. After incubation, the disks were carefully washed three times with sterile saline solution to remove unattached cells. For fixation of biofilms, 300 µl of methanol was added. After 20 minutes, supernatants were removed and the disks were air-dried. Then, the biofilms were

stained using 300 µl of 1% crystal violet solution (Química Clínica Aplicada, Tarragona, Spain), followed by 20 minutes incubation time at room temperature. Then, the excess of unbound dye was removed by washing the plates with water. The bound crystal violet was released by adding 200 µl of ethanol. The amount of biofilm was measured at optical density of 570 nm using a spectrophotometer. The background staining was corrected by subtracting the mean value for crystal violet bound to negative controls. All experiments were performed in triplicate.

Viable counts were used to determine the quantity of viable adherent and planktonic (suspended) bacteria. After biofilm formation, supernatant samples of 200 µl were taken to determine viable planktonic bacteria and expressed as CFU/mL. Then, disks were carefully washed three times with sterile saline solution to remove unattached cells and inserted in tubes containing 5 mL of sterile saline solution. The tubes were vigorously vortexed for 2 minutes to free the bacteria attached on the surface of each disk and sonificated twice for 10 seconds (Microson ultrasonic cell disruptor XL Misonix, Inc., Fanningdale, NY, USA) to disperse bacterial cells. Samples of 200 µl from sonicated biofilms were serially diluted in 0.9% saline solution and plated onto Columbia sheep blood agar to determine the total number of viable cells and expressed as CFU/mm^2. All experiments were performed in triplicate. The limit of detection was 2.5 x 10^2 CFU. Preliminary experiments indicated that sonication was not associated with a loss of viability of the cells.

Surface characterization

The morphology of the surface disks was studied before the biofilm tests by scanning electron microscopy (SEM) (FEI Nova NANOSEM 230, Hillsboro, Oregon).

After biofilm formation, supernatants were removed, the disks were carefully washed with sterile saline solution to remove unattached cells, they were air-dried, and then characterized by surface profilometer (Chapter 8, Section 8.5.9) and SEM. The profilometer was used to determine the three-dimensional topographic map and to calculate the roughness factor or specific surface area (the ratio of the surface to the projected area). Three samples of each surface type were scanned to evaluate the average surface roughness (*Ra*) of the surfaces at five different locations.

A2.3 Results and discussion

Fig.A2-1 shows a representative SEM micrograph of the polished titanium alloy disk face.

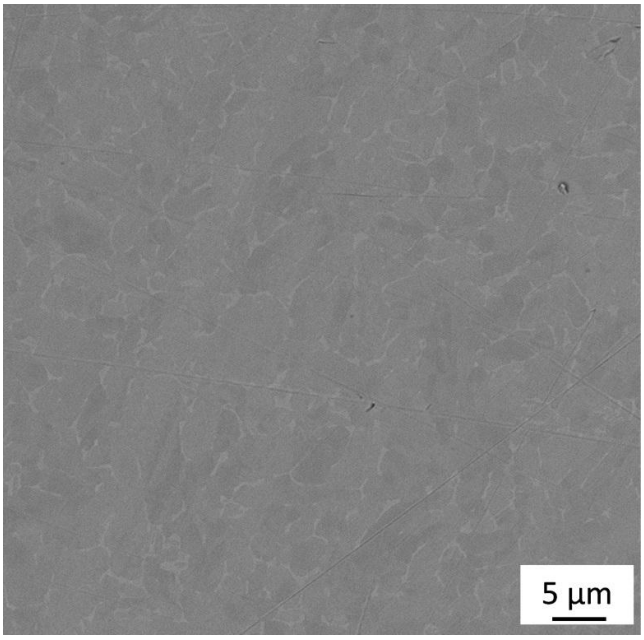

Fig A2-1. SEM image of polished surface of titanium alloy disk

Representative 3D surface topographies of the titanium and 3Y-TZP/Ta biocermet disks are shown in Fig.A2-1 and Fig. 6.2-2C (Chapter 6, Section 6.2.6.1). The figures clearly show that both materials present a nanometrical roughness (*Ra*). Significantly higher average Ra

values were found for 3Y-TZP/Ta biocermet disks (0.12 ± 0.04 µm) than for titanium disks (0.04 ± 0.01 µm). The same trend was observed in the values of specific surface area (A_{spec}). It is always larger than unity, however, in the case of 3Y-TZP/Ta biocermet disks, this value is higher (1.2 ± 0.2) than for titanium disks (1.01 ± 0.01). The obtained data evidenced a higher roughness and specific surface area on 3Y-TZP/Ta biocermet disks surfaces compared with titanium alloy disks.

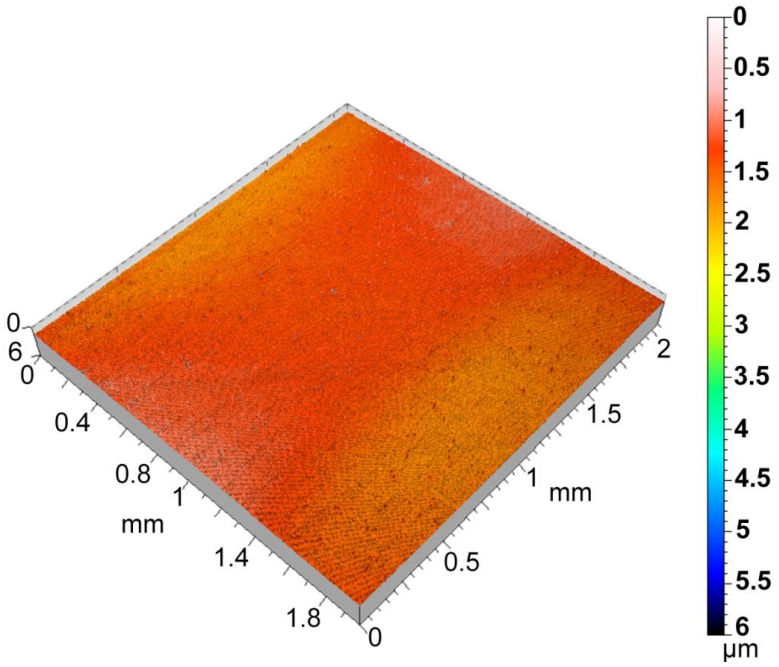

Fig.A2-1. 3D topography image of titanium alloy disk

Fig.A2-2 shows the total biofilm mass for all *S. oralis* strains determined by crystal violet staining. No significant differences were observed between absorbance values from 3Y-TZP/Ta biocermet and from titanium disks.

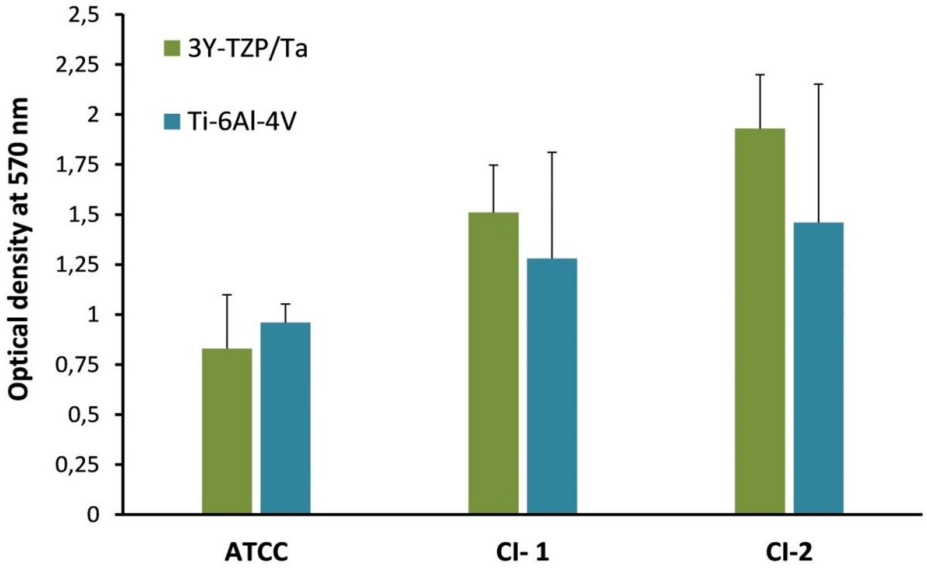

Fig.A2-2. Comparison of total biofilm mass for the studied *S. oralis* strains determined by crystal violet staining among 3Y-TZP/Ta and titanium alloy disks

Fig.A2-3 shows the adherence of the viable *S. oralis* strains (log_{10} CFU/mm^2) to 3Y-TZP/Ta biocermet and titanium surfaces. No significant differences were observed between colony counts from 3Y-TZP/Ta biocermet and titanium disks.

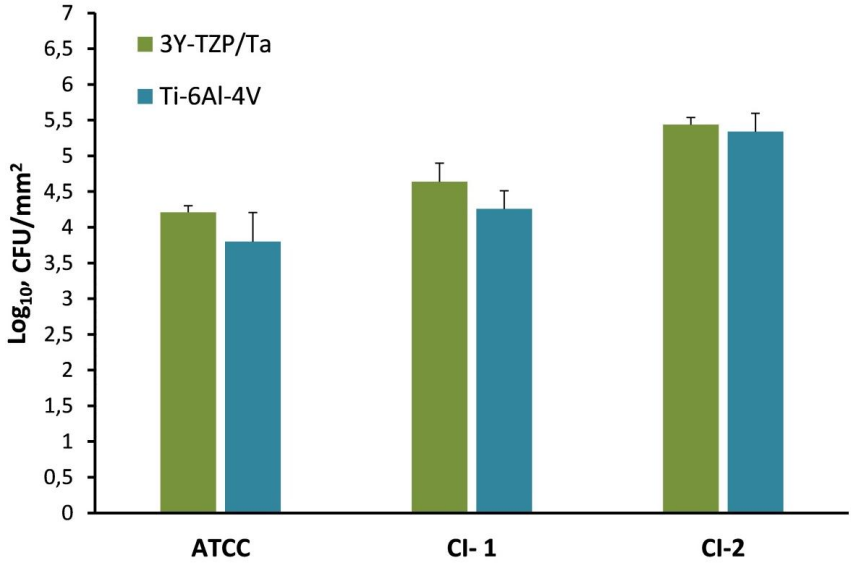

Fig.A2-3. Comparison of the viable adherent bacteria (CFU/mm^2) for the studied *S. oralis* strains among 3Y-TZP/Ta and titanium alloy disks

Fig.A2-4 shows the viable planktonic cells (suspended) of the *S. oralis* strains (log_{10} CFU/mL) in THY-glucose after 24 h incubation in the different materials surfaces. No statistically significant differences were observed in the colony counts of planktonic (suspended) cells for the 3Y-TZP/Ta biocermet and titanium disks.

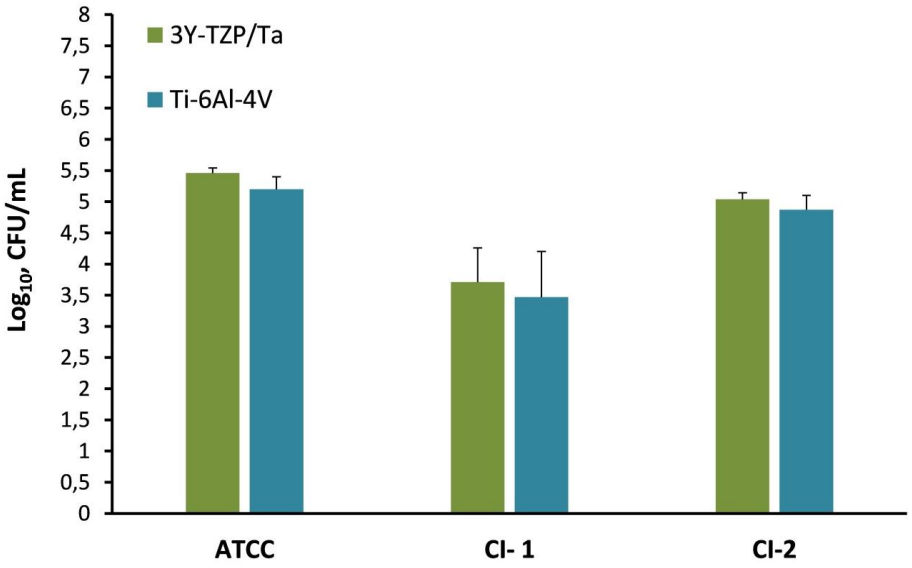

Fig.A2-4. Comparison of the viable planktonic bacteria (CFU/mL) for the studied *S. oralis* strains among 3Y-TZP/Ta and titanium alloy disks

The bacteria colonization and biofilm formation has been also verified by scanning electron microscopy as shown in Fig.A2-5. Representative SEM images of the 3Y-TZP/Ta biocermet and titanium alloy disks surfaces after 24 h incubation with CI-1 are shown. It can be seen that the bacterial cells colonized densely onto the surface of both materials.

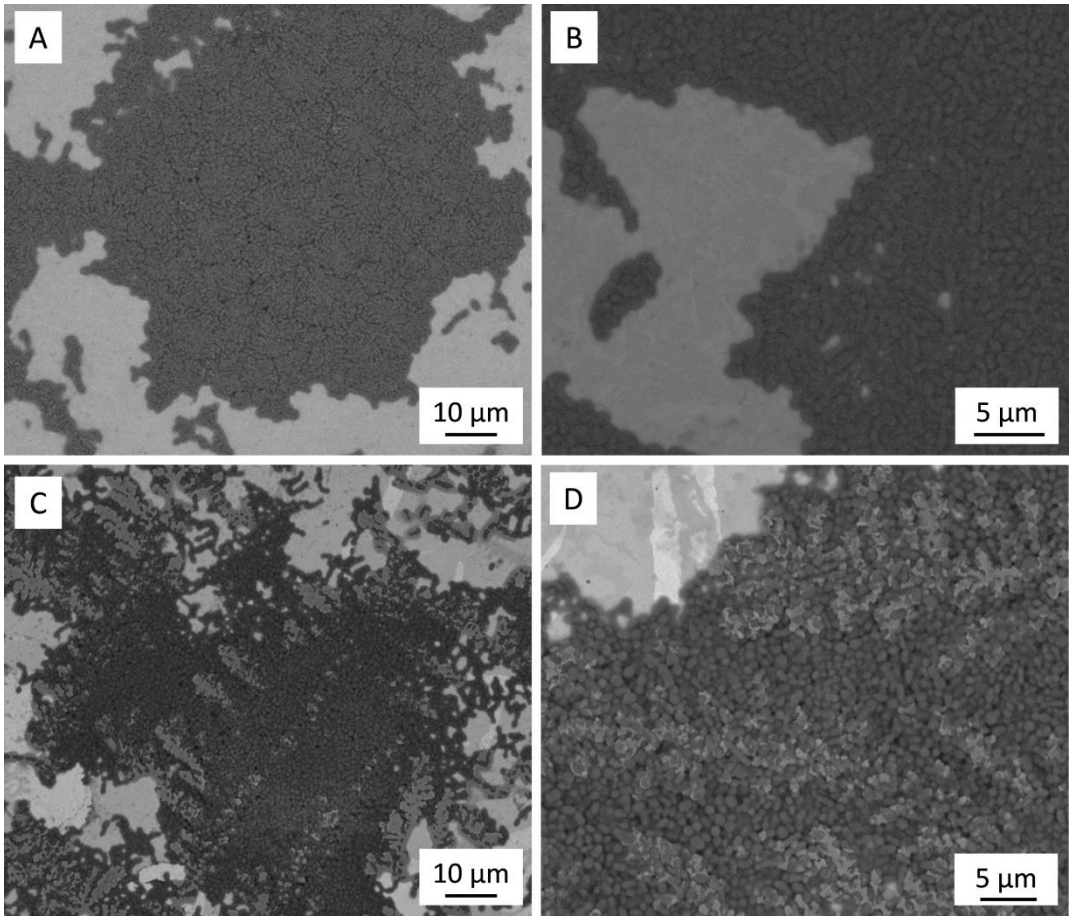

Fig.A2-5. Scanning electron micrographs after biofilm formation of the CI-1 strain on: a, b) titanium alloy disk; c, d) 3Y-TZP/Ta disk

The physico-chemical characteristics of specific material surfaces are known to significantly influence the bacterial adhesion process [9] but the surface roughness has been suggested to play a major role in this process [10-11]. Roughened surfaces promote bacterial adhesion and biofilm formation more than ultrasmooth surfaces. This may happen since a rough surface has a greater surface area and the depressions in the irregularities provide more favorable sites for colonization. Thus, a *Ra* value of 0.2 µm has been generally accepted as the average roughness threshold below which the amount of bacterial adhesion cannot be reduced any further [12]. In these previous studies, it has demonstrated that a reduction of surface roughness is accompanied with reduced plaque formation. On

the other hand, a recent study showed that, compared with polished titanium, the number of adhering bacterial colonies was significantly reduced on titanium surfaces coated with inherently stable titanium hard materials such as zirconium nitride and titanium nitride although roughness was not altered (similar *Ra* values) [13]. In our study, despite higher *Ra* value (i.e., 0.12 μm) and higher specific surface area, of the 3Y-TZP/Ta biocermet surfaces with respect to that of titanium surface (i.e., 0.04 μm), similar microbial quantity of adhering *S. oralis* on the disks of different materials was found by both methods used (crystal violet staining and colony counts). Although as mentioned before, substratum roughness probably plays an important role in the rate and extent of bacterial colonization, little conclusive evidence is available to quantitatively evaluate the effects within our study. However, it is generally regarded that cells located inside pores on surfaces are sheltered from shear forces; therefore their removal rate is decreased and retention of a larger amount cells is ensured. This result could suggest that the biofilm formation and accumulation is lower in the case of the rougher 3Y-TZP/Ta biocermet surfaces. At the moment we can not fully explain this aspect of our results. The reduction of oxygen gaps at the biocermet surface resulting in a more apolar surface structure is a possible reason. Several studies have shown that titanium surfaces are very reactive [14, 15]. Titanium is covered by a surface oxide approximately 2 to 5 nm thick. This oxide (mainly titanium dioxide) has amphoteric character and supports cationic and anionic exchange adsorption. At the interface between titanium oxides and saliva covalent, ionic or hydrogen bonding can contribute to the adsorption of biopolymer molecules, thus providing a very reactive surface. Experimental clinical study evaluating plaque adhesion to titanium and ceramics materials showed that the highest plaque accumulation was found on polished titanium whereas the accumulation on zirconium oxide ceramic and aluminum oxide ceramic was

almost fifty percent lower [16]. It appears that bacterial adherence on ceramic material is lower as compared to titanium alloys [17]. However, this effect needs further investigations in the case of ceramic-metal biocomposites. On the other hand, salivary protein adsorption reduced differences originally present in surface free energies. Therefore, the extrapolation of our findings into the clinical situation requires experimental validation. In addition, the colonization pattern of other oral bacteria might be different.

A2.4 Conclusions

Within the limitations of this study, rather similar adhesion of *Streptococcus oralis* to the rougher 3Y-TZP/Ta biocermet and smother titanium surface was found, which suggests better clinical performance of biocermet material concerning plaque formation may be expected.

A2.5 References

[1] Rosan B, Lamont RJ. Dental plaque formation. *Microbes Infect*., 2000; 2(13):1599-607.

[2] Filoche S, Wong L, Sissons CH. Oral biofilms: emerging concepts in microbial ecology. *J Dent Res*., 2010; 89(1):8-18.

[3] Sánchez MC, Llama-Palacios A, Blanc V, León R, Herrera D, Sanz M. Structure, viability and bacterial kinetics of an in vitro biofilm model using six bacteria from the subgingival microbiota. *J Periodontal Res*., 2011; 46(2):252-60.

[4] Wecke J, Kersten T, Madela K, Moter A, Göbel UB, Friedmann A, Bernimoulin J. A novel technique for monitoring the development of bacterial biofilms in human periodontal pockets. *FEMS Microbiol Lett*., 2000;191(1):95-101.

[5] Davey ME, Costerton JW. Molecular genetics analyses of biofilm formation in oral isolates. *Periodontology*, 2000, 42:13–26.

[6] Brunette DM, Tengvall P, Textor M, Thomsen P. Titanium in medicine: Material science, surface science, engineering, biological responses, and medical applications. In: Brunette DM, Tengvall P, Textor M, Thomsen P, editors. Berlin, Germany: Springer (2006).

[7] Das K, Bose S, Bandyopadhyay A, Karandikar B, Gibbins BL. Surface coatings for improvement of bone cell materials and antimicrobial activities of Ti implants. *J. Biomed. Mater. Res*., 2008; 87:455–460.

[8] Simchi A, Tamjid E, Pishbin F, Boccaccini AR. Recent progress in inorganic and composite coatings with bactericidal capability for orthopaedic applications. *Nanomed. Nanotechnol. Biol. Med*., 2011; 7:22–39.

[9] Teughels W, Van Assche N, Sliepen I, Quirynen M. Effect of material characteristics and/or surface topography on biofilm development. *Clin Oral Implants Res*., 2006; 17:68-81.

[10] Quirynen M, De Soete M, van Steenberghe D. Infectious risks for oral implants: a

review of the literature. *Clin Oral Implants Res*., 2002;13(1):1-19.

[11] Bürgers R, Gerlach T, Hahnel S, Schwarz F, Handel G, Gosau M. *In vivo* and *in vitro* biofilm formation on two different titanium implant surfaces. *Clin Oral Implants Res*., 2010; 21(2):156-64.

[12] Bollen CM, Papaioanno W, Van Eldere J, Schepers E, Quirynen M, van Steenberghe D. The influence of abutment surface roughness on plaque accumulation and peri-implant mucositis. *Clin Oral Implants Res*., 1996; 7(3):201-11.

[13] Grössner-Schreiber B, Griepentrog M, Haustein I, Müller WD, Lange KP, Briedigkeit H, Göbel UB. Plaque formation on surface modified dental implants. An in vitro study. *Clin Oral Implants Res*., 2001; 12(6):543-51.

[14] Kasemo B, Lausmaa J. Biomaterial and implant surfaces: a surface science approach. International *J. Oral and Maxillofacial Implants*, 1988; 3:247–259.

[15] Lausmaa J. Surface oxides on titanium: preparation, characterization and biomaterial applications. Thesis. Department of Physics, Chalmers University of Technology, Göteborg (1991).

[16] Krämer A, Weber H, Geis-Gerstorfer J. Plaqueansammlung an Implantat- und prothetischen Werkstoffen – eine klinische Studie. Zeitschrift für Zahnärztliche Implantologie, 1989;V: 283–286.

[17] Siegrist BE, Brecx MC, Gusberti FA, Joss A, Lang NP. In vivo early human dental plaque formation on different supporting substances. *Clinical Oral Implants Research* 1991; 2:38–46.

Appendix II

Appendix III

ZINC CONTAINING ANTIMICROBIAL GLASS COATED 3Y-TZP/Ta BIOCERMET

A3.1 Introduction

Despite biocompatibility of newly developed biocermet another critical problem associated with implants is the risk to infections. Most surgical infections are acquired during the surgery mainly due to the formation of biofilm on the surface of the implant. The biofilm compromises the immune response at the implant/tissue interface because bacteria in biofilm are protected from the immune defences and they are usually resistant to antibiotics, even high local concentrations of antibiotics cannot eradicate biofilms. In spite of several methods for prevention of implants infections [1], the problem of biofilms formation is still unresolved. In this regard, new approach to biomedical device-associated infections is based on biocide materials [2].

The present work presents new biocide coatings based on non-toxic glasses belonging to the B_2O_3-SiO_2-Na_2O-ZnO system which can avoid the biofilm formation on the implant surface. The ZnO containing glasses were previously studied as biocidepowders [3]. It is widely reported that ZnO even in the form of nanoparticles exhibits a minimal effect on human and animal cells [4-6]. The aim of this study was the evaluating of biocide glass/cermets interface adhesion and biocompatibility of coating.

A3.2 Materials and Methods

Previously produced 3Y-TZP/Ta biocermet (Chapter 3, Section 3.2.3) and glass belonging to the B_2O_3-SiO_2-Na_2O-ZnO system [3, 7] were used as substrate and coating, respectively. Reference materials in the testing were 3Y-TZP ceramic and 3Y-TZP/Nb composite (Chapter 3, Section 3.2.3). Microstructural analysis and surface characterization of substrates materials was made in the same manner as described in Chapter 3 (Section 3.1.5). Preparation and characterization of coating was described previously [7]. In order to study the adherence of the coatings, the relative crack resistance and weak fracture path was qualitatively evaluated by Vickers indentation (2.9N load) performed in air on polished cross-sections close to the interfaces.

The measurement of the antibacterial activity was carried out following the ISO 22196 standard method [8]. Assays were carried out by triplicate. The microorganism studied was *Escherichia coli*. These studies were carried out at the Nanomaterials and Nanotechnology Research Center (CINN, El Entrego, Asturias, Spain) by Dra. Catuxa Prado Cueto.

The potential cytotoxic effect of our samples on mammalian cells was determined following the procedure described in ISO 10993-part 5 standard, which is designed to evaluate the adverse biological effects of materials and medical devices (direct contact method) [9]. The Neutral Red Uptake (NRU) assay was chosen. NIH-3T3 cells (mouse embryonic fibroblast cells) were used for this test. The percentage of viable cells after 24 hours in each culture condition was calculated as:

$$\% \text{ viable cells} = 100 \times Abs_{540}(\text{extract})/Abs_{540}\ (\text{blank})$$

Plates of 3Y-TZP, 3Y-TZP/Ta and 3Y-TZP/Nb as polished were tested as negative controls.

A3.3 Results and discussion

SEM micrographs from the top surface of the coatings are shown in Fig.A3-1. No cracking was observed due to the good match in the thermal expansion coefficients between substrates and glassy coating.

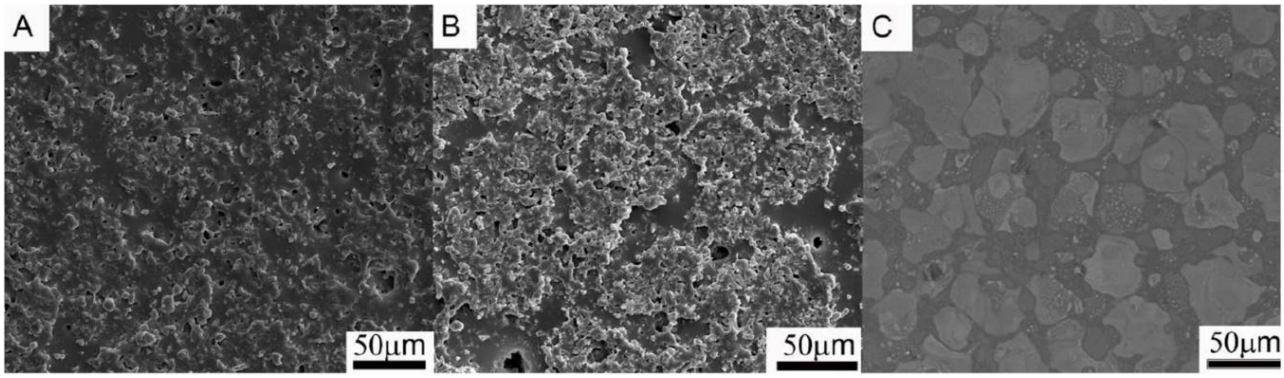

Fig.A3-1. Scanning electron micrographs from the top surface of the coatings on 3Y-TZP/Nb (A), 3Y-TZP/Ta (B) and 3Y-TZP (C)

The thermal expansion coefficient α ($10^{-6}K^{-1}$) for the ZnO containing glass, 3Y-TZP, 3Y-TZP/Ta and 3Y-TZP/Nb were found to be: 7.74; 10.6; 9.82 and 9.94, respectively.

The results of average surface roughness (*Sa*) were obtained: 0.1µm, 0.25µm, 0.3µm for 3Y-TZP, 3Y-TZP/Ta and 3Y-TZP/Nb substrates and 2.3µm, 2.9µm, 2.6µm for 3Y-TZP, 3Y-TZP/Ta and 3Y-TZP/Nb glass coatings, respectively. No significant difference was found between roughness values of polished substrate disc and glass surface of different materials but substantially rougher surface on the coatings.

The SEM micrographs of the polished cross-section of the glass-ceramic and glass-ceramic/metal composites interface, after thermal treatment at 725 °C for 1 hour are shown in Fig. A3-2A. A good wetting regime and continuous interfaces with no cracks or gaps were revealed. The extent of diffusion of constituent elements from the substrates into the glass and vice-versa has been observed through EDS line scanning (Fig. A3-2B). No

significant diffusion of elements was observed. As, expected, Boron was very difficult to be detected by EDS. The glass shows chemical compatibility with substrates, where no interfacial reaction was detected.

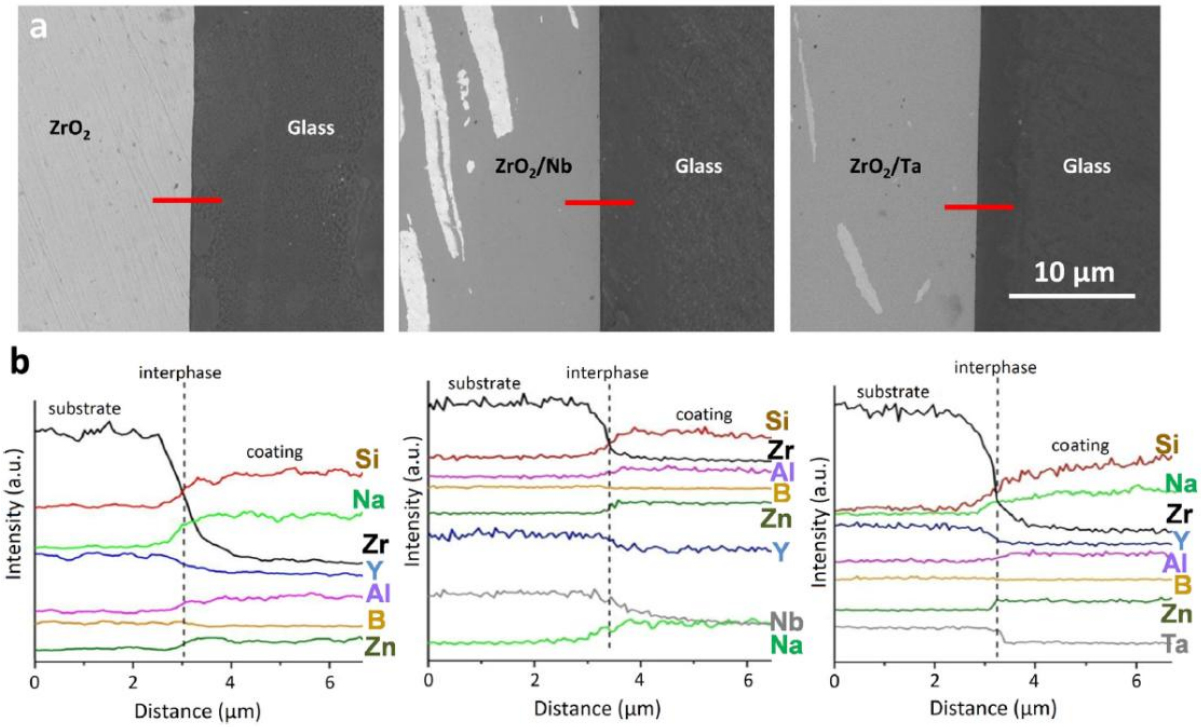

Fig.A3-2. (A) Scanning electron micrographs of the polished cross-section interface after thermal treatment at 725°C for 1h for 3Y-TZP/glass, 3Y-TZP/Nb-glass and 3Y-TZP/Ta-glass coatings and (B) EDS elemental concentration of B, Zn, Al, Si, Na, Zr, Y, Nb and Ta along the red scan line

In the Vickers indentations performed on polished cross sections of these coatings, cracks did not propagate along the interfaces, but rather tended to be driven into the glass coating (Fig.A3-3), which is a qualitative indication of a strong glass/substrate adhesion. The indentation induced cracks orthogonal to the interface with the substrate but without detaching the coating from the substrate.

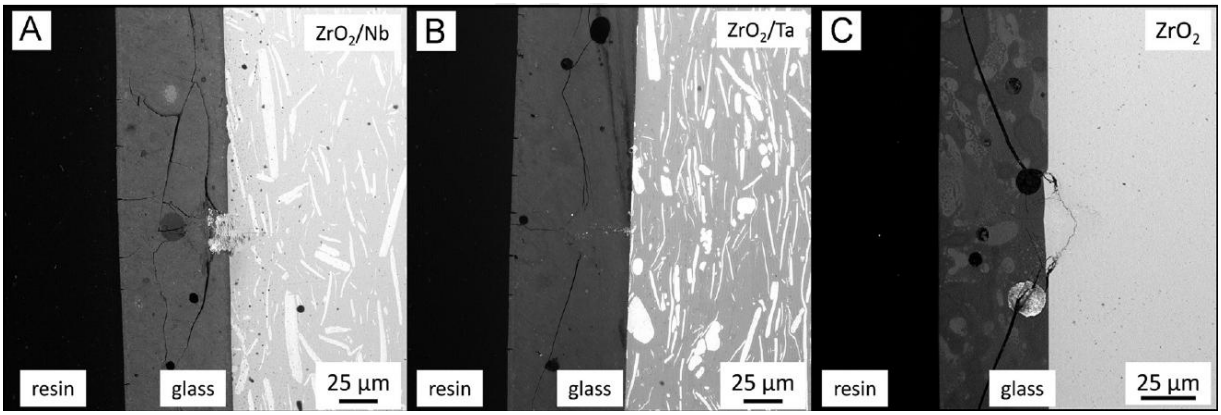

Fig.A3-3. Vickers indentations (0.3 kg load in ambient air) at the coating cross section. Cracks emanating from the indentations in the cross section do not cause delamination indicating good interface adhesion

The linear expansion coefficient of the glass is lower than the substrates. This feature should be a cause of residual compressive stress at the interface between the glass and the substrates. The magnitude of the expected stresses according to the properties of the material (the thermal expansion and Young's modulus mismatch) at the coating-substrate interface has been determined by the empirical Dietzel equation [11] and was < 5 MPa. Therefore, the coatings were well bonded to the substrate, and the interface appeared to be continuous. Moreover, the best behavior of the biocermets coatings in terms of crack propagation could be ascribed to the possibility of tailoring the thermal expansion coefficient (α), which minimizes the α mismatch between the substrate and the coatings.

The antibacterial activity was evaluated against *E. coli* and the results are presented in Fig.A3-4.

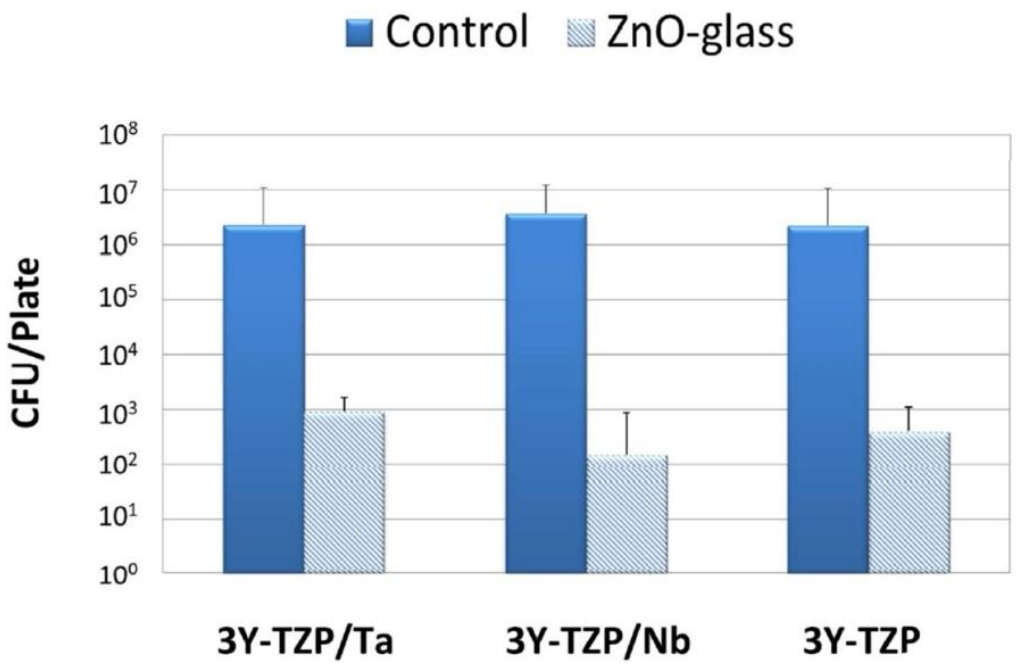

Fig.A3-4. Antibacterial activity against E. coli of the coatings on 3Y-TZP/Ta, 3Y-TZP/Nb and 3Y-TZP. Bars represent media (SD) from 3 replicates

The antimicrobial effectiveness was studied based on the logarithm reduction in viable counts of the tests bacteria. It was calculated by subtracting the log10 colony counts in the control sample (no biocide added) from those present in the problem samples. It can be seen that all coatings achieve a logarithm reduction >3, that means a safe disinfection. The antimicrobial properties of the glass powder are due to the Zn release to the media as was determined in previous studies together with the glass corrosion in different media [3].

Besides the antimicrobial properties, the specific physicochemical characteristics of the material surfaces influence on the biofilm adhesion process [12]. For instance, roughened surfaces promote a higher bacterial adhesion and the subsequently higher biofilm formation than ultrasmooth surfaces. This is due to irregularities and the higher surface area provide more favorable sites of colonization [13, 14]. In this study, despite higher specific area for the coatings, significantly lower quantity of *E. coli* adhesion on the coated surfaces was

found. These results demonstrate that the bacterial adhesion and proliferation is inhibited by the coating.

To test the in vitro biocompatibility of samples, we determined the eventual cytotoxicity of 6 biomaterial discs (coatings on 3Y-TZP/Ta, 3Y-TZP/Nb and 3Y-TZP and their respective controls with no coating) by the NRU assay following the protocol described in ISO 10993-5. Fig.A3-5 shows the percentage of viable cells cultured in contact with the different biomaterials during 24h.

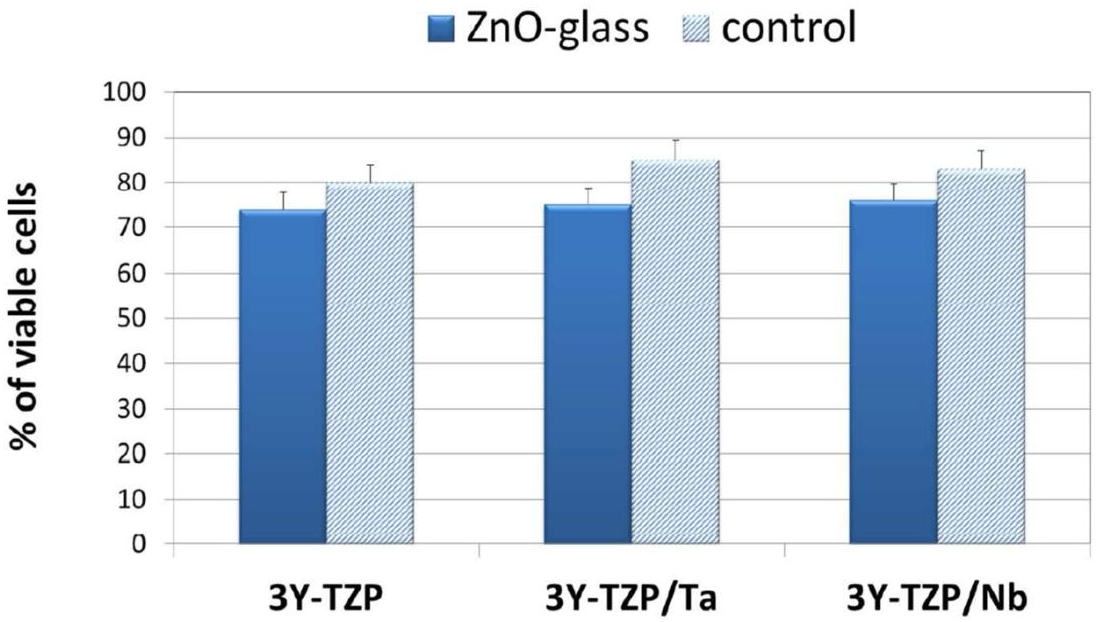

Fig.A3-5. Percentages of viable cells (NIH-3T3) after 24h of culture in presence of the coatings on 3Y-TZP/Ta, 3YTZP/ Nb and 3Y-TZP. Bars represent media (SD) from 3 replicates

The percentage of viable cells was calculated as described in Experimental section. According to ISO 10993-5, no potential cytotoxicity was observed with any material since the percentage of viability was >70 %. These results indicates that our coating are free of harmful extractable or have an insufficient quantity of them to cause deleterious effects in vitro on selected cells under conditions used in the test.

A3.4 Conclusions

A mechanically stable glass antimicrobial coating has been obtained on biocermets (3Y-TZP/Ta and 3Y-TZP/Nb) and on 3Y-TZP ceramic at 725ºC in argon and air atmosphere, respectively. A high antimicrobial activity (>3 log of reduction) versus the gram-bacterium *E.coli* without toxicity for NIH3T-cells has found. The results obtained *in vitro* study suggest that this new zirconia-Ta biocomposite display biocompatibility and therefore, its suitability as a promising candidate for orthopaedic implants and dental devices.

A3.5 References

[1] Lyndon J, Boyd B, Birbilis N. Metallic implant drug/device combinations for controlled drug release in orthopaedic applications. *J. Control. Release*, 2014; 179:63-75.

[2] Sreenivasan P, Gaffar A. Antiplaque biocides and bacterial resistance: a review. *J. Clin Periodontology*, 2002; 29:965–974.

[3] Esteban LT, Prado C, Cabal B, Sanz J, Torrecillas R, Moya JS. Antibacterial and antifungal activity of ZnO containing glasses. *Plos One*, 2015; 10:e0132709

[4] Brayner R, Iliou RF, Brivois N, Djediat S, Benedetti M, Fiévet F. Toxicological Impact Studies Based on *Escherichia coli* Bacteria in Ultrafine ZnO Nanoparticles Colloidal Medium. *Nano letters*, 2006; 6:866-870.

[5] Huh AJ, Kwon YJ, "Nanoantibiotics": A new paradigm for treating infectious diseases using nanomaterials in the antibiotics resistant era. *J. Control. Release*, 2011; 156:128-145.

[6] Reddy KM, Feris K, Bell J, Wingett D, Hanley C, Punnoose A. Selective toxicity of zinc oxide nanoparticles to prokaryotic and eukaryotic systems. *Appl. Phys. Lett*., 2007; 90:213902.

[7] Esteban LT, Díaz L, Prado C, Cabal B, Torrecillas R, Moya JS. Calcium and Zinc Containing Bactericidal Glass Coatings for Biomedical Metallic Substrates. *Int. J. Mol. Sci*., 2014; 15:13030–1304.

[8] ISO 22196-2011, standard method (Measurement of antibacterial activity on plastics and other non-porous surfaces).

[9] ISO 10993-2009. Biological evaluation of medical devices. Part 5: Tests for cytotoxicity: in vitro methods.

[10] Borenfreund E, Puerner J. Toxicity determined in vitro by morphological alterations and neutral red absorption. *Toxicol. Lett*., 1985; 24:119–124.

[11] Heimann RB, Lehmann HD. Bioceramic Coating for Medical Implants: Trends and Techniques KGaA, Wiley-VCH Verlag GmbH & Co., 2015.

[12] Teughels W, Van Assche N, Sliepen I, Quirynen M. Effect of material characteristics and/or surface topography on biofilm development. *Clin Oral Implants Res*, 2006; 17:68–81.

[13] Bürgers R, Gerlach T, Hahnel S, Schwarz F, Handel G, Gosau M. In vivo and in vitro biofilm formation on two different titanium implant surfaces. *Clin Oral Implants Res*, 2010; 21:156–164.

[14] Quirynen M, De Soete M, Van Steenberghe D. Infectious risks for oral implants: A review of the literature. *Clin Oral Implants Res*, 2002; 13:1–19.